

**Alma Mater Studiorum – Università di Bologna**

**DOTTORATO DI RICERCA IN**

**Ingegneria Civile, Chimica, Ambientale e dei Materiali**

**Ciclo XXXIII**

**Settore Concorsuale: 09/D3 - IMPIANTI E PROCESSI INDUSTRIALI CHIMICI**

**Settore Scientifico Disciplinare: ING-IND/25**

**SUSTAINABILITY AND RISK MANAGEMENT OF LNG AS A FUEL FOR  
MARINE TRANSPORTATION**

**Presentata da: Tommaso Iannaccone**

**Coordinatore Dottorato**

**Prof. Luca Vittuari**

**Supervisore**

**Prof. Valerio Cozzani**

**Co-Supervisore**

**Dr. Byongug Jeong**

**Esame finale anno 2021**



*All'uomo, nella sua fragile barchetta, è dato il remo in mano proprio perché  
segua non il capriccio delle onde ma la volontà della sua intelligenza.*

*-Johann Wolfgang Goethe*



# Table of Contents

Abstract .....	1
Chapter 1. Introduction.....	1
1.1. Shipping emissions.....	1
1.2. Ship emissions abatement technologies .....	2
1.3. Other alternative marine fuels .....	3
1.4. LNG operations safety record .....	4
1.5. Objectives and outline of the work .....	6
Chapter 2. State of the art on LNG as an alternative fuel for marine propulsion .....	8
2.1. Drivers for the use of LNG .....	8
2.2. LNG-fuelled ships .....	9
2.3. Development of the bunkering infrastructure.....	10
2.4. Categories of LNG storage tanks.....	11
2.5. Description of fuel systems .....	13
2.5.1. High pressure Dual-Fuel technology .....	14
2.5.2. Low pressure Dual-Fuel technology.....	14
2.5.3. Lean-Burn Spark Ignited technology .....	15
2.6. Overview of LNG bunkering operations.....	15
2.7. Main LNG hazards.....	17
Chapter 3. Literature review .....	18
3.1. Regulatory framework of LNG as a ship fuel.....	18
3.1.1. Higher level regulations .....	19
3.1.2. Technical standards.....	21
3.1.3. Class rules and industry guidance .....	22
3.2. Emergency planning guidelines .....	26
3.3. Inherent safety and risk assessment.....	27
3.4. Numerical modelling of cryogenic tanks pressurization dynamics .....	28
3.5. Sustainability studies of alternative marine fuels .....	29
Chapter 4. Research questions .....	31
Chapter 5. Sustainability of LNG as an alternative marine fuel .....	32
5.1. Case study definition.....	33
5.2. Environmental impact .....	35
5.3. Economic implications .....	36
5.4. Safety implications.....	38
5.5. Normalisation of indicators.....	40

5.6.	Aggregation of indicators .....	41
5.7.	Results.....	43
5.7.1.	Level 1 impact indicators .....	43
5.7.2.	Aggregated key performance indicators (Level 2 and Level 3).....	46
5.7.3.	Sensitivity analysis.....	48
5.8.	Conclusions .....	50
Chapter 6.	Risk assessment of LNG bunkering operations.....	51
6.1.	Inherent safety assessment of LNG bunkering technologies.....	51
6.1.1.	Reference systems for LNG bunkering and supply .....	52
6.1.2.	Reference systems for conventional bunkering with diesel fuels .....	55
6.1.3.	Methodology .....	57
6.1.4.	Description of inherent safety KPIs .....	58
6.1.5.	Results and discussion .....	60
6.2.	Integration of managerial aspects and simultaneous operation in LNG bunkering risk analysis .....	64
6.2.1.	Overview of the developed approach.....	64
6.2.2.	Definition of the test-case .....	69
6.2.3.	Results and discussion .....	71
Chapter 7.	Numerical simulation of LNG tanks exposed to fire.....	84
7.1.	Description of experimental fire test of double-walled LNG tanks.....	85
7.1.1.	TNO test (2015).....	85
7.1.2.	US DOT's FRA test (2017).....	88
7.2.	CFD modelling .....	90
7.2.1.	Theoretical background .....	90
7.2.2.	Set of governing equations .....	91
7.2.3.	Tank insulation.....	97
7.2.4.	Case study definition.....	100
7.2.5.	Mesh generation and numerical setup .....	101
7.2.6.	Safety Key Performance Indicators (KPIs).....	103
7.3.	Modelling results.....	105
7.3.1.	Validation of the model .....	105
7.3.2.	Analysis of the results of the case studies.....	108
7.3.3.	Assessment of safety Key Performance Indicators .....	116
7.4.	LNG tanks exposed to distant pool fires.....	118
7.4.1.	Definition of boundary condition.....	118
7.4.2.	Main results .....	120
7.5.	Conclusions .....	123

Chapter 8. Safety of fuel preparation room on-board LNG fuelled ships.....	124
8.1. Description of the case study .....	125
8.2. Detailed modelling of on-board LNG pool fires.....	126
8.2.1. Pool characteristics.....	127
8.2.2. Definition of simulation cases and numerical setup.....	130
8.3. Modelling results.....	133
8.3.1. Grid independence .....	134
8.3.2. Pool fire consequences and gas species concentration inside FPR.....	135
8.4. Conclusions .....	140
Conclusions .....	141
Limitations and suggestions for future research.....	144
Acknowledgments.....	145
References .....	146
Nomenclature .....	160
Greek letters.....	164
Subscripts .....	164
Acronyms .....	165
List of figures .....	166
List of tables.....	170
Appendix.....	173
Appendix A - Details of sustainability assessment.....	174
Appendix B – Detailed results of inherent safety assessment .....	178
B.1 Main features of reference schemes .....	178
B.2 Consequence evaluation for inherent safety assessment.....	181
B.3 Sensitivity analysis for the management modification factor.....	185
B.4 Dangerous scenario frequencies.....	187
Appendix C - One-dimensional transient heat conduction analysis .....	189
Appendix D - Additional CFD results .....	190
D.1 Cases A85 and B85.....	190
D.2 Cases A15 and B15.....	190
D.3 FDS modelling results for cases HP-1 and HP-2.....	196

# Abstract

The shipping sector contributes significantly to global greenhouse gas emissions, along with a number of other pollutant species, since maritime activities typically rely on the use of heavy, less refined fossil fuels. As the worldwide energy demand is predicted to grow in the near future, international authorities have started developing mitigation strategies to curb the amount of pollutant emissions generated by maritime activities. More stringent environmental regulations have been adopted, introducing tight emission limits and requirements for ship fuels' sulphur content. In this context, the use of liquefied natural gas (LNG) as an alternative ship fuel is currently considered by shipowners as an economical and feasible solution to comply with the regulations in force. The growing interest for LNG-fuelled vessels also determined the development of a network of small-scale LNG facilities as part of the fuel supply chain, as well as an increase in road transportation of LNG.

Substituting conventional marine fuels with LNG marks a fundamental step towards a reduction of emissions due to maritime transportation of goods and passengers. However natural gas is a highly flammable substance and concerns over the safety of its use onboard ships demand a thorough evaluation, especially when considering passenger ships and port activities.

Despite the positive safety record of the LNG shipping industry, the fire hazard posed by this substance cannot be disregarded. Moreover, process conditions encountered throughout the small-scale supply chain and in fuel gas supply systems installed on board typically differ from those of LNG carriers or large-scale storage terminals.

The present study aims at a comprehensive safety assessment of marine LNG technologies, focusing on small-scale applications and passenger ships, seeking to fill the current knowledge gap in this field. An in-depth evaluation of the safety of existing technologies for LNG bunkering and onboard fuel gas supply is carried out, providing key information about the credible accident scenarios and their expected consequences. The safety criticalities are identified based on the application of specifically developed models for the evaluation of the inherent safety performance of LNG bunkering and propulsion technologies.

As a starting point, a sustainability assessment methodology is developed, to evaluate the performance of alternative LNG ship fuel systems, allowing a comparison with conventional technologies based on marine fuel oil. A multi-criteria decision approach is defined to rank the sustainability performance of the alternative systems considered with a focus on environmental, economic and safety aspects. Specific impact indicators are defined and aggregated to calculate an overall sustainability impact index and obtain a synthetic sustainability fingerprint of the alternatives. The results allowed a quantification of the trade-off issues between environmental and safety performance of LNG versus conventional propulsion technologies.

A quantitative method for inherent safety assessment is developed to allow a comparative evaluation of the inherent safety performance of the main LNG bunkering technologies, also with respect to conventional fuel bunkering processes that were considered as a reference baseline. The developed methodology allowed to rank the inherently safer solution among the assessed technologies, also allowing the identification of critical process units and operations.

A dedicated methodology for accident frequency estimation was used to introduce operational and organizational factors into the conventional quantitative risk assessment framework, aimed at determining the impact of managerial aspects over the risk level of port-to-ship LNG bunkering process while also addressing the effect of simultaneous port operations. Societal and individual risk figures are estimated considering two opposite management scenarios and compared to baseline risk levels predicted using the typical quantitative risk assessment approach.

The results of the application of the above methods allowed the identification of two safety critical elements onboard LNG fuelled ships: the fuel preparation room and the LNG storage tanks.

Part of the work is thus dedicated to set up a specific modelling approach for the performance of pressurised cryogenic storage tanks exposed to fire scenarios. A computational fluid dynamic (CFD) setup is developed to predict the consequences of accidental fires attacking double-walled, vacuum insulated tanks used for storage and transportation of LNG in a range of different small-scale applications. The model allows the numerical simulation of cryogenic tanks exposed to extremely high heat loads, overcoming the limitations of the previous works, and providing precise data for further analysis of the tank structural integrity under extreme conditions. The model was also applied to evaluate the response of LNG storage tanks exposed to distant hydrocarbon pool fires.

Finally, a consequence modelling of LNG fire scenarios occurring inside the fuel preparation room of gas-fuelled ships is carried out using CFD tools. This approach allowed for a preliminary evaluation of the heat flux received by the ship structure also considering the influence of the forced ventilation system, providing valuable results for performance-based design approaches and to assess the possibility of accident escalation.

The obtained results represent a first step towards a wider approach aimed at enhancing the safety level of the entire LNG supply chain for maritime propulsion. Furthermore, these results can make a valuable contribution to support the decision-making process for shipowners and port authorities in the design and safety assessment of such systems, both in port areas and onboard ships, and may provide guidance for emergency responders.

# Chapter 1. Introduction

## 1.1. Shipping emissions

Shipping is an essential link in the global supply chain, and a key part of the European Union economy. It is also one of the most energy-efficient modes of transport available. According to the 2017 European Environment Agency report on aviation and shipping (European Environment Agency, 2018), transport accounts for almost a quarter of Europe's greenhouse gas (GHG) emissions. Within this sector, shipping is responsible for about 13% of EU's GHG emissions and of 2.2% of global GHG emissions, as reported by the third International Maritime Organization (IMO) GHG study (International Maritime Organization, 2015). By the end of the twentieth century, the IMO started addressing the environmental impact caused by marine activities, adopting MARPOL Annex VI, which introduces emission limits for SO<sub>x</sub> and NO<sub>x</sub> (Thomson et al., 2015). However, it is expected that world energy consumption will rise nearly 50% between 2018 and 2050 and energy-related CO<sub>2</sub> emissions will grow at an average rate of 0.6% per year between 2018 and 2050 (US Energy Information Administration, 2019). IMO and EU committed to strongly reduce GHG emissions from the shipping sector to achieve the objectives set by the Paris agreement. On a global scale, the IMO recently revised Annex VI of MARPOL convention (International Maritime Organization, 2008) introducing requirements for fuels' sulphur content and emissions abatement technologies installed on seagoing vessels. Starting from 2020, fuel sulphur content is drastically reduced from 3.5% in mass up to 0.5% globally and further cut to 0.1% for sensible sea zones defined as Emission Control Areas (ECAs).

In order to meet the 60% GHG emissions reduction target (with respect to 1990 levels) by 2050 set for the transport sector in the European Commission's 2011 Transport White Paper (European Commission, 2011), more sustainable behaviour was encouraged, resulting in the adoption of the alternative fuels Directive (European Parliament, 2014). Moreover, EU was the first organization to set out a strategy in 2018 to monitor and report CO<sub>2</sub> emission from any large ship (over 5,000 gross tonnage) loading or unloading cargo or passengers at ports in the European Economic Area (European Commission, 2017), followed by IMO, which implemented its Data Collection System in 2019 (International Maritime Organization, n.d.).

The mentioned European alternative fuels Directive promotes the use of fuels having a lower environmental impact than oil such as hydrogen, electricity, biofuels, and natural gas (either compressed or liquefied). For the maritime industry viable solutions to achieve the emission reduction goals are represented by the adoption of exhaust gas treatment systems or the switch towards alternative cleaner fuels (Horvath et al., 2018). Recent trends in international emission regulations, technology development and shipping economics make liquefied natural gas (LNG) an increasingly attractive marine fuel. Switching from traditional fuel oil to natural gas can allow a relevant reduction in SO<sub>x</sub> emissions, along with negligible emissions of NO<sub>x</sub> and particulate matter (PM). Moreover, a CO<sub>2</sub> emission reduction up to 25% may be achieved if LNG is used since it is less carbon-intensive than fuel oil (Helfre and Boot, 2013).

## 1.2. Ship emissions abatement technologies

Several solutions can be adopted to reduce shipping emissions, which can be identified in four different groups (Smith et al., 2019):

- 1) Technologies aimed at improving ships' energy efficiency;
- 2) Operational measures and practices improving energy efficiency;
- 3) The use of alternative fuels or renewable energy sources (e.g., wind propulsion);
- 4) Technologies specific to the capture or treatment of exhaust emissions (GHG and air pollutant emissions).

Besides the emissions regulations, the IMO has adopted mandatory energy-efficiency measures to reduce emissions of greenhouse gases from international shipping as amendments to MARPOL Annex VI in 2011 which came into force on 1 January 2013. The regulations make the Energy Efficiency Design Index, which provides a measure of the CO<sub>2</sub> emissions per cargo carried, mandatory for new ships, and the Ship Energy Efficiency Management Plan, mandatory for all ships regardless their age (International Maritime Organization, 2018).

To achieve carbon-neutrality in the shipping sector, a number of different technological solutions are currently being explored, ranging from the use of alternative fuels such as LNG, methanol, biogas or hydrogen, to a radical change of energy source, with the exploitation of solar or wind energy. As reported in a survey conducted among Baltic shipping companies (Stalmokaite and Yliskylä-Peuralahti, 2019), the recent technological evolution in the maritime industry is a response to the tightening of environmental regulations; however some of the companies surveyed believe that the use of cleaner fossil fuels can only be a short-term solution to tackle emission reduction. Investing in more radical propulsion technologies, such as electricity, wind and solar energy is perceived as the most promising pathway towards carbon-neutral shipping. A study carried out for the Danish maritime cargo sector investigates the emissions of different alternative energy sources for ships under different socio-economic scenarios (ben Brahim et al., 2019). The authors conclude that sailing cargo ships, driven by a combination of wind and electricity from batteries seem to be cost-efficient only in the case of a very strong fall in battery and power conversion hardware costs. Among the technological solutions explored, hydrogen, methanol and ammonia have comparable cost performance and could represent longer term solutions for emission reduction. An insight into the different technical challenges concerning the use of alternative fuels is given in Section 1.3.

At the present date, the use of “end of pipe” abatement technologies like scrubbers and Selective Catalytic Reduction systems (SCR) represents an economical solution to meet requirements for SO<sub>x</sub> and NO<sub>x</sub> emission levels, especially when considering compliance to environmental regulation of existing vessels, since they do not require a switch to different machinery. Scrubber and SCR systems are well consolidated technologies developed for land applications. Scrubbers can work either exploiting an “open-loop” or a “closed-loop” configuration: the former type uses only seawater to neutralize the SO<sub>2</sub> contained in the exhaust gas that is re-emitted into the sea, while the closed-loop configuration relies on the use of wash water added with a caustic reagent (e.g., sodium hydroxide). The bleed off from closed-loop scrubbers is sent to the water treatment system and then directly discharged overboard or sent to a dedicated holding tank in cases when a “zero discharge” mode is required.

SCR systems require the use of urea solutions combined with a metal catalyst to perform reduction of NO<sub>x</sub> to N<sub>2</sub> and water. This system allows for a reduction in levels of NO<sub>x</sub> by above 90% when working in optimal conditions (Brynnolf et al., 2014b).

It is important to remark that an optimal solution for emission reduction cannot be easily identified since a number of economic variables come into play, first of all the variability of oil prices, that can significantly influence the benefits of the mentioned solutions.

### **1.3. Other alternative marine fuels**

The growing interest towards alternative marine fuels is mainly motivated by the IMO 2020 sulphur cap that limits the sulphur content of marine fuels. Shipowners and building companies are exploring the use of unconventional fuels, anticipating a possible increase in the prices of low-sulphur fuel oil. Indeed, IMO 2020 compliant fuel prices spiked during the last months of 2019 in preparation to sulphur cap transition; however, the price spread with traditional fuel oil (i.e., high-sulphur fuel oil) has significantly reduced during the first trimester of 2020. Moreover, investing in less pollutant fuels might be beneficial for shipping companies' reputation as reported by Stalmokaite and Yliskylä-Peuralahti, (2019).

As of today, the most promising alternative fuels are LNG, methanol, biofuels, hydrogen, Liquefied Petroleum Gas (LPG), and ammonia. Among the different options, LNG is deemed to be the most technological-ready and cost-effective alternative: as of July 2020, a total of 117 LNG-fuelled ships are currently in operation and 220 more are on order as reported by DNV-GL (2020). Switching to LNG should allow for a reduction in emissions of CO<sub>2</sub> up to 20%, SO<sub>x</sub> up to 100%, NO<sub>x</sub> up to 90%, and PM up to 99% as claimed by (IGU, 2015).

Methanol is typically produced from synthesis gas, which can be produced from either natural gas or biomass. Similarly to LNG, it has very low sulphur content, but it is liquid at standard temperature and pressure, therefore much easier to handle. Moreover, vessel retrofitting costs are advantageous compared to LNG (Brynnolf et al., 2014a).

As reported in (DNV GL, 2019), there is currently a limited uptake of biodiesel fuels in shipping. The limited availability of biomass to produce biodiesel can also lead to a lack of available fuel for maritime use, being in competition with road and aviation use. The main advantage of using biodiesel relies on the bunker infrastructure, since the conventional petroleum-based fuel infrastructure can readily be used.

Hydrogen represents an ideal alternative fuel thanks to the absence of operational GHG emissions, even if there can be upstream GHG emissions, depending on its production pathway, that need to be considered. Hydrogen is most efficiently used in fuel cells (around 50-60 % efficiency), but can also be used with internal combustion engines, with a lower efficiency. Onboard storage of hydrogen is currently challenging due to space uptake. Furthermore, the lack of bunkering infrastructure and the significant costs of safety measures required to handle such dangerous material are limiting the interest in such alternative fuel to research. A number of EU-funded research project are currently active, such as H2SHIPS (H2SHIPS Partners, 2019) and FLAGSHIPS (FLAGSHIPS Partners, 2019).

Despite showing environmental benefits comparable to LNG, very limited experience is available related to the use of LPG as a ship fuel. Although technical rules and standards for the use of low-flashpoint fuels (such as LPG) are already in place, there are currently only 34 vessels running on LPG according to latest figures by DNV-GL (2020). Low energy cost (close to LNG) and low capital costs make this fuel as attractive as LNG. On the other hand, a major downside to LPG as an alternative fuel is its environmental performance when produced from fossil sources. According to Hammer, (2019) using LPG as a fuel might eliminate SO<sub>x</sub> and PM emissions and reduce NO<sub>x</sub> emissions depending on the engine technology used.

Similarly to hydrogen, GHG emissions from ammonia are high with the current production from fossil energy sources without Carbon Capture and Storage, until the transition to renewable power production is well under way (DNV GL, 2019). Ammonia can be used either in internal combustion engines or fuel cells where it can be used directly or split into hydrogen and nitrogen. According to Hansson et al. (2020) there are no commercially available ammonia propulsion systems, even if research in this field is currently ongoing. Ammonia is a toxic substance both for humans and environment, thus safety systems and mitigation measures need to be put in place that will raise installation costs. In addition to this, the bunker infrastructure would need to be completely developed, making ammonia a possible alternative fuel for the future, provided that issues related to NO<sub>x</sub> emissions are tackled (Valera-Medina et al., 2018).

#### **1.4. LNG operations safety record**

Historical accident analysis allows a better understanding of the root causes and consequences of accidents involving LNG releases, contributing to the identification of hazards posed by LNG technologies. Handling, storage and transportation of LNG is distinguished by a positive safety record: nearly 100,000 cargoes have been delivered since the first LNG carrier sailed off in 1964 without recording loss of cargo tank containment or cargo-related loss of life (Riviera Maritime Media Ltd, 2019). In recent years the expansion of the LNG market increased the operational activity in the LNG transportation chain, paving the way for onshore transportation via tanker trucks, and more recently starting the discussion about rail transportation in the USA (Roman, 2020). Consequently, LNG accidents shifted from production or import terminals to transportation chain.

According to figures reported by the US DOT Pipeline and Hazardous Materials Safety Administration (U.S. DOT PHMSA, 2020), the total number of accidents involving LNG reported during the last 20 years (2000-2019) was 18, for an estimated total cost of about 82 billion dollars. No fatalities are associated with these incidents and only one operator injury resulted according to the source (accident at Plymouth LNG Peak Shaving Plant in 2014). A summary of LNG accidents is reported in Table 1.

Table 1: List of LNG-related accidents

Year	Location (Vessel)	Facility type	Type of event	Fatalities/Injuries	Reference
1944	Cleveland, OH, USA	Peak shaving	Flash fire, explosion	128/200-400	(National Association of State Fire Marshals, 2005)
1971	Panigaglia, Italy	Regasification terminal	Gas release due to rollover	-/-	(Sam Mannan, 2012)
1979	Cove Point, MD, USA	Regasification terminal	Confined Explosion	1/1	(National Association of State Fire Marshals, 2005)
1983	<i>Norman Lady</i>	LNG carrier ship	LNG spillage	-/-	(Woodward and Pitblado, 2010a)
1989	<i>Tellier</i>	LNG carrier ship	LNG spillage	-/-	(Woodward and Pitblado, 2010a)
1989	Thurley, UK	Peak shaving	Flash fire	-/2	(Woodward and Pitblado, 2010a)
1993	Bontang, Indonesia	Export facility	LNG spillage	-/-	(CHIV International, 2014)
2002	Tivissa, Spain	LNG tanker truck	BLEVE	1/2	(Planas-Cuchi et al., 2004)
2004	Skikda, Algeria	Liquefaction plant	Explosion	27/80	(National Association of State Fire Marshals, 2005)
2011	Zarzalico, Spain	LNG tanker truck	BLEVE	1/-	(Planas et al., 2015)
2014	Plymouth, USA	Regasification terminal	Gas release following damage to LNG tank insulation	-/1	(Rukke and Katchmar, 2016)
2019	Shaanxi, China	LNG tanker truck	BLEVE	-/-	(Wang et al., 2020)

## 1.5. Objectives and outline of the work

The overall objective of this PhD research project was to address the safety aspects of the use of LNG as a marine fuel, integrating such issues with an economic and environmental analysis to outline the current state of marine LNG industry and provide a comprehensive framework of the safety of LNG-fuelled ships. Specific emphasis was given to the quantification of risks related to the LNG bunkering operations and to the modelling of pressurized LNG storage tanks exposed to hydrocarbon fires. Furthermore, the consequences of fires originating onboard LNG-fuelled ships were investigated. More specifically, the main aims of the project are:

1. To outline the inherent safety profile of different LNG bunkering concepts, understanding which part of the delivery chain for LNG as a fuel can be considered the most hazardous;
2. To provide a computational model that can be used to predict the thermo-fluid dynamic behaviour of commonly used LNG storage vessels in case of flame engulfment;
3. To extend the scope of quantitative risk assessment (QRA) of LNG bunkering operations integrating the effect of managerial policies;
4. To investigate the effects of onboard fire scenarios inside the fuel preparation room of LNG-fuelled vessels in terms of radiation levels to which the ship hull and the gas fuel equipment can be exposed;
5. To integrate safety aspects of different Fuel Gas Supply Systems into the sustainability assessment of LNG propulsion technologies in order to support the decision-making process.

Chapter 2 presents the state of the art in the use of LNG as alternative marine fuel. An overview of the main information regarding the existing LNG-fuelled fleet is given, together with a description of the LNG as a fuel supply chain structure and an outline of the current technologies used for gas-fuelled ship propulsion.

Chapter 3 reports a literature review of the main aspects concerning safety of LNG-fuelled ships, defining the current context for the use of LNG as an alternative marine fuel. The regulatory framework is firstly presented, discussing the relevant international regulations, standards, and guidelines. The Chapter also includes a review of the latest studies, tools, and assessment methodologies addressing the three core areas discussed in this thesis. A review of risk assessment studies of LNG installations is presented in Section 3.3, along with approaches proposed for the quantification of inherent safety. An overview of the numerical and experimental studies carried out to model the behaviour of cryogenic tanks exposed to fire conditions is given in Section 3.4, while a description of recent environmental impact and sustainability studies for alternative marine fuels is presented in Section 3.5.

The main research questions addressed in the present study are summarised in Chapter 4.

Chapter 5 describes the sustainability assessment of the main LNG-based fuel system used in the maritime sector. A reference case study is defined as the basis for the application of the proposed sustainability assessment methodology, that encompasses three fundamental domains: environmental impact, economic feasibility, and the inherent safety profile of the assessed fuel systems. A set of indicators is used to quantify the impact for each domain, then results are used to determine a sustainability fingerprint and define a ranking of the evaluated marine fuelling technologies.

Chapter 6 focuses on the safety aspects related to LNG bunkering operations. More specifically, a comparative safety assessment between marine LNG and conventional fuel bunkering technologies is presented in Section 6.1. The characteristics of four different bunkering concepts are outlined, providing the basis for the application of a specific methodology aimed at the quantification of the inherent safety profile of LNG, marine gasoil (MGO) and intermediate fuel oil (IFO) bunkering processes. A consequence-based approach is developed and applied to rank the assessed alternatives and identify the inherently safer solutions for maritime fuel bunkering, also highlighting criticalities to be address for the future development of green shipping technologies. In Section 6.2 a case study is defined to perform a holistic safety analysis of the LNG refuelling operations carried out in port. A dedicated methodology for accident frequency estimation is exploited to integrate operational and managerial aspects in the conventional QRA framework, with the objective to quantify the risk modification induced by human-related elements during the bunkering process. The influence of management on the expected safety performance is evaluated comparing the risk calculated assuming two different management scenarios against risk figures obtained disregarding the effect of organizational factors.

Chapter 7 focuses on the computational modelling of pressurized cryogenic vessels exposed to full engulfing hydrocarbon pool fires. Firstly, a description of the publicly available experimental investigation of accident scenario involving the engulfment of cryogenic tanks in fires is proposed to help identifying the most relevant results and criticalities of the experimental activity carried out in the recent years. A Computational Fluid Dynamic (CFD) model developed to evaluate the dynamic behaviour of cryogenic tanks exposed to an engulfing fire scenario is then presented. The model allows the evaluation of tank pressurization rates and temperature distribution of its content, providing the basis for the definition of a set of specific key performance indicators (KPIs) intended to support the safety assessment of LNG tanks during fire exposure. In addition, the proposed modelling approach is also used to evaluate the effects of distant hydrocarbon pool fires on cryogenic LNG tanks, as described in Section 7.4. Advantages and limitations of the modelling setup are analysed in detail.

Lastly, a specific demonstration of CFD tools capabilities is presented in Chapter 8. A detailed consequence assessment study for selected accident scenarios of interest occurring inside an onboard confined space is described. A comparative assessment of LNG pool fire consequences is performed, analysing the incident radiation levels to which the ship structure can be exposed in case of fire originating from two different fuel gas supply systems. Such analysis is aimed at providing useful information to drive performance-based design of gas-fuelled ships and enhance their safety level.

## Chapter 2. State of the art on LNG as an alternative fuel for marine propulsion

Since the early exploitation of Boil-Off Gas (BOG) on cargo ships, the use of methane as an alternative fuel for marine propulsion has experienced a significant growth. Starting from 1970's, LNG was used as a fuel in LNG carriers. In these applications, the BOG produced inside the LNG tanks is used in traditional boiler/steam turbine systems (Curt, 2004). More recently, the Baltic region states have pioneered the use of LNG as a ship fuel in ferries and offshore service vessels for the oil and gas industry (Canadian Natural Gas Vehicle Alliance, 2015). Nowadays the use of methane as alternative fuel for marine propulsion has experienced a significant growth: larger LNG-fuelled vessels, including bulk and chemical carriers and cruise ships, are under construction or already operating (Speirs et al., 2019). The current price of LNG, lower than conventional marine fuel oils, is another attractive factor. Speirs et al. (2019) estimated that the higher capital costs for ships' LNG-based propulsion systems may be recovered between 5- and 16-years payback period considering current price regimes.

### 2.1. Drivers for the use of LNG

The use of LNG for marine vessels is largely driven by the need to comply with stricter international emission control regulations curbing sulphur and nitrogen oxides emissions. Most ships today use heavy fuel oil or marine gas oil as fuel, significantly contributing to the emission of transport-related air pollutants which impact on public health. Due to the high sulphur content of bunker fuel oil, even up to 3,500 times as much sulphur as road vehicle fuel (Sharples, 2019), it is estimated that the shipping sector is responsible for more than 10% of Europe's total SO<sub>x</sub> emissions and about 20% and 8% of NO<sub>x</sub> and PM European total emissions respectively. As reported by Stenersen and Thonstad (2017), the high sulphur amount of ship fuels also affects the emissions of nitrogen oxides and promotes the formation of large particulates.

Having recognized shipping as one of the main transportation sectors contributing to global air pollution, international actors such as IMO and EU have tightened emission regulations pushing navigation companies and shipowners to adapt their activities and consider the use of alternative fuels. In this scenario, LNG is seen as the readiest alternative fuel that can be used during the transition period towards the use of carbon-neutral energy sources.

The key environmental benefits of LNG come from the absence of sulphur (as required for the liquefaction process) and from the reduced well-to-propeller CO<sub>2</sub> emissions that can be around 20% lower than conventional oil fuels according to figures provided by DNV GL – Maritime (2018). However, the reduction of GHG emission might be impaired by methane slip since methane has a global warming potential 28 times higher than the same quantity of CO<sub>2</sub>. This kind of downside mainly affects Lean-Burn Spark Ignited (LBSI) engines that suffer higher methane slips than Diesel cycle gas engines, as reported by Stenersen and Thonstad (2017). On the other hand, Diesel cycle engines, regardless of whether they are fuelled by LNG or by fuel oils, have higher NO<sub>x</sub> emissions compared to engines operating on the otto cycle, therefore a SCR or Exhaust Gas Recirculation system (EGR) will be needed to comply with the IMO tier III NO<sub>x</sub> limits.

Another factor that favours the use of LNG is its competitive price. Compared to other alternative fuels, especially to low-sulphur fuel oil, which is the main alternative for compliance with IMO global sulphur cap, LNG has advantageous price levels.

For the year 2019, LNG had an average price of 4.9 \$/MMBtu (around 15 €/MWh), about four times cheaper than ECA-compliant low-sulphur MGO (0.1 MGO), and around 16 \$/MMBtu cheaper than methanol.

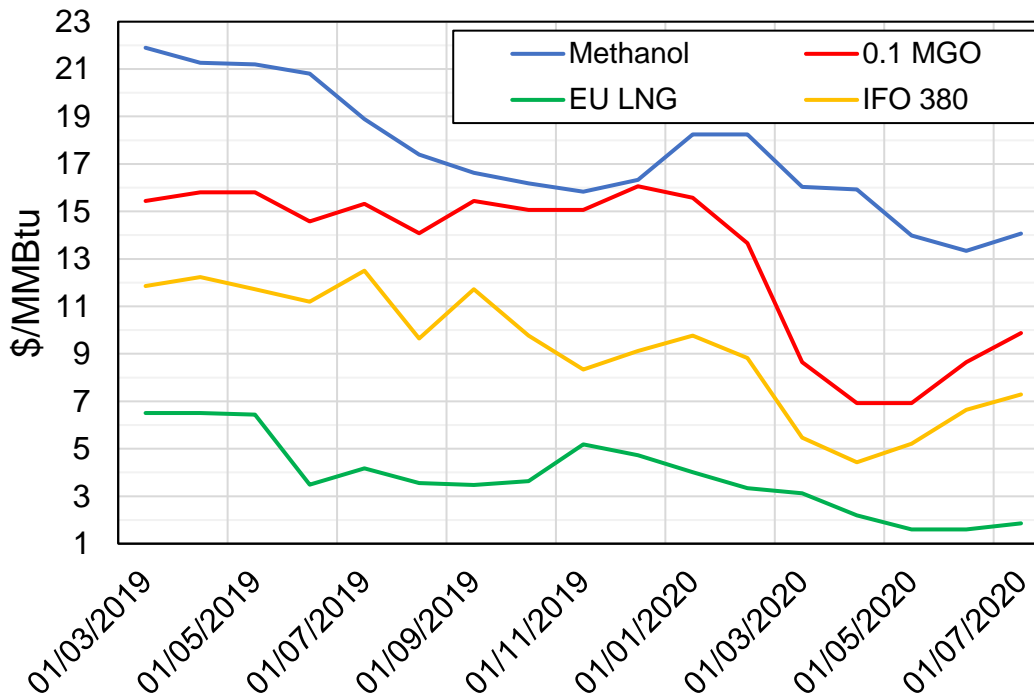


Figure 1: Bunker fuel price in \$/MMBtu. Data retrieved from DNV GL – Maritime (2020).

A further advantage of using LNG as a fuel is the fact that LBSI gas engines are intrinsically compliant with NOx emissions restrictions. This aspect is especially appealing when choosing the propulsion system of newbuild vessels, as from 2021 onwards, all newly built ships operating in the North and Baltic Seas shall be compliant with IMO Tier III emission limits (Sharples, 2019). Therefore, using LNG will not require any additional investment to meet emission requirements and will also allow savings in fuel costs relative to MGO. Besides considerations on the availability of LNG bunker fuel at ports, the economic feasibility of investing on LNG propulsion for newbuild vessels will ultimately depend on the balance between fuel price levels. Considering the actual price levels of IMO-compliant fuels (MGO and low sulphur fuel oil) and high sulphur fuel oil, LNG has currently a significant premium over the mentioned fuels, with a price differential of about 200 \$ per metric tonne and 140 \$ per metric tonne for IMO-compliant fuels and high sulphur fuel oil, respectively.

## 2.2. LNG-fuelled ships

The number of LNG-fuelled ships has been growing steadily during the last 20 years and as of the first half of 2020 it reached a total of 391 seagoing vessels, as reported in Section 1.3. Comparing the figures for the last two years the number of LNG-fuelled ships in service grew by 24.6% between 2018 and 2019 and by 23.8% between 2017 and 2018 (DNV-GL, 2020). A breakdown of LNG-fuelled ships by vessel type is provided in Figure 2. The largest part of the operating LNG fleet, about 25 %, consists of ferries, that together with offshore supply vessels and tanker represent almost half of the operating LNG-fuelled ships. If ship orders were confirmed, crude oil tankers and container ships will almost double their share in the future LNG fleet. An interesting case is represented by cruise ships: the first LNG-fuelled cruise ship is the newly-built *AIDAnova*, owned by Aida Cruises that entered into service in 2019 (Kalosh, 2019), followed by *Costa Smeralda* of Costa Crociere, launched in the late 2019 (Carnival Corporation & PLC, 2019).

As can be seen in Figure 2, shipowners have an evident interest in investing in this market segment. According to DNV-GL (2020) the ordered cruise ships will be delivered between the end of 2020 and 2027.

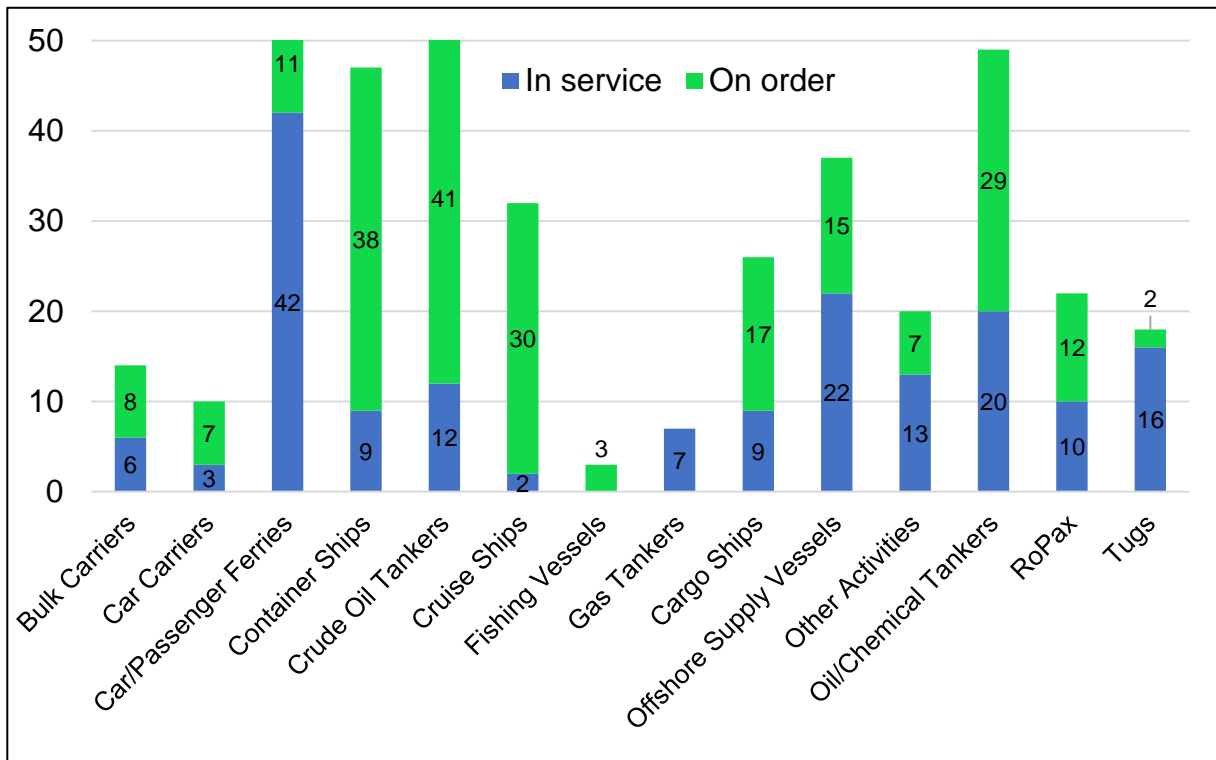


Figure 2: Total number of LNG-fuelled ships sorted by type as of July 2020. Source: Alternative Fuels Insight platform (DNV-GL, 2020).

Based on the data provided by the Alternative Fuels Insight platform (DNV-GL, 2020), there are currently 15 operating LNG bunker vessels, and 22 more to be delivered by 2023. The majority of bunker vessels are operating in European waters, including the world's largest LNG bunkering vessel *Gas Agility* that has a storage capacity of 18,600 m<sup>3</sup> (Bankes-Hughes, 2020). Except for this ship, other bunker vessels have capacities ranging from 5,000 to 10,000 m<sup>3</sup> and one third of operating vessels can store between 1,000 and 5,000 m<sup>3</sup> of LNG. The smallest and oldest bunker vessel is the Swedish *Seagas*, which has a capacity of only 187 m<sup>3</sup>. It is performing refuelling operations for the M/S *Viking Grace* since 2013.

### 2.3. Development of the bunkering infrastructure

The expansion of the LNG market fostered several new investments: as of February 2020, 13 LNG regasification terminals in Europe provide supplementary value-adding services such as reloading, transshipment, small-scale LNG bunkering and truck-loading (IGU, 2020). The supply chain of LNG traditionally relied on large-scale facilities exploiting economies of scale. However, in the recent years a network of small-scale LNG terminals (SSLNG) began to develop driven by favourable investment costs and by the necessity to accommodate an increasing number of smaller volumes demands of LNG. The International Gas Union (IGU) defines small scale liquefaction and regasification facilities as plants with a capacity of less than 1 million tonnes per annum (MTPA), whilst SSLNG carriers are defined as vessels with a capacity of less than 30,000 m<sup>3</sup> (IGU, 2015).

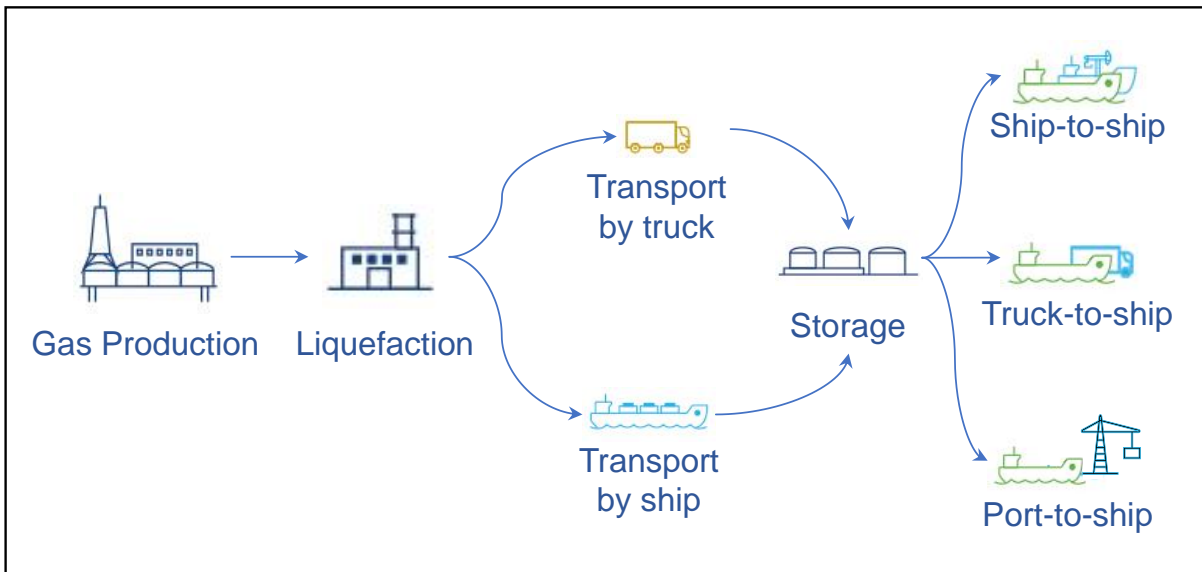


Figure 3: Schematic supply chain of LNG as maritime fuel. Adapted from (SNAM, 2020).

Besides an increased modularity, SSLNG terminals represent a valid solution for supplying energy to remote areas not reached by gas pipelines or where investing in larger installations might not be economical. Moreover, SSLNG projects, offer to the investors immediate and potentially more attractive returns in a shorter term than large-scale LNG projects (Lo Brutto, 2019). The emission reduction measures implemented and the consequent use of LNG as a transport fuel for road and marine uses represent a further driver for the expansion of SSLNG sites: according to Gas Infrastructure Europe, 32 small-scale terminals are already in operation and 6 more are expected to be built in Europe as of June 2020 (Gas Infrastructure Europe, 2020). Small-scale bunkering facilities are a necessary element for the supply chain of LNG as a fuel. An increasing number of LNG-fuelled vessels is already operating, and a growth is expected with 155 ships on order, of which 30 cruise liners. However, this growth requires an adequate number of bunkering infrastructures and a more homogeneous distribution of bunkering sites along the main shipping routes as DNV GL forecasts that by 2050 up to 41% of marine fuel will be LNG (SeaLNG LTD, 2019). In addition to that, coastal SSLNG terminals represent the final step in completing the LNG supply chain, enabling the loading of LNG onto trucks, for onward distribution to power stations and industrial consumers in off-grid locations and also delivering LNG to road filling stations for the use as vehicle fuel (Sharples, 2019).

## 2.4. Categories of LNG storage tanks

Depending on the volume of LNG to be stored two main types of tanks can be used in SSLNG facilities: flat bottom vertical cylindrical tanks or vacuum insulated bullet tanks. The former type are atmospheric cryogenic tanks with capacities ranging from 7,500 m<sup>3</sup> up to 160,000 m<sup>3</sup> for very large terminals, consisting of a primary container made of austenitic steel and an outer shell. As shown in Figure 4, flat bottom tanks can be divided into single, double, or full containment tanks, depending on leakage retaining capacities of the outer shell.

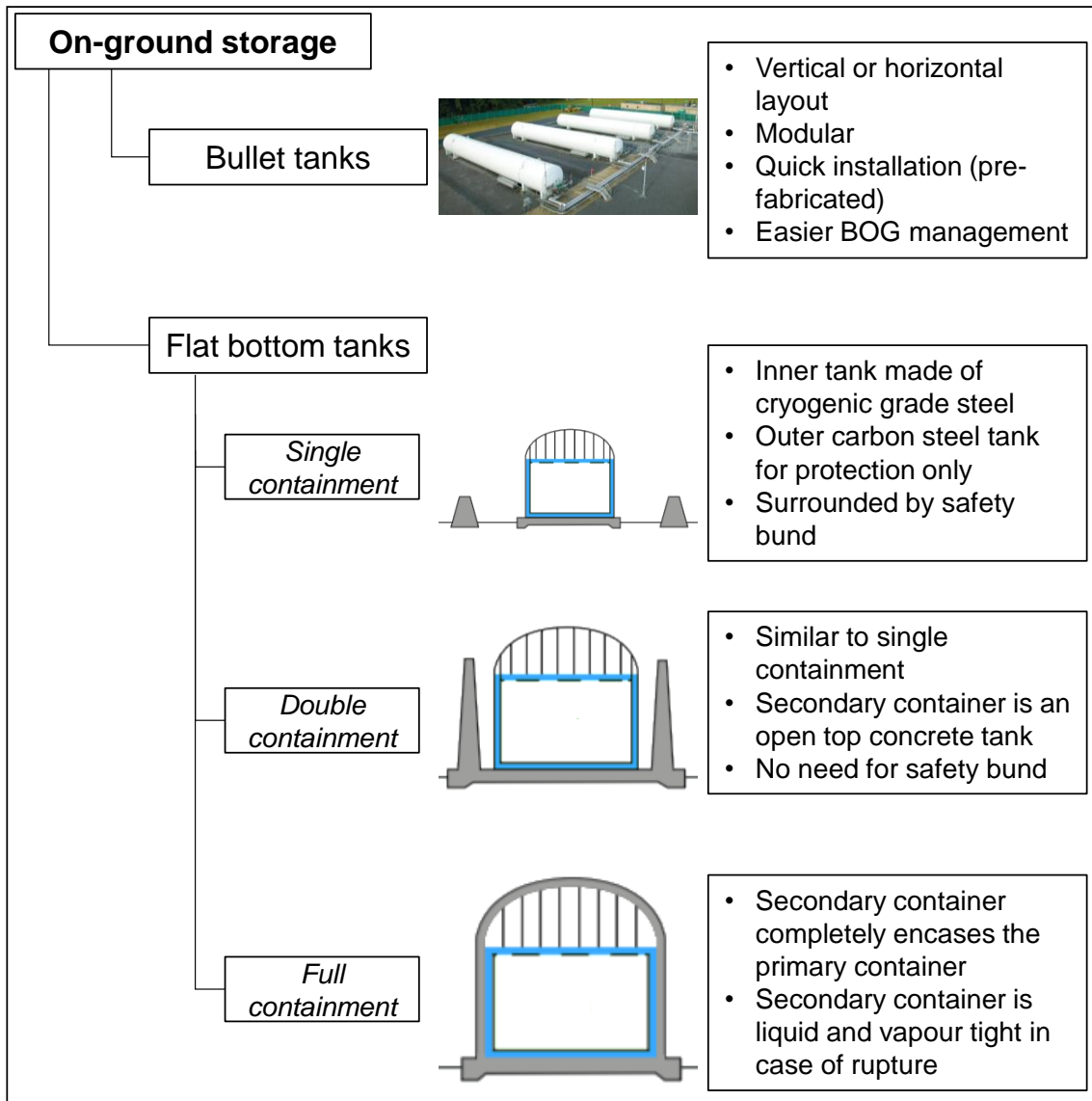


Figure 4: Classification of onshore LNG storage tanks

In a single containment tank, the inner shell made of austenitic steel holds the LNG and an outer shell retains the insulating material but do not provide any containment in case of vapour or liquid release, for which a safety bund is needed. Double containment tanks are built encasing the inner shell in a concrete structure that forms the secondary barrier against liquid spills but will not hold vapour releases. Full containment tanks are designed as a double tank: both inner and outer shells can retain any liquid or vapour release. Bullet tanks are pressure vessels operating between 0.5 - 8 barg with maximum capacities up to 1,200 m<sup>3</sup>. They consist of an inner tank made of cryogenic grade steel and an outer vessel that can be either cryogenic or non-cryogenic steel. The gap between the inner and outer tanks is kept under vacuum conditions and filled with insulating materials. These tanks are modular, flexible and can be installed either in vertical or horizontal positions.

According to Lo Brutto, (2019), the cost of LNG storage for bullet tanks is roughly 2,000 \$/m<sup>3</sup> (for capacities of 1,000 to 15,000 m<sup>3</sup>), while the cost for LNG flat bottom tank is around 1,000 to 1,300 \$/m<sup>3</sup> (for tanks from 15,000 to 30,000 m<sup>3</sup>). For smaller terminals (up to around 15,000 m<sup>3</sup>) bullet tanks are the preferred solution due to cheaper foundation costs and the possibilities to build such equipment as prefabricated modules in factories, reducing site costs (Lo Brutto, 2019). Moreover, pressurised tanks are designed and operated so that no BOG compressor is needed in the terminal, allowing for an easier management of BOG.

Despite the positive safety record of LNG industry, as reported in Section 1.4, the small-scale business has some peculiarities that can arise safety issues. SSLNG installations are likely to be constructed in the proximity of populated areas, such as coastal or harbour zones mainly due to logistic needs (e.g., ease of supply, access to main routes, etc.), whereas larger terminals are located in more remote areas or industrial sites. As outlined in a previous work by Tugnoli et al., (2010), the societal acceptability of newly-built storage and distribution facilities requires a proof that risk for population is negligible. Furthermore, the SSLNG business results scattered and more challenging to manage than large facilities due to the large number of smaller parcels and multiple players involved. For these reasons relevance is given to SSLNG facilities in the present work, since they represent a novel and expanding branch of the LNG industry.

## **2.5. Description of fuel systems**

A fuel gas supply system (FGSS) is designed to deliver the methane fuel to ship' engines at the required operating conditions that depend mainly on the type of engine working pressure. The three principal engine technologies and relative FGSS are briefly discussed in the following. These engine concepts have different combustion characteristics that result in different efficiency and exhaust emissions. The main gas engine technologies are:

1. Low pressure Dual-Fuel engines (LPDF)
2. High pressure Dual-Fuel engines (HPDF)
3. Lean-Burn Spark Ignited engines (LBSI)

As reported by Stenersen and Thonstad (2017), LPDF engines can be either medium speed, 4-stroke, with a power output ranging between 1-18MW, or slow speed, 2-stroke, generating 5-63 MW. LBSI and 2-stroke HPDF engines have more limited power outputs, currently reaching 8 MW at maximum. LBSI are single fuel gas engines used on all gas powered ferries in Norway, whereas LPDF represent the preferred solution for offshore supply vessels (Stenersen and Thonstad, 2017). Slow speed 2-stroke LPDF engines using low pressure gas have entered the market recently and are mainly installed on commercial ships. The slow speed HPDF 2-stroke concept, such as MAN B&W's ME-GI engines, are particularly appreciated for service on large freight ships, such as LNG carriers (Sharples, 2019).

A more detailed analysis of the different features of gas engine concepts is provided in the following. Simplified process flow diagrams (PFD) of the above mentioned FGSS are shown in Figure 5. Typical operating conditions and key features of the FGSS are based on data collected from various research papers (Jeong et al., 2017a) and (Lee et al., 2015a) together with confidential technical information.

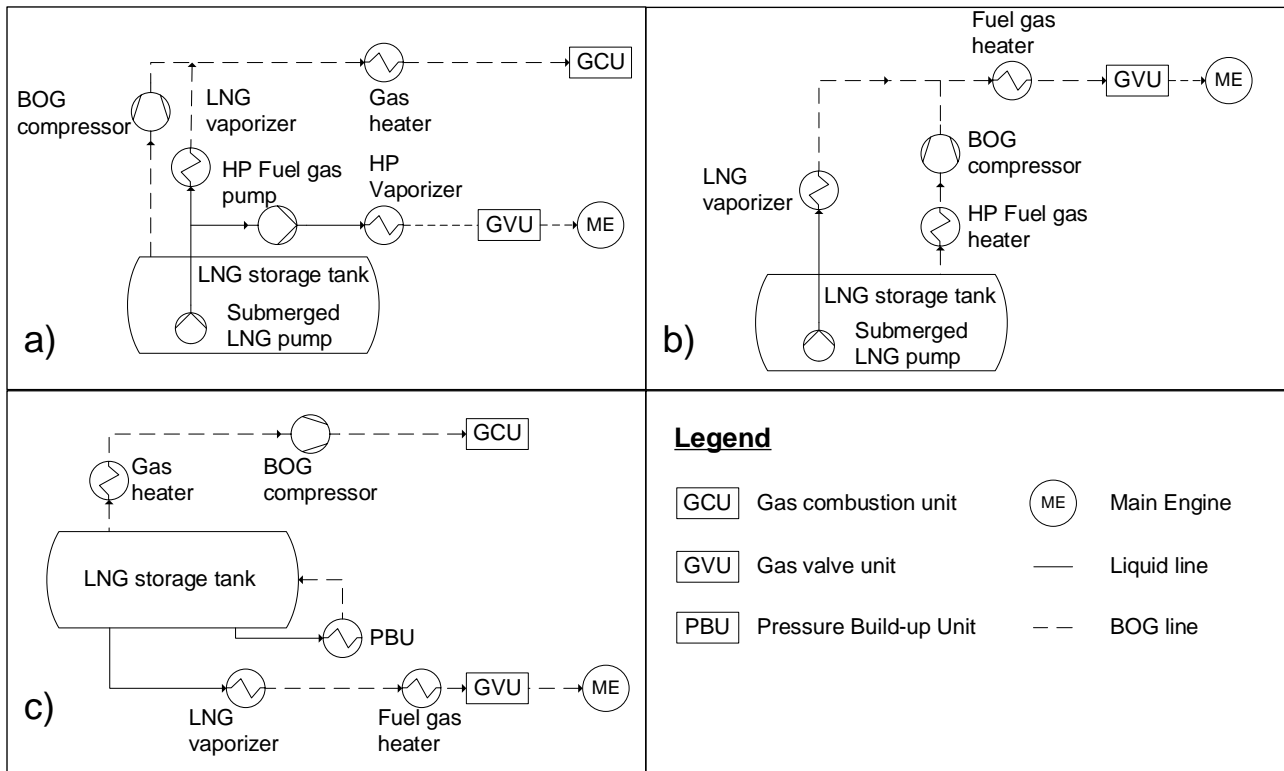


Figure 5: Simplified FGSS schemes for different gas engine concepts: a) High pressure Dual-Fuel; b) Low pressure Dual-Fuel; c) Lean-Burn Spark Ignited.

### 2.5.1. High pressure Dual-Fuel technology

The PFD of a FGSS exploiting HPDF engine technology is shown in Figure 5a. This engine concept is based on diesel operating principle. The LNG is stored in pressurized tanks and pumped up to 300-350 bar before being vaporized. The fuel gas pressure in this system is a function of the liquid flow at the pump discharge and the consumption by the engines. Therefore, the primary pressure control is done by adjusting the pump speed to meet the consumption of the engines. Since the high-pressure pump is a reciprocating unit, there are unavoidable pulsations due to each delivery stroke. In order to smoothen these pulsations, a damper is fitted to each pump skid to absorb these fluctuations. Finally, natural gas is injected directly into the cylinder, after the pilot diesel fuel has ignited. This kind of engine ensures multi fuel capability with no particular requirements for the gas mixture quality and the advantage of eliminating methane slips as there is no gas during the compression stroke (methane is burned as it is injected). On the other hand, it needs an exhaust gas after-treatment to comply with IMO Tier III NO<sub>x</sub> emission limits. This could be implemented using either an Exhaust Gas Recirculation (EGR) or a Selective Catalytic Reduction stage (SCR). A compressor provides the gas combustion units (GCU) with boil-off gas at the required pressure level. The heat generated in the GCU can be transferred into the ship's other system that requires heating, such as domestic hot water or water-glycol (WG) systems for example (Chorowski et al., 2015).

### 2.5.2. Low pressure Dual-Fuel technology

The LPDF system, shown in Figure 5b, relies on a diesel-ignited gas engine with dual fuel capability. The engine is based upon Otto cycle, which guarantees low NO<sub>x</sub> emissions and high efficiency. Gas is supplied at low pressures (4-5 bar), and a constant feed of pilot diesel fuel is required to ignite fuel mixture. Such engines may also run completely on liquid fuel. Bunkered LNG is stored in slightly pressurized tanks. A Pressure Build-up Unit (PBU) can be used to maintain the tank pressure: LNG from the tank is evaporated in a WG heat exchanger and vapours are sent back to the tank until the pressure set point is reached (see panel C of Figure 5).

Alternatively, a cryogenic submerged pump can be used in place of PBU unit (as illustrated in Figure 5b). Fuel gas supply system is made up of a low-pressure LNG vaporizer followed by a heater, needed to increase gas temperature up to the operative values of the engine. Feed gas pressure is regulated by the Gas Valve Unit (GVU). The main functions of the GVU are to regulate the gas feeding pressure to the engine, and to ensure a fast and reliable operation and shut down of the gas supply (Babic, 2015).

The low-pressure dual fuel LNG engine is currently the dominating engine type in the marine gas propulsion market and can be considered a proven technology (Stenersen and Thonstad, 2017).

### 2.5.3. Lean-Burn Spark Ignited technology

LBSI engines are “single fuel” Otto gas engines running with high air excess. Vaporized LNG is fed at low pressures (4-5 bar) into the combustion chamber. The homogeneous combustion allows compliance with IMO Tier III limits, but this engine is sensitive to fuel gas quality. The FGSS, illustrated in Figure 5c has the same features of the one described in 2.5.2 for LPDF technology. Lean burn spark ignition initially came into the marine industry as engines for short-distance ferries since it needs a permanent gas supply and cannot be run on oil if LNG is not available. Boil off gas generated inside LNG storage tanks can be managed in two different ways:

- 1) Using a GCU. Before gas vapour is provided into the GCU, it needs to be warmed-up to room temperature in a gas heat exchanger.
- 2) Using a BOG re-liquefaction system. Natural gas is compressed and liquefied by means of a cryogenic refrigerator, and then LNG is sent back to the tank. This solution is typically featured on LNG carriers that need to manage large amounts of BOG, where is coupled with low-pressure membrane LNG tanks (IMO type B tanks).

## 2.6. Overview of LNG bunkering operations

As described in an LNG bunkering study conducted by DNV-GL, (2014) three main bunkering concepts are usually exploited to supply LNG to vessels: truck-to-ship, ship-to-ship and port-to-ship. The choice between different fuel delivery configurations depends on three main parameters: required bunkering volumes, bunkering frequency, and physical and logistical limitations. More specifically, the total LNG volume handled on a yearly basis in a harbour area, along with possible time constraints for operations, drives the selection of the most suitable bunkering method.

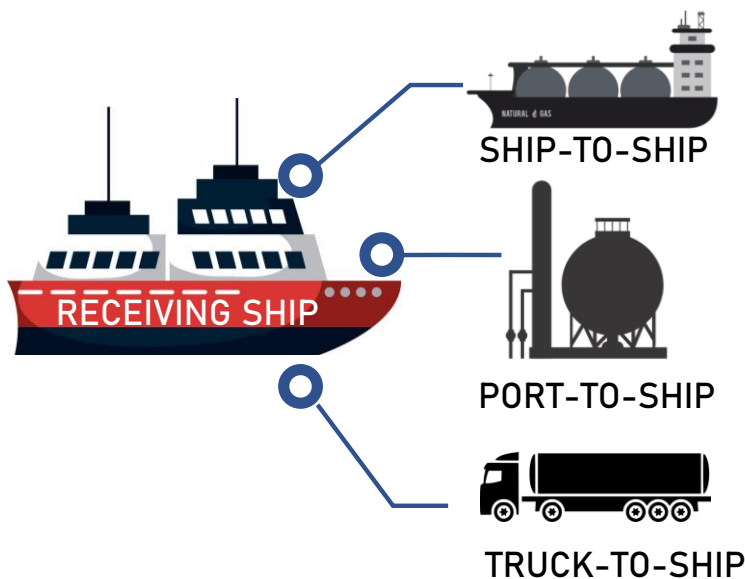


Figure 6: Main LNG bunkering options.

The port-to-ship (PTS) concept is typically implemented for ports with stable, long-term bunkering demand. The LNG is delivered to receiving vessels through flexible cryogenic hoses or loading arms, designed in accordance with standards presented in Section 3.1. When transfer arms are used, larger hose diameter can be installed, increasing the bunkering rate, and reducing the required time at berth. Flexible bunker hoses are typically made of a layered polyester fabric outer layer, ceramic fibre, and a thermoplastic polymer sheath lining. The hose is reinforced both internally and externally with cryogenic grade steel wire. Hose flexibility allows for relative movements between shore and the receiving ship. One end of the hose (either the receiving ship end or the bunker facility end) or its mid-section is usually fitted with emergency release systems, such as drip-free breakaway couplings that allow a safe hose disconnection, without any LNG or vapour release, in case of excessive motion or tension. The typical range of hose diameters spans from 3" up to 16", with working pressures up to 10-20 bar depending on the hose type and manufacturer (Gutteling Composite Hoses, 2020), (Trelleborg, 2020). Although the PTS option has great flexibility in the design for transfer rate and volume, it is the least flexible with respect to geography since the bunkering facility must be sited at a fixed location, in proximity to LNG import terminals or connected to transportation routes (i.e., railways, major roads).

Conversely, ship-to-ship LNG bunkering (STS) can take place at different locations: along the quayside, at anchor or at sea. STS is suitable both for large and small-scale applications depending on the bunker ship capacity, which can range from 1,000 to 10,000 m<sup>3</sup>. This bunkering concept is currently the preferred solution for refuelling LNG-fuelled cruise ships, using a feeder vessel with 7,500 m<sup>3</sup> storage capacity (Gallarati, 2020). Since the bunker vessels are moored alongside LNG-fuelled ships, the STS bunker concept could allow simultaneous cargo handling if approved by the relevant authorities (e.g., port authority). Possible disadvantages of STS bunkering may arise when conducting the operation out at sea: strong currents, winds and waves increase the risk of collision between LNG feeder and receiving vessels. While transfer rates are not as high as PTS bunkering, the transfer capabilities widely exceed the truck-to-ship (TTS) bunkering rates and volumes.

The TTS is a suitable bunkering concept for small-scale applications since the volume of LNG that can be transferred is significantly limited compared to the other bunkering concepts. The size of tanker truck in Europe is usually limited around 55-60 m<sup>3</sup>, hence longer bunkering times or multiple trucks are needed to meet the required bunkering volume. Tanker trucks are connected to the receiving ship on the portside, using a flexible hose, assisted by a manual hose-handling crane. TTS bunkering offers great flexibility to vessel owners, operators, and to bunkering facility since any jetty can be potentially used, combining economic attractiveness thanks to low capital investments and the possibility to deliver LNG to remote locations. However, the limited transfer flowrates (around 40-60 m<sup>3</sup>/h) and the significant impact on other operations carried out at the quay due to the presence of the tanker trucks represents the main disadvantages of TTS bunkering concept.

## 2.7. Main LNG hazards

Physical properties of LNG, which is a mixture mainly made of methane (87–99 mol%) and other light hydrocarbons (Migliore, 2013), vary with composition, which depends on the gas origin. LNG has radically different characteristics and behaviour with respect to conventional marine fuels: it is stored at cryogenic conditions and boils at approximately  $-160\text{ }^{\circ}\text{C}$ . Release of small volumes of liquid will result in the formation of large gas clouds due to the high thermal expansion coefficient of LNG (approximately 600 times the volume of spilled liquid). At  $-160\text{ }^{\circ}\text{C}$ , the vapour is denser than air, and cold gas clouds will spread by gravity at low heights until they become warmer. LNG for fuel supply may be delivered at elevated pressure (e.g., at 5 bar and  $-155\text{ }^{\circ}\text{C}$ ), exceeding the boiling point at atmospheric conditions. In such conditions, LNG releases will result in instantaneous flashing and much larger vapour clouds.

Natural gas flammability represents the main threat related to LNG handling: natural gas has a flashpoint of  $-187\text{ }^{\circ}\text{C}$  and a self-ignition temperature of approximately  $650\text{ }^{\circ}\text{C}$ , compared with a flashpoint in excess of  $60\text{ }^{\circ}\text{C}$  and a self-ignition temperature of  $300\text{ }^{\circ}\text{C}$  for marine gas oil (MGO). The flammability range of natural gas at atmospheric conditions is between 5 vol. % and 15 vol.% as reported by Mannan (2012a). However, such range is dependent on both temperature and mixture composition (Pio and Salzano, 2019). Besides the main hazards connected to its flammable nature, LNG spills may cause brittle fracture of non-cryogenic grade steel structure exposed to spills and frostbite due to cryogenic temperatures.

# Chapter 3. Literature review

## 3.1. Regulatory framework of LNG as a ship fuel

In the following, a brief overview is provided concerning the international and national regulations governing the use of LNG as a marine fuel. The Baltic region states have pioneered the use of LNG as a ship fuel in ferries and offshore service vessels for the oil and gas industry (Canadian Natural Gas Vehicle Alliance, 2015). The first LNG-fuelled passenger ship was the Norwegian vessel MV *Glutra*, built in 2000 (Riviera Maritime Media Ltd, 2016). Since then, Norway has played an important role in the widespread utilization of LNG as a ship fuel: according to DNV GL (2019), 43% of the total LNG-fuelled ships were based in Norway in 2016. The results of a survey conducted by Lloyd's Register (Lloyd's Register, 2014) highlighted that shipowners agree that legislation regulating ship-source emissions would play an important role in encouraging the use of LNG as a marine fuel. However, the increasing number of ships opting to utilize LNG as their choice of marine fuel is in sharp contrast with the state of development of the international legal framework governing the use of LNG as a marine fuel, as reported by (Xu et al., 2015). Moreover, as concluded by Aneziris et al. (2020), there are still gaps in the harmonization of LNG safety regulations issued by different countries and also for regulations covering different aspects of LNG operations at ports. The regulatory framework addressing the use of LNG as a marine fuel is presented following the hierarchy illustrated in Figure 7.

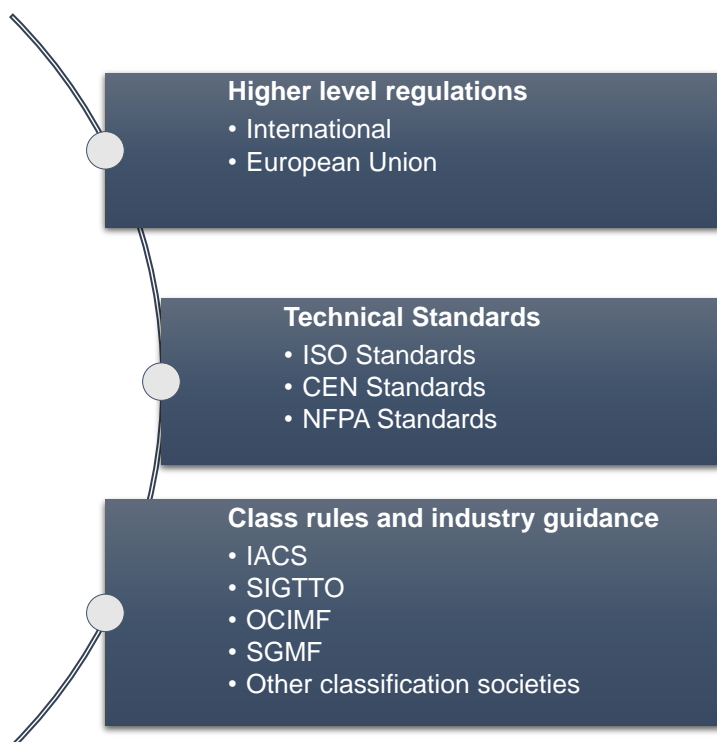


Figure 7: Regulatory framework for the use of LNG as marine fuel.

The set of rules encompassing the safe use of LNG as a fuel, and bunker operations in particular, comprises international regulations and standards and guidelines issued by classification societies or industry. These regulatory instruments follow a hierarchy and cover different aspects of the LNG bunkering chain depicted in Figure 3: rules applicability can be either for the shore-side of the bunkering process or for the ship-side. In this Chapter the rules are presented following the hierarchy of Figure 7, specifying to which side of the LNG bunkering chain they are applicable.

### **3.1.1. Higher level regulations**

#### *IMO Codes and Regulations*

The first regulatory instrument aiming at the strengthening of safety of merchant ships was the IMO convention for Safety of Life at Sea (SOLAS) (IMO, 1974). This international maritime safety treaty, applicable both to receiving ships and bunker vessels, requires Flag States to ensure that their ships comply with minimum safety standards in construction, equipment, and operation. Several amendments were introduced since the first adoption of this treaty, among which the International Code for the Construction and Equipment of Ships Carrying Liquefied Gases in Bulk (IGC), mandatory under SOLAS chapter VII since 1<sup>st</sup> July 1986, and more recently the International Code of Safety for Ships Using Gases or Other Low-Flashpoint Fuels (IGF), mandatory since 1<sup>st</sup> January 2017.

The relevance of the IGC Code to the broader use of LNG as a marine fuel is limited. This Code is aimed to provide an international standard for the safe transportation of liquefied gases and other hazardous substances by sea in bulk. Design and construction standards of cargo ships involved in such carriage are prescribed, along with the equipment they should carry so as to minimize the risk to the ship, to its crew and to the environment. The most recent comprehensive amendments of the IGC Code were adopted by resolution MSC.370(93), entered into force on 1<sup>st</sup> July 2016 (IMO, 2016). The IGF Code is an international standard applicable to ships operating with gas or low-flashpoint liquids (such as LNG) as fuel other than ships covered by the IGC Code. IMO resolution MSC.391(95) amended the text of SOLAS convention, making the IGF Code mandatory for ships built or converted after 1<sup>st</sup> January 2017 (IMO, 2015b). The goal of the Code is to provide criteria for the arrangement and installation of machinery for propulsion and auxiliary purposes addressing all areas that need special consideration for the usage of gas or low-flashpoint fuels. The basic philosophy of the IGF Code is to reach an equivalent level of integrity in terms of safety, reliability, and dependability as that which can be achieved with a new and comparable conventional oil fuelled main and auxiliary machinery.

The Seafarers' Training, Certification and Watch-keeping code (STCW) contains requirements for a minimum standard of competence in basic and advanced training for ships subject to the IGF Code. The STCW Code first came into force in 1978, following SOLAS convention, with the main objective of promoting safety of life and property at sea and the protection of the marine environment. The latest amendments by Resolution MSC.396(95) harmonized the regulation with IGF Code provisions in 2015 (IMO, 2015c).

#### *European measures*

It is important to remark upon the difference between EU Directives and Regulations. The former instruments set goals that must be achieved, but the transposition of Directives into national laws is delegated to each Member State. Conversely, EU Regulations have binding legal force throughout every Member State and enter into force on a set date in all the Member States.

Two Directives reflect the commitment of the European Union towards reduction of pollutant emissions from maritime activities: Directive 2016/802/EU (European Parliament, 2016), which establishes limits on the maximum sulphur content of gas oils, heavy fuel oil in land-based applications as well as marine fuels (also known as "Sulphur Directive"), and the Directive 2014/94/EU (European Parliament, 2014) on the deployment of alternative fuels infrastructure. Both Directives are relevant in the context of LNG as a fuel since they recognize the use of LNG as alternative fuel that can be used to significantly reduce emission amounts from shipping.

Starting from January 2010, all ships at berth in European ports were required to use fuels with a sulphur content below 0.1% in mass. This Directive also anticipated the IMO 2020 global sulphur cap by five years, requiring that passenger ships operating on regular services to or from any EU port should not use marine fuels if their sulphur content exceeded 1.50% in mass in sea areas outside the ECAs, when at that time the sulphur limit outside ECAs was set at 3.50%. Even if not dealing with technical aspects, the Regulation (EU) 2017/352 (European Parliament, 2017), applicable from March 2019, establishes a framework for the provision of port services, also including LNG bunkering. The Regulation sets the minimum requirements for the provision of port services and port staff training.

Depending on the amount of hazardous substance stored, LNG bunkering terminals can be subject to Directive 2012/18/EU, also known as “Seveso III” Directive (European Parliament, 2012), addressing the prevention of major accidents and the mitigation of their consequences on human health and the environment. The Directive introduces a distinction between lower and upper-tier establishments based on the amount of hazardous substance present inside the facility. For LNG, the lower-tier requirement is set at 50,000 kg, whilst facilities processing more than 200,000 kg of LNG (about 435 m<sup>3</sup> considering a density of 460 kg/m<sup>3</sup> for LNG) are defined as upper-tier establishments. Therefore, even SSLNG terminals are likely to fall under the scope of the Seveso III directive. Transport outside establishments and directly related intermediate temporary storage of dangerous substances (including loading and unloading) are specifically excluded from this directive and are governed by legislation on transport. Bunker vessels are therefore not subject to Seveso III Directive. It is important to remark that also establishments with less than 50 tonnes of stored LNG can be covered by the Directive if other dangerous substances are present (e.g., storage of other fuels in the port area).

The European Agreement concerning the International Carriage of Dangerous Goods by Inland Waterways (ADN) entered into force on February 2008 (United Nations Economic Commission for Europe (UNECE), 2019). The Regulations annexed to the ADN are applicable to LNG bunker vessels and barges operating in rivers and port areas. The mentioned Regulations define a list of dangerous substances and articles, providing rules for the transportation in packages and in bulk on board inland navigation vessels or tank vessels, as well as including provisions for the construction and operation of such vessels. Part 8 of the ADN set requirements concerning the training of vessels’ crew applicable to personnel of LNG bunker vessels, barges, or riverine LNG carriers.

Operations involving LNG tanker trucks, including loading and unloading, are covered by the European Agreement concerning the International Carriage of Dangerous Goods by Road (ADR), recently amended and updated (United Nations Economic Commission for Europe (UNECE), 2018). The newest version of the ADR, entered into force in January 2019, is made of two annexes that set requirements for packaging and labelling of the dangerous goods transported and requirements for the construction, equipment and operation of the vehicle carrying the goods in question. Specific provisions for design, construction, inspection, and testing of LNG tanks are also included in ADR in Part 6.

### **3.1.2. Technical standards**

Several international standards have been developed to regulate the use of LNG as a fuel, technically and operationally implementing the provisions contained in higher level regulations and directives. Moreover, standards simplify international trade by ensuring compatibility and interoperability of components, products, and services by setting out requirements for specific items, material, or equipment, and describing in detail methods or procedures. European Norms (ENs) are documents that have been ratified by one of the three European Standardization Organizations (i.e., CEN, CENELEC or ETS). These standards must be implemented at national level by each member country of CEN-CENELEC. Furthermore, laws and regulations may refer to standards and make compliance with them compulsory.

#### *ISO Standards*

The two most relevant ISO standards addressing the use of LNG as a marine fuel are the EN ISO 20519:2017 and ISO/TS 18683:2015. Both standards are applicable to the LNG bunkering interface between the fuel provider and the receiving ship. As defined in ISO/TS 18683, the bunker interface is the area of LNG transfer which comprises manifold, valves, safety and security systems and other equipment, also including the personnel involved in the bunkering operations. The scope of this standard is to give guidance on the minimum requirements for the design and operation of LNG bunkering facilities, including the interface as previously defined. It covers LNG bunkering from shore or ship LNG supply facilities, whereas the use of portable storage tanks such as containers or trailers to load and store LNG onboard ships to be used as fuel is outside the scope of this standard. This document set requirements for the design of installations supplying LNG as a ship fuel, and for risk assessment, also suggesting risk criteria to be adopted. Similar guidance is provided in the ISO/TS 16901:2015 standard (ISO, 2015), applicable to both onshore LNG export and import terminals or peak shaving plants.

The EN ISO 20519:2017 is the most recent standard addressing LNG bunkering. It has a scope similar to ISO/TS 18683, setting requirements for transfer systems and equipment used to bunker LNG fuelled vessels, also including operational procedures and requirements for training and qualification of the personnel. This standard supports the implementation of the IGF Code, providing the frame for the application of IGF provisions on bunkering operations. Risk-based criteria for the determination of bunker safety and security zones are outlined in EN ISO 20519 as well as in ISO/TS 18683.

Other relevant standards addressing LNG operations in port are the ISO 28460:2010, ISO/TR 17177:2015, and EN ISO 16904:2016. The ISO 28460 standard specifies the requirements for ship, terminal, and port service providers to ensure the safe transit of an LNG carrier through the port area and the safe transfer of its cargo. Hybrid floating and fixed LNG terminal not included within the scope of ISO 28460 are addressed in ISO/TR 17177. This standard provides guidance for installations, equipment and operation at the ship-to-terminal and ship-to-ship interface of the beforementioned LNG terminals. Lastly, the EN ISO 16904 specifies the design, minimum safety requirements and inspection and testing procedures for LNG marine transfer arms intended for use on onshore terminals. This standard is supplementary to local or national standards and regulations and is additional to the requirements of ISO 28460, also covering the minimum requirements for safe LNG transfer between ship and shore.

### *CEN Standards*

A large part of the European Norms relevant to LNG terminals covers the different aspects of the design of onshore installations. A fundamental standard is EN 1473:2016 that makes provisions for the design, construction and operation of LNG installations with a storage capacity of more than 200 t of LNG (CEN, 2016). This standard is applicable to terminals storing LNG at relative pressures lower than 0.5 bar, including liquefaction, regasification, and peak-shaving plants. Complementary to EN 1473, EN 13645 addresses the design of onshore LNG installations with a storage capacity between 5 and 200t (CEN, 2002). Design and manufacture specifications for vertical, cylindrical steel tanks built on site for the storage of cryogenic liquids are given in EN 14620:2006 (CEN, 2006). The maximum design pressure of the tanks covered by this European Standard is limited to 0.5 barg. Requirements for the design, fabrication, inspection and testing of static vacuum insulated cryogenic vessels with a design pressure greater than 0.5 barg are given in part 2 of EN 13458:2002 (CEN, 2002b). Another important standard is EN 1474:2008 which gives general guidelines for the design and testing of LNG marine transfer systems (CEN, 2008). Part 2 of this norm addresses transfer hoses to be used either during offshore or coastal transfer operations, whereas part 3 applies exclusively to offshore transfer facilities (e.g., between floating units, or between floating and fixed units).

### *NFPA Standards*

Similar in scope to EN 1473, the NFPA 59A standard (NFPA, 2018) provides requirements for the design, construction operation and maintenance of LNG facilities. It also provides the essentials requirements in terms of fire protection and safety of such facilities, including a chapter addressing SSLNG terminals.

#### **3.1.3. Class rules and industry guidance**

Various associations and classification societies have published guidelines and best practices for the use of LNG as a marine fuel with the objective of supporting all the stakeholders involved in the LNG marine industry.

A relevant document is the one published in 2016 by the International Association of Classification Societies (IACS) (IACS, 2016) This guideline is intended to give recommendations for procedures and equipment required for LNG bunkering operations and to provide a methodology for risk management so as to achieve a similar level of safety as reached for traditional oil fuel bunkering operations. IACS guidelines are completely integrated in the more recent second version of the LNG bunkering guidelines published by the Society for Gas as a Marine Fuel (SGMF) (SGMF, 2017) that provides best practice guidance derived from the industry. The SGMF has also published a number of other documents that help to define a procedural framework for specific issues of LNG bunkering operations, such as recommendations for the determination of control zones or for the arrangement of manifolds. Other relevant guidelines for LNG bunkering have been published by the Society of International Gas Tanker and Terminal Operators (SIGTTO) (SIGTTO, 2013), the American ABS Group (ABS, 2017), the European Maritime Safety Agency (EMSA) (EMSA, 2017) and the Oil Companies' International Marine Forum (OCIMF) (OCIMF, 2018). In 2015, the classification society DNV-GL issued its recommended practice for the development and operation of LNG bunkering facilities (DNV-GL, 2015a), with the aim of ensuring global compatibility and to secure a high level of safety, integrity and reliability for LNG bunkering facilities.

Table 2: Summary of the most relevant regulatory instruments for the use of LNG as a fuel

<b>Document</b>	<b>Applicability</b>	<b>Scope</b>	<b>Type</b>	<b>Issued by</b>
IGC Code	LNG bunker vessel	Construction, equipment, and operation of ships carrying liquefied gases in bulk.	International code	IMO
IGF Code	LNG-fuelled ships	Mandatory provisions for the arrangement, installation, control and monitoring of machinery, equipment and systems using low-flashpoint fuels	International code	IMO
STCW	LNG bunker vessel and Receiving ship	Requirements for minimum standards of competence for seafarers	International code	IMO
Directive 2016/802/EU	LNG-fuelled ships	Reduction of sulphur content of marine fuels including requirements for ships calling at EU ports	European Directive	EC
Directive 2014/94/EU	Shore side and bunkering interface	Directive on the deployment of alternative fuels infrastructure for European transport.	European Directive	EC
Regulation 2017/352	Shore side and bunkering interface	Rules for the provision of port services and financial transparency	European Regulation	EC
Directive 2012/18/EU	Shore side and bunkering interface	Control of major-accident hazards for establishments involving dangerous substances	European Directive	EC
ADN	LNG bunker vessel	Transport of dangerous goods via inland waterways	Convention	UNECE
ADR	LNG tanker truck	Transport of hazardous materials by road	Convention	UNECE
EN ISO 20519:2017	Bunkering interface	Requirements for transfer systems and equipment used for bunkering LNG not covered by the IGC Code	International Standard	ISO
ISO/TS 18683:2015	Bunkering interface	Minimum requirements for the design and operation of LNG bunkering facilities, including recommendations for operator training	ISO Technical Specification	ISO
ISO/TS 16901:2015	Bunkering interface	Guidance on risk assessment for LNG facilities onshore and at shoreline, excluding environmental risks associated with an LNG release.	ISO Technical Specification	ISO
ISO 28460:2010	Shore side and bunkering interface	Provisions to ensure the safe transit of an LNG carrier through the port area and the safe and efficient transfer of its cargo	International Standard	ISO

ISO/TR 17177:2015	Bunkering interface	Guidelines for the marine interfaces of hybrid LNG terminals not included in ISO 28460:2010	ISO Technical Report	ISO
EN ISO 16904:2016	Bunkering interface	Specifications for the design, minimum safety requirements and inspection and testing procedures for LNG marine transfer arms installed in conventional onshore LNG terminals. Additional to requirements of ISO 28460:2010, it also covers the minimum safety requirements for LNG transfer between ship and shore.	International Standard	ISO
EN 1473:2016	Shore side	Functional guidelines including recommended procedures and practices for the design, construction, and operation of all onshore LNG installations with storage at pressure lower than 0,5 barg and capacity above 200 t.	European Norm	CEN
EN 1474:2008	Bunkering interface	Part 2 provides general guidelines for the design, material selection, and testing details for LNG transfer hoses. Part 3 addresses the design and testing of offshore transfer systems.	European Norm	CEN
EN 13645:2002	Shore side	Requirements for the design and construction of onshore stationary LNG installations with a total storage capacity between 5 t and 200 t. Complementary to EN 1473:2016	European Norm	CEN
EN 14620:2006	Shore side	Specifications for the design and construction of above ground vertical, cylindrical tanks, built on site, with a steel primary liquid container. is made of steel. The maximum design pressure of the tanks covered by this standard is limited to 0,5 barg. Tanks for the storage of liquefied oxygen, nitrogen and argon are excluded.	European Norm	CEN
EN 13458:2002	Shore side	Requirements for the design, fabrication, inspection, and testing of static vacuum insulated cryogenic vessels designed for a maximum allowable pressure of more than 0,5 bar.	European Norm	CEN
IACS Rec.142	Bunkering interface	Recommendations and procedures for LNG bunkering operations, including requirements for transfer equipment. This document also sets harmonized minimum baseline recommendations for bunkering risk assessment, equipment, and operations.	Guidelines	IACS
DNVGL-RP-G105	Bunkering interface	Functional requirements for LNG bunkering facilities, addressing risk assessment, safety management system and operation of LNG terminal.	Recommended Practice	DNV-GL
IAPH Checklists	Bunkering interface	Checklists for ship-to-ship, shore-to-ship and truck-to-ship bunkering scenarios, including a list of relevant actions by the Port Authority when authorizing, overviewing, or evaluating bunkering operations.	Checklists	IAPH

SGMF Bunkering Guidelines	Bunkering interface	Guidance providing a description of potential LNG hazards, and roles and responsibilities of bunkering crew. Description of best practices Bunkering Procedure and implemented safety systems	Guidelines	SGMF
Ship to Ship Transfer Guide for Petroleum, Chemicals and Liquefied Gases	Bunkering interface	Guidelines addressing ship-to-ship transfer from LNG carriers. Useful reference when establishing rules and procedures for transfer operations between seagoing ships and LNG regasification vessels.	Guidelines	SIGTTO
LNG Bunkering Technical and Operational Advisory	Bunkering interface	Advisory providing requirements on vessel design and operational issues. Bunkering checklists and risk assessment methodology and reporting are also addressed.	Technical and Operational Advisory	ABS
Mooring Equipment Guidelines	Bunkering interface	Overview of the requirements for safe mooring from both a ship and terminal perspective	Guidelines	OCIMF
Guidance on LNG Bunkering to Port Authorities/Administrations	Shore side, Bunkering interface, LNG receiving ship	Informative and guidance document aiming at harmonization of requirements throughout ports in Europe. It is intended to provide Port Authorities and Administrations with necessary advice addressing the planning and operational stages of LNG bunkering.	General guidance	EMSA

## 3.2. Emergency planning guidelines

As explained in Section 3.1, the Seveso III directive distinguishes between lower and upper-tier establishments based on the amount of hazardous substance inside the facility. The Directive requires that the operator of upper-tier establishments shall produce a safety report to demonstrate that a major accident prevention policy is implemented, and internal emergency plans have been drawn up. Moreover, the operators are required to provide all necessary information to competent authorities in order to set up external emergency plans. An emergency plan is a written set of instructions that describes what workers and other personnel at the establishment should do in an emergency. The external emergency plan includes procedures to ensure close coordination with local authorities and emergency response teams. The emergency plan should be based on a realistic assessment of the hazards originating from the work activity considered, and the possible consequences of an emergency occurring as a result of those hazards. External hazards should also be examined in preparing an emergency plan. Internal and external emergency plans must be reviewed, tested, updated (when necessary) at least every three years.

Different documents address the emergency planning of LNG bunkering facilities. The EMSA provides some good practice and minimum requirements for emergency plans in its guidance document on LNG bunkering (EMSA, 2017). A summary of the information required for internal and external emergency plans is reported in Table 3.

*Table 3: Non-exhaustive list of information to be included in emergency response plans.*

<b>Internal emergency plans</b>	<b>External emergency plans</b>
Designation of responsibilities for local authorities, hospitals, local fire brigades, person in charge and selected personnel from the bunkering facility.	Names or positions of persons authorized to start emergency procedures and of persons authorized to take charge of and coordinate off-site action.
Name or position of the person with responsibility for liaising with the authority responsible for the external emergency plan.	Arrangements for receiving early warning of incidents, and alert and call-out procedures.
Description of the actions which should be taken to control the conditions or events that could result in a major accident and to limit their consequences, including a description of the available safety equipment.	Arrangements for coordinating resources necessary to implement the external emergency plan.
Arrangements for limiting the risks to persons on site including how warnings are to be given and the actions to be taken on receipt of a warning	Provisions for assisting with on-site mitigation action.
Procedures for providing early warning of the incident to the authority responsible for setting the external emergency plan in motion, including how to communicate more detailed information as it becomes available.	Arrangements for off-site mitigation action, including responses to major-accident scenarios as set out in the safety report and considering possible domino effects, including those having an impact on the environment.
Arrangements for training staff in the emergency response's duties and for providing assistance with off-site mitigation action.	Arrangements for providing the public and any neighbouring establishments with specific information relating to the accident and the behaviour that should be adopted.

An Emergency Response Plan for an LNG installation should be prepared to address cryogenic hazards, potential cold burn injuries to personnel and firefighting techniques for the control, mitigation and elimination of a gas cloud fire, jet fire or an LNG pool fire.

Other publications provide emergency planning indications such as the LNG Fire Protection and Emergency Response guidance by BP, (2007). Different response strategies are outlined specifically for the possible dangerous scenarios resulting from LNG releases. A set of specific procedures are suggested for addressing release events or fire scenarios occurring at LNG tanker manifolds, clearly stating actions to be taken by ship crew and onshore terminal personnel.

A detailed list of information that must be included in emergency response plans is also provided by the US Federal Energy Regulatory Commission, (2006) that sets out the requirements for emergency planning that should be followed by LNG terminal operators in the USA. Other relevant publications addressing LNG emergency response are the guide to contingency planning for marine terminals handling liquefied gases in bulk by SIGTTO, (2001), and the emergency response strategies outlined in the book "Liquefied Gas Fire Hazard Management" by SIGTTO, (2004).

### **3.3. Inherent safety and risk assessment**

Several studies have investigated the safety issues related to LNG operations, such as those of Alderman, (2005) and Lee et al. (2015), who conducted a fire risk assessment of different LNG fuel supply systems. Various studies focused specifically on LNG bunkering: Jeong et al. (2018), discussed the definition of safety exclusion zones for LNG bunkering site and performed an integrated quantitative risk assessment (QRA) to determine the extension of the safety zones for cargo ships of different size (Jeong et al., 2017b). A risk assessment study for different LNG bunkering operations performed in port areas was carried out by DNV (DNV, 2012). However, due to the recent exploitation of LNG as a marine fuel, there is still limited information about safety performance of bunkering installations. The technical literature still lacks a comparative safety assessment addressing both traditional diesel fuels and LNG ship bunkering technologies. The quantification and following assessment of the expected safety performance of bunkering technologies relied on a screening tool based on inherent safety principles. The inherent safety philosophy is hinged on five fundamental principles firstly outlined by Kletz (1978): minimization of inventories, substitution of hazardous materials, attenuation of process conditions, limitation of the effects and process simplification. Such principles are now widely applied in pursuing the reduction of the hazards related to industrial processes. Several authors developed inherent safety KPI suitable for decision-making and for the comparison of alternatives. Among these, Tugnoli et al., (2007) developed a consequence-based method independent from expert judgment and applicable to processes for which little information is available. Such an approach was later applied successfully by Landucci et al., (2008) to investigate and compare the safety performance of hydrogen storage technologies, pointing out critical safety issues that need to be considered for further development of these technologies. More recently, Tugnoli et al., (2012) applied the inherent safety KPI approach for the analysis of the safety profile of design alternatives proposed for LNG import terminals, allowing the identification of critical elements in the safety performance of the alternative plant designs. The inherent safety KPI method was exploited in the present work to perform a direct comparison among safety performance of different marine fuels and related technologies.

Concerning the QRA of LNG installations, Aneziris et al., (2014) estimated the risk level of onshore and offshore LNG regasification terminals, also including transfer operations. More recently, Martins et al., (2016) and later Lee (2020) conducted a QRA for an LNG floating storage and regasification unit, evaluating the individual and societal risk levels for such installations.

A first methodological analysis of the human element involved during LNG bunkering was performed by Stokes et al., (2013) who highlighted the importance of a robust competency management system. Despite the numerous works addressing safety aspects of LNG installations, a study integrating the impact of managerial aspects over the risk profile of an LNG bunkering facility is still missing in the technical literature. Another important aspect, often disregarded in process safety studies related to LNG bunkering, is represented by simultaneous operations (SIMOPs). Performing SIMOPs at berth while bunkering LNG might help to maintain similarity between fuel oil and LNG refuelling operations, enabling the long term viability of LNG as a marine fuel while keeping down cost and ensuring process efficiency thanks to the reduction of the time spent at berth by vessels and an optimized usage of available port infrastructure (American Petroleum Institute, 2016). However, it is also recognized that SIMOPs have the potential to increase the risk level by adding new ignition sources and exposing a higher number of individuals to dangerous scenarios. Despite this, only a few studies have addressed this issue, as highlighted by Aneziris et al., (2020).

### **3.4. Numerical modelling of cryogenic tanks pressurization dynamics**

In cryogenic storage tanks, LNG is stored as a boiling liquid at saturation conditions. Although cryogenic tanks are equipped with state-of-the-art insulation systems, heat leaks from the surrounding environment leading to interface evaporation and tank self-pressurization (Choi et al., 2017) are still present, even during normal operation.

Several numerical approaches have been used to model thermal response of cryogenic vessels exposed to external heat sources. Liquid hydrogen tank thermal stratification and self-pressurization effects were modelled by Gursu et al. (1993) using three different lumped models. They concluded that thermal stratification of the tank lading is one of the primary factors that determine the pressure rise rate.

Safety-oriented studies involving cryogenic storages were mainly aimed at understanding and modelling thermal stratification phenomena, which can lead to rollover events (Hubert et al., 2019). A one-dimensional thermal diffusion model was developed by Seo and Jeong (2010), who assume stagnant vapor and liquid phases. A lumped parameter model was developed by Deshpande et al. (2011) in order to predict time to rollover and to investigate its sensitivity to variation of heat and mass transfer coefficients. More recently, Migliore et al. (2015) developed a non-equilibrium thermal model for the prediction of the weathering of stored LNG in above-ground tanks.

Recent Computational Fluid Dynamics (CFD) studies of cryogenic containment systems addressed the issue of BOG generation and tank self-pressurization, such as the works by Barsi and Kassemi (2008) and Saleem et al. (2018). A numerical study of natural convection inside pressurized LNG tanks was carried out by Roh and Son (2012), who quantified the effects of tank pressure, size and pressurization procedure on the BOG generation pattern. A CFD-based method for the prediction of LNG rollover was recently developed by Hubert et al. (2019). Ovidi et al. (2019) investigated the pressurization behaviour of vertical cryogenic storage tanks considering the effect of different fluids, tank filling level and the possibility of insulation damage. All the aforementioned models and studies considered values of heat flux comprised between 2-50 W/m<sup>2</sup>, representative of heat flows through the thermal insulation during normal operation of cryogenic tanks, as can be derived from the works by Migliore et al. (2015) and Roh and Son (2012) and reported by Deshpande et al. (2011). Only a very limited number of experimental studies were carried out to assess the thermodynamic response of cryogenic tanks exposed to higher heat loads: Xie et al. conducted an experimental study aimed to simulate a sudden catastrophic loss of insulating vacuum of high-vacuum multilayer-insulated tanks under conventional ambient conditions (Xie et al., 2012, 2010), reaching heat flux values up to 600 W/m<sup>2</sup>.

In case of fire engulfment of an LNG tank, for instance due to the ignition of liquid spills that may occur following the leakage of tank connection pipes or due to the ignition of diesel fuel pools after a road accident, a more significant heat release rate is expected. The heat released from the fire is transferred by radiation and convection to the outer surface of the vessel, then by conduction through tank walls and insulating layer. The heat load is then transferred to the tank lading by convection and radiation from the vessel internal surface (Landucci and Birk, 2013). During the fire exposure of the tank, the internal wall in contact with liquid phase might superheat significantly, potentially inducing a transition of the boiling mechanism towards nucleate boiling phenomena (Gong et al., 2009). Heat ingress induces free convection currents that establish close to the walls, which transfer warmer liquid up to the vapor-liquid interface leading to thermal stratification of the lading and enhancing evaporation.

To date, a limited number of studies were developed in the technical and scientific literature with the aim of evaluating the thermal response of cryogenic vessels exposed to fires. Scarponi et al. (2016) set up a non-equilibrium lumped model for the dynamic simulation of pressure build up and temperature behaviour of LNG tanks under fire attack. Despite the model can replicate real accidents dynamics, taking into account the effect of PRV (pressure relief valve) opening, it considers a single node for the liquid phase. Thus, it is unable to predict liquid temperature stratification. A similar model was developed by Hulsbosch-dam et al. (2017) and was compared against the results of the only experimental study of fire exposure of a cryogenic pressure vessel available at the time in the technical and scientific literature. The non-equilibrium model predicts the PRV opening time with good accuracy and can reproduce the experimental results obtained from the bonfire test of a 3 m<sup>3</sup> double-walled tank filled with liquid nitrogen. However, the model is not able to predict liquid thermal stratification, which is a key parameter for assessing tank pressurization (Gursu et al., 1993).

### **3.5. Sustainability studies of alternative marine fuels**

During the last 10 years, a number of different studies addressed the issues connected to ship pollutant emissions. Trozzi (2010) describes in detail a methodology for the estimation of emission for maritime navigation which uses installed engine power and fuel consumption and takes into account the different navigation phases of ships (cruising, at the dock in port, or when approaching harbours). A study aimed at the evaluation of the social cost of cruise ships pollutant air emissions for major Greek ports was conducted by Maragkogianni and Papaefthimiou (2015) who estimated the economic health impacts related to NO<sub>x</sub>, SO<sub>2</sub> and PM<sub>2.5</sub> emissions in port cities. Gaseous and particle emissions from a LPDF ferry operating in the Baltic Sea were measured by Anderson et al. (2015) for different engine loads and different mixtures of LNG and MGO. Several inventories of ship emissions have been published, such as the work by Whall et al. (2010) that provides a detailed emission dataset for the UK based on year 2007 ship movements, or the study by Jalkanen et al. (2016) in which the emissions originating from ship traffic in European sea areas for the year 2011 were modelled using data from the Automatic Identification System installed onboard to describe ship traffic activity. A global emission inventory is presented in the recently published fourth IMO greenhouse gas study (IMO, 2020), in which greenhouse gas inventories are distinguished between domestic shipping and international emissions on a voyage basis. Other studies were addressed to understand the balance between environmental and economic benefits of switching to LNG fuel, such as the work by Banawan et al. (2009) that analyse the case of a short-range passenger ship, or the study conducted by Burel et al. (2013) who assessed the operational costs and pollutant emission reduction for a tanker ship equipped with dual fuel engines. A similar study was carried out by Jafarzadeh et al. (2017) who performed a trade-off analysis considering technical, environmental and economic aspects of LNG-fuelled fishing vessels operating in Norwegian waters.

Various Life Cycle Assessments were aimed at estimating the environmental impact of using LNG as an alternative marine fuel. Brynolf et al. (2014a) carried out a comparative study assessing the environmental performance of LNG, liquefied biogas, methanol, and bio-methanol. An extensive study by Baresic et al. (2018) provides a techno-economic analysis of LNG as a fuel in four different future LNG demand scenarios for the period 2010-2050. Hwang et al. (2019) compared the Life Cycle Environmental impact of LNG as a marine fuel with conventional MGO for a bulk carrier engaged in domestic services in South Korea. Recently, a wider conceptual sustainability assessment of alternative marine fuels was performed by Ren and Liang (2017) who used a fuzzy group multi-criteria decision making approach to determine the sustainability order of the alternatives, considering environmental, economic, technological and social aspects. Trivyza et al. (2018) adopted a multi-objective decision support method to evaluate the most sustainable ship energy system optimising environmental and economic objectives. An hybrid decision making model was developed by Jeong et al. (2019) to evaluate the best LNG propulsion system integrating economic, environmental and technical features.

## Chapter 4. Research questions

The use of LNG as a marine fuel has become a tangible reality during recent years. Numerous studies were carried out to investigate different LNG related aspects, ranging from the environmental impact of gas engine emissions to the understanding of physical phenomena occurring in cryogenic storage tanks subject to heat leaks. Despite the advancements promoted by such studies, some gaps need to be filled to provide a holistic approach to the evaluation of the overall safety of LNG as a fuel. In particular, a screening tool based on inherent safety principles that could be used to drive the development of future LNG-based projects in the maritime sector is still lacking.

The review of studies addressing the numerical modelling of cryogenic tanks pressurization dynamics has identified many contributions focused on the prediction of BOG generation, which is a relevant issue for both spaceflight equipment and long-term storage, but only few studies investigated the response of cryogenic tanks exposed to high heat loads. Simplified approaches, such as lumped models based on thermal nodes, were used to model the fire impact over LNG storage tanks. However, such a modelling approach suffers various limitations that need to be overcome in order to improve modelling accuracy and robustness.

Several risk assessment studies have investigated the safety issues related to LNG operations, focusing on offshore and onshore LNG regasification terminals or specifically on LNG bunkering activities. Recently, a methodological analysis of the human element involved during LNG bunkering was performed, highlighting the importance of a robust management system. Despite the numerous studies addressing safety aspects of LNG installations, the scientific literature still lacks a study integrating the impact of managerial aspects over the risk profile of an LNG bunkering facility.

Many studies addressed the environmental impact associated with ship emissions, pointing out the benefits of using LNG as marine fuel and current limitations of such technology. Several publications presented approaches or methodologies to guide the selection of sustainable alternative energy sources for shipping, using multi-criteria decision-making methods that account for social, economic, and environmental aspects. However, a comprehensive sustainability assessment encompassing safety features of alternative LNG-based fuel systems is still lacking in the literature as well as a structured comparison among such systems and conventional technologies based on marine gas oil (MGO).

To fill the above discussed knowledge gaps and to provide a framework for the evaluation of novel green shipping technologies with emphasis on safety issues, the following research questions are outlined and tentatively answered in the present study:

1. What is the most sustainable gas-fuelled propulsion system for ships when considering safety together with economic and environmental aspects?
2. To which extent the use of LNG as a marine fuel is inherently safer (or unsafe) compared to traditional fuels?
3. What is the risk related to LNG bunkering operations and how and to what extent is it affected by human actions?
4. What are the consequences of LNG fire scenarios on infrastructures, including storage tanks?

# Chapter 5. Sustainability of LNG as an alternative marine fuel

This Chapter describes a method proposed for the sustainability assessment of alternative LNG-based fuel systems for large cruise ships, which is aimed at the identification of the most sustainable fuel system technology considering environmental, economic and safety aspects. The ultimate goal of the developed methodology is to provide a decision-making support tool for shipowners and stakeholders, providing guidance in the selection of the most appropriate ship propulsion technology considering the different factors impacting on the three sustainability domains (economic, social and environmental).

The proposed approach is motivated by a dearth of studies integrating process safety quantification into marine fuel sustainability and multi-criteria decisional analyses, as highlighted in Section 3.5. To capture specific safety features, the consequence-based approach for inherent safety evaluation that will be further detailed in Chapter 6 is here exploited with some specific features in order to allow its use within the specific framework of sustainability assessment. Moreover, the method described, here applied for the assessment of LNG fuel gas systems, has a general validity, and may be used to evaluate any other type of alternative marine fuel system.

A tiered system of key performance indicators is defined to quantify the impact for each of the three sustainability domains evaluated. A profitability index is also defined to capture the economic attractiveness of the assessed alternatives. Upon definition of normalisation and aggregation criteria for the impact KPIs, an overall sustainability index is calculated to provide a synthetic measure of the sustainability fingerprint of each alternative. As reported in Figure 8, the first step of the approach requires the definition of a reference ship type and installed engine power for which different alternative fuel systems are considered. The necessary process equipment, operating conditions, fuel consumption, and machinery-related costs are the main data required for the characterization of the alternatives. A set of different impact indicators are selected for each sustainability domain (i.e., environmental, societal, and economic), then they are normalised and aggregated (steps 3 and 4) in order to calculate the overall sustainability indicator.

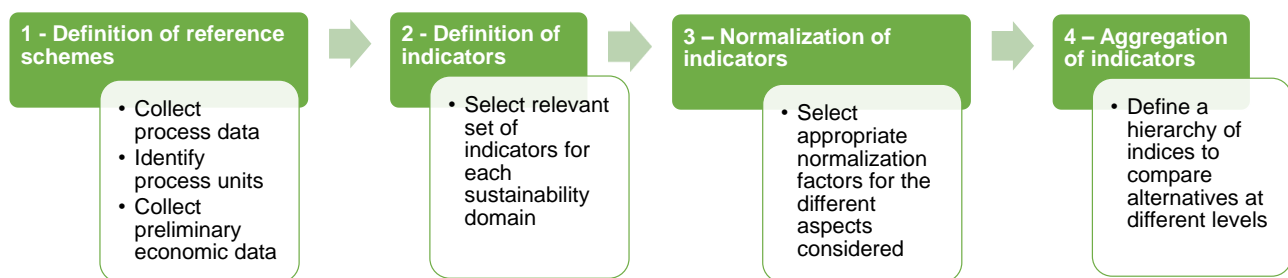


Figure 8: Overview of the approach followed for the sustainability assessment.

The sustainability performance of LNG-based alternative systems is compared to that of conventional MGO fuel systems and a ranking of the alternatives is obtained on the basis of overall sustainability index values. In addition, a sensitivity analysis is performed to test the results robustness against variations of the aggregation factors and of other parameters influencing model results.

## 5.1. Case study definition

A Hyperion-class cruise ship (The Maritime Executive, 2016) was chosen as a representative case study to provide a common basis for the sustainability assessment of different fuel systems. (Caterpillar Motoren GmbH & Co. KG, 2018, 2012)

Four reference technology schemes were defined based on the ship characteristics reported in Table 4. Three of the reference schemes consider the different LNG FGSS described in Section 2.5, then the analysis also included a conventional MGO fuel system. A simplified process flow diagram of each alternative fuel system is shown in Figure 9.

*Table 4: Main data for the reference cruise ship type considered for the analysis*

Item	Value	Unit
Gross tonnage	125,572	-
Breadth	38	m
Length	300	m
Passenger number	3,300	-
Trip number/year	20	-
Trip time	6,264	h/y
Power	36 (4×9,000 kW)	MW
Ship fuel autonomy	10 <sup>a</sup>	days

<sup>a</sup> based on fuel consumption data

The fuel tanks were included in the technology scheme to consider the potential safety issues related to the storage of hazardous substances. According to available technical information, gas-fuelled cruise ships with a gross tonnage in the order of 100,000 feature an overall LNG storage capacity of about 3,600 m<sup>3</sup> divided over three type-C cryogenic tanks (Corkhill, 2018). The capacity of MGO tanks was estimated on the basis of the considered days of autonomy and engines specific fuel consumption data. The resulting required storage capacity of about 2,000 m<sup>3</sup> was assumed to be split over five storage tanks. A SCR abatement unit (not shown in Figure 9) was considered for schemes 2 and 4 to make them compliant with IMO NO<sub>x</sub> Tier III emission limits since those technologies are not intrinsically compliant as opposite to the other considered alternatives.

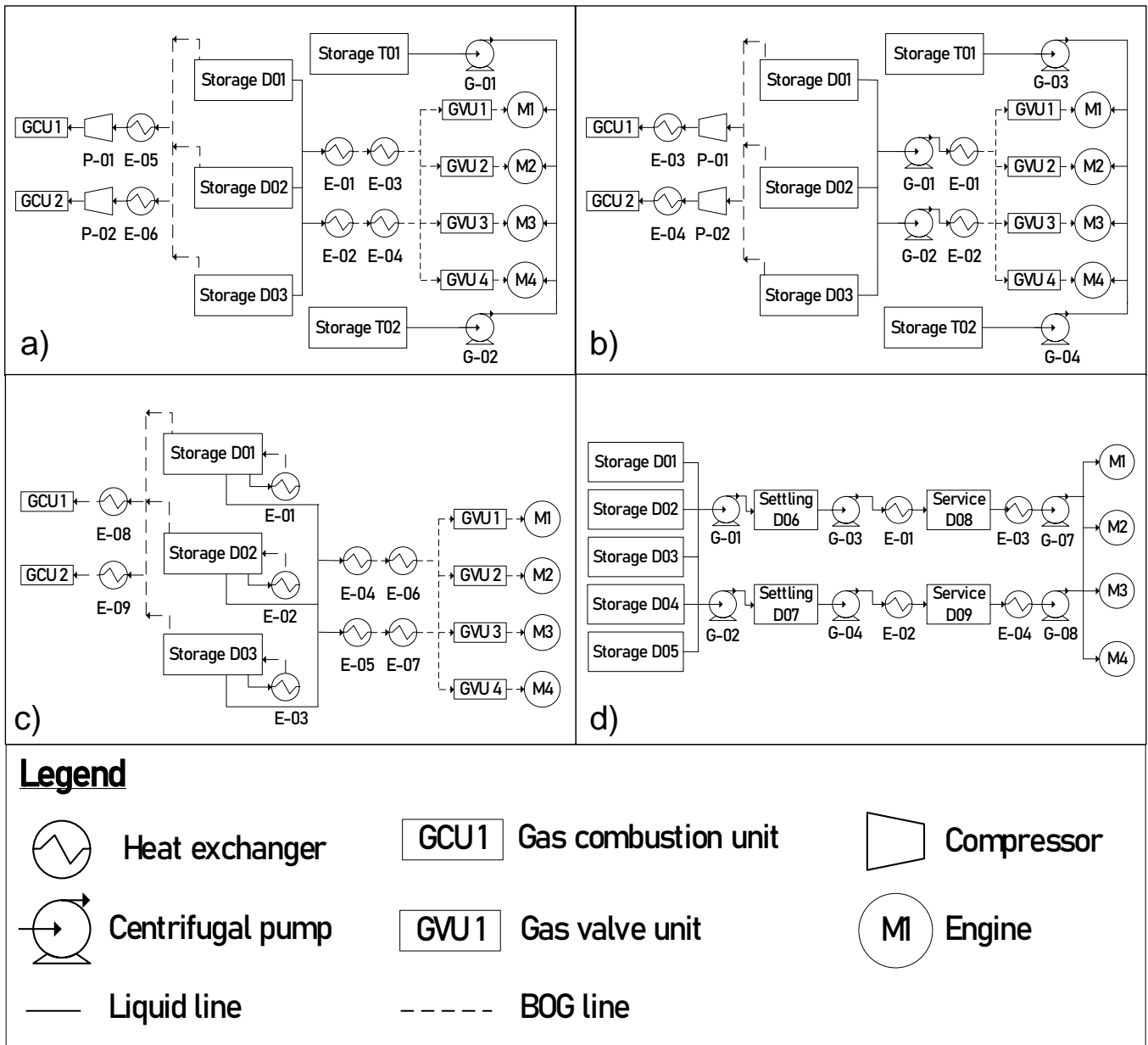


Figure 9: Reference schemes considered for alternative fuel system technologies: a) Scheme 1 - LPDF; b) Scheme 2 - HPDF; c) Scheme 3 - LBSI; d) Scheme 4 - MGO.

## 5.2. Environmental impact

Shipping activities generates different amount and quality of gaseous emissions. As shown in Figure 10, the exhaust gas emissions impact mainly on two distinct targets: air and water, the latter due to the eutrophication potential of NO<sub>x</sub> emissions. A conventional “activity-based” (or bottom-up) approach was used in this assessment to estimate exhaust emissions amounts on a yearly basis for each pollutant.

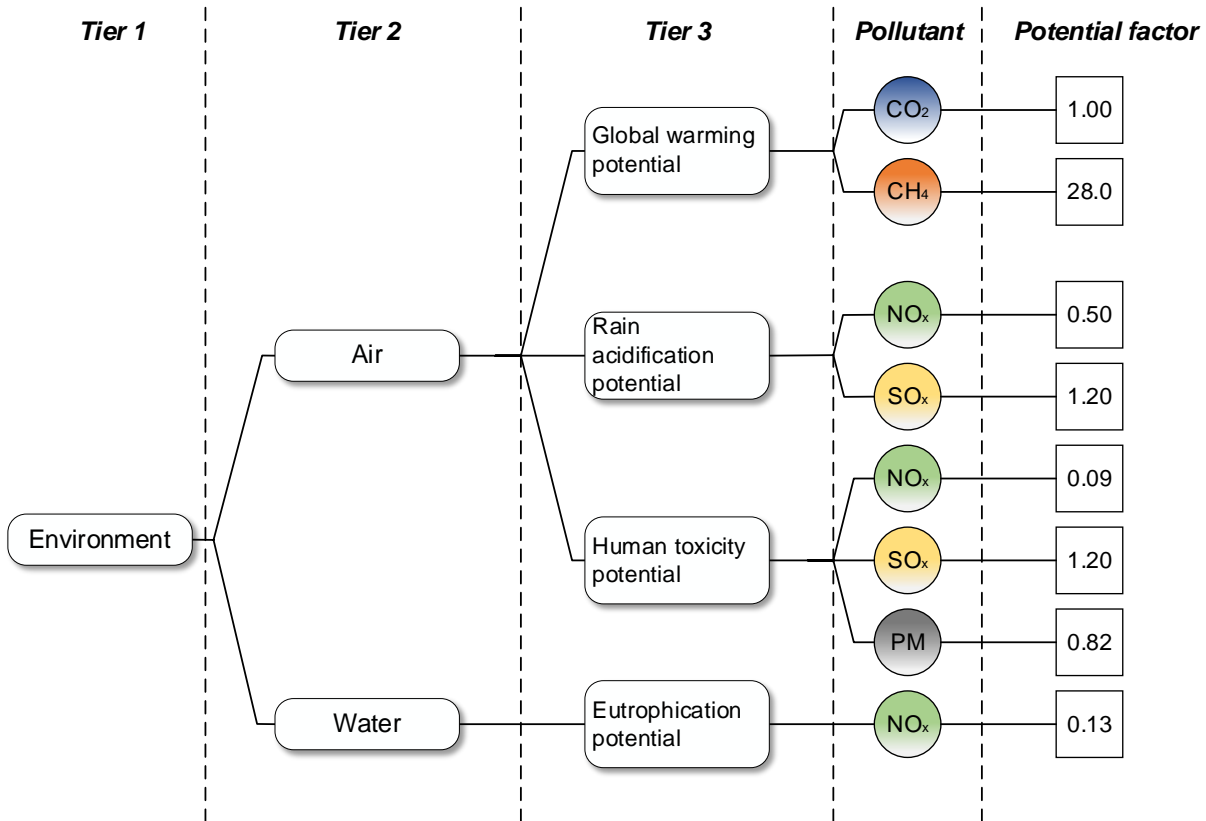


Figure 10: Environmental impact tree used for the assessment of the impact of the alternative solutions considered. Potential emission factors, PF, values were collected from the study by Guinée (2001).

As suggested by Maragkogianni and Papaefthimiou (2015) three different navigation activities, namely berthing, manoeuvring and navigation were taken into account and the emission amounts were estimated as:

$$E_p = \sum_{a,eng} (P_{eng} \cdot LF_{a,eng} \cdot T_a \cdot ef_{a,eng}) \quad \text{Eq. 5.1}$$

where  $E$  represents the emissions amount (in g) for the pollutant species  $p$ ;  $P$  is the engine power (in kW); subscript  $eng$  indicates the engine type, (i.e., main engine -ME- or auxiliary -AE-);  $LF$  is the engine load factor associated with the specific navigation activity, indicated by subscript  $a$ ;  $T$  is the activity time (h/y) and  $ef$  is the emission factor expressed in g/kWh.

Four environmental indicators, each addressing a different impact category, were calculated based on emission amounts estimated with Eq. 5.1. The four impact indicators are:

1. Global warming (GW);
2. Rain acidification (RA);
3. Human toxicity (HT);
4. Eutrophication (EU).

GW is mainly related to CO<sub>2</sub> emissions and methane slips from fuel systems, while the other indicators account for the effects of NO<sub>x</sub> and SO<sub>x</sub> emissions.

Environmental impact quantification requires the use of potential factors for each different substance and impact category assessed, which were collected from a reference database (Guinée, 2001). The potential factors used in this assessment are reported in Figure 10. Finally, the scores associated with the environmental indicators were calculated multiplying the emission amount  $E$  by the relevant potential factor ( $PF$ ), as described by Eq. 5.2.

$$I_c = \sum_p E_p \cdot PF_{p,c} \quad \text{Eq. 5.2}$$

The subscripts  $p$  and  $c$  in Eq. 5.2 refer to the pollutant species and impact category, respectively.

### 5.3. Economic implications

The economic assessment of the alternative fuel system technologies relied on the Net Present Value (NPV) technique. The investment profitability is calculated subtracting the present value of future costs from the present value of cash incomes over project lifespan, here assumed as 25 years. The NPV is calculated as follows:

$$NPV = \sum_{t=0}^n \frac{B_t - C_t}{(1 + r)^t} \quad \text{Eq. 5.3}$$

where  $B_t$  and  $C_t$  represent the benefits and costs of the considered investment at time  $t$ , and  $n$  is the lifespan of the project. The main source of uncertainty of this approach is represented by the value of the discount rate  $r$ . This quantity depends on various factors, such as the interest rate paid by the government on treasury bonds and the prime rate charged by major banks to their best customers as highlighted by Jafarzadeh et al. (2017). Since the exact estimation of  $r$  is beyond the scope of this study, a value of 8% was assumed as a reference economic scenario, as suggested by Jafarzadeh et al. (2017). A dedicated sensitivity analysis (reported in Section 5.7.3) was performed to assess the sustainability performance considering different discount rate values since other similar studies use a  $r$  value ranging from the lower 5% (Jeong et al., 2019) up to a maximum 15% (Acciaro, 2014).

As defined by Eq. 5.3, a positive NPV value corresponds to a remunerative investment. Thus, the economic indicator was obtained multiplying the NPV by -1, to obtain a profitability index ( $PrI$ ) for which the highest value implies the worst alternative, coherently with the definition of the other impact indicators.

A summary of the cost items considered in the economic evaluation is reported in Table 5. In the application of the method, a newly built ship was considered. Capital costs were estimated considering all investments needed to implement the fuel system such as the engine, the LNG tanks, and the pollutant abatement technology (when needed to comply with current regulations), accounting for purchase and installation costs.

The annual operating costs considered include fuel consumption, maintenance and the application of an environmental tax calculated over CO<sub>2</sub> emissions. For HPDF and MGO systems, a maintenance cost of 0.006 €/kWh was assumed for the SCR system needed for NO<sub>x</sub>-Tier III compliance.

The cost related to the environmental tax was retrieved from a study which discusses about the possibility of a carbon tax as a key element of a GHG mitigation strategy for international maritime transport. The study explores different taxation policy schemes using a discrete time-period model for forecasts up to 2040. The carbon tax value considered in this study is representative of a pure (revenue-raising) carbon tax for year 2030.

*Table 5: Capital and operating costs for LNG and MGO fuelled ships.*

Cost Item	Unit	Value	Source
<i>LNG technologies</i>			
Gas dual fuel engine	[€/kW] <sup>a</sup>	350 <sup>b</sup>	Faber et al. (2017)
Generators and electric system	[€/kW] <sup>a</sup>	400	
SCR investment (including installation)	[€/kW] <sup>a</sup>	45	
Installation costs	[€/kW] <sup>a</sup>	100	
LNG fuel supply system (including tanks)	[€/kW] <sup>a</sup>	130	Data gathered from European manufacturers
Maintenance	[€/kWh]	0.015	Trivyza et al. (2018)
Fuel price	[€/t]	201.25	Market Observatory for Energy of the European Commission (2019)
Environmental tax – CO <sub>2</sub>	[€/t CO <sub>2</sub> ]	75	Parry et al. (2018)
<i>MGO technology</i>			
MGO engine	[€/kW] <sup>a</sup>	180	Faber et al. (2017)
Generators and electric system	[€/kW] <sup>a</sup>	240	
MGO fuel system	[€]	100,000	
SCR investment (including installation)	[€/kW] <sup>a</sup>	45	
Maintenance	[€/kWh] <sup>a</sup>	0.014	Trivyza et al. (2018)
Fuel price	[€/t]	434	Bunker Index (2018)
Environmental tax – CO <sub>2</sub>	[€/t CO <sub>2</sub> ] <sup>c</sup>	75	Parry et al. (2018)

<sup>a</sup>: Cost basis is the overall main engine power, except for SCR investment and installation costs, which consider the total installed power on board.

<sup>b</sup>: High-pressure dual fuel engine cost is 280 €/kW.

<sup>c</sup>: The SCR system is only considered for HPDF and MGO systems

## 5.4. Safety implications

In the context of sustainability assessment, the social impacts may be extended to several potential target categories, as reported by Santoyo-Castelazo and Azapagic (2014). The impact quantification follows a cause-effect logic that involves subjective aspects that are difficult to estimate if the available information is limited to technical aspects. In this sustainability assessment, the inherent safety of the proposed alternative fuel system technologies was considered as a measure of social acceptability. Therefore, the social impact evaluation was based on the inherent safety quantification of the alternative reference schemes. The approach adopted in this assessment relies on the evaluation of consequence-based KPIs. The set of indicators used was firstly developed by Tugnoli et al., (2007) and adapted within the present study to evaluate the key features of alternative ship propulsion technologies. The procedure required for the evaluation of the inherent safety KPI is summarized in the following. Upon identification of the main fuel system process units and relevant operating conditions, which are reported in Appendix A, a set of specific literature-based LOCs (loss of containment events) was associated with each process unit, defining the release events to be considered for the consequence assessment. A “credit factor” (*Cf*) was then assigned to each LOC event associated with every process unit under analysis. Credit factor values were derived from statistical data on equipment leak frequency reported in the work by P.A.M. Uijt de Haag and Ale, (2005). This approach allows for the estimation of “standard” credit factors for each reference class of equipment units, which may be modified to account for improved safety standards of specific equipment items if further information is available. Therefore, credit factors should not be intended as equipment failure frequencies, but only as factors summarizing the past performance of similar equipment items. These factors allow identifying the worst credible scenarios in the analysis. An example of standard sets of LOCs and related credit factors proposed for some unit categories is given in Table 6.

*Table 6: Definition of LOC events considered in the present analysis and of related credit factors (1/y). Adapted from Tugnoli et al., (2009). n.a.: not applicable; n.c.: not considered.*

LOC Type	Pressurized storage vessel	Atmospheric storage vessel	Shell and tube heat exchanger	Pump	Loading arm/hose
R1: small leak, continuous release from a 10 mm equivalent diameter hole	$1 \times 10^{-5}$	$1 \times 10^{-4}$	$1 \times 10^{-3}$	<i>n.a.</i>	<i>n.c.</i>
R2: catastrophic rupture, release of the entire inventory in 600 s	$5 \times 10^{-7}$	$5 \times 10^{-6}$	$5 \times 10^{-5}$	<i>n.a.</i>	<i>n.c.</i>
R3: catastrophic rupture, instantaneous release of the entire inventory and release from the full-bore feed pipe	$5 \times 10^{-7}$	$5 \times 10^{-6}$	$5 \times 10^{-5}$	<i>n.a.</i>	<i>n.c.</i>
R4: pipe leak, continuous release from a hole having 10% of pipe diameter	<i>n.c.</i>	<i>n.c.</i>	<i>n.c.</i>	$5 \times 10^{-4}$	$6 \times 10^{-4}$
R5: pipe rupture, continuous release from the full-bore pipe	<i>n.c.</i>	<i>n.c.</i>	<i>n.c.</i>	$1 \times 10^{-4}$	$6 \times 10^{-5}$

Process units were divided into two categories according to the criteria proposed by Scarponi et al. (2016), based on the following inequality:

$$PUI > \max_i(\dot{V}_i) \times 180 \quad \text{Eq. 5.4}$$

where  $PUI$  is the LNG inventory ( $\text{m}^3$ ) of the process unit considered and  $\dot{V}_i$  is the flow rate of the stream  $i$  entering or leaving the process unit ( $\text{m}^3/\text{s}$ ). When Eq. 5.4 was verified, the process inventory is considered as the most relevant hazard factor and LOCs of type R1, R2 and R3 are assigned. Otherwise, the inlet and outlet streams of the process unit are considered the more relevant hazard factors and LOCs of type R4 and R5 are assigned. Dangerous scenario consequences resulting from each LOC event were estimated following a threshold-based approach. The values of the damage threshold considered in this thesis, derived from the works of Landucci et al., (2008) and Cozzani et al., (2013) for effects on humans and escalation hazard respectively, are reported in Table 7.

Table 7: Threshold values adopted for damage distances evaluation. LFL: lower flammability limit; n.a.: not applicable.

Accidental scenario	Threshold values	
	Effect on humans	Domino escalation
Flash fire	$\frac{1}{2}$ LFL, %vol.	n.a.
Jet fire	7 kW/m <sup>2</sup>	15 <sup>a</sup> – 45 <sup>b</sup> kW/m <sup>2</sup>
Pool fire	7 kW/m <sup>2</sup>	15 <sup>a</sup> – 45 <sup>b</sup> kW/m <sup>2</sup>
Vapor cloud explosion	0.14 bar	0.20 <sup>b</sup> – 0.22 <sup>a</sup> bar

<sup>a</sup> Value for atmospheric equipment; <sup>b</sup> Value for pressurized equipment

Standard event trees are used to identify the scenarios, while source terms and physical effects are calculated using conventional literature models such as those proposed by Van Den Bosh and Weterings, (2005). For the sake of simplicity, the composition of the hazardous materials considered in this sustainability assessment was assumed as pure methane for LNG and as pure n-nonane for MGO. These assumptions were introduced to facilitate the accident consequence assessment and the following calculation of damage distances for the different LOC events considered. It is important to remark that this simplified approach was followed to compare the accident outcomes severity, rather than to carry out a detailed consequence analysis, which should need a more accurate characterization of the fuel properties. Finally, the damage distances obtained are used to calculate an inherent safety KPI for each reference scheme described in Section 5.1. For this goal, a unit inherent hazard index ( $UHI$ ) was calculated for each process unit featured in the fuel system as follows:

$$UHI_u = \sum_{LOC=1}^{n_u} C_{f_{u,LOC}} \cdot h_{u,LOC}^2 \quad \text{Eq. 5.5}$$

where  $n_u$  is the number of LOCs considered for a specific unit  $u$  of the reference scheme considered,  $h_{u,LOC}$  is the maximum damage distance obtained for a specific LOC type, identified by the index  $LOC$ , and  $C_{f_{u,LOC}}$  is the credit factor relevant for the LOC event being accounted. To avoid uncertainties introduced by consequence analysis models in describing “near field” effects, the actual damage distance used in Eq. 5.5 is the maximum between the calculated damage distances and 5 m. Successively, the unit indicators were aggregated summing over all the  $N$  process units of each scheme to obtain an overall inherent hazard index ( $HI$ ):

$$HI = \sum_{u=1}^N UHI_u \quad \text{Eq. 5.6}$$

## 5.5. Normalisation of indicators

The normalisation step was carried out comparing the indicator values against a reference term which acts as normalisation factor ( $NF$ ), as described by Eq. 5.7:

$$NI_i = \frac{I_i}{NF_i} \quad \text{Eq. 5.7}$$

where the subscript  $i$  refers to a specific impact category,  $I_i$  is the indicator to be normalised and  $NF_i$  is the normalisation factor.

The selection of an appropriate  $NF$  among the variety of values proposed in the literature is of utmost importance, since an improper choice may introduce a bias in the results (Bare et al., 2006). In the present analysis, an external normalisation approach was applied to avoid the introduction of biases and to provide a comparison independent from the type of technology under evaluation. The normalised indicators obtained represent the relative impact of the specific alternative assessed over the local area of impact, selected as reference. European territorial water was considered as the reference area to assess the impact scale. Thus, the external normalisation factors in this study were determined on the basis of available data for Europe. The European gross domestic product was considered as a  $NF$  for the profitability index. The frequency value for the total loss of passenger ships in European territorial waters was multiplied by the extension of European member states Mediterranean Sea waters and considered as the  $NF$  for the safety indicator. A summary of the  $NF$  values used in this work is reported in Table 8. Normalisation of environmental indicators was performed considering the indicator-specific aggregate emission (in kg eq., see Table 8) for the European member states during a reference year (Wegener Sleeswijk et al., 2008).

The data needed to determine the numerical values of the external  $NFs$  were retrieved from several free access databases that report widely used economic and environmental data (Oers, 2016; International monetary fund, 2018; The World Bank Group, 2018).

Table 8: Normalisation factors adopted in the present work.

<b>Indicator</b>	<b>Description</b>	<b>NF</b>	<b>Unit</b>	<b>Reference</b>
<b>GW</b>	Global warming impact indicator	$5.22 \times 10^{12}$	kg CO <sub>2</sub> eq./y	Wegener Sleeswijk et al. (2008)
<b>RA</b>	Rain Acidification impact indicator	$1.68 \times 10^{10}$	kg SO <sub>2</sub> eq./y	Wegener Sleeswijk et al. (2008)
<b>HT</b>	Human toxicity impact indicator	$5.00 \times 10^{11}$	kg 1,4-dichlorobenzene eq./y	Wegener Sleeswijk et al. (2008)
<b>EU</b>	Eutrophication impact indicator	$1.85 \times 10^{10}$	kg PO <sub>4</sub> <sup>3-</sup> eq./y	Wegener Sleeswijk et al. (2008)
<b>PrI</b>	Profitability Index	$3.96 \times 10^8$	M€	International monetary fund, (2018)
<b>HI</b>	Inherent safety Index	$4.92 \times 10^{7a}$	m <sup>2</sup> /y	Eliopoulou et al. (2016), and European Environmental Agency, (2015)

<sup>a</sup>: total loss frequency for passenger ship is  $3.83 \times 10^{-5}$  events/year. European Mediterranean Sea waters cover a surface of  $1.28 \times 10^6$  km<sup>2</sup>.

## 5.6. Aggregation of indicators

As illustrated in Figure 11, the aggregation procedure is based on a three-level hierarchy, allowing the comparison of the alternatives accounting for the different domains of sustainability.

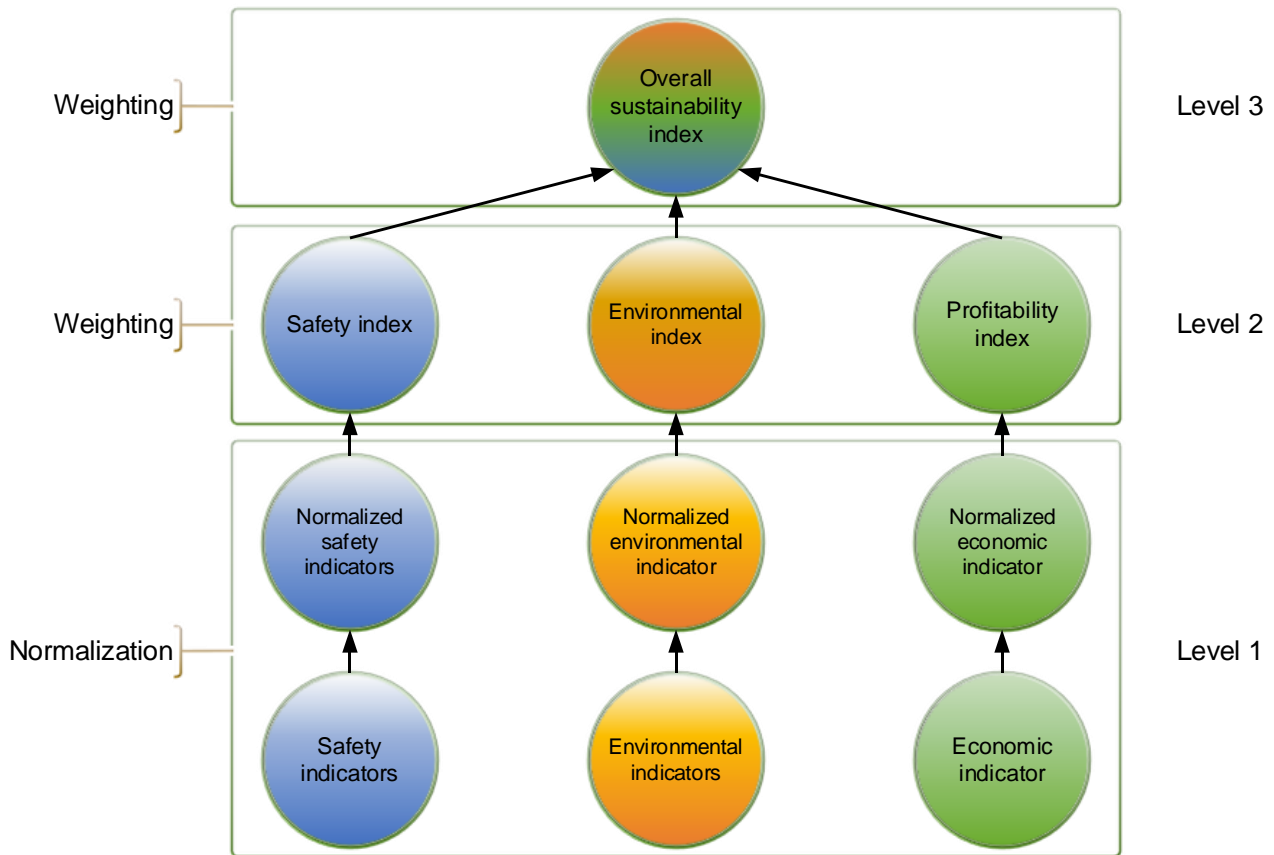


Figure 11: Hierarchy of considered sustainability key performance indicators.

Table 9 reports the Level 2 KPIs that reflect the impact of the assessed alternative over the three main sustainability domains. As shown in the table, the four environmental impact indicators described in Section 5.2 were aggregated into a single environmental KPI value, *EnvI*, by a weighed sum. The weight set used, also reported in Table 9, emphasizes the importance given to greenhouse gases emissions, which is one of the main drivers for using LNG as a fuel.

Table 9: Summary of KPIs adopted in the study for the sustainability assessment.

Domain	KPI	Brief description
Environment	Environmental index ( <i>EnvI</i> )	Synthetic indicator accounting the impact of air and water pollution. $EnvI = GW * w_{GW} + RA * w_{RA} + HT * w_{HT} + EU * w_{EU}$ $w_{GW} = 0.3; w_{RA} = 0.3; w_{HT} = 0.2; w_{EU} = 0.2$
Economic	Profitability index ( <i>PrI</i> )	Sum of discounted annual cash flows generated over a timespan (multiplied by factor -1)
Safety	Inherent safety index ( <i>HI</i> )	Damage extent and credibility of accidental scenarios

A single overall indicator was defined for Level 3, the overall sustainability index (*OSI*). This allows for a direct comparison among the alternatives, providing a compact overview of the global sustainability performance of each reference scheme. *OSI* is a normalised overall index obtained from the weighted summation of Level 2 KPIs as follows:

$$OSI = \sum_i W_i I_i \quad \text{Eq. 5.8}$$

where  $I_i$  is the level 2 KPI for the  $i$ -th impact domain, and  $W_i$  is the weight factor considered for the specific domain.

The weight values used to calculate the *OSI* (reported in Table 14) were derived from a similar work by Tugnoli et al. (2008). The selected values are intended to emphasize inherent safety aspects (which are given a weight of 0.4), whereas environmental and economic domains share a value of 0.3. Different combinations of weight factors were explored in a specific sensitivity analysis which results are reported in Section 5.7.3.

Internal normalisation of *OSI* allows for an immediate comparison of global sustainability performance of the assessed alternative fuel systems. The normalised indicator ( $OSI_N$ ) is calculated as:

$$OSI_{N,k} = \frac{OSI_k}{\max_k(OSI_k)} \quad \text{Eq. 5.9}$$

where  $OSI_k$  is the overall sustainability index for the  $k$ -th alternative.

## 5.7. Results

### 5.7.1. Level 1 impact indicators

The assessment of exhaust gas emissions resulting from the different navigation activities represents the starting point for the calculation of environmental impact indicators. The required cruise ship activity timing was calculated assuming the time percentage spent in each operation mode (manoeuvring, at berth, or in navigation) on a yearly basis. Activity time percentages were obtained from an extensive study of ship traffic in the European sea areas for the year 2011 conducted by Jalkanen et al. (2016), who used accurate vessel activity data acquired by automatic position reporting systems. Average auxiliary (AE) and main engine (ME) load factors for berthing and manoeuvring were retrieved from the work by Tzannatos, (2010), whilst navigation load factors were collected from a ship emissions inventory by Whall et al., (2010). A summary of the considered values is reported in Table 10.

Table 10: Considered time scheduling and engine load factors for environmental impact assessment.

Activity	Activity time [%]	Activity time [h/y]	Engine load factor [%]	
			AE	ME
Manoeuvring	3.0%	188	75%	20%
At berth	44.0%	2,756	60%	0%
Navigation	53.0%	3,320	30%	80%

Literature emission factors and yearly emission amounts estimated using Eq. 5.1 for each different fuel system considered, are reported in Table 11.

Table 11: Emission factors and total emission amount of main and auxiliary engines. Values in brackets refer to navigation, the others to in-port activities.

Scheme	Engine type	Emission factors [g/kWh]						Reference
		NO <sub>x</sub>	SO <sub>x</sub>	PM 2.5	CO <sub>2</sub>	VOC	CH <sub>4</sub>	
1	Main	1.15 <sup>a</sup>	0.02 <sup>b</sup>	0.10 <sup>b</sup>	450 <sup>a</sup>	0.50 <sup>b</sup>	6.90 <sup>a</sup>	a) Stenersen and Thonstad (2017)
	Auxiliary	1.90 <sup>a</sup>	0.02 <sup>b</sup>	0.10 <sup>b</sup>	444 <sup>a</sup>	0.50 <sup>b</sup>	6.90 <sup>a</sup>	
2	Main	2.50 <sup>c</sup>	0.02 <sup>b</sup>	0.10 <sup>b</sup>	417 <sup>b</sup>	0.50 <sup>b</sup>	0.00 <sup>a</sup>	b) Kristenen (2015)
	Auxiliary	2.50 <sup>c</sup>	0.02 <sup>b</sup>	0.10 <sup>b</sup>	445 <sup>b</sup>	0.39 <sup>c</sup>	0.00 <sup>a</sup>	
3	Main	0.90 <sup>a</sup>	0.00 <sup>b</sup>	0.03 <sup>b</sup>	472 <sup>a</sup>	0.50 <sup>b</sup>	4.10 <sup>a</sup>	c) Caterpillar Motoren GmbH & Co. KG (2012)
	Auxiliary	0.90 <sup>a</sup>	0.00 <sup>b</sup>	0.03 <sup>b</sup>	472 <sup>a</sup>	0.50 <sup>b</sup>	4.10 <sup>a</sup>	
4	Main	2.50 <sup>e</sup>	0.47 <sup>e</sup>	0.22 <sup>e</sup>	710 <sup>d</sup> (645) <sup>d</sup>	1.50 <sup>d</sup> (0.50) <sup>d</sup>	- <sup>d</sup>	d) Whall et al. (2007)
	Auxiliary	2.50 <sup>e</sup>	0.90 <sup>e</sup>	0.30 <sup>e</sup>	690 <sup>d</sup>	0.40 <sup>d</sup>	- <sup>d</sup>	
Scheme		Total emission amount [t/y]						
1		58.42	1.18	4.94	15,345.02	24.68	340.56	-
2		94.71	1.18	4.94	21,285.18	22.01	0.00	-
3		44.42	0.13	1.48	23,316.34	24.68	202.36	-
4		123.39	23.15	11.08	32,987.57	22.51	0.45	-

Methane emissions accounted in this study are only related to the engine and do not consider operational emissions due to venting or refuelling. Fuel sulphur content of MGO was assumed to be equal to 0.1% in mass, in compliance with threshold values for ECAs reported in annex VI of MARPOL regulation. Methane slips from diesel propulsion systems were estimated as 2% of total VOC (volatile organic compounds) emissions following the approach suggested by the IMO (2015a).

The results obtained for the economic impact assessment are reported in Table 12. Values for capital expenses (CAPEX) and operational expenses (OPEX) were estimated using the method described in Section 5.3. For the sake of brevity, the complete summary of consequence assessment results and inherent safety KPIs calculated for the process units included in all the reference schemes considered is reported in Appendix A. The considered LOC events and associated  $Cf$  are shown for each single process unit for all the reference schemes assessed, together with calculated damage distances and resulting  $UHI$ .

Table 12: Results of economic impact assessment and calculated value of  $PrI$  indicator (not normalised) for the alternative fuel systems.

Scheme	1	2	3	4
<b>CAPEX [M€]</b>	<b>35.28</b>	<b>34.38</b>	<b>35.28</b>	<b>16.84</b>
<i>Fuel consumption [t/y]</i>				
LNG	36,456.48	31,119.55	36,581.76	0.00
MGO	405.91	563.76	0.00	39,914.21
<i>Maintenance cost [M€/y]</i>	6.90	10.12	6.84	9.50
<i>Fuel cost [M€/y]</i>	7.51	7.51	7.34	17.32
<i>Environmental tax [M€/y]</i>	0.74	1.30	1.42	2.01
<i>OPEX [M€]</i>	15.15	18.93	15.59	28.83
<b>Σ OPEX - end of project life [M€]</b>	<b>363.57</b>	<b>454.41</b>	<b>374.27</b>	<b>692.03</b>
<b><i>PrI [M€]</i></b>	<b>198.92</b>	<b>237.87</b>	<b>203.61</b>	<b>293.76</b>

A summary of non-normalised Level 1 indicators for the alternative fuel systems is reported in Table 13. The calculated values of environmental indicators clearly point out the reduction of pollutant emission achieved with LNG-based fuel systems (Schemes 1, 2 and 3) with respect to conventional technologies (Scheme 4). The total  $SO_x$  emissions of LNG-based technologies are reduced by more than 95% compared to MGO-fuelled ships, whereas  $NO_x$  emissions mark a significant reduction (more than 60%) comparing scheme 3 with scheme 4. It is important to remark that fuel supply systems of schemes 2 and 4 are both equipped with SCR exhaust gas treatment system; thus, the calculated yearly emissions are already mitigated. As expected, PM emission resulting from dual fuel and gas only technologies are less than half the amount of those coming from MGO, since the emission of particles is particularly affected by the fuel sulphur content (Kristenen, 2015).

Using LNG for cruise ship propulsion can also save more than 30% of total  $CO_2$  yearly emissions. The only exception to this general trend is related to VOC emissions, which show a slight increase for the LNG-based schemes. In particular, methane emission figures are significantly higher for gas engines than traditional diesel engines (with the only exception of Scheme 2), thus limiting the environmental benefits of LNG fuel systems.

Table 13: Summary of non-normalised values for level 1 impact indicators and KPIs. Reference schemes are reported in Figure 9.

Indicator	Scheme 1	Scheme 2	Scheme 3	Scheme 4	Unit
<i>Environment</i>					
<b><i>GW</i></b>	2.49×10 <sup>7</sup>	2.13×10 <sup>7</sup>	2.90×10 <sup>7</sup>	3.30×10 <sup>7</sup>	kg CO <sub>2</sub> eq./y
<b><i>RA</i></b>	3.06×10 <sup>4</sup>	4.88×10 <sup>4</sup>	2.24×10 <sup>4</sup>	8.95×10 <sup>4</sup>	kg SO <sub>2</sub> eq./y
<b><i>HT</i></b>	7.43×10 <sup>4</sup>	1.18×10 <sup>5</sup>	5.45×10 <sup>4</sup>	1.59×10 <sup>5</sup>	kg 1,4-dichlorobenzene eq./y
<b><i>EU</i></b>	7.59×10 <sup>3</sup>	1.23×10 <sup>4</sup>	5.77 ×10 <sup>3</sup>	1.60×10 <sup>4</sup>	kg PO <sub>4</sub> <sup>3-</sup> eq./y
<i>Economic</i>					
<b><i>PrI</i></b>	206.68	211.22	207.90	298.20	M€
<i>Inherent safety</i>					
<b><i>HI</i></b>	17.92	27.26	17.26	16.75	m <sup>2</sup> /y

From an economic perspective, Scheme 1 results to be the most convenient solution, closely followed by Scheme 3, even if this latter solution shows a larger environmental tax amount. The higher installation costs of dual fuel systems and the increased maintenance costs related to SCR equipment required to comply with Tier III limits slightly penalise Scheme 2, making it the least economic option among gas alternatives. Scheme 4 shows the lowest profitability (i.e., highest value of *PrI*) having the highest OPEX among all alternatives and the highest environmental tax load. The initial advantage of lower investment costs is eroded by the higher fuel costs. Maintenance and fuel costs account for the majority of total OPEX, reaching a maximum share of 51 and 59% (for Scheme 2 and 4 respectively). It should be noted that the environmental taxation scheme applied has a limited impact when considered as a proportion of total annual expenses since its share reaches a maximum 13% for Scheme 3 gas propulsion technology. The cost item related to fuel oil consumption for dual fuel alternatives (Schemes 1 and 2) marginally affects total fuel costs, contributing about 2.3 and 3.8% of the total value, respectively.

With respect to safety, the conventional MGO-based fuel system shows, as expected, the lowest *HI* value. The low *HI* score of Scheme 4 is mainly determined by the lower number of fuel system components. For this scheme booster pumps are deemed as the critical units and have a negative impact over safety performance due to their high value of *UHI* index (see Table A4 in Appendix A). Scheme 2 exhibits the worst expected safety performance, with a *HI* about 50% higher than the other alternatives. Such a difference can be explained considering that the *HI* index is influenced by the complexity of the reference scheme in terms of number of process units, equipment type (i.e., rotating, heat exchanger, etc.) and severity of operating conditions (see Table A1 in Appendix A). All these factors worsen the LNG fuel systems safety level with respect to the conventional system. In particular, Scheme 2 shows the worst performance, due to the higher operating pressure and the presence of high-pressure LNG pumps that significantly affect the overall *HI* value. Substitution of rotating equipment with PBU in the fuel gas supply system of Scheme 3 makes this solution the inherently safest LNG fuel system option.

### 5.7.2. Aggregated key performance indicators (Level 2 and Level 3)

The complete set of normalised Level 1 indicators together with aggregated Level 2 and Level 3 indicators is reported in Table 14, whereas Figure 12 shows a radar plot comparing the normalised values of aggregated level 2 indicators.

Table 14: Normalised values of Level 1, Level 2, and Level 3 indicators. Weight factors used for the aggregation of indices are reported in the last column of the table.

Indicator	Scheme 1	Scheme 2	Scheme 3	Scheme 4	Weight factors
<b>Level 1</b>					
<i>GW</i>	$4.76 \times 10^{-6}$	$4.08 \times 10^{-6}$	$5.55 \times 10^{-6}$	$6.32 \times 10^{-6}$	0.3
<i>RA</i>	$1.82 \times 10^{-6}$	$2.90 \times 10^{-6}$	$1.33 \times 10^{-6}$	$5.32 \times 10^{-6}$	0.3
<i>HT</i>	$1.48 \times 10^{-7}$	$2.36 \times 10^{-7}$	$1.09 \times 10^{-7}$	$3.19 \times 10^{-7}$	0.2
<i>EU</i>	$4.10 \times 10^{-7}$	$6.65 \times 10^{-7}$	$3.12 \times 10^{-7}$	$8.67 \times 10^{-7}$	0.2
<i>PrI</i> <sup>a</sup>	$2.76 \times 10^{-6}$	$2.81 \times 10^{-6}$	$2.77 \times 10^{-6}$	$3.90 \times 10^{-6}$	1.0
<i>HI</i> <sup>a</sup>	$3.64 \times 10^{-7}$	$5.54 \times 10^{-7}$	$3.51 \times 10^{-7}$	$3.41 \times 10^{-7}$	1.0
<b>Level 2</b>					
<i>EnvI</i>	$2.09 \times 10^{-6}$	$2.27 \times 10^{-6}$	$2.15 \times 10^{-6}$	$3.73 \times 10^{-6}$	0.3
<i>PrI</i> <sup>a</sup>	$2.70 \times 10^{-6}$	$2.76 \times 10^{-6}$	$2.72 \times 10^{-6}$	$3.90 \times 10^{-6}$	0.3
<i>HI</i> <sup>a</sup>	$3.64 \times 10^{-7}$	$5.54 \times 10^{-7}$	$3.51 \times 10^{-7}$	$3.41 \times 10^{-7}$	0.4
<b>Level 3</b>					
<i>OSI</i>	$1.58 \times 10^{-6}$	$1.73 \times 10^{-6}$	$1.60 \times 10^{-6}$	$2.42 \times 10^{-6}$	-
<i>OSI<sub>N</sub></i>	0.653	0.714	0.660	1.000	-

<sup>a</sup> Only one indicator is defined at Level 1 for safety and economic domains, namely *HI* and *PrI* respectively. Thus, both indexes are considered for Level 1 and 2.

As shown in Figure 12, all LNG-fuelled alternatives share a very similar economic impact indicator, while the result for Scheme 4 is sensibly higher (+39% compared to Scheme 2). This difference confirms that the higher fuel and taxation costs are a crucial economic limitation for the MGO scheme, despite the lower initial investment costs. Safety performance has a relevant impact on the overall sustainability of alternative fuel systems. Conventional MGO option (Scheme 4) shows the best safety performance, with a *HI* index 61% lower than Scheme 2, confirming the inherent safety of fuel oil when compared to low flash point fuels, such as natural gas.

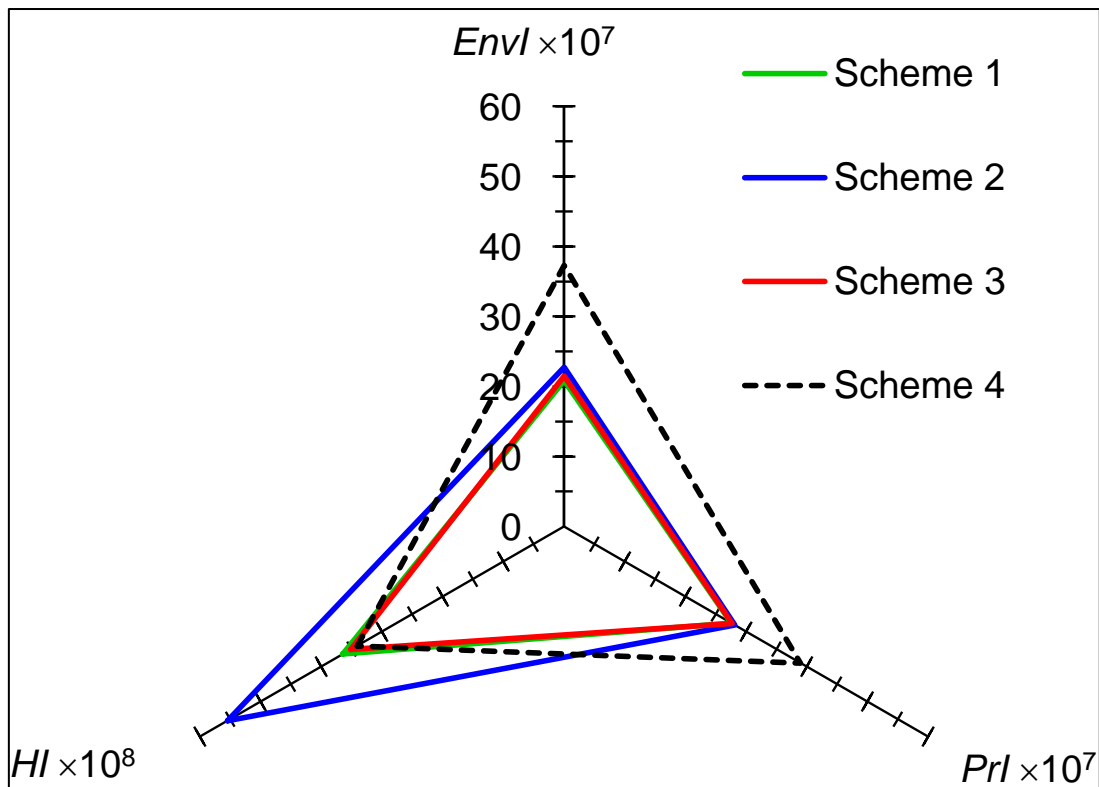


Figure 12: Radar plot showing the values of Level 2 indicators defined in Table 9 for the alternative fuel systems considered. Notice the different scale factor of HI axis.

As shown in Figure 12, this is compensated by the worst environmental performance of the MGO propulsion system, which significantly penalizes the sustainability of this technology. Overall, LNG-based alternatives feature similar environmental impact, with Scheme 1 performing better than others due to reduced CO<sub>2</sub> emissions. Figure 13 shows the sustainability ranking based on the calculated values of  $OSI_N$ , and the weight factors listed in Table 14.

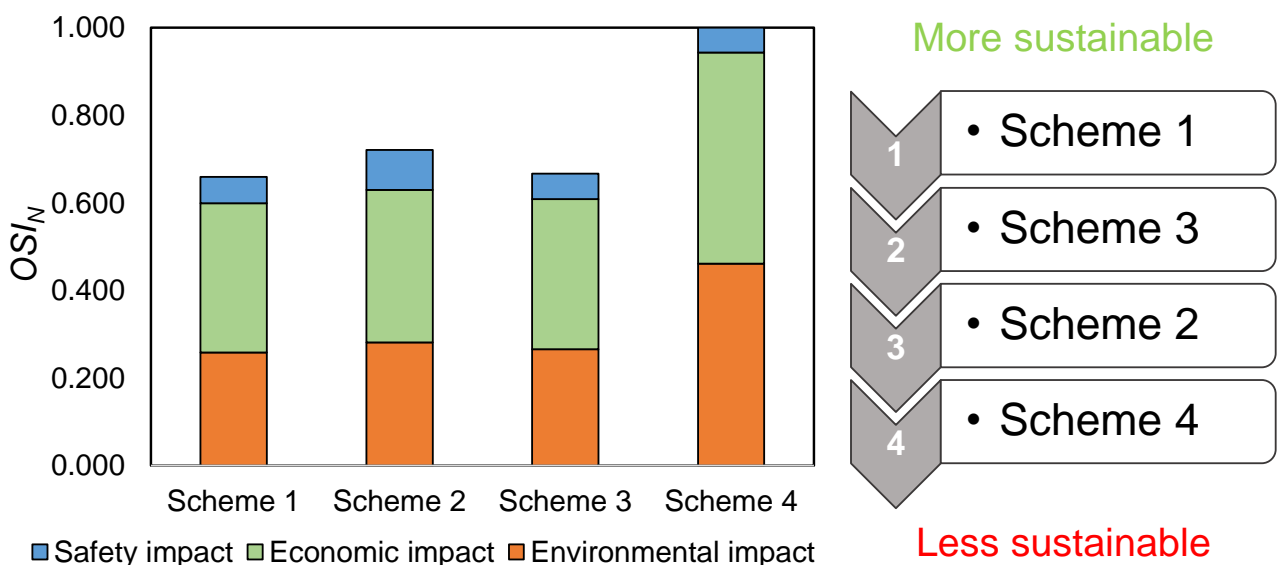


Figure 13: Values of the overall normalised sustainability indicator,  $OSI_N$ , and ranking resulting for the four alternatives considered based on the weight factors reported in Table 14. Colours indicate the contribution of the different impact domains to  $OSI_N$ .

The MGO fuel system (Scheme 4) results the least sustainable alternative for cruise ships, having the highest  $OSI_N$  value. This result is mainly due to the negative impact of both environmental and economic aspects (see Table 14).

Considering dual fuel technologies, the reduced methane slip achieved in Scheme 2 is not sufficient to counterbalance the higher cost figures related to additional maintenance. Moreover, the high-pressure level and the need of compressors worsen the inherent safety level of this scheme. Schemes 1 and 3 have a very similar overall index, with Scheme 3 technology favouring of the lowest value of the inherent safety index thanks to the absence of rotating equipment. However, when compared to Scheme 1, the almost double amount of environmental tax cost linked to higher CO<sub>2</sub> emission levels makes this option slightly less favourable. In conclusion, Scheme 1 may be deemed as the most sustainable solution for newly built large cruise ships, due to the lowest values of the estimated KPIs for all the three impact categories, as shown in Figure 13.

### 5.7.3. Sensitivity analysis

The set of weight factors used for index aggregation clearly affects the final value of the overall index and the sustainability-based ranking of the alternative fuel systems. As proposed by Dal Pozzo et al. (2017), ternary diagrams can be used to show the results obtained using different weight factors in the aggregation process. Each point of the diagram shown in Figure 14a represents a possible combination of weights for Level 2 aggregation, and the surface of the triangle represent all possible weight sets. Weight combinations falling in the white area in the plot still result in Scheme 1, showing the best overall performance. This is the case if a set of equal weights is used for the three impact categories (black square in Figure 14a). The blue area in the plot is the region of weight combinations in which Scheme 4 shows the best sustainability performance. Diesel propulsion becomes the most sustainable solution only when limited relevance is given to environmental aspects (weight factor less than 0.35), confirming that the higher environmental impacts associated with this technology represent an important limit for its sustainability performance. The range of weight values for the safety domain that result in a low  $OSI_N$  value for Scheme 4 is limited. This confirms that only when inherent safety is deemed crucial for the analysis, the MGO scheme might benefit from its inherently safer profile. Nevertheless, the figure shows that the high operating costs represent a penalization of conventional fuel system, even when considering the higher complexity and capital costs of LNG-based systems.

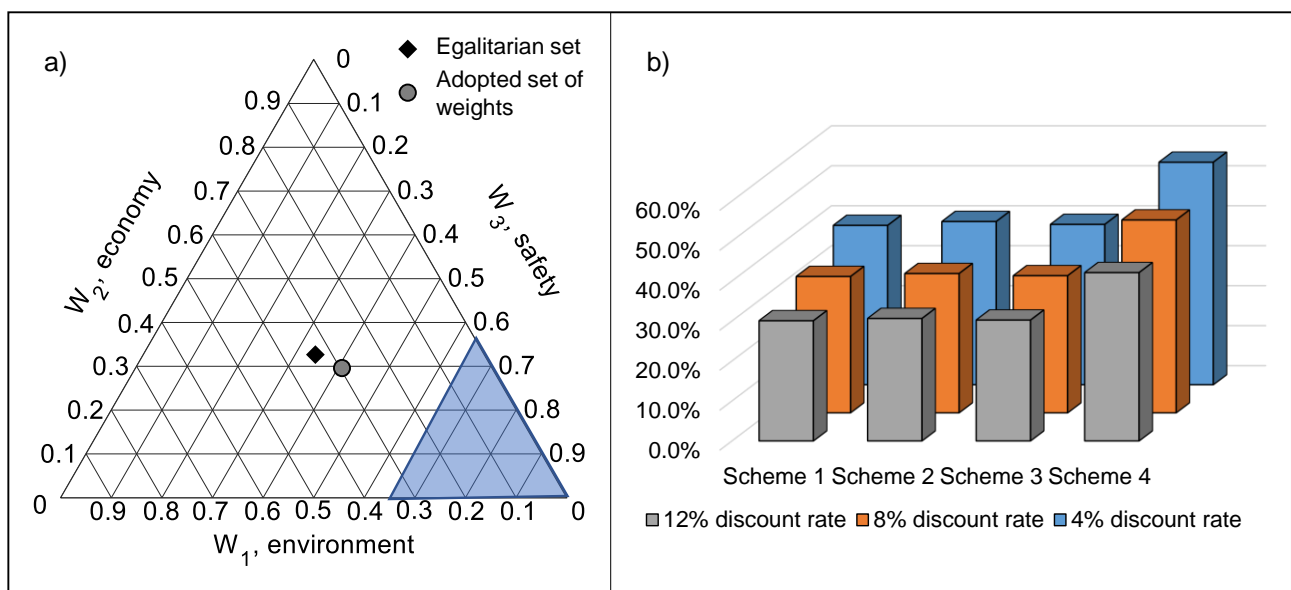


Figure 14: Influence of different sets of weight factors on the  $OSI$  values for a conventional MGO fuel system (a); PrI percent impact over  $OSI_N$  for different discount rate values (b).

A different type of sensitivity analysis was performed to prove the stability of the results against the variation of discount rate  $r$ . A  $\pm 50\%$  modification of the baseline  $r$  value (i.e., 8%) was considered, covering the range of possible values reported in the literature. As shown in Figure 14b, the variation of economic index impact over the  $OSI_N$  value is limited. When compared to the baseline scenario, the influence of  $PrI$  over the calculated  $OSI_N$  increases by a maximum +7.4% imposing  $r = 4\%$  (i.e., a -50% variation), whereas a -6.1% difference is obtained for  $r = 12\%$  (i.e., a +50% variation). Scheme 4 is the alternative that is mostly affected by discount rate variation.

Furthermore, a Monte Carlo method was applied to perform a sensitivity analysis among the ranking of alternatives, following the approach suggested by Tugnoli et al. (2008). This analysis was aimed at calculating the cumulative probability of an inversion in the ranking due to the variation of level 2 aggregation weight set. The variability range of level 2 indicator weight factors was assumed equal to  $\pm 50\%$  of the initial value selected for each weight factor. A symmetric beta distribution (National Institute of Standards and Technology, 2012) with shape parameters  $\alpha = \beta = 4$  was considered to assess the values within the variation interval. The robustness of the ranking of the alternative technologies based on the calculated  $OSI$  values was assessed calculating the distribution of the differences between selected pairs of alternatives. The difference is indicated as  $\Delta OSI$  in Figure 15. A positive  $\Delta OSI$  value indicates that there is no shift in the ranking of alternatives and that the original preference order shown in Figure 13 is maintained.

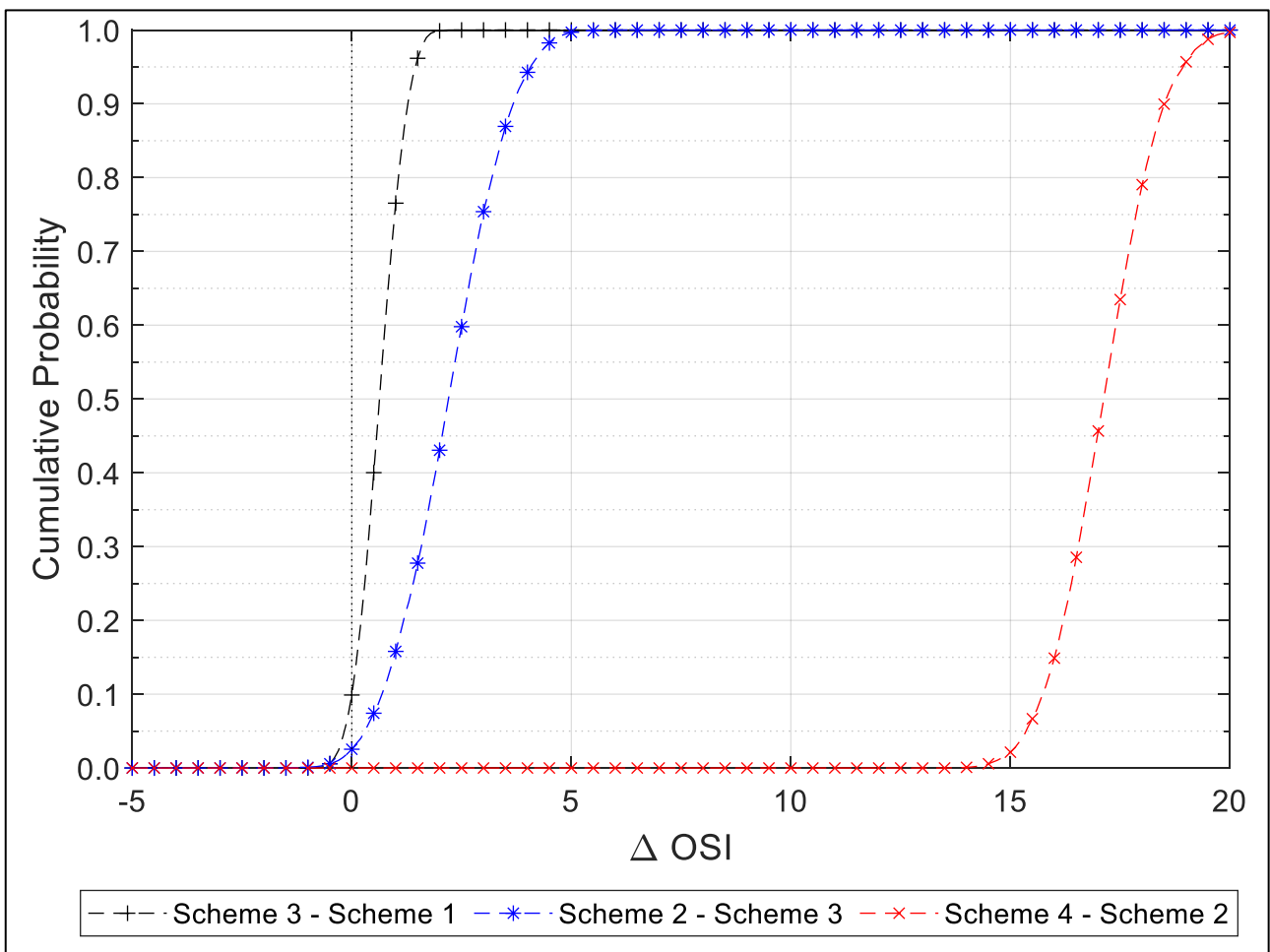


Figure 15: Distribution of cumulative probability for  $OSI$  differences ( $\Delta OSI$ ) between reference schemes

As shown in Figure 15, the cumulative probability of having negative values of  $\Delta OSI$  when varying the set of weights selected is negligible for reference scheme 4. Focusing on Schemes 3 and 2, there is about a 10% probability that Scheme 3 can result more sustainable than Scheme 1, whereas Scheme 2 has a probability lower than 5% to perform better than Scheme 3.

As a matter of fact, the occurrence of a swap in the original alternative ranking reported in Figure 13 for Schemes 3 and 1 could be expected, due to the almost identical value of the overall  $OSI$  index and to the wide variation of impact target weights considered for the sensitivity analysis. Differently, even if the sustainability performance of Schemes 3 and 2 is very similar, the original ranking was proven robust, since the shift in probability values resulted very limited, as shown from the sensitivity analysis. The obtained results confirm that a moderate uncertainty in the selection of weights does not drastically affect the outcomes obtained with the approach described in this Chapter.

## 5.8. Conclusions

The sustainability assessment methodology presented in this chapter allowed comparing the performance of different cruise ship fuel systems. A multi-criteria analysis was performed, considering the three main domains of sustainability: environment, economics, and safety. KPIs were calculated and further aggregated into an overall sustainability index that was used as a metric to rank the assessed technologies. The results obtained from the multi-criteria analysis performed evidenced that the use of LPDF systems (Scheme 1) results the most sustainable solution thanks to the lowest figures for all the impact indicators. This scheme shares a similar  $OSI$  value with LBSI systems (Scheme 3). However, the better safety profile of the latter is counterbalanced by a higher environmental impact caused by larger amounts of emitted  $CO_2$ , which also negatively affects the economic profile of Scheme 3. One of the main advantages of the HPDF technology (Scheme 2) is the low global warming impact achieved thanks to the substantial reduction of methane slip. However, the need of a SCR exhaust gas treatment system and the additional costs for its maintenance penalize the economic profile of this scheme that, combined with the highest  $HI$  value, make this solution the least sustainable among the gas-based alternatives. As expected, Scheme 4 solution, based on the use of MGO, results the least sustainable fuelling alternative due to its negative environmental profile, which also downgrades its economic appeal due to the taxation scheme considered. Finally, the ranking obtained for the alternative technologies was proven robust by means of a Monte Carlo sensitivity analysis that explored different values of the weights used for KPI aggregation. Overall, the method developed allowed obtaining a synthetic sustainability fingerprint, identifying the critical points that will be crucial for the development of “green ships” accounting for a holistic perspective of safety, environmental and economic aspects. However, an inherent limitation of the proposed methodology, correlated to its application during early design phases, is the exclusion of safety barriers installed on board, since details needed for their assessment are usually defined at a later design stage. Technological aspects such as the safety and security of fuel supply for gas-only fuel systems or the availability of required infrastructures (more broadly, technological readiness) might also influence the preference order of the alternatives. Lastly, no assumptions were made regarding the time spent by ships inside ECA zones. However, such aspect may be considered in further analysis since it might affect the economic performance of the alternatives.

# Chapter 6. Risk assessment of LNG bunkering operations

This Chapter is focused on the risk assessment of the different LNG bunkering options presented in Section 2.6. In the first part of the Chapter, an inherent safety assessment of the more common LNG bunkering technologies is carried out, comparing the results with those obtained for conventional marine fuels bunkering operations. To this end, a tool for the quantitative assessment of the inherent safety performance of bunkering technologies is developed. Such a tool aims to support decision-making in the early process design of LNG bunkering technologies, allowing the identification of the safest alternative. Moreover, this approach can integrate economic and environmental considerations in broader sustainability assessment studies, providing a metric to address societal aspects, as described in Chapter 5. A set of inherent safety indicators based on consequence evaluation of potential accident scenarios with respect to human and asset targets is proposed, allowing the evaluation and the ranking of different hazard sources characteristic of each ship bunkering technology assessed. Furthermore, the credibility of loss of containment events is introduced in the analysis using equipment-specific credit factors, which summarise the past performance of similar process units, providing a useful estimation of release credibility in the early phase of design. Reference schemes for the different bunkering concepts are outlined to support the inherent safety assessment and to identify the characteristic process conditions needed for consequence assessment.

A methodological approach aimed at understanding the influence of managerial aspects on the risk level of LNG bunkering facilities is presented in Section 6.2. The proposed approach integrates the conventional QRA workflow with a previously developed methodology for the modification of leak frequencies that accounts for external influencing elements related to both operational and organizational issues named TEC2O (Frequency modification methodology based on TEChnical Operational and Organizational factors). A case study is outlined to demonstrate the application of the approach. Following the identification of main process units and operating conditions, individual and societal risk levels connected with LNG bunkering operations carried out at ports are estimated. Release occurrence frequencies are then modified according to TEC2O methodology and risk levels for two opposite management scenarios are calculated and compared, leading to the identification of the more influential operating and organizational factors. Finally, a sensitivity analysis is carried out to assess the effect of variations of TEC2O parameters on the values of the modified occurrence frequencies.

## 6.1. Inherent safety assessment of LNG bunkering technologies

To facilitate the inherent safety assessment of the different bunkering technologies, the overall bunkering process was considered as a “system”. Each system was considered to be based on a specific “concept” and constituted of different process “blocks”, as illustrated in Figure 16. Although concepts C and D are representative of a PTS bunkering arrangement, conventional marine fuels bunkering for passenger ships is typically carried out through a small-scale auxiliary bunker vessel having an overall storage capacity in the range of 100-800 m<sup>3</sup> of fuel. Intermediate Fuel Oil (IFO) and MGO bunkering operations are normally carried out at berth during passenger boarding using flexible rubber hoses compliant to EN 1765:2016 (CEN, 2016b) and not through the use of transfer arms, as considered for Concept A.

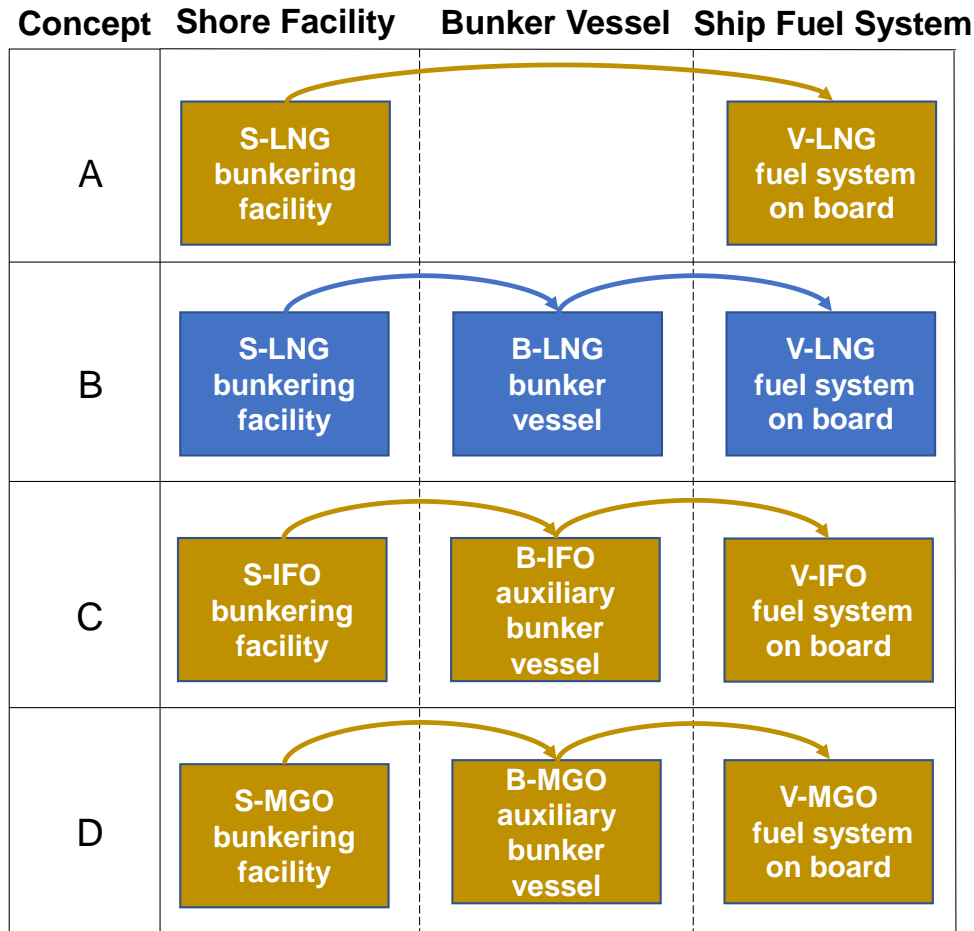


Figure 16: Overview of the different concepts and relative process blocks considered for the alternative ship bunkering systems analysed. Blue blocks refer to STS bunkering configuration, while dark yellow indicates a PTS arrangement.

Reference schemes for each onshore bunkering facility were elaborated based on a survey of the technical literature and current industrial practice and data retrieved from detailed studies by the Danish Maritime Authority, (2012) and Gas Infrastructure Europe, (2020). The reference scheme of the LNG-fuelled vessel is based on the LBSI FGSS described in Section 2.5.3, whereas schemes of the IFO/MGO bunker and user vessels were defined based on the data from Caterpillar, (2013). The defined schemes provided the required basis for gathering the main process data necessary in the framework of the present study, and to allow the quantification and comparison of the expected inherent safety performance of alternative bunkering technologies. Other technological aspects, such as economics, different possible storage solutions or energy efficiency fall out of the scope of the present analysis and were not considered.

### 6.1.1. Reference systems for LNG bunkering and supply

In the present study, only two main alternative LNG bunkering systems were considered: Concept A, featuring the typical PTS configuration (Figure 16a); and Concept B, with a STS configuration (Figure 16b). The TTS technology was not considered in the present analysis as it is only suitable for small-scale applications and therefore not comparable to any conventional fuel bunkering operation. The simplified reference process flow diagrams (PFDs) including the equipment tags for all the blocks present in the two alternative systems (see Figure 16) are reported in Figure 17 and described in detail in the following. Process operating conditions and equipment features are summarized in Appendix B.

### S-LNG block: LNG shore-based bunkering facility

The reference PFD considered for LNG shore-based bunkering facilities is reported in Figure 17a for both Concepts A and B. In both concepts, cryogenic loading pumps (G01 A/B) transfer LNG from storage tanks (D01, D02, etc.), connected with a common manifold, up to the loading arm (S02). Similarly, a boil-off gas (BOG) line connects tanks to BOG transfer arm (S01), allowing tank pressure regulation and equalization during LNG transfer to either user vessel fuel system (Concept A) or bunker vessel (Concept B).

### B-LNG block: ship-to-ship bunker vessel

Ship-to-ship operations for LNG bunkering may be carried out either in port areas or in the open sea. In this study, only ship-to-ship transfer in port areas was considered for sake of comparison with conventional fuel bunkering.

Figure 17b provides a reference scheme for a small-scale bunker vessel with a storage capacity of about 6,000 m<sup>3</sup>. LNG is stored in two bi-lobe IMO independent type C tanks (D01 and D02) and is delivered to the receiving ship using submerged cryogenic pumps installed inside the tanks through a flexible hose for cryogenic applications (LNG line S04), designed according to EN 1474-2. During bunkering operations, the BOG line (S03) is connected to the receiving vessel. Moreover, the BOG produced is managed by means of a compressor (P01) which allows tank pressure compensation and the fuel supply to the vessel dual fuel engine. In addition, the bunker vessel is equipped with a LBSI type FGSS for feeding its dual fuel engines.

### V-LNG block: user vessel

The reference scheme assumed for the LNG fuel system installed on a ship is based on the LBSI technology described Section 2.5.3. This kind of FGSS was assumed as representative of a passenger ferry boat with an installed power of about 38 MW (DNV-GL, 2015b). The considered reference scheme, shown in Figure 17c, includes a single LNG storage tank (D01), an LNG vaporizer and a fuel gas heater (E01 and E02, respectively) needed to control gas temperature. The BOG compressor (P01) is used to manage tank pressure. A BOG pre-heater (E03) is installed upstream the compressor to control vapor temperature.



### **6.1.2. Reference systems for conventional bunkering with diesel fuels**

Reference process schemes for conventional diesel fuel bunkering were defined with the collaboration of a team of experts involving port operators (either qualified personnel of port authorities or operating companies) of several Italian harbour areas. A specific survey was submitted to the expert team, to integrate the information available from the technical literature (Caterpillar, 2013; OCIMF, 2010). Conventional fuel bunkering operations were considered to be carried out adopting only PTS configurations, by using a small-scale auxiliary bunker vessel. As shown in Figure 16, two alternative concepts, based on different fuel types and thus requiring different operating conditions, were considered for the sake of comparison. The two alternative fuels considered were:

1. IFO 380, in Concept C;
2. MGO in Concept D.

Further technical characteristics of both fuels can be found in the work by Mohd Noor et al., (2018).

The simplified reference schemes including the equipment tags for concepts C and D are reported in Figure 18. Due to the similarities, a single reference scheme was considered for IFO and MGO in each block of Figure 16. Process operating conditions and equipment features are summarized in Section B.1 of Appendix B.

#### S-IFO and S-MGO blocks: onshore bunkering facilities

Figure 18a shows the reference scheme considered for the land based IFO and MGO facilities. The fuel is stored in several atmospheric tanks (T01-T06) connected with a pipe network and pumping stations (pumps G01/02). Fuel is delivered to the bunker vessel at about 2 bar pressure (OCIMF, 2010).

#### B-IFO and B-MGO blocks: ship-to-ship auxiliary bunker vessel

Figure 18b shows the reference scheme considered for a typical auxiliary bunker vessel employed for refuelling operations for ferry boats, either adopting IFO or MGO. The onboard storage system consists of atmospheric tanks (T01-T07) that are heated to reduce fuel viscosity and to ease fuel transfer operations. A bunker pump (G01) is used to deliver the required fuel at about 2 bar pressure to the receiving vessel tanks (OCIMF, 2010).

#### V-IMO and V-MGO blocks: fuel system on the end-user vessel

Figure 18c shows the reference scheme of a typical diesel fuel supply system installed on ferry boats. Fuel is stored onboard in two prismatic atmospheric tanks (D01 and D02). A gear pump (G01) transfers the fuel towards two settling tanks (D03 and D04). A heater (E01) follows the settling tanks, then the oil is transferred by pump (G02) to two daily service tanks (D05 and D06). Prior to engine injection, the fuel is heated again (in heater E02) in order to reach an adequate viscosity grade as required by the engine, and finally injected into the engine through a booster pump (G03).

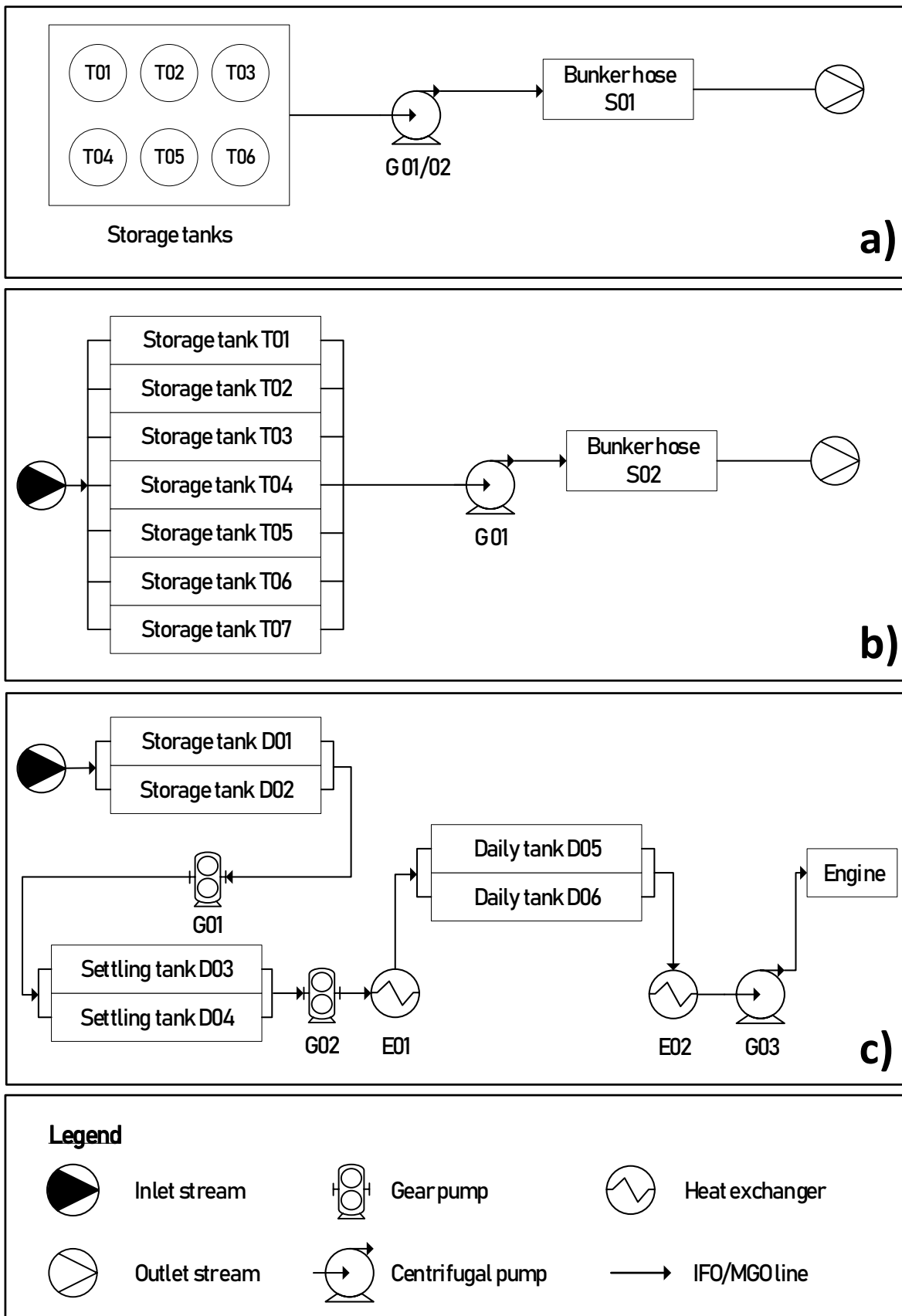


Figure 18: Reference schemes considered for the storage and supply blocks based on the utilization of conventional fuels in Concepts C and D of Figure 16: a) S-IFO and S-MGO shore-based storage facility; b) B-IFO and B-MGO bunker vessel; c) V-IFO and V-MGO fuel system onboard ship.

### 6.1.3. Methodology

The consequence based KPI approach described in Section 5.4 was adopted in this Chapter and further expanded in order to assess the inherent safety profile of vessel bunkering operations, thus extending its applicability to the entire bunker supply chain of marine fuels. The procedure required for the evaluation of KPIs is schematized in Figure 19.

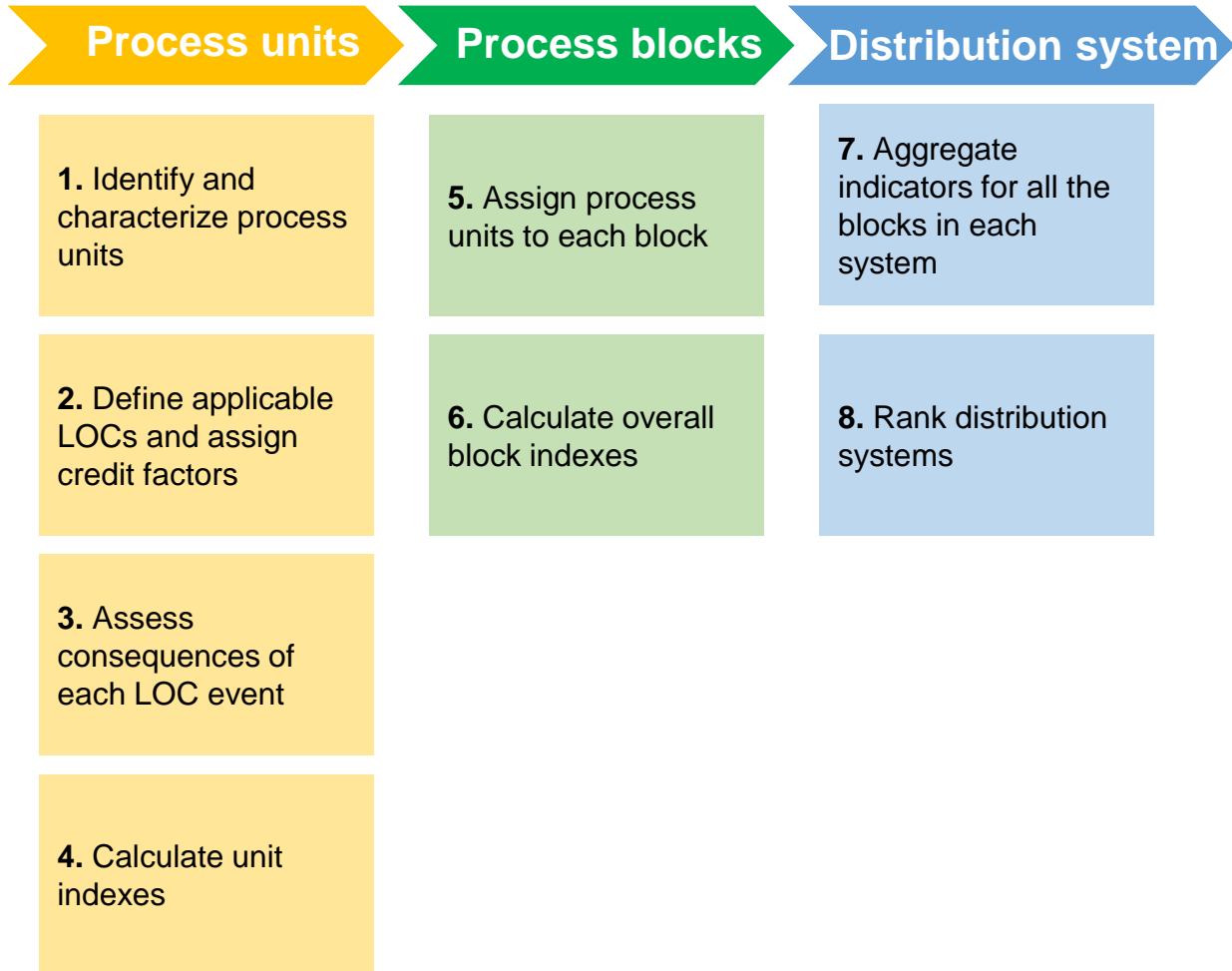


Figure 19: Overview of the methodology implemented for the inherent safety assessment of alternative technologies for marine fuel bunkering.

The preliminary part of the analysis (Step 1 in Figure 19) consists in the definition of reference schemes for vessel bunkering to support the inherent safety assessment of each technology considered. LOC events categorization was carried out considering the reference release types and credit factors listed in Table 6 (Step 2 in Figure 19). In step 3 of the methodology the consequence analysis of the possible scenarios following each LOC was performed using the well-known integral models proposed by Van Den Bosh and Weterings, (2005). To avoid introducing uncertainties related to fuel composition, dangerous effects were estimated assuming LNG as pure methane, while IFO and MGO were assumed as pure n-dodecane and pure n-nonane, respectively. Differently from what done in Chapter 5, an escalation distance was also calculated considering the damage threshold relative to process equipment reported in Table 7. Such an extension in scope led to the calculation of additional unit KPIs (Step 4 of Figure 19), as specified in the following. All the assessed units were then allocated to the relevant process blocks (Step 5 of Figure 19). Successively, unit indicators were aggregated to obtain block and overall inherent hazard indexes (Step 6 and 7 of Figure 19). Finally, the alternative distribution systems were ranked on the basis of the overall KPIs calculated in the previous steps (Step 8 in Figure 19).

#### 6.1.4. Description of inherent safety KPIs

In addition to the unit inherent hazard index (*UHI*) defined in Section 5.4, a unit potential hazard index (*UPI*) was defined for each unit as follows:

$$UPI_{u,B} = \max_{LOC} (h_{u,B,LOC}^2) \quad \text{Eq. 6.1}$$

where  $h_{u,B,LOC}$  is the maximum damage distance obtained for a specific LOC type, and process unit,  $u$ , belonging to the block ( $B$ ) of the system. The  $UPI_{u,B}$  index is representative of the largest area affected by the worst-case scenario originated from the considered process unit, being hence proportional to the squared value of damage distance.

Adapting the definition of the *UHI* to the concept schematization of Figure 16, equation Eq. 5.5 can be rearranged as:

$$UHI_{u,B} = \sum_{LOC=1}^{n_{u,B}} Cf_{u,B,LOC} \cdot h_{u,B,LOC}^2 \quad \text{Eq. 6.2}$$

where  $n_{u,B}$  is the number of LOCs considered for a specific unit  $u$  of the block  $B$  considered and  $Cf_{u,B,LOC}$  is the credit factor relevant for the LOC being accounted. The sum of the  $UPI_{u,B}$  and of  $UHI_{u,B}$  values for a particular block of a bunkering system (defined as a group of  $N$  units – see Table B1, Table B2 and Table B3 reported in Appendix B for a detailed list of equipment considered in each block) is used to calculate the block potential hazard index ( $BPI_B$ ) and the block inherent hazard index ( $BHI_B$ ) that are respectively defined as:

$$BPI_B = \sum_{u=1}^N UPI_{u,B} \quad \text{Eq. 6.3}$$

$$BHI_B = \sum_{u=1}^N UHI_{u,B} \quad \text{Eq. 6.4}$$

These aggregated indexes allow the assessment of the expected inherent safety performance of each block of fuel bunkering systems, based either on a direct assessment of potential worst-case scenarios ( $BPI$ ) or on the safety performance and release scenarios of the process units ( $BHI$ ). Therefore, the aggregation at the level of the overall system, thus considering all the blocks in the bunkering system, is also needed. In particular, the sum of the overall KPIs for each block is adopted to evaluate the overall inherent safety performance of the system:

$$PI = \sum_{B=1}^M BPI_B \quad \text{Eq. 6.5}$$

$$HI = \sum_{B=1}^M BHI_B \quad \text{Eq. 6.6}$$

where  $M$  is the number of blocks in each bunkering system, while  $PI$  and  $HI$  are the overall potential and overall inherent hazard indexes, respectively.

Considering the limited space available on board of vessels, and the limited distances between process units in bunkering facilities, escalation indexes were deemed necessary for the evaluation of the inherent safety profile of the systems considered. These indexes account for the possibility of severe “domino” scenarios, due to the simultaneous damage and release from several units, not accounted in the assessment of single units. The KPIs considered for escalation are based on the evaluation of an escalation distance ( $e_{u,LOC}$ ) for each credible scenario, which is calculated using the domino effect thresholds reported in Table 7. A “near field” cut-off approach was adopted in this case as well, thus considering  $e_{u,LOC}$  as the maximum value between the calculated escalation distance and 5 m.

Similarly to  $UPI_{u,B}$  the unit potential domino index,  $UPD_{u,B}$ , is defined as the square of the maximum escalation distance calculated for the unit:

$$UPD_{u,B} = \max_{LOC} (e_{u,B,LOC}^2) \quad \text{Eq. 6.7}$$

The unit domino hazard index,  $UHD_{i,k}$ , is defined as follows, in analogy to  $UHI_{i,k}$ :

$$UHD_{u,B} = \sum_{LOC=1}^{n_{u,B}} Cf_{u,B,LOC} \cdot e_{u,B,LOC}^2 \quad \text{Eq. 6.8}$$

A block domino potential hazard index,  $BPD_B$ , and a block domino inherent hazard index,  $BHD_B$ , are defined summing up respectively the  $UPD_{u,B}$  and  $UHD_{u,B}$  values for all the units in the B-th block of the bunkering system.

Aggregation of block indexes was performed to calculate the overall inherent safety domino indicators of the considered bunkering concept. In analogy with Eq. 6.5 and Eq. 6.6, the overall domino potential hazard index,  $PD$ , and the overall domino inherent hazard index,  $HD$ , were defined as:

$$PD = \sum_{B=1}^M BPD_B \quad \text{Eq. 6.9}$$

$$HD = \sum_{B=1}^M BHD_B \quad \text{Eq. 6.10}$$

The different indexes defined contribute to score different inherent safety aspects and may be used to obtain either an inherent safety fingerprint of the whole bunkering process or for single units.

### **6.1.5. Results and discussion**

The complete set of results for the KPI assessment of the alternative technologies for LNG bunkering is reported in Table B4 of Appendix B. The obtained results highlight that in Concept A, LNG storage tanks account for the highest *UPI* and *UPD*. The presence of external loading pumps in the shore facility is a critical issue, since these units show a *UHI* value of 43.3 m<sup>2</sup>/y and a *UHD* of 40.4 m<sup>2</sup>/y. These values are the highest of the entire system, very similar to those of the LNG transfer arm. This is a direct consequence of pumps and compressors credit factor values that are particularly high due to the presence of rotating parts, which increase the equipment failure likelihood as reported in Table 6. Submerged LNG transfer pumps are installed inside the double walled storage tank. Hence, release events from these units are excluded from the present analysis.

With reference to STS operations (Concept B), the main LNG storage tanks onboard the bunker vessel show both the higher unit potential index, *UPI*, and the higher unit potential domino, *UPD*, of the entire bunkering system, respectively, 8.04×10<sup>6</sup> m<sup>2</sup> and 7.87×10<sup>6</sup> m<sup>2</sup>. These values are almost twice those calculated for the shore facility storage tanks. This is due to the fact that bunker ship tanks have a capacity almost twice as big as that of each individual tank used for LNG storage in the shore facility and that the operating conditions in the bunker ship tank are more severe than those encountered in shore facility storages (higher temperature and pressure, as reported in Table B1 of Appendix B).

When considering the influence of credit factors, the LNG loading pumps located in the shore facility appear also in this case the least inherently safe equipment involved in this system, with the highest *UHI* and *UHD*.

For the sake of comparison, the KPIs were calculated for the conventional bunkering technologies as well. The results obtained are reported in Table B5 and Table B6 of Appendix B, for Concept C (IFO bunkering) and Concept D (MGO bunkering) respectively. Storage tanks located on the shore facility feature the highest *UPI* and *UPD* values due to the largest amount of stored hazardous substance. The bunker hose used in the shore facility is the most critical unit in terms of inherent hazard index, being characterized by the highest values of both *UHI* and *UHD*. It is worth mentioning that the indexes obtained in the case of Concept D are higher than those obtained for Concept C, due to the lower flash point and wider flammability range of MGO with respect to IFO.

## Comparison among the alternative bunkering systems

A comparison among the normalised values of the potential and hazard indexes calculated for the alternative technologies is reported in Figure 20. The figure also reports the correspondent normalised indexes for domino effect.

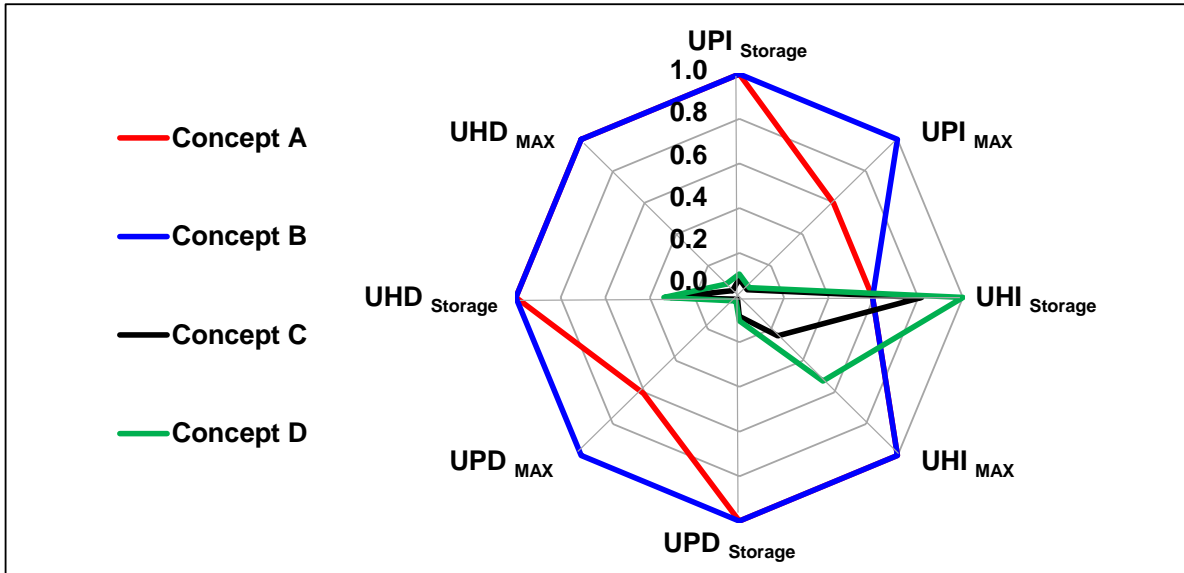


Figure 20: Normalised values of unit potential hazard and inherent hazard indexes for the bulk storage unit ( $UPI_{Storage}$  and  $UHI_{Storage}$ ); maximum unit potential hazard and inherent hazard indexes ( $UPI_{MAX}$  and  $UHI_{MAX}$ ); domino unit potential hazard and domino inherent hazard indexes for the bulk storage unit ( $UPD_{Storage}$  and  $UHD_{Storage}$ ); maximum domino unit potential hazard and domino inherent hazard indexes ( $UPD_{MAX}$  and  $UHD_{MAX}$ ).

When credit factors are introduced in the analysis, a completely different result is obtained from the comparison among the inherent hazard indexes for the shore facility storage tanks ( $UHI_{Storage}$  in Figure 20). In fact, credit factors of atmospheric vertical tanks adopted for conventional fuels storage are one order of magnitude higher than those of the pressurized or semi-pressurized tanks adopted for LNG storage (see Table 6). This leads to doubled  $UHI_{Storage}$  values with respect to LNG storage tanks, despite the more limited severity of accident scenarios resulting from conventional fuel releases compared to those calculated for LNG. Credit factors also affect the relative ranking among the performance of the worst critical equipment of each system, reducing the difference among the inherent safety performance of LNG and conventional technologies (see Figure 20). The same qualitative considerations can be extended to the comparison among the domino indexes. In particular,  $UPD$  and  $UHD$  for shore facility tanks and the most critical equipment drastically penalize LNG-based concepts compared to the conventional systems (see Figure 20).

Figure 21 reports the KPIs calculated for each block of the different bunkering systems considered. Considering both the  $BPI$  (reported in Figure 21a) and the  $BHI$  (reported in Figure 21b) it is evident that the shore facility is the most critical unit amongst all bunkering blocks. This is mainly due to the larger inventories of hazardous materials and the more severe conditions in fluid handling and transfer. However, the analysis also points out that the KPIs of the LNG-based FGSS are quite high, comparable to those of the shore facility. Despite the limited onboard inventory of hazardous substances, the complexity of LNG fuel system in terms of required auxiliary units is the main cause of such result. Moreover, while the inherent hazard level of the LNG FGSS is comparable with that of the shore facility, the vulnerability is higher, due to the presence of passengers onboard during

bunkering operation. This highlights an important issue that should be considered in the safe development of LNG-fuelled vessels.

The analysis of domino effect results crucial to identify the potential interference among the different operations carried out within each bunkering system, possibly leading to accident propagation. On the one hand, as shown in Figure 21c and Figure 21d, that report the values of the *BPD* and *BHD* respectively, a relevant escalation hazard is present in LNG bunkering systems. This is due to the possibility of severe scenarios which may induce the catastrophic failure of neighbouring units. On the other hand, in both Concepts C and D, the scenarios associated with the release of IFO and MGO have a reduced escalation potential due to their limited severity and extension.

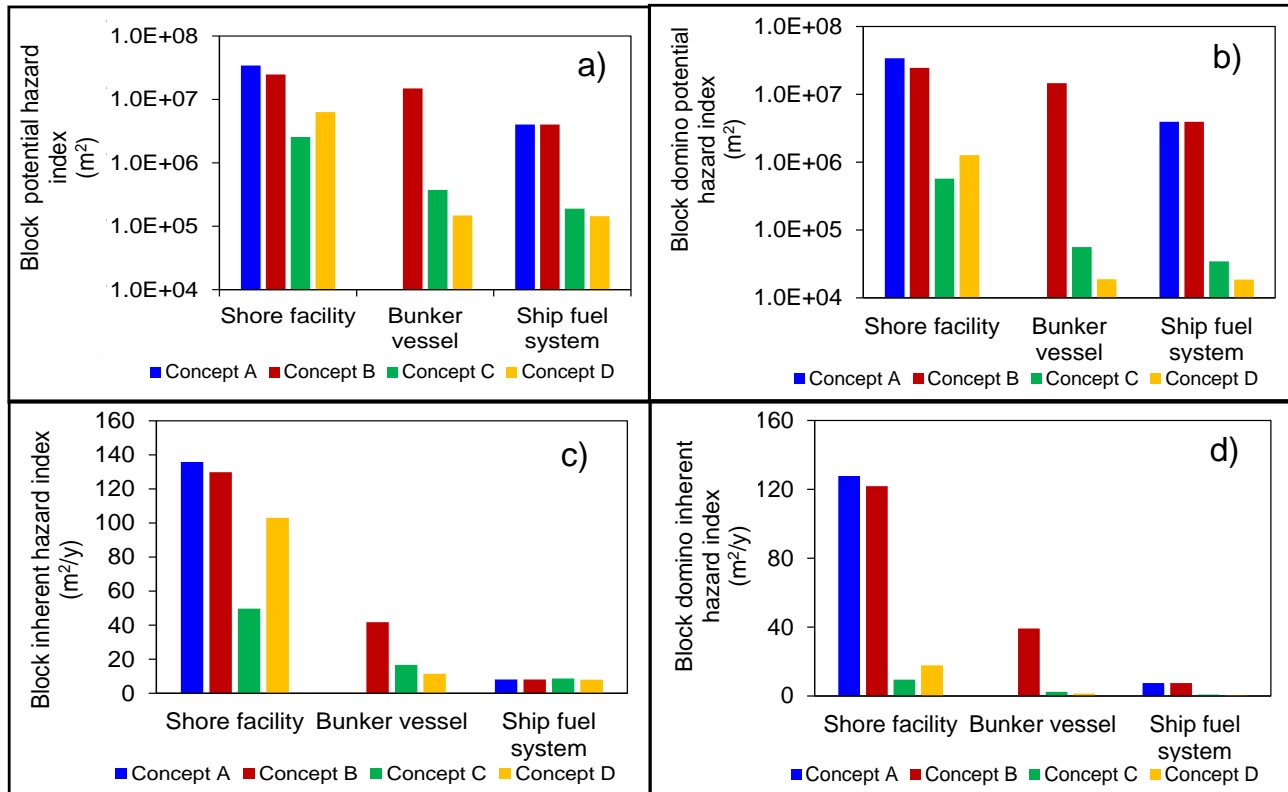


Figure 21: KPI values for the single blocks of the alternative bunkering systems: a) block potential hazard index *BPI* ( $m^2$ ), b) block inherent hazard index *BHI* ( $m^2/y$ ), c) block domino potential hazard index *BPD* ( $m^2$ ), d) block domino inherent hazard index *BHD* ( $m^2/y$ ).

A comparison of the overall inherent safety KPIs for the bunkering concepts considered is shown in Figure 22. It is evident how LNG based technologies (Concepts A and B) result in much higher values of the KPIs with respect to conventional technologies (Concepts C and D). As shown in Figure 22a, the overall potential and domino indexes (*PI* and *PD*) for conventional fuel bunkering systems are at least one order of magnitude lower than those calculated for LNG. When comparing the overall inherent hazard index (*HI*, see Figure 22b), the differences among the four alternative fuelling concepts are attenuated, but the LNG-based technologies still feature KPI values almost twice than those obtained for conventional technologies. Also, when considering the domino overall inherent hazard (*HD*, see Figure 22b), conventional technologies (Concepts C and D) show again KPIs that are at least one order of magnitude lower than those of LNG (Concepts A and B).

Based upon the values of the overall potential and inherent indexes, it is possible to rank the alternative bunkering technologies considered, as illustrated in Figure 22c. This ranking is independent from the selection of a particular KPI, since all the overall indexes have the same qualitative trend, as can be seen from Figure 22a and Figure 22b).

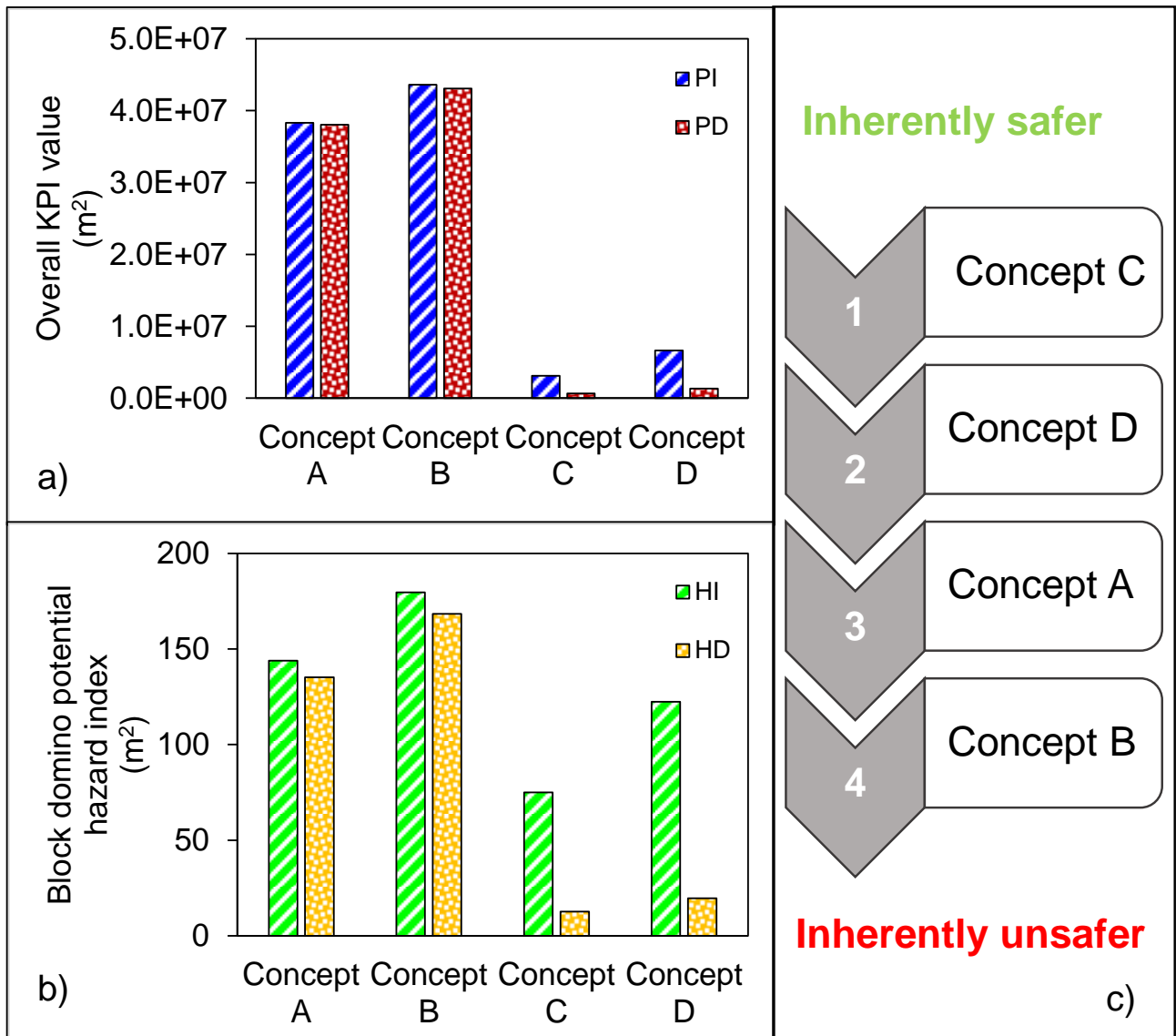


Figure 22: Overall KPIs for the alternative bunkering systems considered: a) overall potential hazard index PI (m<sup>2</sup>) and overall domino potential hazard index PD (m<sup>2</sup>); b) overall inherent hazard index HI (m<sup>2</sup>/y) and overall domino inherent hazard index HD (m<sup>2</sup>/y); c) qualitative ranking among the four Concepts considered based on overall inherent safety KPIs.

## **6.2. Integration of managerial aspects and simultaneous operation in LNG bunkering risk analysis**

As described in the introduction of this Chapter, a holistic safety analysis was performed exploiting the approach of quantitative risk assessment. Individual and societal risk related to shore-to-ship bunkering operation were calculated and compared to the risk figures resulting from two different management scenarios: one prioritizes emergency preparedness and safety culture, while the other accounts for a less safety-oriented management. Either operational mistakes or organizational flaws may lead to unwanted spillages causing hazardous situations. To reduce the time spent at berth by ships and ensure the cost-effectiveness of LNG refuelling operations, simultaneous port operations, such as passengers boarding, might be performed during bunkering. This kind of activities, as well as other managerial and operational aspects, have an influence over the risk profile of LNG bunkering installations.

A reference case study, reproducing the characteristics of a small-scale touristic port, was defined in the following to demonstrate the applicability of the proposed approach and to quantify the risk modification due to managerial factors.

### ***6.2.1. Overview of the developed approach***

#### Baseline QRA

The “baseline” QRA workflow (highlighted in blue in Figure 23) was defined in accordance with the guidelines for the risk assessment of installations supplying LNG as fuel to ships provided in ISO/TS 18683. Comparably to the methodology illustrated in Section 6.1.3, the first steps of the QRA approach require the identification of the main equipment involved in the process and its layout and the gathering of main operating conditions. Each process unit was then associated with a set of possible LOC event types among those listed in Table 6.

Each LOC was then associated with a baseline release frequency value based on the size of equipment connection and the assumed hole size range. Release frequencies were retrieved from a collection of process equipment leak frequency data for use in QRA issued by DNV, (2013a), whereas more detailed reliability data for transfer hoses, collected from a report by UK health and safety executive (HSE, 2019) were used.

Baseline LOC frequency values, estimated without considering the influence of operational and organizational factors, represent the input of an event tree analysis (ETA), which was performed to identify the dangerous scenarios originating from release events and their occurrence frequency. Here, the effect of the presence of safety barriers (e.g. the activation of the emergency shut down), the activation of mitigation measures (e.g. the intervention of the emergency squad) and the occurrence of other possible events affecting the final outcome (e.g. immediate or delayed ignition) was quantified in terms of probabilities of success, following the indications of Aneziris et al., (2014) and Vilchez et al., (2011). More details on this aspect are presented in Section 6.2.3.

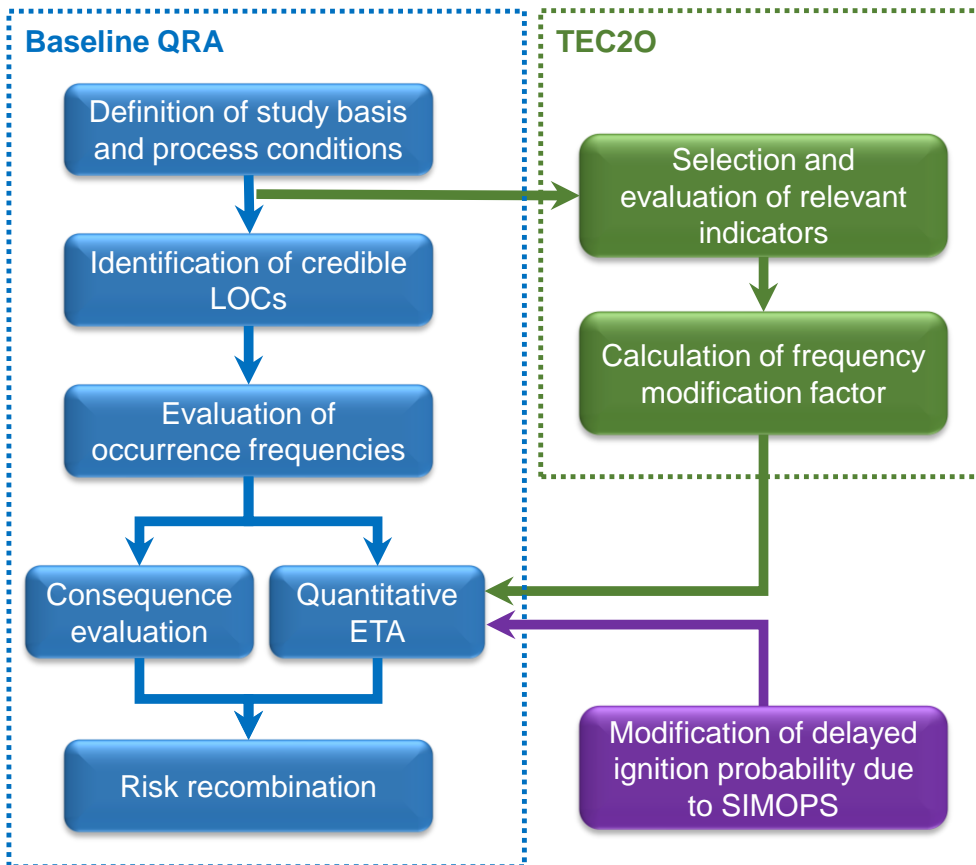


Figure 23: Workflow of the enhanced risk assessment analysis

Besides the estimation of the occurrence frequencies of the scenarios identified in the ETA, the risk assessment process required the evaluation of their consequences. This task was carried out using the same models mentioned in Section 6.1.3.

In the last step of the baseline QRA, the resulting frequencies of hazardous scenarios were combined with the outcomes of consequence evaluation to assess the risk level generated by the process or activity under assessment.

Location-specific individual risk (LSIR) and societal risk are the two metrics used in this study to quantify the risk level associated with LNG bunkering activities. Values of death probabilities ( $P_d$ ) due to heat radiation and overpressure were estimated according to the guidance provided by Uijt de Haag and Ale, (2005). Probit functions retrieved from the technical literature (Van Den Bosh and Twilt, 1992) were used to correlate dangerous effects with  $P_d$ , allowing the calculation of the LSIR. Death probability values were then combined with figures available for the persons present inside the port area to yield societal risk values which were compared against the risk acceptance criteria reported in the ISO technical specification 18683:2015, concerning supply of LNG as a ship fuel (European committee for standardization, 2015).

The spatial distribution of dangerous effects represents the basis for risk calculation. Risk figures were calculated discretizing the area under analysis (corresponding to the port area illustrated in Figure 25) using a grid (squares featuring 0.5 m edges were considered in the present work). Each cell of the grid (the centre of the cell was assumed to be representative of the entire cell for LSIR calculations) is subject to a different combination of dangerous effects (due to different distances from the release source) and likelihood of effects exposure (affected by distribution of wind probability for the specific grid point under analysis and LOC frequency).

Every dangerous scenario (identified by index  $S$ ) resulting from the ETA contributes to the overall LSIR value for a fraction ( $\Delta IR_{LOC,w,S}$ ) that was calculated as follows:

$$\Delta IR_{LOC,w,S} = f_{LOC} \cdot P_w \cdot P_d \cdot P_S \quad \text{Eq. 6.11}$$

The subscript  $LOC$  refers to a particular LOC event characterized by a frequency ( $f_{LOC}$ ), while the subscript  $w$  refers to weather class and direction, whose probability value is ( $P_w$ ). The term  $P_S$  indicates the dangerous scenario probability.

$$LSIR_P = \sum_{LOC,w,S} \Delta IR_{LOC,w,S} \quad \text{Eq. 6.12}$$

Equation Eq. 6.12 was used to calculate a value of LSIR for each cell centre point ( $P$ ) under consideration. This value was obtained summing all the considered LOC events, weather classes and identified dangerous scenarios. Concerning the estimation of societal risk, this was calculated in terms of the relation between incidents that cause at least a number  $N$  of expected fatalities and the cumulative frequency ( $F$ ) of such incidents, and it was expressed using F-N curves. The total number of deaths ( $N_{LOC,w,S}$ ) resulting from the combination of a specific LOC event, weather class and dangerous scenario was calculated summing over all the cells ( $C$ ) of the domain the expected number of deaths of each grid cell. The latter value was obtained multiplying the estimated  $P_d$  and the assumed cell population ( $N_C$ ) derived from population density:

$$N_{LOC,w,S} = \sum_C P_d \cdot N_C \quad \text{Eq. 6.13}$$

The frequency value at which a number of fatalities equal to  $N_{LOC,w,S}$  can be expected was calculated as:

$$f_{LOC,w,S} = f_{LOC} \cdot P_w \cdot P_S \quad \text{Eq. 6.14}$$

The calculations of Eq. 6.13 and Eq. 6.14 were repeated for all LOC events, weather class and dangerous scenarios, then  $F$  was obtained cumulating all  $f_{LOC,w,S}$  values for which the condition  $N_{LOC,w,S} > N$  is true.

The expected value of casualties per year, or potential loss of life index ( $PLL$ ), was also derived from the calculated societal risk profile. This index is expressed as the number of expected fatalities per year and was calculated as follows.

$$PLL = \sum_{LOC,w,S} f_{LOC,w,S} \cdot N_{LOC,w,S} \quad \text{Eq. 6.15}$$

The  $PLL$  index gives a quick measure of the societal risk level and it can be used to compare the risk increment due to managerial aspects.

## TEC2O methodology

The TEC2O method developed by Landucci and Paltrinieri, (2016) is intended to support dynamic risk assessment studies by determining modification factors aimed at a periodical update of the baseline leak frequency values. Specific modification factors are introduced in the methodology to increase/decrease the baseline LOC frequency values on the basis of the analysis of technical, human, and managerial elements. As illustrated in Figure 24a, the impact quantification of the mentioned factors relies on a weighted scoring system capable to account for their different importance in the considered process through the analysis of specific indicators, namely a technical modification factor (*TMF*) and a management modification factor (*MMF*). In the present study, the TEC2O methodology was adopted in order to modify baseline LOC frequency values, accounting for managerial aspects, thus addressing e.g., safety procedures, number of SIMOPs performed, frequency of maintenance operations, etc. Technical features were hereby excluded from the evaluation of the modification factor since equipment and process aspects remain unchanged from the baseline condition. The modified LOC frequencies ( $f'_{LOC}$ ) were thus obtained as follows:

$$f'_{LOC} = f_{LOC} \times MMF \quad \text{Eq. 6.16}$$

As illustrated in Figure 23, the modified LOC frequency values were used as an input for a quantified ETA in which increased delayed ignition probabilities were considered, reflecting an operational strategy that allows SIMOPs. The modified dangerous scenario frequencies calculated were then used to evaluate LSIR and societal risk together with consequence assessment results, as described previously.

The *MMF* accounts for managerial aspects related to definition of safety procedures, training and competencies of operators, safety culture, frequency of maintenance operations and communication at different levels of the organization. Those elements are evaluated following the Resilience based Early Warning Indicators (REWI) methodology developed by Øien et al., (2010), which proposes the use of specific indicators to quantify the mentioned aspects. As indicated by the authors, the TEC2O uses a selection of relevant indicators provided by the REWI methodology (Landucci and Paltrinieri, 2016). As indicated by Øien et al. (2010), the *MMF* is divided into two main subfactors to obtain more precise indications: operational subfactor (*OP*) and organizational subfactor (*OR*).

Each subfactor is evaluated by giving a score to specific indicators (*SOP* and *SOR*, for operational and organizational indicators respectively) that are associated with correspondent weight values ( $wOp_n$  and  $wOr_p$  for operational and organizational indicators respectively) leading to the calculation of the overall scores for *OP* and *OR* subfactors as follows:

$$OP = \sum_{n=1}^{Nop} SOP_n wOp_n \quad \text{Eq. 6.17}$$

$$OR = \sum_{p=1}^{Nor} SOR_p wOr_p \quad \text{Eq. 6.18}$$

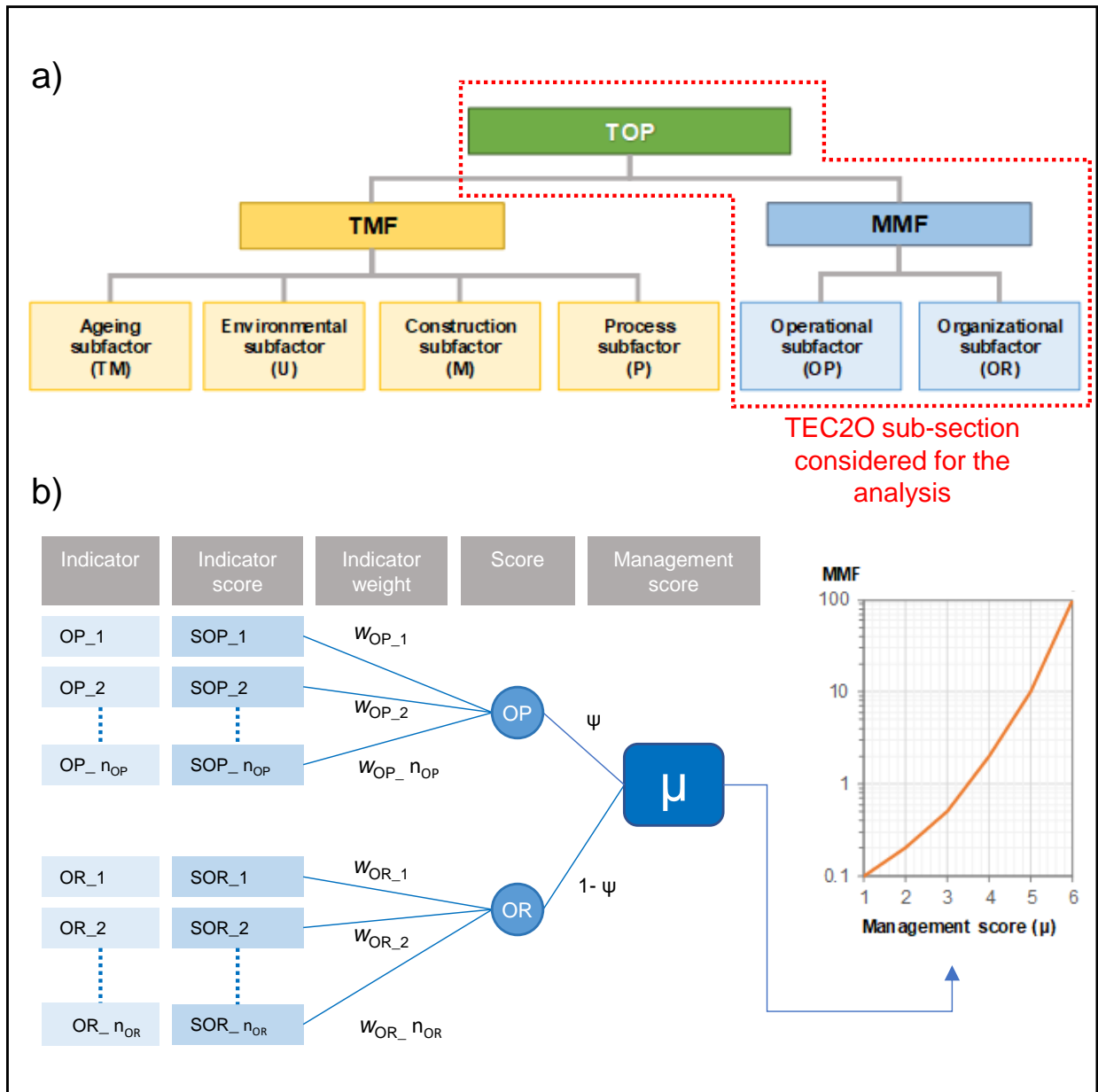


Figure 24: Sub-section of TEC20 method considered in the analysis (a) and procedure for the calculation of the management score and the MMF (b).

As indicated by Landucci and Paltrinieri, (2016), an equal weight was assigned to each indicator score (i.e.,  $w_{OP_n} = 1/N_{op}$ ,  $w_{OR_p} = 1/N_{or}$ ; where  $N_{op}$  and  $N_{or}$  are the total number of operational and organizational indicators, respectively), giving the same importance to all the operational and organizational aspects considered in the present study. Then,  $OP$  and  $OR$  subfactors were combined using the following relationship to calculate the overall management score,  $\mu$ :

$$\mu = \psi OP + (1 - \psi)OR \quad \text{Eq. 6.19}$$

where  $\psi = 0.5$  in the present study. The analytical expressions for the rules used for the conversion of the management score  $\mu$  into a  $MMF$  value are reported in the original paper by Landucci and Paltrinieri (2016). An example of correlation is illustrated in Figure 24b. A dedicated sensitivity analysis was carried out to assess the variation of the calculated  $MMF$  value with different sets of weights ( $w_{OP_n}$  and  $w_{OR_p}$ ). Assumptions and results of this analysis are reported in Section B.3 of Appendix B.

## Impact of SIMOPs on delayed ignition probability

A significant aspect that needs to be considered when including SIMOPS in the QRA framework is the increased delayed ignition probability due to the presence of additional sources of ignition in the areas where a flammable gas cloud may form. To consider this issue, a specific step was combined with the results of TEC20 methodology (purple block in Figure 23) and the baseline event tree was modified accordingly. Further details about the modification of ignition probabilities are reported in the following Sections.

### 6.2.2. Definition of the test-case

The case selected as a reference to illustrate the application of the methodology shown in Figure 23 is a PTS LNG bunkering facility serving a roll-on/roll-off ferry. This is representative for a small-scale installation: the port infrastructure is intended as a seasonal touristic hub with a limited traffic density, and comprises a passenger waiting area, and a 160 m long berth on which an LNG storage tank and the bunkering equipment are installed. A general layout of the onshore LNG delivery infrastructure is given in Figure 25. Fuel is delivered to the ship via two cryogenic pumps through a 3" (DN 80) flexible transfer hose. Including ramp-up and purging time, the bunker operation is expected to be completed in two-hours timeframe. Pressure balancing between the on board and port LNG storage tanks is achieved using a 3" vapour return line during refuelling operations. Manoeuvring of the transfer hoses is facilitated by a handling crane installed on the pier. To provide a frequency basis for the study, two bunkering operations per day are assumed to take place at the facility, thus resulting in 720 bunkering operations per year, allowing for some maintenance downtime.

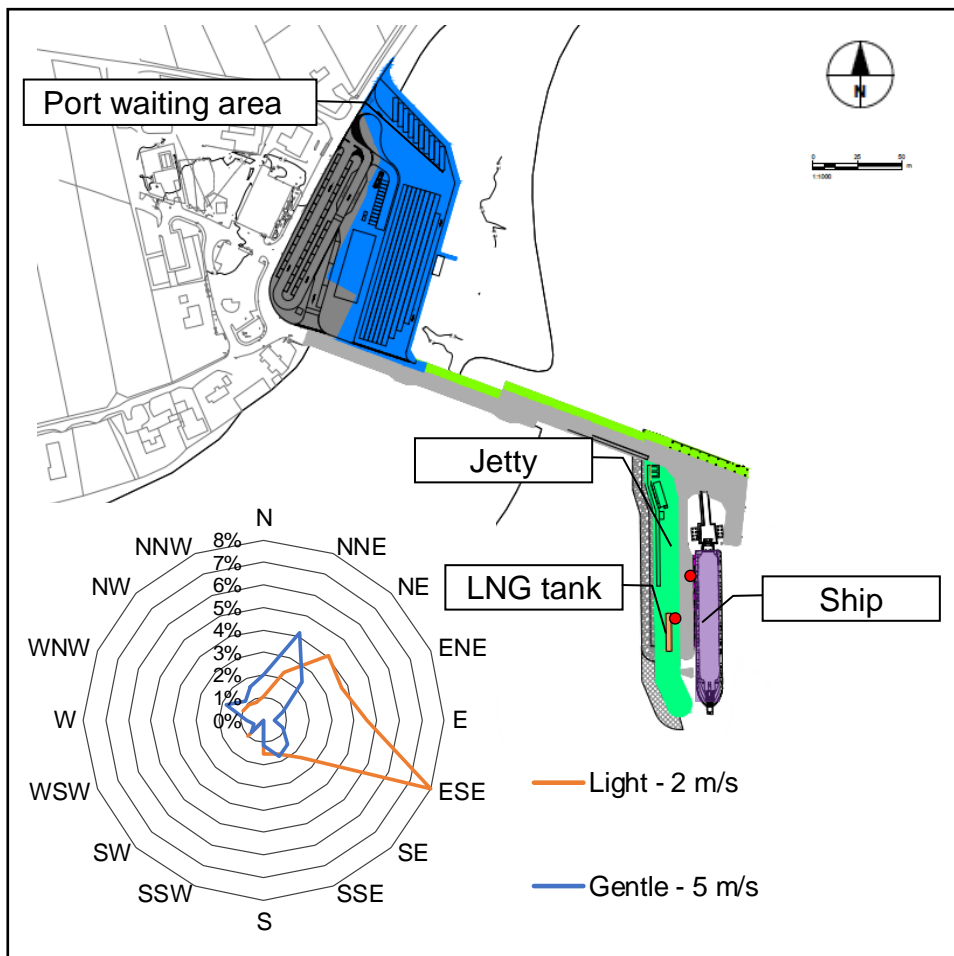


Figure 25: Layout and wind rose considered for the case study. Red dots indicate the assumed release points.

## Process units and operating conditions

The boundaries of the analysis encompass all the process units installed onshore and extent up to the manifold of ships bunker station. A simplified process flow diagram of the considered bunkering facility is shown in Figure 26.

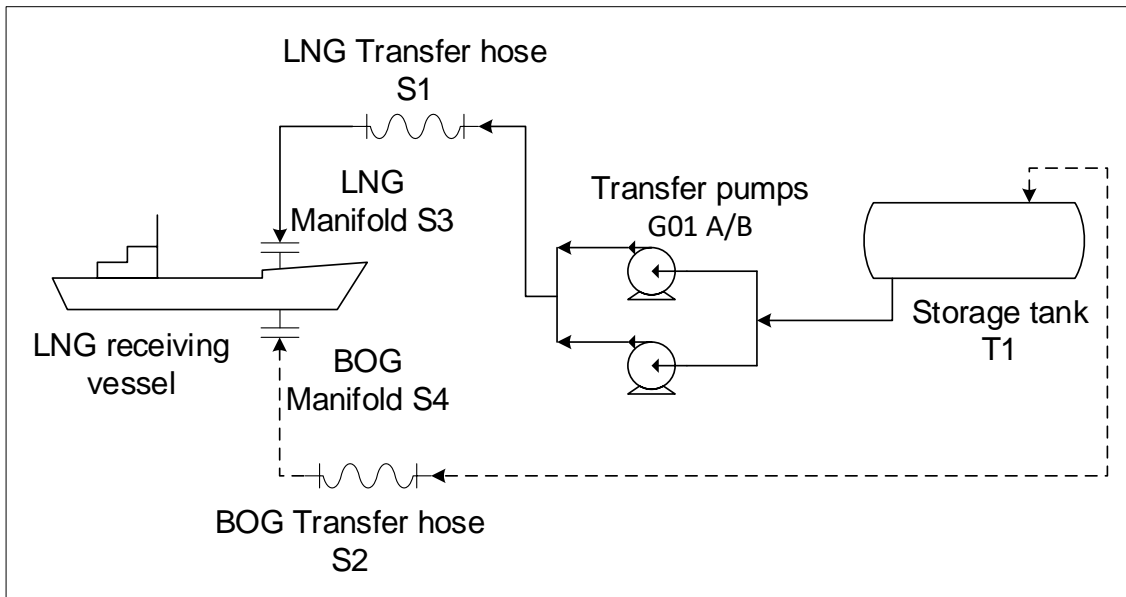


Figure 26: Simplified process flow diagram of the considered bunkering installation.

LNG is loaded on board of the receiving ship using cryogenic pumps (G01 A/B in Figure 26) installed in proximity of the storage tank, at a maximum loading rate of 12.5 kg/s (approximately equivalent to 100 m<sup>3</sup>/h at delivery conditions) and stored at saturation conditions in a double-walled, horizontal cryogenic tank (T1). It was assumed that the distance between fixed cryogenic pipeline and the ship LNG bunker station is covered by flexible cryogenic hoses (S1 and S2) that are maneuvered with the help of a hose crane. LNG and BOG transfer hoses are manufactured according to requirements set by EN 1474-2. The fixed cryogenic pipeline installed onshore consists of a tube-in-tube piping, housed in a culvert, for additional protection of the pipework from rams and other accidental damages. As done for the inherent safety evaluation, pure methane was assumed as reference substance for this analysis to avoid introducing uncertainties related to LNG composition.

A summary of the main process conditions considered is reported in Table 15.

Table 15: Process units and operating conditions considered for the analyzed bunkering operation.

Parameter	Process unit					
	Storage tank T1	Transfer pump G01 A/B	LNG transfer hose S1	BOG transfer hose S2	LNG manifold S3	BOG manifold S4
Nominal capacity (m <sup>3</sup> )	450	-	-	-	-	-
Inventory (kg)	201,414	4,558	21	10	21	10
Line diameter (mm)	-	76.2	76.2	76.2	76.2	76.2
Flowrate (kg/s)	-	27.5	12.66	12.66	12.66	12.66
Pressure (bar)	3.5	4.0	4.0	4.0	4.0	4.0
Temperature (K)	128	128	128	132	128	132
State	Liquid	Liquid	Liquid	Vapor	Liquid	Vapor

## Simultaneous operations considered for the analysis

As reported in the study conducted by Chen and Deal, (2016), passenger and vehicle boarding are among the various port operations that can be carried out during LNG bunkering and may represent a possible hazardous situation. The different SIMOPs that can be carried out while bunkering ships with LNG are mainly dependent on the type of vessel that is being refuelled and on the operational mode of bunkering (e.g., STS, PTS or TTS). Simultaneous activities are likely to raise the overall risk level of the LNG bunkering operation due to their potential to increase the likelihood of dangerous accident scenarios, the ignition probability and to expose a larger number of individuals to hazardous situations. In the present study, boarding operations of passengers and vehicles taking place while refuelling the ferry with LNG were deemed as the most representative events to be integrated in the QRA framework. To do so, the quantified ETA performed for the baseline QRA was updated considering the increased ignition probability due to the presence of both passengers and vehicles in proximity of the bunker location. It was assumed that 65 vehicles per hour and 250 passengers per hour are boarded onto the ferry within the bunkering timeframe.

### **6.2.3. Results and discussion**

#### Results of baseline QRA

As illustrated in Figure 27 the dangerous scenarios accounted in this study are pool fires (or jet fires for pressurized releases) and flash fires. The vapour cloud explosion scenario was excluded from the analysis following a preliminary estimation of the resulting effects performed using the Multi Energy model (Van Den Bosh and Weterings, 2005). This showed that beyond the distances at which the half-value of the lower flammability limit (LFL/2) is achieved, the explosion overpressure reaches limited values, not sufficient to cause any fatality. The common approach followed in QRA studies is to assume a 100% death probability for individuals within the LFL/2 distance (Uijt de Haag and Ale, 2005) in case of flash fires. Therefore, the impact of vapour cloud explosions on the risk level would be outpaced by that of flash fires. The effect of safety barriers, more specifically the intervention of ESD system and of the emergency team at the site was also considered in the analysis. The activation of safety barriers limits the released amount of hazardous material: to consider this effect in the ETA, a separated tree branch, which refers to a limited spillage following leak isolation, was considered.

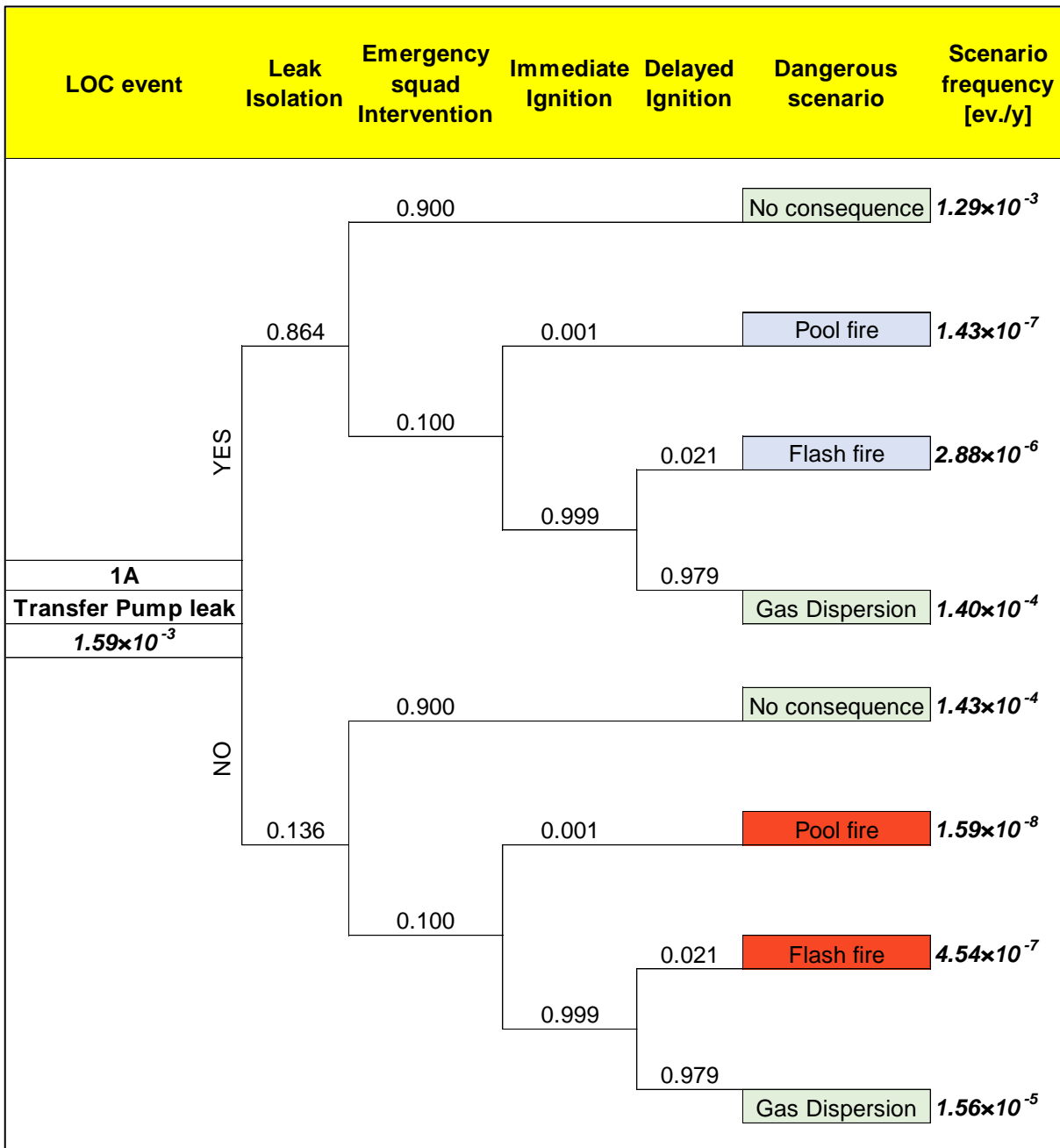


Figure 27: Example of event tree considered for the analysis. Dangerous scenarios originating from limited releases are shaded in blue, while scenarios resulting from an unlimited release are highlighted in red. Scenarios highlighted in green do not generate dangerous effects.

According to guidance provided by DNV, (2013b) and OGP, (2010), immediate and delayed ignition probabilities were estimated on the basis of calculated release rates, following the criteria reported in Table 16.

As suggested in the Guidelines for Preventing Human Error in Process Safety published by the Center for Chemical Process Safety (2010), the probability that an operator fails when taking action to contain a spillage ( $P_{Hum\ Err.}$ ) can be assumed as 10%. The leak isolation failure probability used in the ETA was estimated as follows:

$$P_{Isolation\ failure} = 1 - (1 - P_{Hum\ Err.}) \cdot (1 - P_{ESD}) \quad \text{Eq. 6.20}$$

Where the failure probability of the ESD system ( $P_{ESD}$ ) was calculated according to the equation reported below.

$$P_{ESD} = 1 - (1 - PFD_{ESD})^n \quad \text{Eq. 6.21}$$

It was assumed that each process section is equipped with two ESD devices for isolation (hence  $n=2$  in Eq. 6.21) and that the probability of failure on demand of the single ESD device ( $PFD_{ESD}$ ) is 2% (DNV, 2013b). Under these circumstances, the leak isolation failure probability calculated with Eq. 6.20 resulted equal to 13.6%.

Table 16: Criteria for the estimation of immediate and delayed ignition probabilities

<b>Immediate ignition</b>		
<b>Release phase</b>	<b>Leak rate [kg/s]</b>	<b>Probability</b>
<b>Gas</b>	< 1	$1.00 \times 10^{-4}$
	1 – 10	$1.00 \times 10^{-3}$
	> 10	$1.00 \times 10^{-2}$
<b>Liquid</b>	< 1.2	$1.00 \times 10^{-4}$
	1.2 – 25	$1.00 \times 10^{-3}$
	> 25	$1.00 \times 10^{-2}$
<b>Delayed ignition</b>		
<b>Gas or Liquid</b>	0.1	$1.00 \times 10^{-3}$
	0.2	$2.30 \times 10^{-3}$
	0.5	$6.60 \times 10^{-3}$
	1.0	$1.50 \times 10^{-2}$
	2.0	$1.74 \times 10^{-2}$
	5.0	$2.13 \times 10^{-2}$
	10	$2.47 \times 10^{-2}$
	20	$2.87 \times 10^{-2}$
	50	$3.50 \times 10^{-2}$
	> 100	$4.00 \times 10^{-2}$

A common aspect of uncertainty in QRA is associated with the frequency of inter-unit pipeline releases (DNV, 2013a). Application of process pipework failure data will tend to give overly conservative values with respect to longer inter-unit pipe segments. Due to the limited extension of fixed cryogenic pipework of the considered bunkering facility (<100 m), releases originating from this type of piping were assumed as already included in the LOC frequency value of the connected process units. LOC events categories reported in Table 17 are identical to those listed in Table 6, however the LOCs occurrence frequency values considered in this analysis were based on more detailed data sources, improving the estimation carried out with credit factors described in Section 6.1.3. The leakage frequency of LNG and BOG transfer hoses was assumed equal to  $4.0 \times 10^{-7}$  per transfer operation whereas full bore ruptures have a frequency of  $2.0 \times 10^{-7}$  per transfer (HSE, 2019). These values were adjusted to account for their actual usage, considering the assumptions reported in Section 6.2.2.

The LOCs occurrence frequency values obtained in the baseline QRA are summarized in Table 17, while the estimated probabilities of immediate and delayed ignition are reported in Table 18. Finally, Table 19 reports the calculated  $P_i$  values resulting from the ETA.

Table 17: Considered baseline LOC event frequencies (1/y). n.a.: not applicable.

LOC Type	Storage tank T1	Transfer Pump G01 A/B	LNG Transfer Hose S1	BOG Transfer Hose S2	LNG Manifold S3	BOG Manifold S4
R1	$1.00 \times 10^{-5}$	n.a.	n.a.	n.a.	n.a.	n.a.
R2	0*	n.a.	n.a.	n.a.	n.a.	n.a.
R3	0*	n.a.	n.a.	n.a.	n.a.	n.a.
R4	n.a.	$1.59 \times 10^{-3}$	$2.88 \times 10^{-4}$	$2.88 \times 10^{-4}$	$3.01 \times 10^{-4}$	$3.01 \times 10^{-4}$
R5	n.a.	$6.10 \times 10^{-4}$	$1.44 \times 10^{-4}$	$1.44 \times 10^{-4}$	$6.81 \times 10^{-5}$	$6.81 \times 10^{-5}$

\*LOC types 2 and 3 were deemed not credible for double-walled, cryogenic storage tank having frequencies lower than  $1.00 \times 10^{-6}$  (HSE, 2019)

Table 18: Estimated ignition probabilities. Values in italic are those subject to modification due to SIMOPs, as explained in Section 6.2.2.

LOC Type	Storage tank T1	Transfer Pump G01 A/B	LNG Transfer Hose S1	BOG Transfer Hose S2	LNG Manifold S3	BOG Manifold S4
<i>Immediate Ignition</i>						
R1	0.01%	-	-	-	-	-
R2	-	-	-	-	-	-
R3	-	-	-	-	-	-
R4	-	0.10%	0.10%	0.01%	0.01%	0.01%
R5	-	0.10%	0.10%	1.00%	0.10%	0.10%
<i>Delayed Ignition</i>						
R1	1.50%	-	-	-	-	-
R2	-	-	-	-	-	-
R3	-	-	-	-	-	-
R4	-	2.13%	2.13%	0.66%	0.10%	2.87%
R5	-	2.47%	2.87%	3.50%	1.50%	0.10%

Table 19: Baseline dangerous scenario probability values for limited and unlimited releases. Colour gradient highlights higher probability values.

Process unit	LOC Type	Dangerous scenario			
		Jet/Pool Fire		Flash Fire	
		Limited	Unlimited	Limited	Unlimited
Storage tank T1	R1	$8.64 \times 10^{-6}$	$1.36 \times 10^{-6}$	$1.30 \times 10^{-3}$	$2.04 \times 10^{-4}$
Transfer Pump G01 A/B	R4	$8.64 \times 10^{-5}$	$1.36 \times 10^{-5}$	$1.84 \times 10^{-3}$	$2.89 \times 10^{-4}$
	R5	$8.64 \times 10^{-5}$	$1.36 \times 10^{-5}$	$2.13 \times 10^{-3}$	$3.36 \times 10^{-4}$
LNG Transfer Hose S1	R4	$8.64 \times 10^{-5}$	$1.36 \times 10^{-5}$	$1.84 \times 10^{-3}$	$2.89 \times 10^{-4}$
	R5	$1.36 \times 10^{-5}$	$1.36 \times 10^{-5}$	$3.90 \times 10^{-4}$	$3.90 \times 10^{-4}$
BOG Transfer Hose S2	R4	$8.64 \times 10^{-6}$	$1.36 \times 10^{-6}$	$5.70 \times 10^{-4}$	$8.98 \times 10^{-5}$
	R5	$8.64 \times 10^{-4}$	$1.36 \times 10^{-4}$	$2.45 \times 10^{-3}$	$4.71 \times 10^{-4}$
LNG Manifold S3	R4	$8.64 \times 10^{-6}$	$1.36 \times 10^{-6}$	$1.30 \times 10^{-3}$	$2.04 \times 10^{-4}$
	R5	$8.64 \times 10^{-5}$	$1.36 \times 10^{-5}$	$2.48 \times 10^{-3}$	$3.90 \times 10^{-4}$
BOG Manifold S4	R4	$8.64 \times 10^{-6}$	$1.36 \times 10^{-6}$	$8.64 \times 10^{-5}$	$1.36 \times 10^{-5}$
	R5	$8.64 \times 10^{-5}$	$1.36 \times 10^{-5}$	$1.84 \times 10^{-3}$	$2.89 \times 10^{-4}$

The consequence evaluation step was carried out considering two different weather classes to account for distinct atmospheric stability conditions that affect gas cloud dispersion: class 5D, representative of dispersion-neutral conditions, and class 2F for high stability conditions (Ikealumba and Wu, 2017). Location-specific wind data was collected from an online database (WillyWeather, n.d.). All the dangerous effects were evaluated at a reference height of 1 m, representative for human vulnerability, assuming an ambient temperature of 15°C and a relative humidity of 70%. Transfer hoses inventory was estimated considering the volume of hazardous substance potentially trapped in an isolated section, which length was assumed equal to 10 m, while no limited inventory was considered for the transfer pumps so as to conservatively model a stationary release at worst possible conditions. Liquid spills were modelled as continuous releases, with an outflow rate given by Eq. 6.22, whereas pressurized gas release rates were calculated using Eq. 6.23, which assumes isentropic expansion to atmospheric conditions.

$$\dot{m} = C_D A_{hole} \sqrt{2\rho_{Liq}(p_0 - p_{atm})} \quad \text{Eq. 6.22}$$

Where the term  $\dot{m}$  is the release rate (kg/s);  $A_{hole}$  is the hole area (m<sup>2</sup>);  $\rho_{Liq}$  is the liquid density (kg/m<sup>3</sup>);  $C_D$  is the discharge coefficient, considered equal to 0.61; and the terms  $P_0$  and  $P_{atm}$  indicate the initial liquid absolute pressure and the atmospheric pressure values (Pa), respectively.

$$\dot{m} = C_D A_{hole} p_0 \sqrt{\frac{\gamma M}{RT_0} \left( \frac{2}{\gamma + 1} \right)^{\frac{\gamma + 1}{\gamma - 1}}} \quad \text{Eq. 6.23}$$

Here, the term  $\gamma$  is the ratio of gas specific heats, which is equal to 1.32 for methane;  $M$  is the molecular weight (kg/mol);  $T_0$  is the initial gas temperature (K) and  $R$  is the universal gas constant (J/kg mol K).

The maximum release duration was assumed to be 900 s and 90 s for unlimited and limited releases, respectively. The higher cut-off value, adapted from Landucci et al., (2015) is intended to limit the consequence assessment to a credible timeframe prior to emergency responders' intervention, while the lower limit is associated with an estimated ESD intervention time, as reported in another QRA study performed by DNV, (2013b).

#### Application of TEC2O methodology and modification of delayed ignition probabilities due to SIMOPs

The set of TEC2O indicators selected in this study is reported in Table 20, along with their scores. Site-specific data can be used to obtain a quantitative characterization of indicator scores and get a tailored frequency modification factor. However, the quantitative monitoring of the selected indicators was beyond the scope of the work and a qualitative evaluation was carried out instead, following the indications by Landucci and Paltrinieri, (2016).

Two extreme (and opposite) situations were considered: the first one reflects an ideal management strategy combined with an effective process equipment maintenance program; the second one is representative of a process management policy less safety-oriented, for which, as example, maintenance operations are scheduled with a lower frequency. For the ideal management situation (referred to as TEC2O – Good in the following), the selected operational and organizational factors were all given scores indicative of a well-established safety attitude in the management of bunkering operation, as considered, for example, by factors #2 and #3.

Conversely, for the other management situation (referred to as TEC2O - Bad in the following), all factors were given a mediocre or negative connotation, considering for example a more limited experience with the LNG bunkering process (see factor #5), with some exceptions as described in the following. All the TEC2O indicators considered in this study intrinsically implement human factor in the analysis as explained in the original work of Landucci and Paltrinieri (2016). An important distinction between TEC2O – Good and TEC2O – Bad situations was made on the basis of the maximum number of SIMOPs performed each month: for the TEC2O – Good situation it was assumed that a maximum of two SIMOPs are carried out each month, accounting for sporadic necessities, whereas for the TEC2O – Bad situation the factor #1, relative to SIMOPs, was given a value three times greater, reflecting the worse management of the simultaneous port activities. It must be noted that the only process units affected by such factor are the transfer hoses S1/S2 and bunker manifolds S3/S4 since these units are the closest to the ferry embarking lines.

Having considered four operational factors and four organizational factors, the weights  $wOp_n$  and  $wOr_p$  (used in Eq. 6.17 and Eq. 6.18 respectively) are equal to 0.25 assuming that all factors share the same importance.

As highlighted in Section 6.2.2 the presence of vehicles and passengers during bunkering operations increases the ignition probability. An average delayed ignition probability ( $P_{DI}$ ) in a 90 s time interval was calculated using the line model described in the Dutch guidelines for quantitative risk assessment (Uijt de Haag and Ale, 2005), reported below.

$$P_{DI} = \frac{1}{90} \int_0^{90} d(1 - e^{-\Gamma t}) dt \quad \text{Eq. 6.24}$$

The term  $d$  in Eq. 6.24 indicates the traffic density value, which was calculated on the basis of the assumptions reported in Section 6.2.2, considering an embarkment line with a length of 50 m. The ignition effectiveness values ( $\Gamma$ ) for vehicles and passengers were retrieved from the abovementioned guidelines (Uijt de Haag and Ale, 2005). The additional delayed ignition probability value calculated with Eq. 6.24, equal to 0.0681, was then added to the baseline values of relevant units reported in Table 18 to account for the risk modification induced by SIMOPs. Modified dangerous scenario probabilities ( $P_i$ ) were calculated updating the baseline event tree with the increased ignition probability values.

The modified dangerous scenario frequencies ( $f_s$ ) were finally obtained as the product among the modified LOC frequencies ( $f'_{LOC}$ ) and  $P_i$  values, as expressed by the following equation:

$$f_s = f'_{LOC} \cdot P_i \quad \text{Eq. 6.25}$$

Values of the frequency modification factor estimated according to TEC2O methodology are reported in Table 20.

The calculated  $MMF$  value is finally used to modify the baseline LOC frequencies according to Eq. 6.16, allowing to evaluate the modified dangerous scenario frequencies that are calculated multiplying the modified LOC frequency by the relevant dangerous scenario probability, as expressed by Eq. 6.25. For the sake of brevity, baseline and modified dangerous scenario frequencies are reported in Section B.4 of Appendix B.

Table 20: Comparison among selected TEC2O indicators used for the calculation of LOC frequency modification factor. The original factor ID from Landucci and Paltrinieri, (2016) is reported in brackets for ease of reference.

Factor ID	Process unit							
	Storage tank T1		Transfer pump G01 A/B		LNG/BOG transfer hoses S1/S2		LNG/BOG bunker manifolds S3/S4	
	TEC2O - Good	TEC2O - Bad	TEC2O - Good	TEC2O - Bad	TEC2O - Good	TEC2O - Bad	TEC2O - Good	TEC2O - Bad
<i>Operational factors</i>								
1 - Maximum no. of simultaneous operations last month (OPE 1.3.3.1)	2	2	2	2	2	6	2	6
2 - Average no. of exercises completed by operating personnel each month (OPE 2.1.1.1)	6	2	6	2	6	2	6	2
3 - No. of emergency preparedness exercises last three months (OPE 2.1.1.3)	18	6	18	6	18	6	18	6
4 - No. of exceptions handled by operating personnel last month (OPE 2.2.1.1)	2	6	2	6	2	6	2	6
<i>Organizational factors</i>								
5 - No. of years of experience with this particular system (ORG 1.1.1.1)	15	5	15	5	15	5	15	5
6 - Fraction of operating procedures that were risk assessed (ORG 1.2.1.2)	0.9	0.3	0.9	0.3	0.9	0.3	0.9	0.3
7 - Amount of overtime worked (ORG 2.2.1.1)	0.05	0.15	0.05	0.15	0.05	0.15	0.05	0.15
8 - No. of cases in which communication between actors has been inadequate (ORG 2.2.2.1)	2	6	2	6	2	6	2	6
<b>Calculated MMF</b>	0.168	1.189	0.168	1.189	0.168	2.446	0.168	2.446

Compared to baseline frequencies, dangerous scenario frequencies estimated assuming an ideal management situation are on average about 68% lower than frequencies calculated for the baseline condition. Some significant exceptions from this trend are represented by flash fires resulting from BOG hoses and manifold releases: the increased delayed ignition probability considered makes these dangerous scenarios up to about 12 times more frequent than correspondent baseline scenario. However, this effect is less important for BOG hose releases, for which the scenario frequency is almost twice the correspondent baseline frequency. On the other hand, final scenario frequencies of the TEC2O-Bad management situation result significantly increased with respect to the baseline situation. The combined effect of the additional ignition probability and modified LOC frequencies leads to a generalized increase of dangerous scenario frequencies, of about one order of magnitude for each of the aforementioned process units. It must be noted that the bunkering equipment located far away from the ship (i.e., storage tank T1 and transfer pumps G01/G02), which are not influenced by the simultaneous boarding operations, show increased LOC frequencies in line with the estimated *MMF* value reported in Table 20. Conversely, dangerous scenarios originating from transfer hoses and bunker manifolds will occur with an average frequency about 30 times higher than for the baseline case.

#### Comparison of individual and societal risk profiles

The calculated spatial distribution of LSIR for the baseline situation is represented in Figure 28. As shown in the figure, the highest risk value is experienced in proximity of the bunkering point, where most of the LOC events were considered to happen. The risk level gradually decreases moving away from bunkering point, where LNG and BOG transfer hoses and manifolds are located. Iso-risk curves of Figure 28 are not symmetrical: the effect of predominant winds coming from north-eastern/eastern sectors (see Figure 25) increases the distance at which higher LSIR levels can be experienced for points located to the west of release sources. This effect is mainly related to accident scenarios that involve a delayed ignition, such as Flash Fires. In this case, the flammable cloud disperses along the downwind direction, where the jetty is located.

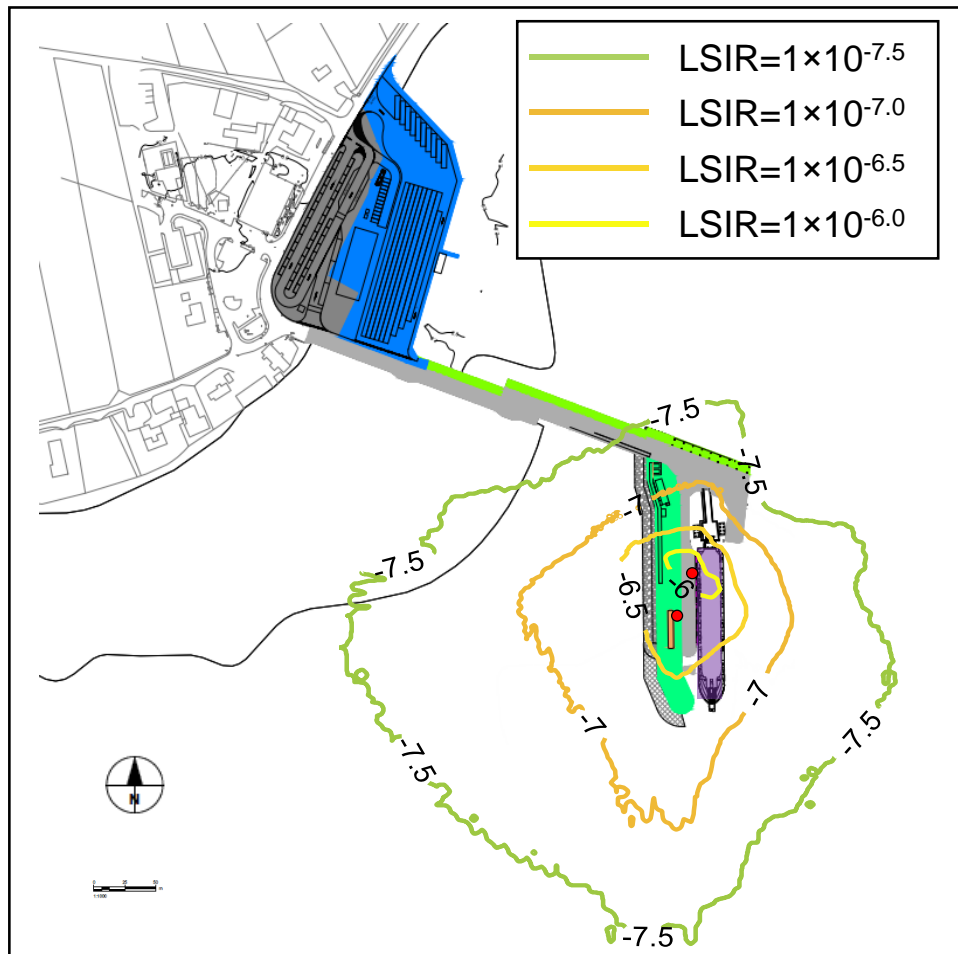


Figure 28: Iso-risk curves showing spatial distribution of LSIR for the baseline management situation

An alternative representation of individual risk is given in Figure 29, which reports the maximum value of the LSIR as function of the distance from the bunkering point (red dot next to the ship in Figure 28) for the two management situations considered and the baseline case. The three risk threshold values highlighted in Figure 29 are those proposed by the ISO technical specification 18683:2015 (European committee for standardization, 2015), as mentioned in Section 6.2.1. The standard identifies different kind of exposed population providing separate risk acceptance criteria: 1<sup>st</sup> party personnel that are crew and bunkering operators directly involved in the activity; 2<sup>nd</sup> party personnel that refers to port and terminal personnel; and 3<sup>rd</sup> party personnel with prolonged risk exposure. The 3<sup>rd</sup> party personnel risk threshold also applies to the general public not involved in bunkering operations (e.g., passengers).

It can be noted that for the TEC20-Good situation intolerable risk levels for the 3<sup>rd</sup> party personnel and the general public are only reached within 10 m from the bunkering point, whereas for the baseline case this distance increases up to around 55 m. For the TEC20-Bad situation the risk acceptance limits for 1<sup>st</sup> and 2<sup>nd</sup> party personnel are exceeded nearby the bunker point and high LSIR values are still reached farther than 100 m from this point. An interesting feature that can be noticed from Figure 29 is that the maximum LSIR for the baseline curve is located about 30 meters from the bunkering point. As can be seen in Figure 28 the LNG storage tank and transfer pumps are located about 27 m south-west to the bunkering point. This explains the different position of the risk maximum for the baseline case: the highest LSIR value is shifted towards the location of the storage tank and transfer pumps since the flash fire scenario originating from pumps G01/02 has the highest occurrence frequency among all the dangerous scenarios of this case (see Section B.4 of Appendix B).

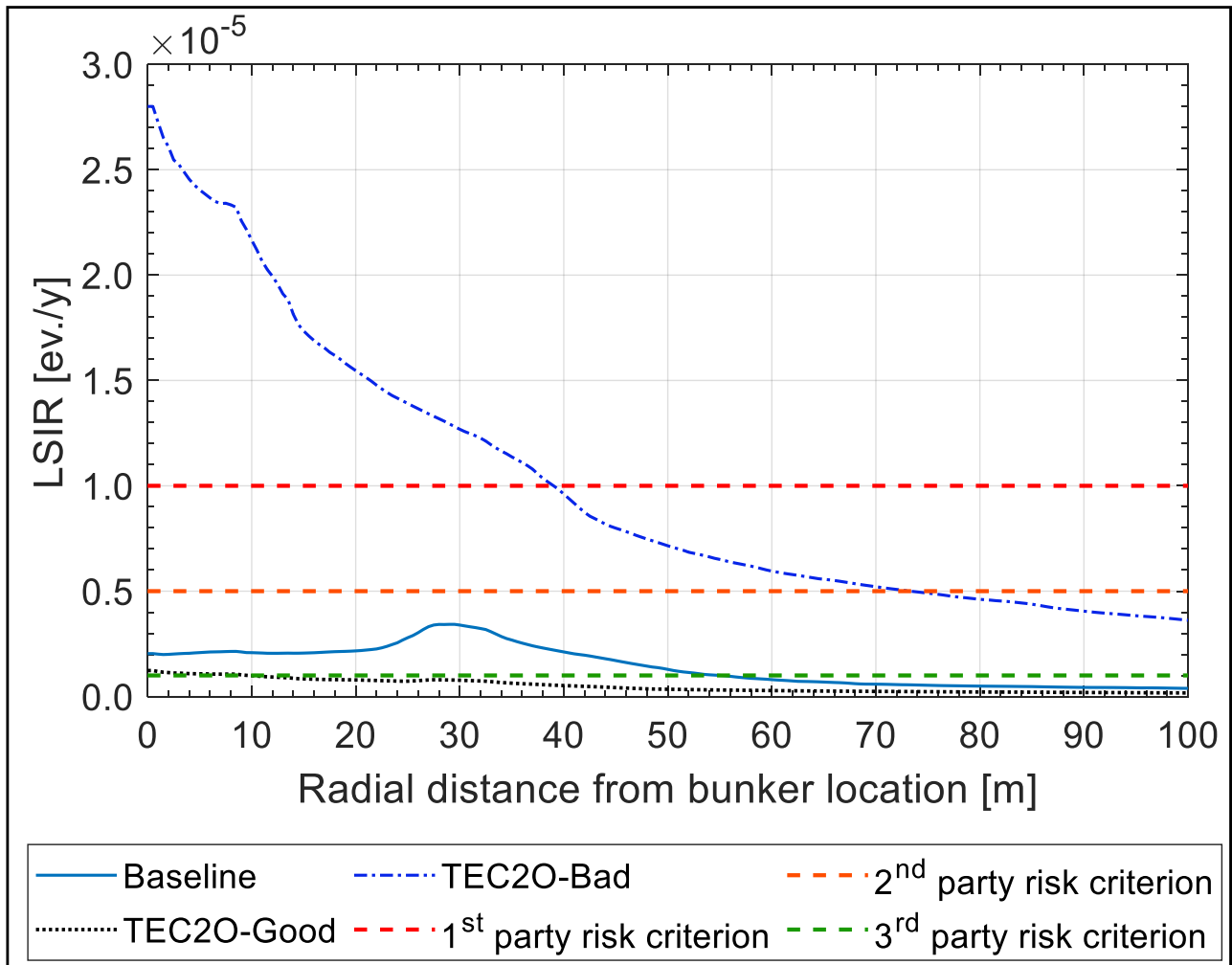


Figure 29: Comparison of maximum calculated LSIR values for different management situations as function of the distance from bunkering point

Two different levels of population density were considered to estimate the number of expected fatalities resulting from the exposure to dangerous scenarios, referred to as “low” and “high” density in Table 21. This allowed to obtain a more generic risk profile which is not linked to a specific LNG port facility. Moreover, a distinction was made between sheltered and unsheltered fractions of people since sheltering affects the estimation of  $P_d$ . It was assumed that the fraction of indoor population for grid points covering the ship area is equal to unity, whereas lower fractions were considered for the other port zones, as specified in Table 21. A uniform population distribution was assumed.

Table 21: Values of population density and indoor fraction considered for societal risk estimation. Refer to Figure 25 for the identification of the different port areas.

		Port waiting area	Jetty	Ship
Population density (persons/m <sup>2</sup> )	Low	0.005	0.050	0.100
	High	0.050	0.500	1.00
Indoor population fraction		0.25	0.75	1.00

Societal risk results are reported in Figure 30 as F-N curves for high and low port population density. The societal risk spectrum can be divided in three regions based on societal risk acceptance criteria provided by IMO, (2000): a negligible risk region (below green dashed line in Figure 30), an intolerable risk region (above red line in Figure 30) and the intermediate ALARP region.

Under no circumstances the calculated risk exceeds the upper acceptability criterion proposed by the IMO, (2000). When a lower population density is assumed the societal risk level results negligible with the only exception of a bad management scenario. The higher dangerous scenario frequencies estimated in this latter case are shifting the F-N curve up, thus increasing the societal risk level, eventually reaching the ALARP region. As evident from Figure 30a, a higher port population density results in an increased number of fatalities, thus moving F-N curves to the right. Under these circumstances the baseline case and TEC20-Bad situations have a significant part of their F-N curves within the ALARP region, whereas the TEC20-Good maintenance situation slightly exceeds the lower acceptability criterion.

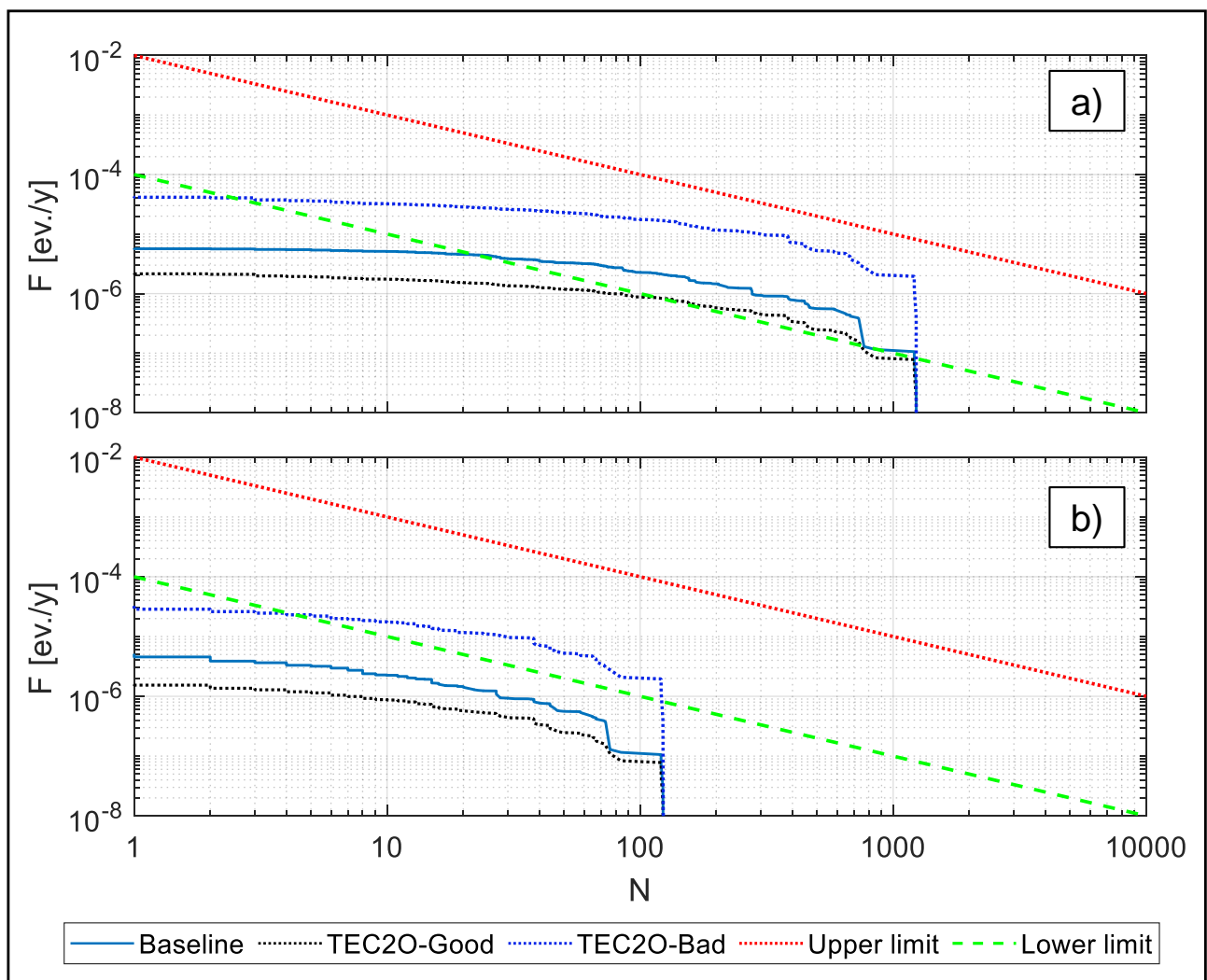


Figure 30: F-N curves obtained for high port population density (a) and low population density (b) compared to upper and lower acceptability limits proposed by the IMO, (2000).

Different *PLL* values were calculated according to Eq. 6.15 for each of the three management conditions and accounting for low and high port population densities. *PLL* value provides a useful measure to compare different societal risk levels. As shown in Figure 31, the highest *PLL* value refers to the badly managed bunkering operation when a high port population density is assumed.

For such case, the *PLL* value is about seven times greater than the baseline situation, while assuming a good management, *PLL* is reduced to 40% of the baseline value. The same trend can be observed when a lower population density is assumed. These results clearly show how the societal risk is affected by the human element, particularly managerial aspects.

Comparing the *PLL* figures of the baseline and of the good management situations it can be noticed that, despite the latter situation accounts for the performance of SIMOPs, the societal risk can be reduced if the operations are managed prioritizing the safety culture at organizational and operational levels.

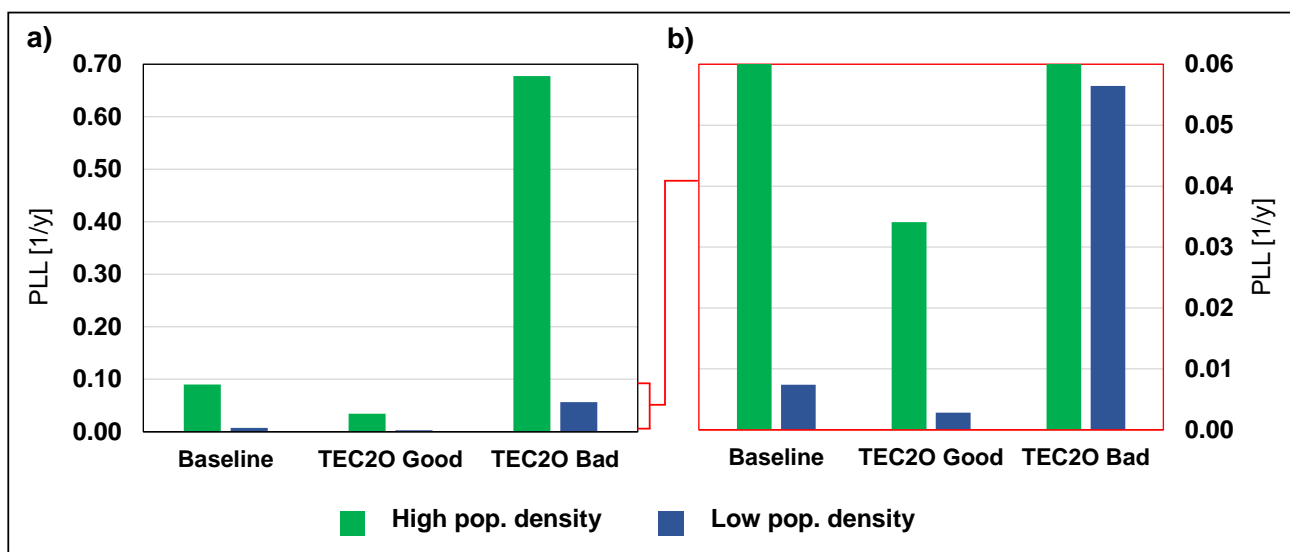


Figure 31: Comparison of calculated *PLL* values. Results for low population density are detailed in panel b) for clarity.

Based on the results of the consequence assessment and of the estimated death probabilities, it was possible to quantify the impact of single dangerous scenarios over the total expected number of fatalities and the LSIR figure. The impact of different dangerous scenarios on LSIR evaluated at the bunkering point is illustrated in Figure 32a. It is evident that the larger contribution to individual risk is due to flash fire events, that are responsible of more than 90% of the estimated risk for the baseline scenario, reaching a share up to 99% when a bad management scenario is assumed. The impact of jet and pool fires over the generated individual risk is ranging from 1% to 10%. As shown in Figure 32b, which reports the share of fatalities that may be attributed to the different dangerous scenarios, flash fires are responsible for the large majority of the total deaths (91% and 89% for low and high port population density respectively), followed by the combined consequences of jet and pool fires that account for 9% and 11% of the deaths.

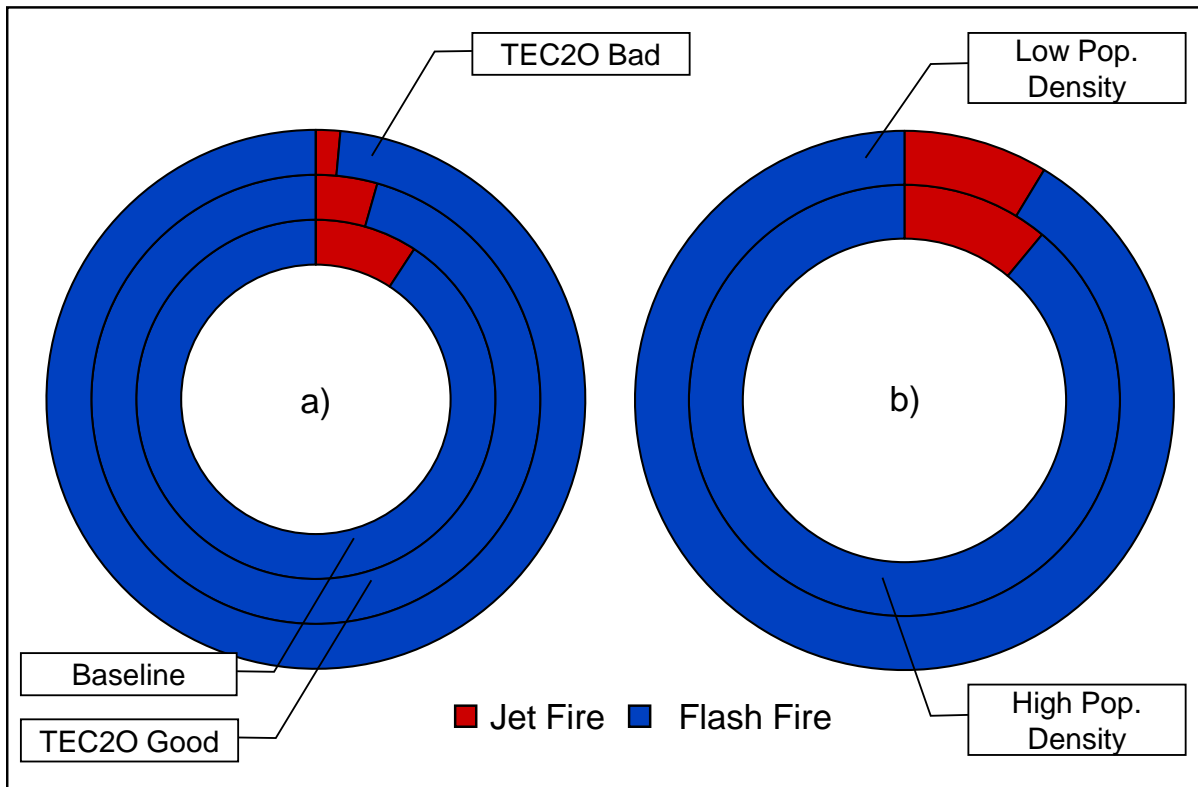


Figure 32: Relative contribution of dangerous scenarios to LSIR experienced at the bunkering point (a) and to estimated number of fatalities (b)

The results obtained from ETA stress the importance of managerial aspects in the evaluation of dangerous scenario frequencies. The adoption of safety-oriented management policies allows mitigating the negative impact that SIMOPs may have on risk figures: estimated dangerous scenario frequencies for TEC2O-Good management situation result in most of the cases lower than correspondent baseline scenarios. A direct consequence of the increased delayed ignition probability linked to SIMOPs is the high occurrence frequency of flash fire scenarios originating from type 4 LOC events, which increases (compared to the baseline frequency) regardless of management quality. Whenever safety is not a priority for the management and SIMOPs are ordinarily carried out while bunkering LNG, as in the case assumed for the TEC2O-Bad situation, LOC frequencies can be more than doubled and consequently dangerous scenarios frequencies can reach values as high as  $9.33 \times 10^{-6}$ .

The discussed trend is also captured by societal risk results illustrated in Figure 30, which shows that the risk posed by ill-managed bunkering operations should be reduced when favourable to do so, regardless of the port population density. Conversely, when considering the TEC2O-Good management situation, societal risk acceptance criteria are always met, with the exception of high port population density, for which, indeed, also the baseline scenario for bunkering operations might generate an intolerable risk (see Figure 30a).

As reported in Figure 32, the dangerous scenario that has the greatest impact over individual and societal risk figures is the flash fire. Since this fire scenario may take place following the delayed ignition of a flammable gas cloud, it might be advisable to design bunker jetties so that predominant wind direction could disperse gas clouds away from the jetty itself, achieving an inherently safer design. For situations in which the port layout limits the possibilities to perform LNG bunkering at a safe distance from passengers waiting areas, the use of floating bunker hoses could be considered. This system, described more in detail in the study by Lagarrigue and Hermay, (2018), can be exploited to perform LNG bunkering away from the quay.

## Chapter 7. Numerical simulation of LNG tanks exposed to fire

As discussed in the previous chapter, fire engulfment scenarios involving LNG storage tanks either on board LNG-fuelled ships or that are part of the LNG supply chain for bunkering operations may cause severe accidents. The storage of flammable materials in pressurized tanks is notoriously a source of risk in the process industry. In case of a fire incident, the resulting heat load might affect target equipment and lead to an escalation of the incident (the so-called domino effect). As highlighted by Casal and Darbra (2013) incidents involving the domino effect most commonly occurred in storage areas and the large majority involved flammable substances. Pressurized tanks exposed to fire heat loads might fail catastrophically generating a boiling liquid expanding vapour explosion (BLEVE) and consequently a fireball. While the BLEVE scenario can be ruled out for LNG carrier tanks (Woodward and Pitblado, 2010b), such an accident has occurred at least three times with road tanker trucks, as reported in Section 1.4. As discussed in chapter 3, lumped models may provide preliminary information on the credibility of a failure of an LNG tank engulfed in fire. However, one of the main shortcomings of the lumped parameter model mentioned in Section 3.4 is the inability of such approach to consider gradients in the fluid properties since each tank node is assumed as homogeneous. This limits the capabilities of lumped models since key aspects such as free convection flows and heat transfer mechanisms between the tank wall and the lading cannot be accurately reproduced. At the cost of increased computational resources, a CFD approach can overcome the said limitations allowing for the prediction of liquid thermal stratification, which is fundamental to the assessment of pressure build-up of tanks exposed to fire heat loads.

In this Chapter an overview of the most relevant experimental fire performance tests of cryogenic storage tanks is presented. A description of the testing apparatus and used instrumentation is provided along with the main findings of the discussed experimental campaigns. A CFD model was then developed to simulate the behaviour of the fluid in an LNG tank engulfed in fire. The CFD model was validated using the experimental data available in the literature and described in the first part of the chapter. The CFD modelling approach adopted in the present study is explained in Section 7.2, together with a brief analysis of the thermal insulation characteristics of double-walled, vacuum-insulated storage tanks. The CFD model proposed in this work and the simulations carried out are based on a bi-dimensional (2D) transversal section of the storage tank (see Figure 41). This simplification of the problem allows for a reduction of the required computational time even though it introduces some limitations in the kind of situations that can be analysed. The 2D assumption precludes the possibility to model fire scenarios that are not uniform along the axial direction of the tank or which partially affect the tank surface (such as jet fire impingement). Full engulfing pool fires can be approximately considered uniform along the axial direction and can thus be modelled with the mentioned 2D CFD approach. A preliminary investigation of the effects of distant radiation from hydrocarbon pool fires on cryogenic storage tanks can also be made exploiting the proposed CFD model. Assumptions and model setup used for this kind of simulation are also described in the followings.

## 7.1. Description of experimental fire test of double-walled LNG tanks

Despite the growing interest in the use of LNG as alternative energy source, promoted by the reduced environmental impact of such a fuel, a very limited number of experimental studies have been carried out to investigate the risks linked to the storage and transportation of this hazardous material.

As reported in Chapter 3, the scientific literature is mainly focused on the analysis of BOG generation of storage tanks under normal operating conditions, thus usually considering well-insulated tanks. The only experimental works that investigated the consequences of a sudden catastrophic loss of insulating vacuum in cryogenic tanks are the tests conducted by Xie et al. (2012, 2010). They, however, are limited to the analysis of tank performance at ambient conditions.

From the analysis of the literature, the results of only two studies reproducing fire scenarios affecting LNG tanks are publicly available: the first document reports the work carried out in 2015 by Dutch TNO (Kamperveen et al., 2016), and the second describes the test campaign performed by the US DOT's FRA in 2017 (Huczek et al., 2020). The aims of both experiments were to understand how the fire exposure affects the internal and external heating of the tank and to assess the fire heat loads resistance of double-walled, vacuum insulated cryogenic storage tanks.

Experimental results are fundamental to the development and validation of numerical models. A description of the testing apparatus and main observations of the two experimental works is reported in this Chapter. The results of the TNO test, even though it has some limitations, were used in this work to validate the proposed CFD model. Results of FRA tests, only published in early 2020, were not used for model validation. However, they are reported in the following for sake of completeness.

### 7.1.1. TNO test (2015)

Kamperveen and co-workers pioneered bonfire tank tests with cryogenic contents. The main objectives of the experimental tests carried out in 2015 were to establish if a double-walled pressure tank could endure an exposure to radiation intensities of 35 kW/m<sup>2</sup> or more without failing catastrophically and to determine the heat load and exposure duration necessary to tank rupture. The experiments took place at the Federal Institute for Materials Research and Testing (BAM), in Berlin, Germany. Test fire conditions reproduced a full-engulfing hydrocarbon pool fire. A heat load of 75 kW/m<sup>2</sup> was applied using an array of propane burners.

The test tank was manufactured with an outer carbon steel tank that encloses the inner stainless steel (AISI 304) tank, which had a capacity of 3 m<sup>3</sup>. The 0.2 m wide annular space was filled with perlite powder and vacuumed down to approximately 200 mbar to reproduce actual insulating conditions.

Table 22: Main dimensions and features of the TNO test tank

<b>Quantity</b>	<b>Value</b>	<b>Unit</b>
Inner diameter	1.20	m
Inner wall thickness	3.00	mm
Inner tank length	2.55	m
Outer diameter	1.60	m
Outer wall thickness	4.00	mm
Outer tank length	2.96	m
PRV set point	7.60	bar

For safety reasons, the experimental campaign was carried out filling the tank with liquid nitrogen. The tank was filled up to 66% of its capacity and later set to rest for two hours to reach stable saturation conditions. Tank pressure was monitored throughout the fire test and several K-type thermocouples were installed at different positions to measure wall and lading temperatures. The tank was connected through a vent line to a pair of pressure relief valves located in a safe position behind a fire wall. The total duration of the experiment, between fire ignition and termination, was approximately 120 minutes.



*Figure 33: Impression of the vacuum insulated double-walled test tank engulfed in flames from Kamperveen et al., (2016).*

As illustrated in Figure 34, the initial vapour pressure in the vessel was equal to 1.8 bar and reached 7.6 bar after two hours of flame engulfment. Tank pressure then levelled off around this value, as the PRV began to open and close around its set pressure. This process lasted for approximately 20 minutes until conclusion of the test. Unfortunately, temperature measurements during the test resulted in a highly disturbed signal, compromising the reliability of the specific dataset obtained. The external wall temperature reached values over 800°C on the bottom part, whereas the top section of the tank was heated up to about 600°C due to the disturbing effect of wind and the consequent flame tilting. Weakening of the external carbon steel shell eventually resulted in serious structural damages and distortions on the tank shell, leading to the opening of the vacuum rupture disk on the outer wall and causing the partial release of a non-quantified amount of perlite.

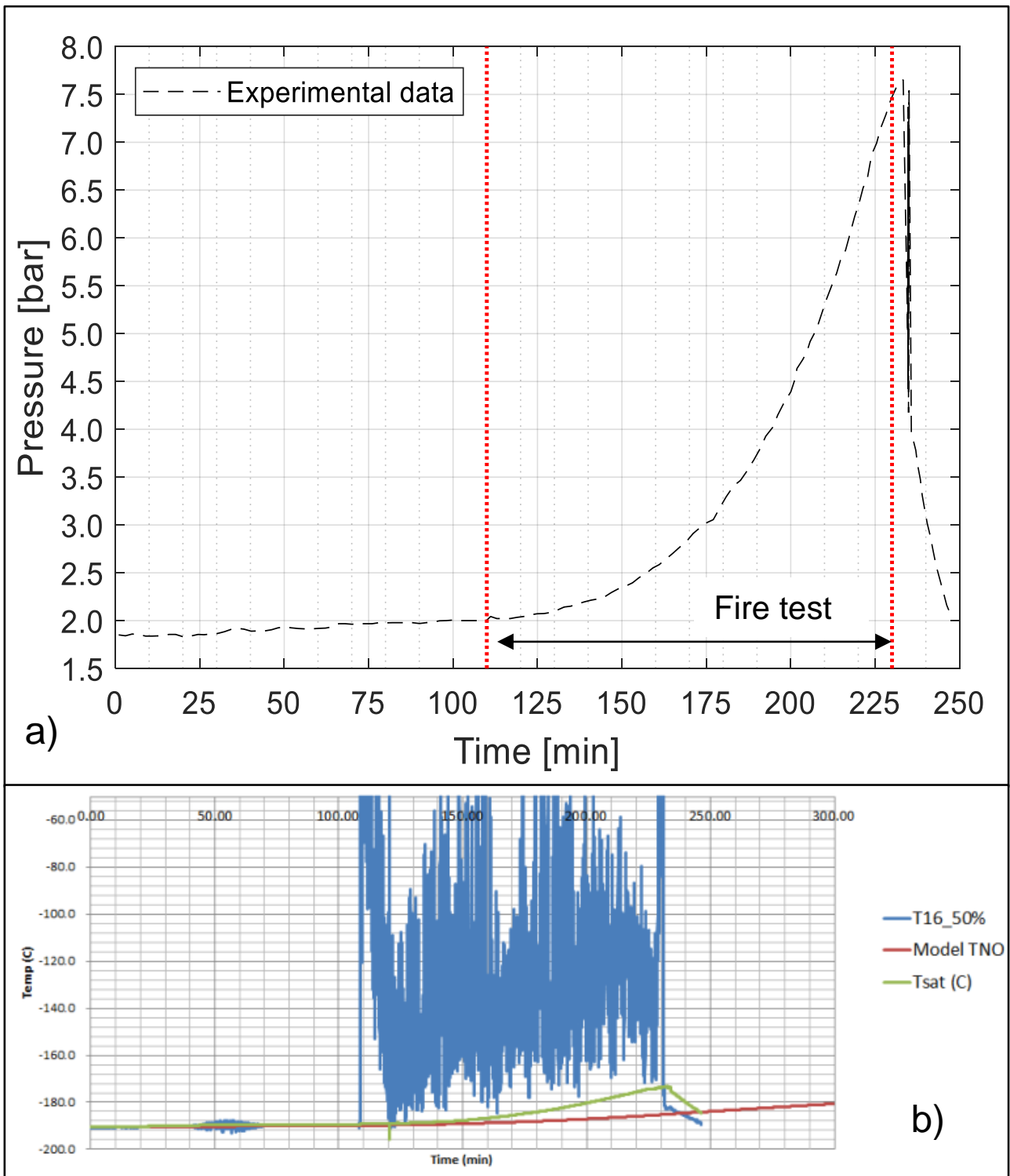


Figure 34: Pressure time evolution during TNO test (a); example of highly disturbed thermocouple experimental measurement (b).

### 7.1.2. US DOT's FRA test (2017)

The objective of the research conducted by the US FRA was to test the fire resistance of a portable ISO LNG tank, evaluating the performance of the PRV system. This type of tank, installed on flatcars, have been proposed as LNG tenders for gas-fuelled locomotives in the USA. The ISO LNG tank measured roughly 12 m long, 2.55 m high and 2.4 m wide (40 feet x 8.5 feet x 8 feet) and was filled with approximately 21,500 kg of liquid nitrogen. A total of 18 internal temperature measurements were taken, in addition to internal tank pressure, and annular space vacuum pressure. Nine thermocouples were installed externally around the tank and fire source to characterize the convective heat transfer rate from the fire and measure boundary layer temperatures. An additional nine directional flame thermometers were used to characterize the total heat flux received by the tank at different locations. A propane burner system was designed to simulate a full engulfing pool fire affecting the LNG tank. The tank was exposed to the fire source for a total of 2 hours and 35 minutes.



*Figure 35: Impression of ISO LNG tank test from Huczek et al., (2020).*

The tank successfully vented its contents and did not rupture. Fire exposure to the tank was not uniform due to wind conditions. This resulted in a more severe exposure of specific sections of the tank shell. The average peak incident heat flux to the east side of the tank was 127 kW/m<sup>2</sup>, while the average peak incident heat flux to the west side of the tank was 207 kW/m<sup>2</sup>.

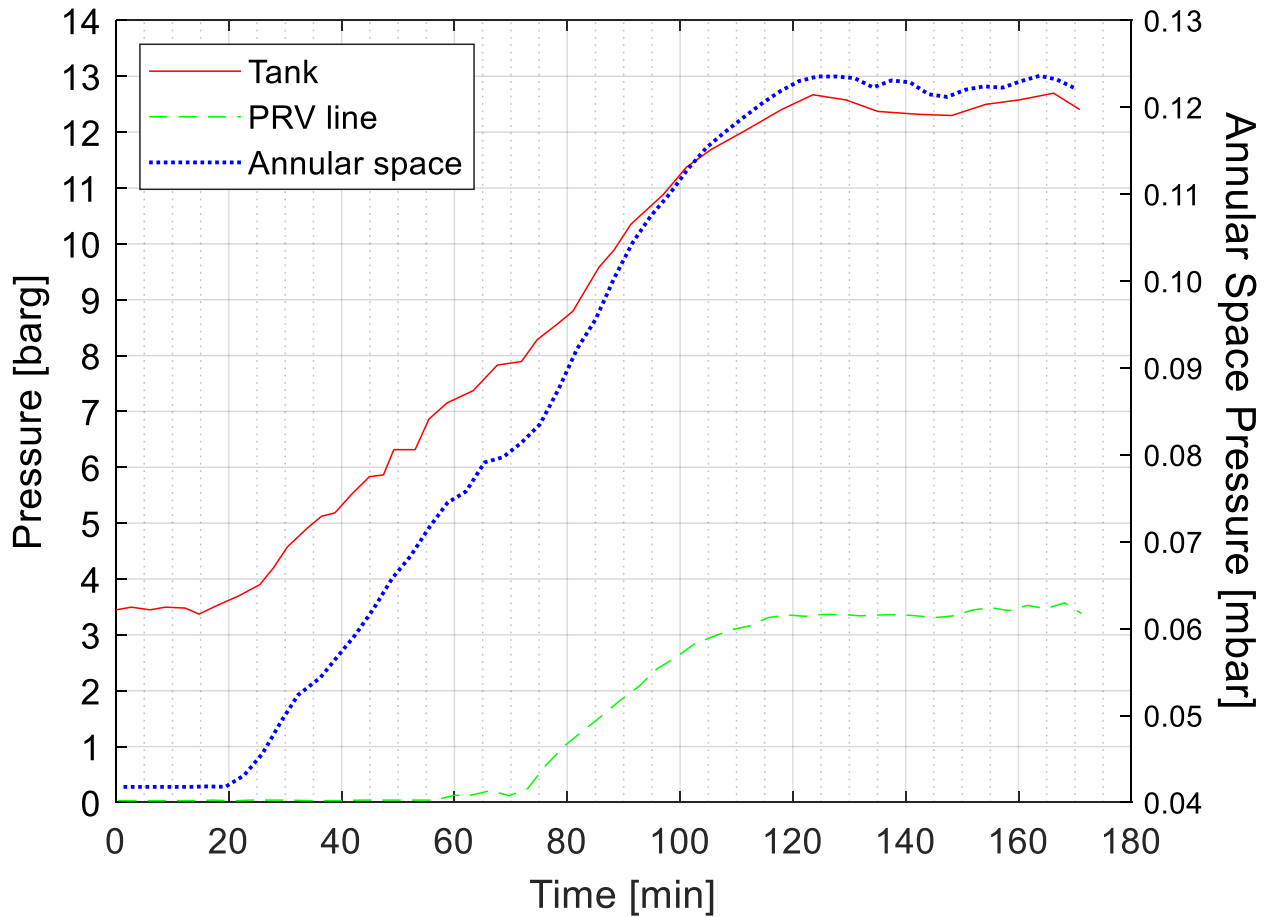


Figure 36: Pressure data for DOT FRA test.

Figure 36 illustrates how the internal temperatures and pressure increased during the fire test. Unfortunately, the signals from all the internal thermocouples were lost after the first 45 minutes of the test. During this period, the thermocouples fit in the vapor space of the tank rose from approximately -132 °C to -38 °C due to the fire exposure. The PRV system worked properly. The lower PRV (set at 8 bar) opened and closed twice and then opened fully. The higher PRV opened at about 10 bar. The pressure continued to rise until 12.4 bar before venting stabilized.

## 7.2. CFD modelling

The 2D CFD model was set up to analyse the response to fire engulfment scenarios of horizontal, double-walled cryogenic tanks. The proposed model, intended for the basic understanding of thermal and fluid dynamics of fire-exposed LNG vessels, does not consider BOG venting or PRV operation. Rather, it models a closed system that represents an extreme condition from a safety perspective, giving valuable information for further and more extensive safety and emergency assessment of LNG processes.

### 7.2.1. Theoretical background

As described by Birk and Cunningham (1996, 1994) and more recently by Abbasi and Abbasi (2007), the mechanical failure of the storage vessel is a required condition for BLEVE to happen: when pressurized tanks are exposed to high heat loads tank walls will reach temperature values well above their design conditions, at which the metal undergoes a degradation of its mechanical properties. At the same time, the pressure inside the tank will start to rise due to the absorbed heat. The combined effect of thermal degradation of the mechanical properties of the tank and the system pressure increase can lead to the catastrophic rupture of the storage vessel.

In a cryogenic double-walled bullet tank the LNG is stored as a boiling liquid at saturation conditions at a pressure a few bar higher than atmospheric. The annular gap comprised between the inner and outer tank shells is typically filled with expanded perlite beads and maintained under vacuum conditions to provide the required insulation performance (Wartsila, 2018). A section view of a horizontal double-walled LNG tank is illustrated in Figure 37.



*Figure 37: Section of a double-walled LNG bullet tank showing perlite insulation (Kamperveen et al., 2016)*

When exposed to a fire, a part of the incoming heat flux is reflected by the external wall, while the remaining fraction is transferred by radiation and convection, then the heat is transferred by conduction through tank walls and the insulating material inside the annular gap. The heat is finally transferred to the tank lading by convection and radiation from the vessel internal surface (Landucci and Birk, 2013).

Different regimes of boiling can establish based on the heat flux received by the LNG lading: as the heat flux increases the regime evolves from free convective boiling (region I in Figure 38a) to nucleate boiling (region II) until a maximum heat flux value (peak nucleate boiling point - PNB - in the figure) is reached. At this point a considerable vapour is being formed at the wall and the boiling mechanism enters in a transition region (III) towards film boiling regime (IV). However, a transition to film boiling regime for the situation under analysis can likely be excluded since it would require a heat flux reaching the liquid lading in the order of 300 kW/m<sup>2</sup> as can be seen in Figure 38b, which is higher than the heat load conditions encountered during an hydrocarbon pool fire (Mannan, 2012b).

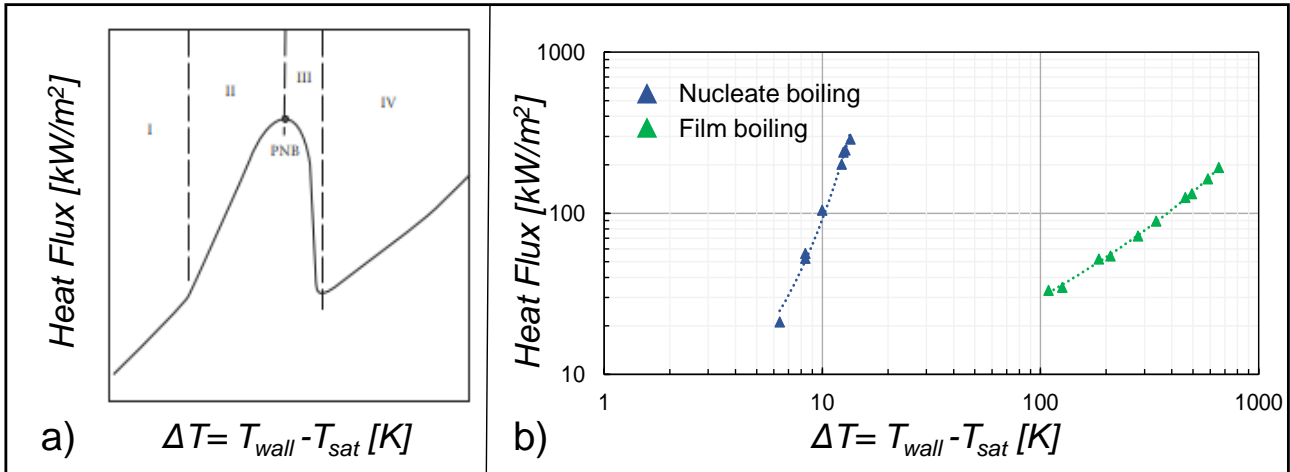


Figure 38: a) Example of pool boiling curve. Adapted from Barron and Nellis, (2016); b) Pure methane pool boiling curve. Adapted from Science et al., (1967).  $T_{wall}$  is the tank internal wall temperature;  $T_{sat}$  indicates the methane saturation temperature.

The heat ingress induces free convection currents that establish close to the walls, which transfer warmer liquid up to the vapour-liquid interface leading to thermal stratification of the lading and enhancing evaporation. Such an effect is one of the primary factors determining the pressure rise rate inside the tank, as concluded by Gursu et al., (1993). As highlighted in Section 3.4, the main shortcomings of the lumped parameters approach used to model fire exposed tanks are the inability to reproduce the thermal stratification of the liquid and the empirical approach needed to model the interactions between the different zones of the model. These are the key reason for the use of CFD tools in the present framework, which can provide a more accurate description of the physical phenomena occurring during fire exposure of storage tanks.

### 7.2.2. Set of governing equations

The solution of Navier-Stokes equations and that of differential equations governing heat and mass transfer requires the discretization of the computational domain. In this study, the finite volume method was used to discretize the LNG tank domain and solve the governing equations.

#### Multiphase modelling

The problem described in 7.2.1 involves both liquid ( $L$ ) and vapour ( $V$ ) phases and thus requires the selection of a multiphase model. Based on the experience of other similar works performed by Kassemi et al., (2018) and Ovidi et al., (2019), the Volume Of Fluid (VOF) model developed by Hirt and Nichols (1981) was used to tackle the multiphase nature of the simulation. This model is widely used for the modelling of two or more immiscible fluids and allows tracking of the gas-liquid interface inside the tank by solving a continuity equation for the volume fraction of one (or more) of the phases. The VOF model needs to define a primary and secondary phase, then it solves a set of continuity equations for the volume fraction of all the secondary phases and calculates the volume fraction of the primary phase requiring that for each cell of the domain all volume fractions must sum to unity.

In the present work, the vapour phase was defined as primary in order to avoid convergence problems as suggested in the software user guide (ANSYS Inc., 2018a). Hence, the continuity equation for the liquid volume fraction ( $\alpha_L$ ) is:

$$\frac{\partial}{\partial t}(\alpha_L \rho_L) + \nabla \cdot (\alpha_L \rho_L \mathbf{u}) = \dot{m}_{V \rightarrow L} - \dot{m}_{L \rightarrow V} \quad \text{Eq. 7.1}$$

Consequently, the vapour volume fraction ( $\alpha_V$ ) is calculated as:

$$\alpha_V = 1 - \alpha_L \quad \text{Eq. 7.2}$$

With this multiphase model, all the material properties needed in the governing equations are calculated as weighted averages of the single-phase property based on volume fraction. Considering for example a generic two-phase average property ( $\varphi$ ), this is calculated using the following formula:

$$\varphi = \alpha_L \varphi_L + (1 - \alpha_L) \varphi_V \quad \text{Eq. 7.3}$$

Terms  $\dot{m}_{V \rightarrow L}$  and  $\dot{m}_{L \rightarrow V}$  in Eq. 7.1 represent the mass transfer rates between vapour and liquid phases and vice-versa, respectively. The calculation of these terms requires the use of an evaporation-condensation model, which is explained in the following.

#### Momentum transport equation

A single momentum equation is solved in the VOF model and the resulting velocity field is shared among the phases. Physical properties are the two-phase averaged properties calculated with Eq. 7.4.

$$\frac{\partial}{\partial t}(\rho \mathbf{u}) + \nabla \cdot (\rho \mathbf{u} \mathbf{u}) = -\nabla p + \rho \mathbf{g} + \nabla \cdot \boldsymbol{\tau} \quad \text{Eq. 7.4}$$

The term  $\boldsymbol{\tau}$  represents the stress tensor. For a Newtonian fluid, it can be expressed as:

$$\boldsymbol{\tau} = \mu \left[ \nabla \mathbf{u} + (\nabla \mathbf{u})^T - \frac{2}{3} \nabla \cdot \mathbf{u} I \right] \quad \text{Eq. 7.5}$$

where the term  $I$  is the identity tensor.

#### Energy transport equation

For energy, as for the momentum transport, the VOF model solves a single transport equation, thus liquid and vapour phases share the same temperature field. The energy transport in the fluid regions of the computational domain is governed by the following equations:

$$\frac{\partial}{\partial t}(\rho E) + \nabla \cdot [\mathbf{u}(\rho E + p)] = \nabla \cdot \left[ \left( k + \frac{C_p \mu_T}{Pr_T} \right) \nabla T \right] + \lambda(\dot{m}_{V \rightarrow L} - \dot{m}_{L \rightarrow V}) \quad \text{Eq. 7.6}$$

In which the quantity  $Pr_T$  is the turbulent Prandtl number which depends on the specific turbulence model adopted. The term  $E$  is a two-phase-averaged energy, calculated as:

$$E = \frac{E_L \alpha_L \rho_L + E_V \alpha_V \rho_V}{\alpha_L \rho_L + \alpha_V \rho_V} \quad \text{Eq. 7.7}$$

While phase-specific energy is calculated in the following way:

$$E_i = H_i - \frac{p}{\rho_i} + \frac{u^2}{2} \quad \text{Eq. 7.8}$$

Where the phase enthalpy ( $H_i$ ) is based on the specific heat of that phase and the shared temperature. The transport equation solved in the solid regions of the computational domain has the following form:

$$\frac{\partial}{\partial t}(\rho_s C p_s T_s) = \nabla \cdot (k_s \nabla T_s) \quad \text{Eq. 7.9}$$

where the index  $s$  indicates solid properties.

#### Evaporation-condensation model

The mass transfer rates between liquid and vapor phases were predicted using the evaporation-condensation model based on the work by Lee (1979). The terms  $\dot{m}_{V \rightarrow L}$  and  $\dot{m}_{L \rightarrow V}$  used in Eq. 7.1 are calculated with the following expressions:

$$\dot{m}_{V \rightarrow L} = C_{cond} \alpha_V \rho_V \left( \frac{T_{sat} - T}{T_{sat}} \right) \quad \text{Eq. 7.10}$$

$$\dot{m}_{L \rightarrow V} = C_{evap} \alpha_L \rho_L \left( \frac{T - T_{sat}}{T_{sat}} \right) \quad \text{Eq. 7.11}$$

According to Eq. 7.10 and Eq. 7.11 evaporation and condensation take place in a specific domain cell based on its temperature ( $T$ ), which is calculated at the cell pressure. If the cell temperature is above the calculated saturation temperature ( $T_{sat}$ ), part of the liquid phase will evaporate, otherwise condensation will occur. Evaporation and condensation rates calculated with the Lee model are proportional to coefficients ( $C_{cond}$  and  $C_{evap}$ ) that can be defined starting from the kinetic theory of gases (Knudsen, 1934). In this work the default value of 0.1 was used for both  $C_{cond}$  and  $C_{evap}$  coefficients as suggested in a similar study carried out by Ovidi et al., (2019). More information on the definition of the evaporation and condensation coefficients can be found in the software theory guide (ANSYS Inc., 2018b).

#### Turbulence modelling

The heating of tank walls due to fire exposure is responsible for the establishment of natural convection flows inside the tank. Both vapour and liquid in contact with the tank internal will have higher temperatures than bulk fluid due to the heat received from the wall, thus generating density gradients that drive the natural convection flows. A correct modelling of the near-wall fluid region has great importance in the prediction of pressurization rate of fire-exposed storage tanks, as pointed out by Birk (1988). Based on the estimation of the Rayleigh number of the system ( $Ra = g\beta\Delta T \delta^3/\alpha$ ), the natural convection phenomena occurring inside the tank can be deemed laminar if  $Ra$  is lower than the critical value that marks the transition to turbulent flow, which is typically assumed as  $10^9$ . The term  $\delta$  is the characteristic length, assumed here as the internal diameter of the tank,  $\beta$  is the thermal expansion coefficient,  $\alpha$  the thermal diffusivity,  $g$  is the gravity acceleration and  $\Delta T$  is the temperature difference between tank wall and liquid bulk. For all the evaluated case studies the estimated  $Ra$  resulted higher than  $10^{10}$ , hence the free convection boundary layer can be considered turbulent. A widely used computational method for solving turbulent flows is the Reynolds-Averaged

Navier-Stokes (RANS) approach that allows the calculation of solutions with reasonable use of computational resources compared to most accurate Direct Numerical Simulation approach which involves the solution of Navier-Stokes's equations.

Using the RANS approach, the solution variables in the instantaneous (i.e., non-averaged) Navier-Stokes's equations are decomposed into a mean and a fluctuating component. The decomposition for a generic variable ( $\varphi$ ) can be expressed as:

$$\varphi = \bar{\varphi} - \varphi' \quad \text{Eq. 7.12}$$

where the terms  $\bar{\varphi}$  and  $\varphi'$  express the mean and fluctuating component, respectively.

As an example, substituting expressions of this form for the velocity into the instantaneous continuity and momentum equations and taking a time average (indicated by the overbar) it is possible to obtain the RANS equations.

$$\left[ \frac{\partial}{\partial t} (\alpha_L \rho_L) + \nabla \cdot (\alpha_L \rho_L \bar{\mathbf{u}}) \right] = \dot{m}_{V \rightarrow L} - \dot{m}_{L \rightarrow V} \quad \text{Eq. 7.13}$$

$$\frac{\partial}{\partial t} (\rho \bar{\mathbf{u}}) + \nabla \cdot (\rho \bar{\mathbf{u}} \bar{\mathbf{u}}) = -\nabla \bar{p} + \rho \mathbf{g} + \nabla \cdot \bar{\boldsymbol{\tau}} - \nabla \cdot \bar{\boldsymbol{\tau}}' \quad \text{Eq. 7.14}$$

The obtained RANS equations have the same general form as the instantaneous Navier-Stokes's equations Eq. 7.1 and Eq. 7.4, with the velocities and other solution variables now representing time-averaged values. The additional term  $\bar{\boldsymbol{\tau}}'$  in Eq. 7.14 is the so-called Reynolds stresses tensor that represent the effects of turbulence. Reynolds stresses are function of the position and turbulence intensity and they are modelled in terms of known quantities, such as mean velocity gradients. A common method used for the modelling of Reynolds stresses is based on the Boussinesq approximation to relate the turbulent stresses to the mean velocity gradients:

$$\bar{\boldsymbol{\tau}}' = \mu_T \left[ \left( \nabla \bar{\mathbf{u}} + \nabla \bar{\mathbf{u}}' \right) \right] - \frac{2}{3} (\rho K + \mu_T \nabla \cdot \bar{\mathbf{u}}) \quad \text{Eq. 7.15}$$

The term  $\mu_T$  is a scalar quantity called turbulent viscosity, while  $K$  represents the turbulent kinetic energy, which is calculated as:

$$K = \frac{1}{2} \left( \overline{(u'_x)^2} + \overline{(u'_y)^2} + \overline{(u'_z)^2} \right) \quad \text{Eq. 7.16}$$

The calculation of  $\mu_T$  and  $K$  requires the use of a RANS-based turbulence model. Among the several models developed, the k- $\omega$  SST turbulence model developed by Launder and Spalding (1972) was selected in this work to reproduce the turbulent natural convection regime. This turbulence model was already proven valid in previous studies dealing with similar systems (Ovidi et al., 2019; Scarponi et al., 2018a).

Flow characteristics are greatly influenced by the presence of the walls. Velocity field and turbulence are affected by the no-slip condition that must be satisfied at the wall (i.e., zero velocity at the wall). An accurate representation of the flow in the near-wall region is fundamental for the successful prediction of wall-bounded turbulent flows since in this region the solution variables have the largest gradients, and the momentum and heat transport phenomena occur most vigorously.

Two dimensionless quantities are introduced to ease the characterization of the flow regime:  $y^+$ , which is a measure of the distance to the wall, and  $u^+$  representing a dimensionless velocity, defined according to Eq. 7.17 and Eq. 7.18, respectively.

$$y^+ = \frac{\rho u_\tau y}{\mu} \quad \text{Eq. 7.17}$$

$$u^+ = \frac{u}{u_\tau} \quad \text{Eq. 7.18}$$

Where the term  $u_\tau$ , having velocity dimensions, is called friction velocity, and is defined as:

$$u_\tau = \sqrt{\frac{\tau_w}{\rho}} \quad \text{Eq. 7.19}$$

Here  $y$  indicates the distance from the wall, and  $\tau_w$  the wall shear stress.

Several experimental studies showed that the near-wall region can be subdivided into three layers, as illustrated in Figure 39:

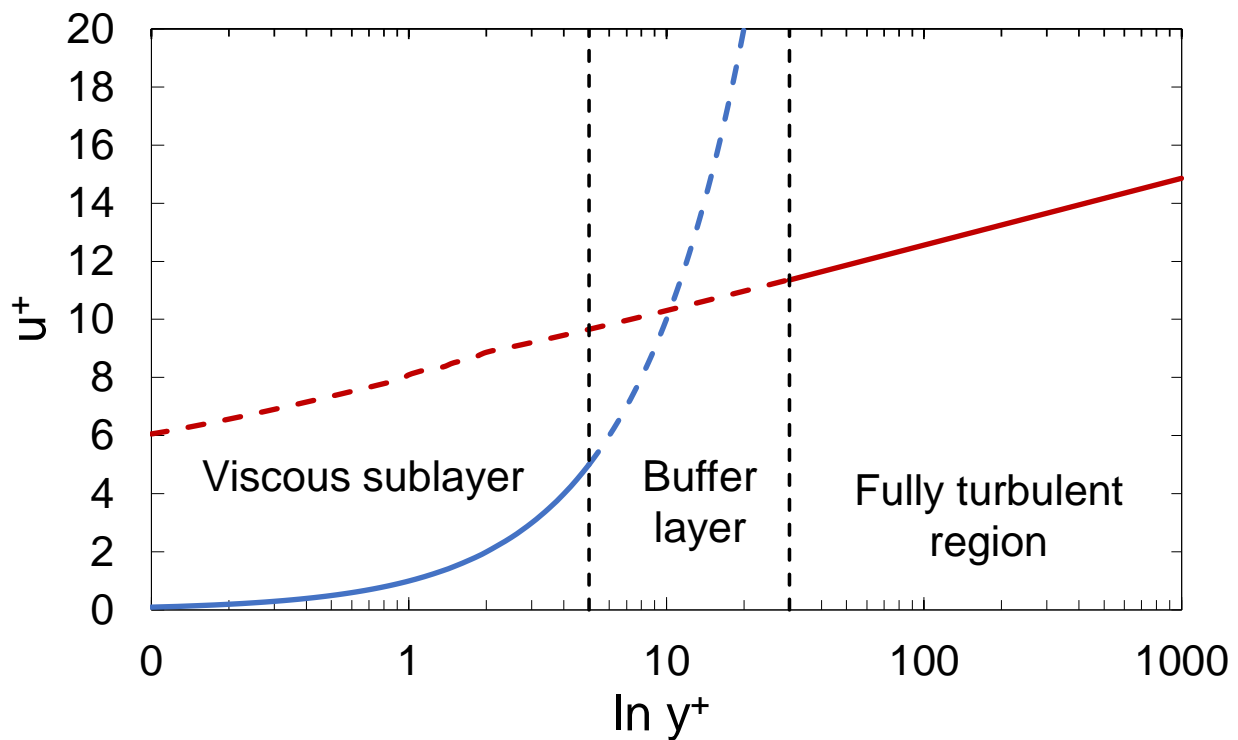


Figure 39: Subdivisions of the near-wall region

In the viscous sublayer ( $y^+ < 5$ ) the flow is almost laminar, and transfer mechanisms are mainly dominated by viscous forces. Here the dimensionless velocity equals the  $y^+$ . Farther from the wall, in the fully turbulent region, the flow is controlled by turbulence and the dimensionless velocity can be expressed as a function of  $y^+$  according to the following logarithmic law (Bird et al., 2006):

$$y^+ = 2.5 \ln y^+ + 5.5 \quad \text{Eq. 7.20}$$

The buffer layer is an intermediate region where the transition from viscous to turbulent layer occurs. No analytical expressions are available to express the relationship between  $u^+$  and  $y^+$  and empirical curve fits are usually used. Outside the near wall region, inertial forces strongly overcome viscous forces.

CFD tools rely on two approaches to model the near-wall region: the wall function and the near-the-wall approaches. In the former approach, viscous and buffer layers are modelled using semi-empirical formulae (the wall functions) that bridge the viscosity-affected region between the wall and the fully turbulent region, simplifying the turbulence model. In the near-the-wall approach the turbulence models are modified, allowing the numerical solution of the viscous and buffer layers.

The  $k$ - $\omega$  SST turbulence model used in this work, which is based on this latter approach, allows the integration of the model transport equation for the turbulent specific dissipation rate  $\omega$  through the viscous sublayer without the need for wall functions.

The turbulent kinetic energy  $K$  and specific dissipation rate  $\omega$  are calculated using the following equations:

$$\frac{\partial}{\partial t}(\rho K) + \nabla \cdot (\rho K \mathbf{u}) = \nabla \cdot (\Gamma_K \nabla K) + G_K - Y_K \quad \text{Eq. 7.21}$$

$$\frac{\partial}{\partial t}(\rho \omega) + \nabla \cdot (\rho \omega \mathbf{u}) = \nabla \cdot (\Gamma_\omega \nabla \omega) + G_\omega - Y_\omega \quad \text{Eq. 7.22}$$

In these equations,  $\Gamma_K$  and  $\Gamma_\omega$  indicate the effective diffusivity of  $K$  and  $\omega$  respectively;  $G_K$  and  $G_\omega$  are generative terms for  $K$  and  $\omega$ , and  $Y_K$  and  $Y_\omega$  represent dissipative terms of the indexed quantities.

Finally, the turbulent viscosity can be calculated according to Eq. 7.28:

$$\mu_T = \frac{\rho K}{\omega L} \quad \text{Eq. 7.23}$$

The term  $L$  is a limiting function whose definition can be found elsewhere together with a complete description of the turbulence model (ANSYS Inc., 2018b).

## Material properties

Methane and nitrogen (for the model validation case V66 – see Table 24) properties were retrieved from the NIST database of thermophysical properties (Lemmon et al., n.d.). Liquid densities, vapour specific heat and thermal conductivity were expressed as function of temperature, whereas all the other fluid properties were kept constant. The NIST dataset was also used to define a piecewise-linear correlation to account for the variation of saturation pressure with liquid temperature, necessary for the evaporation/condensation model. Vapour phase density was calculated using the Peng-Robinson equation of state (Peng and Robinson, 1976), whereas stainless steel thermal conductivity and specific heat were collected from a NIST cryogenic material properties collection (NIST, n.d.) and relevant EN 10088:2014 (European committee for standardization, 2014).

### 7.2.3. Tank insulation

Thermal properties of the insulation material were calculated according to the modelling approach proposed by Beikircher and Demharter (2013), who measured the effective thermal conductivity of perlite samples under vacuum conditions for average temperatures up to 150°C at mid-section of the specimens and for pressures ranging from 0.01 to 1,000 mbar. Perlite effective thermal conductivity is influenced by material temperature and by pressure inside the annular gap. Three main fundamental mechanism govern the heat transport in dry, evacuated perlite: solid conduction ( $k_{solid}$ ), gaseous conduction ( $k_{gas}$ ), and radiation ( $k_{rad}$ ). The solid conduction depends on the structure and material properties. Gaseous conduction by residual gases trapped inside pores depends on the vacuum pressure, while thermal radiation is influenced by the radiative properties of the material. The total effective conductivity ( $k_{tot}$ ) of the insulation material is calculated as the sum of the three aforementioned mechanisms contributing to heat transfer and of an additional coupling term ( $k_{coupling}$ ) that accounts for interactions among the heat transfer mechanisms.

A specific analysis was carried out to determine the value of effective thermal conductivity of perlite in vacuum conditions, in order to properly set the boundary and initial conditions considered in the CFD model developed. The relative importance of the three abovementioned heat transfer mechanisms and the effect of different parameters, such as perlite bulk density, particle and pore sizes, on  $k_{tot}$ , was assessed applying the model equations described in the original work by Beikircher and Demharter (2013).

The main parameter affecting  $k_{solid}$  is the bulk density of the insulating powder ( $\rho_{bulk}$ ). The powder compression method largely influences how  $k_{solid}$  varies with perlite bulk density. In the present work it was assumed that perlite grains are compressed by the mechanical force resulting from tank wall deformation due to fire exposure. A fitting equation for solid thermal conductivity of mechanically compressed perlite grains was derived from the experimental measures reported in a previous work by Demharter (2011), obtaining the following expression:

$$k_{solid} = 0.326 \cdot \rho_{bulk} - 15.4 \quad \text{Eq. 7.24}$$

in which the solid thermal conductivity is expressed in mW/(m K). Radiation contribution is as well function of perlite bulk density,  $\rho_{bulk}$ , and it can be estimated as follows:

$$k_{rad} = \frac{16 \sigma n^2 T_r^3}{3 \rho_{bulk} e^*} \quad \text{Eq. 7.25}$$

where  $\sigma$  is the Stefan-Boltzmann constant, the term  $n$  is the refractive index, considered equal to 1, and  $e^*$  represents the total mass-specific extinction coefficient, which is function of  $T_r$ , a mean value of the perlite boundary temperatures, calculated as follows:

$$T_r = \sqrt[3]{\frac{1}{4}(T_1^2 + T_2^2)(T_1 + T_2)} \quad \text{Eq. 7.26}$$

in which  $T_1$  and  $T_2$  are the inner and outer boundary temperatures, respectively. Further details regarding the calculation of the different terms are reported elsewhere for sake of brevity (Demharter, 2011).

Gas conduction and coupling terms are both function of air thermal conductivity ( $k_{air}$ ), the material-specific half-value pressures ( $p_{1/2}^g$  and  $p_{1/2}^c$ ), and a fitting parameter ( $\Phi$ ), estimated equal to 0.54 on the basis of experimental results obtained by Beikircher and Demharter, (2013). Half-value pressures are the only terms dependent on the vacuum pressure ( $p$ ) of the insulation material. The sum of  $k_{gas}$  and  $k_{coupling}$  terms is calculated as follows:

$$k_{gas} + k_{coupling} = \frac{k_{air}}{1 + \frac{p_{1/2}^g}{p}} + \Phi \frac{k_{air}}{1 + \frac{p_{1/2}^c}{p}} \quad \text{Eq. 7.27}$$

The half-value pressures are material-specific quantities that can be estimated according to Eq. 7.28 and Eq. 7.29, which express  $p_{1/2}^g$  and  $p_{1/2}^c$ , respectively:

$$p_{1/2}^g \approx \frac{230}{d_{pore}} \cdot \frac{(T_1 + T_2)}{2} \cdot \frac{1}{300} \quad \text{Eq. 7.28}$$

$$p_{1/2}^c \approx \frac{230}{d_{gap}} \cdot \frac{(T_1 + T_2)}{2} \cdot \frac{1}{300} \quad \text{Eq. 7.29}$$

in which the half-value pressures are expressed in mbar, boundary temperatures  $T_1$  and  $T_2$  in K;  $d_{pore}$  is the perlite pores diameter (in  $\mu\text{m}$ ), and  $d_{gap}$  is the particle gap dimension (in  $\mu\text{m}$ ). For the present parametric analysis a pore diameter of 30  $\mu\text{m}$  was considered, which is the average value of the range suggested by Beikircher and Demharter (2013). A mean value of the particle gap dimension of 305  $\mu\text{m}$  was calculated as a function of particle size, according to the model reported by Demharter (2011).

Perlite thermal conductivity values under different conditions, calculated with the above-described approach, are reported in Figure 40. The  $k_{solid}$  value was found to increase linearly with bulk density, with a slope depending on the type of compression process to which perlite grains are subjected (Beikircher and Demharter, 2013). Thus, the structural integrity of perlite grains has an important effect on the value of  $k_{tot}$ , since damaged particles (smaller in size) allow for higher bulk density values and higher solid conductivity,  $k_{solid}$ . In the case of cryogenic vessels with annular evacuated perlite insulation, when considering fire exposure, it may be assumed that mechanical compression of perlite grains may occur due to both external tank deformation (following the thermal distortion of the steel work induced by the fire) and compressive forces caused by annular vacuum loss.

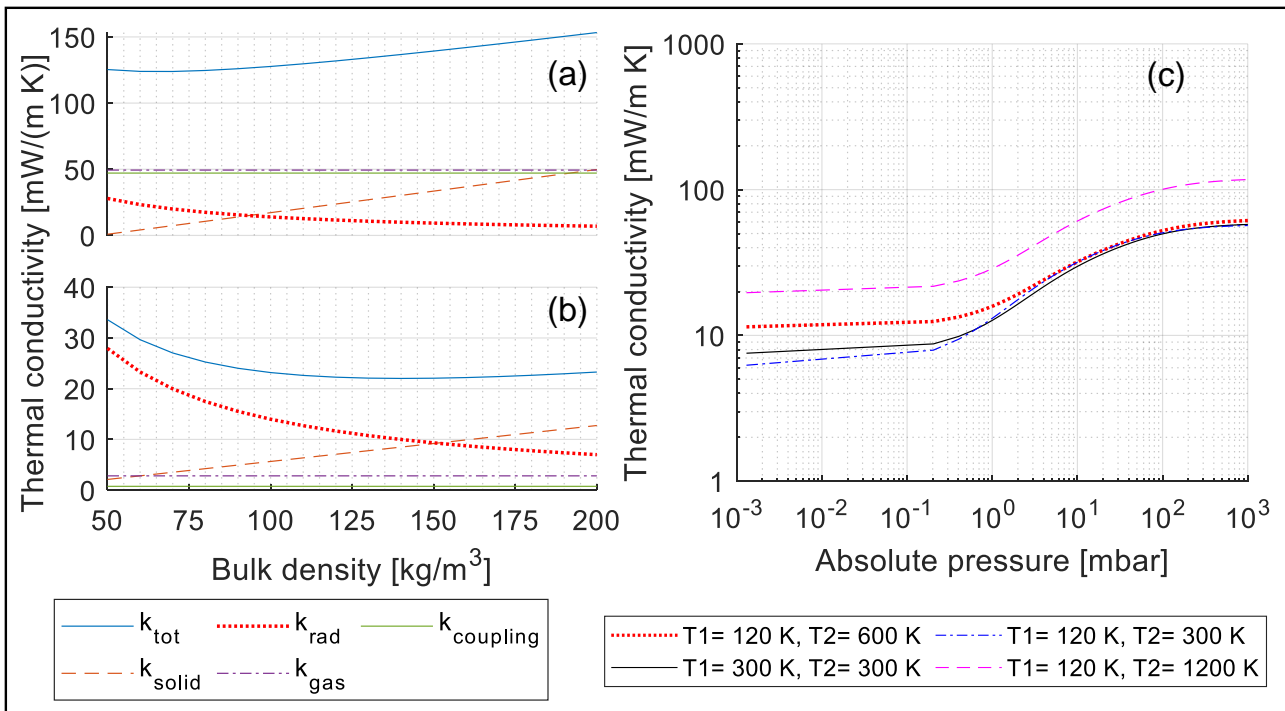


Figure 40: Contribution of the different heat transfer mechanisms and variation of overall perlite thermal conductivity ( $k_{tot}$ ) with bulk density for 1,013 mbar (a) and 1 mbar (b) pressure; (c) Variation of  $k_{tot}$  with absolute pressure for different boundary temperatures ( $T_1$ : inner boundary temperature;  $T_2$ : outer boundary temperature) assuming a bulk density value of 140 kg/m<sup>3</sup>;  $k_{solid}$ : contribution of solid conduction,  $k_{gas}$ : contribution of gaseous conduction;  $k_{rad}$ : contribution of heat radiation;  $k_{coupling}$ : coupling term among the heat transfer mechanisms.

As shown in Figure 40a, when vacuum insulation is lost, the contributions of  $k_{gas}$  and  $k_{coupling}$  become more important. On the other hand, radiation and solid conduction are the dominant heat transfer mechanisms for granular perlite under vacuum conditions (see Figure 40b). The variation of  $k_{tot}$  with vacuum pressure at different boundary temperatures is shown in Figure 40c. The curves were obtained considering the bulk density value adopted for CFD modelling, equal to 140 kg/m<sup>3</sup>. The maximum theoretical value that can be obtained when vacuum inside the tank's annular gap is lost and insulation boundary temperatures are of 1,200 K on the side of the fire and of 120 K on the side of the lading, thus representative of fire engulfment conditions, was estimated of about 150 mW/(m K) as reported in Figure 40c.

To account for the deterioration of insulation performance occurring during fires, the insulation  $k_{tot}$  value used in the CFD simulations was increased to a value of 300 mW/(m K), which is conservatively doubled with respect to the maximum value for complete loss of vacuum insulation estimated using the model by Beikircher and Demharter (2013). This augmented thermal conductivity value is intended to be representative of a seriously compromised cryogenic tank insulation for which part of the perlite is displaced following the abrupt and rapid pressurization ensuing the loss of vacuum in the annular gap. To support this choice, a one-dimensional transient heat conduction analysis was performed to understand the thermal response of an undamaged insulation layer. The results of this analysis, reported and discussed in Appendix C, show that considering the properties of undamaged insulation, the tank lading will start to heat up only after about 48 minutes, thus much later than what observed during the experimental test described in Section 7.1.1, suggesting that an intact vacuumed perlite insulation might not be reasonably assumed for long-lasting full engulfing fires. Further supporting simulations, summarized in Table 23, were carried out to investigate a wider range of possible insulation layer conditions and prove the validity of the assumption made for the thermal conductivity value used in the CFD setup.

Three different insulation conditions were assessed: one assuming an undamaged tank insulation, with a  $k_{tot}$  value compatible with a vacuum pressure of about 200 mbar, a second simulation considering a compromised tank insulation, and an unrealistic case simulating a tank without insulation, which provides an extreme upper credibility limit. For sake of comparison, all the simulations were run considering the same geometry, meshing parameters, initial and boundary conditions of the validation case V66 which reproduces the experimental test conditions described in Section 7.1.1.

Table 23: Short description of simulations supporting the CFD model validation

ID	Insulation $k_{tot}$ [mW/ (m K)]	Description
Insulated tank	92	Undamaged tank insulation assumed for the entire duration of the simulation
Damaged insulation	300	Damaged insulation assumed since the beginning of the simulation
V66	92 / 300	Undamaged tank insulation considered for the first 30 minutes; then damaged status is assumed
Bare tank	-	No insulation present – comparative case

#### 7.2.4. Case study definition

The proposed CFD model was validated against data collected from the experimental bonfire test described in Section 7.1.1. The accuracy of the CFD model was assessed reproducing the results of the experimental test, setting up a dedicated validation simulation (case V66 in Table 24). Once the model was proven satisfactory, the proposed numerical setup was used to evaluate the consequences of engulfing fire exposure of a larger LNG storage tank, used for maritime fuel storage (identified as case A in the following), and a typical road trailer tank used for LNG transportation (case B in the following). Three different tank filling degrees were considered for cases A and B to assess how this parameter affects the thermal response of the tanks. A summary of tank main features for all the three reference simulation cases is reported in Table 24.

Table 24: Main features of the tanks and initial conditions assumed for the simulation cases considered. MAWP: maximum allowable working pressure.

Case ID	Filling degree	Inner diameter [m]	Insulation thickness [m]	Length [m]	Initial pressure [bar]	Initial temperature [°C]	MAWP [bar]	Nominal capacity [m <sup>3</sup> ]
<i>Validation case</i>								
V66	66%	1.2	0.20	2.55	2.0	-189.52	7.0	3.0
<i>Open-deck ship-fuel tank</i>								
A85	85%							
A50	50%	4.3	0.25	16.5	6.0	-134.42	11.0	240
A15	15%							
<i>Road tanker</i>								
B85	85%							
B50	50%	2.3	0.12	13.8	1.0	-161.49	3.0	58.0
B15	15%							

## Real scale open-deck LNG tank for naval propulsion

Most LNG-fuelled vessels (other than LNG carriers) are designed to use IMO Type C tanks (IMO, 2016), which are independent (i.e., not integrated into the ship structure) pressure vessels featuring vacuum insulation and a double wall structure exactly as the bullet tanks described in Section 2.3 for use in SSLNG terminals. Type C tanks can be installed either within the ship or on the deck: in the first case, a gas-tight tank room is required, while the latter arrangement does not need any particular provision. Open deck installations have capacities ranging from few hundreds of cubic meters up to 1,000 m<sup>3</sup>. The annular space enclosed between inner and outer shell contains perlite grains as insulating media, combined with vacuum conditions. To facilitate the comparison with experimental data, a full engulfment fire scenario with two-hour duration was assumed. As reported in Table 24, a damaged perlite insulation layer was assumed to allow an easier comparison with the experimental data.

## LNG road tanker

Cryogenic tanks built for road transport application are designed according to prescription given in the ADR regulation (UNECE, 2018) and technical standard EN 13530-2:2002 (European committee for standardization, 2008). LNG storage tanks used for this purpose can either be double-walled vacuum or single-walled polyurethane insulated vessels. For sake of comparison, the tank concept considered for the CFD modelling is identical to type C tanks installed on ships in which the perlite insulation is kept under vacuum conditions in the annular gap of the double-walled structure. A two-hour full engulfment condition with damaged insulation layer was assumed.

### **7.2.5. Mesh generation and numerical setup**

The solution of the governing equations described in Section 7.2.2 requires the construction of a computational grid. An unstructured mesh was built using the ANSYS® Meshing™ software and it was adopted for each simulation case listed in Table 24. The use of the k- $\omega$  turbulence model requires a fine grid resolution for the near wall region that was achieved through the creation of inflation layers starting from the internal wall boundary (see Figure 41c). Further details of the used computational grid are reported in Table 25.

The transient nature of the analysis was modelled using a first-order implicit scheme, with a fixed time step of 0.01 s. Specific grid and time-step independence studies were carried out, as detailed in Section 7.3.1.

In order to reproduce the operating conditions of cryogenic storage tanks, the fluid was considered to be at saturated conditions at the initial pressure value, whereas a linear temperature gradient was considered between cryogenic lading temperature and ambient temperature (assumed equal to 16°C for all cases). Fluid was assumed to be initially motionless, hence no velocity field was initialized. Moreover, turbulent kinetic energy and specific dissipation rate were initialized at the lowest allowable values ( $10^{-9}$  m<sup>2</sup>/s<sup>2</sup> and  $10^{-3}$  s<sup>-1</sup> for  $K$  and  $\omega$  respectively). No-slip condition was imposed at the tank inner wall.

Typically, LNG consists almost entirely of methane (between 85 to more than 95%), along with a few percent of ethane, propane and butane, and trace amounts of nitrogen. The exact composition of the LNG mixture varies according to its source and processing history. However, pure methane was considered in the CFD simulation setup to avoid uncertainties associated with LNG composition.

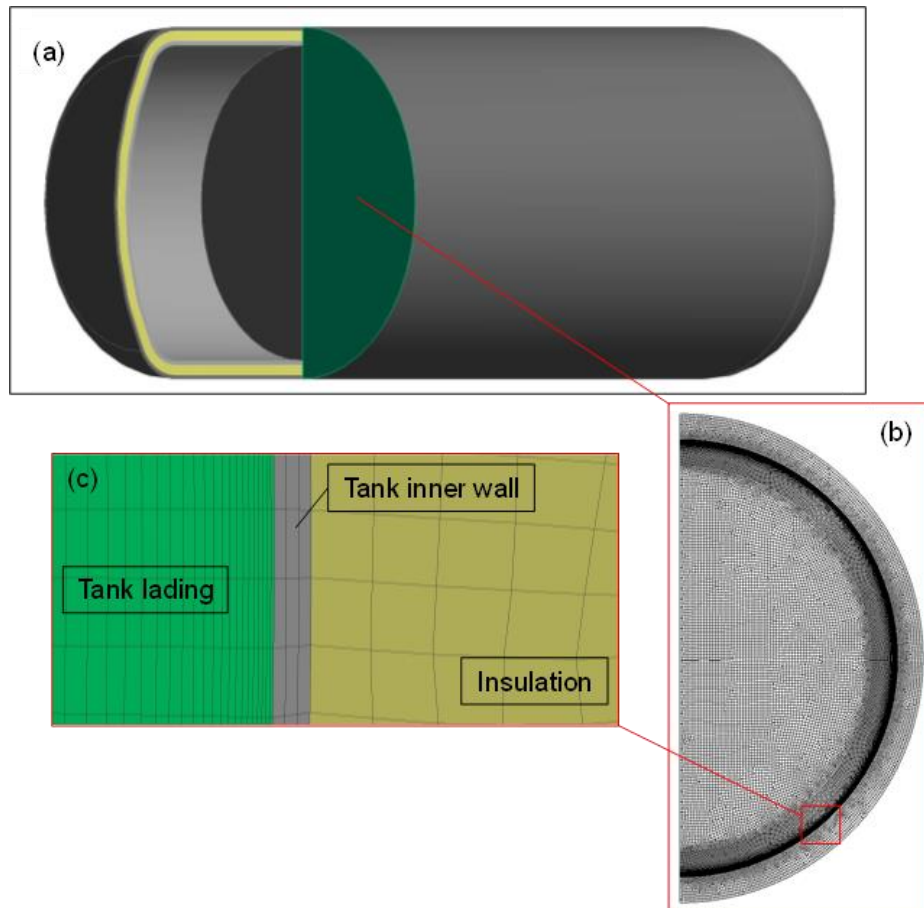


Figure 41: Representation of the computational domain: a) tank section considered for the 2D CFD analysis; b) mesh overview; c) detailed view of the mesh in proximity of the internal wall of the tank, highlighting the different material layers (i.e., insulation, tank inner wall and tank lading).

Simulation of full-engulfing pool fire scenario was achieved setting a variable heat-flux boundary condition at the outer shell wall. The heat flux absorbed by the tank was calculated according to the Stefan-Boltzmann law:

$$\dot{q}'' = \sigma \varepsilon_{wall} (T_{f, BB}^4 - T_{wall}^4) \quad \text{Eq. 7.30}$$

where  $T_{f, BB}$  is the flame blackbody temperature, assumed equal to 860°C based on experimental measurements (Kamperveen et al., 2016). The subscript *wall* refers to wall properties, thus  $\varepsilon_{wall}$  and  $T_{wall}$  are defined as the wall surface emissivity (here conservatively considered equal to 1) and temperature, respectively. This modelling approach has been proven successful in a different range of applications (Landucci et al., 2016; Scarponi et al., 2018b) and allows a satisfactory reproduction of actual engulfing fire boundary conditions, since radiation in hydrocarbon fires may be responsible of up to 80% of the total heat transferred (Birk et al., 2016).

Table 25: Details of numerical setup. Values of under-relaxation factor are reported together with discretization schemes used and main mesh features.

Discretization scheme		Under relaxation factor		
Equation/quantity	Scheme	Variable	Value	
Density	2 <sup>nd</sup> order upwind	Pressure	0.3	
Momentum	2 <sup>nd</sup> order upwind	Density	0.7	
Energy	2 <sup>nd</sup> order upwind	Body forces	0.7	
K & $\omega$	2 <sup>nd</sup> order upwind	Momentum	0.5	
Pressure	PRESTO!	Vaporization mass	0.7	
Volume Fraction	Geo-Reconstruction	Turbulent kinetic energy	0.8	
Pressure-velocity coupling	SIMPLEC	Turbulent dissipation rate	0.8	
<b>Gradients</b>		Turbulent viscosity	1.0	
Least square cell-based		Energy	0.8	
<b>Mesh features</b>				
Case ID	Mesh elements	First layer thickness [m]	Inflation layers	Maximum cell size [m]
V66	18,961			
A15-A50-A85	163,382	$7.0 \times 10^{-5}$	50	0.010
B15-B50-B85	69,533			

### 7.2.6. Safety Key Performance Indicators (KPIs)

The predictions from CFD simulations provide a detailed time-varying description of the tank pressure and of the other variables of interest, such as tank wall temperature values, which represent essential information to understand the response of tanks under fire attack. To facilitate the evaluation of the tank safety profile and provide an indication of potentially hazardous situations, selected CFD quantities were used to define three different KPIs, reported in Table 26.

All the KPIs are defined as positive quantities, and values higher than unity indicate potentially unsafe conditions. The first KPI,  $TI$ , gives a measure of the thermal stresses to which the internal surface of a fire-exposed double-walled cryogenic tank can be subject. The parameter  $S_{max}$  is the extent of the internal surface that results heated by the fire at a temperature higher than the maximum design temperature. Annex B of European standard EN 13458-2:2002 (CEN, 2002b) states that for static vacuum insulated austenitic steel vessels, the maximum design temperature is 50°C. The parameter  $A_{d,c}$  is the value of the “critical size” of the overheated surface, that is, the critical extent of the wall surface that, when heated above the maximum design temperature, becomes sufficient to jeopardize the integrity of the tank shell (Scarponi et al., 2018b). The “critical size” of zones in the tank shell able to compromise the mechanical integrity of a pressurized storage vessel were investigated by Scarponi et al. (2017) for LPG tanks. As a working assumption, the extent of  $A_{d,c}$  obtained through numerical investigations based on finite elements modelling in the original work (Scarponi et al., 2017) and reported in Table 26 was considered for the estimation of  $TI$ . Thus, the value of the indicator should be 0 in normal operating conditions (absence of a fire), and equal to 1 when a portion of the inner wall area with same extension as  $A_{d,c}$  is heated by the external fire to temperatures higher than 50°C.

As expressed by Eq. 7.32, the indicator *IPI* depends on the dynamic evaluation of the pressure inside the tank, providing a measure for the change in the safety margin with respect to the tank MAWP, which is considered equal to tank design pressure.

As for the previous case, the KPI value equals 0 in normal operating conditions. In the presence of an external fire, leading to a pressurization of the tank, the value of the KPI progressively approaches 1, i.e., the limit value at which the internal pressure equals the MAWP. Values above 1 indicate that the internal pressure exceeds MAWP and suggest the possibility of a mechanical failure of the tank.

Table 26: KPIs defined for the assessment of safety performance of pressurized cryogenic vessels. Specific parameters used in KPI definition are also defined.

KPI symbol	Equation	Definition	Equation ID
<i>TI</i>	$\frac{S_{max}}{A_{d,c}}$	Quantification of thermal-induced stresses on tank structure	7.31
<i>IPI</i>	$1 - \frac{MAWP - P_t}{MAWP - P_0}$	Quantification of the reduction of design safety margins with respect to stresses induced by internal pressure	7.32
<i>EI</i>	$\frac{E_{VB}}{E_0}$	Amount of energy released in case of tank failure with respect to a reference value	7.33
Parameter	Value/Equation		Equation ID
$A_{d,c}$	0.48	Critical size of tank insulation defect [m <sup>2</sup> ] (Scarponi et al., 2017)	-
$S_{max}$	*	Surface of tank inner wall with a temperature greater than the maximum design temperature [m <sup>2</sup> ]	-
<i>MAWP</i>	See Table 24	Tank maximum allowable working pressure [bar]	-
$P_0$	See Table 24	Tank initial pressure [bar]	-
$P_t$	*	Tank pressure at time t [bar]	-
$E_{VB}$	$\frac{d\hat{U}}{\widehat{\Delta H}_{TNT}} \times \eta \times 2$	Energy released in case of vessel burst at ground level, expressed in TNT equivalent mass [kg]	7.34
$d\hat{U}$	*	Variation of tank specific internal energy between initial conditions and the considered time step [kJ/kg]	-
$\widehat{\Delta H}_{TNT}$	4,680	TNT specific explosion energy [kJ/kg]	-
$\eta$	0.50	Fraction of $d\hat{U}$ converted into blast wave	-
$E_0$	0.52	Energy needed to generate a blast wave able to damage pressurized equipment at 5 m distance, expressed in TNT equivalent mass [kg]	-

\* Values to be calculated for each time step considered.

While *TI* and *IPI* indicators refer to the inherent safety of the storage tank, *EI* was defined to provide a quantification of the damage potential following the catastrophic rupture of the vessel that might lead to accident escalation (Cozzani et al., 2013). Following the vessel burst, the internal energy accumulated inside the tank is suddenly released to the surroundings. A fraction of this energy (the quantity  $\eta$  reported in Table 26) is converted into a blast wave, with a potential damage to the equipment surrounding the LNG tank. A reference minimum energy required to generate a blast wave able to damage the surrounding equipment,  $E_0$ , is defined. The value of  $E_0$  is assumed equal to a peak static overpressure of 0.2 bar at 5 m from the explosion centre, indicated by Cozzani et al., (2013) as the reference overpressure threshold to damage pressurized equipment. As prescribed in the EN 1473:2016 (CEN, 2016), the separation distance between two LNG tanks must be at least equal to half the diameter of the secondary container of the larger tank. The 5 m limit used for the definition of *EI* avoids considering an unrealistic too short distance between adjacent tanks.

Thus, as defined by Eq. 7.33,  $EI$  represents the ratio between the explosion energy resulting from vessel burst ( $E_{VB}$ ) and the reference value for escalation,  $E_0$ . Among the different models available in the literature for the estimation of explosion effects, the TNT-equivalence model was used in the present work for the sake of simplicity. Using this model, the explosion energy (thus, both  $E_0$  and  $E_{VB}$ ) can be expressed as an equivalent amount of TNT, as mentioned in Table 26. Detailed descriptions of the TNT equivalence model can be found in the literature (Kinney and Graham, 1985). In accordance with the other defined KPIs, a value of  $EI > 1$  indicates that blasts following the LNG tank rupture might have the potential to start a domino accident sequence.

### 7.3. Modelling results

#### 7.3.1. Validation of the model

Pressure profiles obtained for two-hour engulfing fire simulations for the validation case V66 are reported in Figure 42 together with the data obtained from the experimental test and the supporting simulations listed in Table 23. A drastic change of the experimental pressurization rate can be observed roughly 30 minutes after the start of fire exposure. The sudden pressure increase started immediately after the opening of the vacuum rupture disk and the partial release of perlite insulation material, as described in Section 7.1.1.

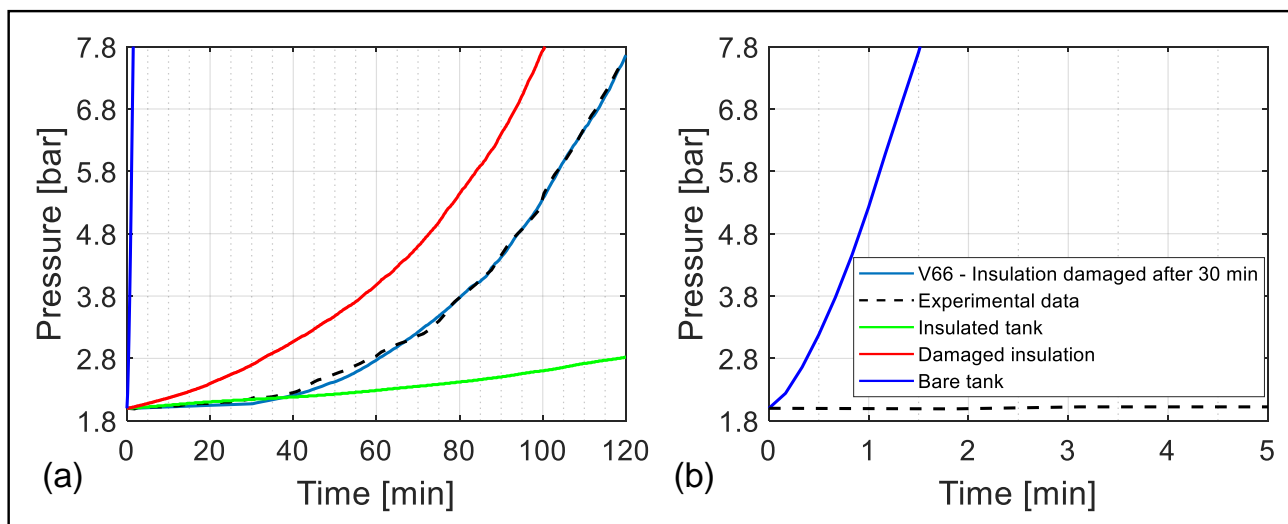


Figure 42: (a) Comparison between experimental and modelled pressurization profiles for the validation case assuming different conditions of the insulation; (b) detail of the pressure build up obtained for bare tank simulation.

Considering the extreme and unrealistic situation of a bare LNG tank reported in Figure 42b, it can be noted that under these conditions the tank will reach the final test pressure level in less than 2 minutes, following a pressurization transient similar to fire-engulfed LPG storage tanks reported in the work by Scarponi et al., (2018b).

When assuming an undamaged insulating layer, the pressurization rate is well predicted for the first 30 minutes, but afterwards the model underestimates the pressurization rate as can be seen in Figure 42a. The undamaged insulation thermal conductivity was estimated according to the model described in Section 7.2.3 considering the vacuum pressure value in the annular gap of the tank used in the experimental test (Kamperveen et al., 2016). The worsening of insulation performance experienced during the bonfire test was likely to be caused by loss of vacuum insulation together with displacement of granular perlite, possibly explaining the sudden increase of pressurization rate shown by the experimental data curve in Figure 34a.

As stated in the experiment report of the validation test (Kamperveen et al., 2016), after 30 minutes a complete loss of vacuum and partial discharge of perlite occurred in the insulation layer of the tank. In order to account for this event, the properties of the damaged insulation layer considered in the simulation were calculated according to the model described in Section 7.2.3 (see Table 24). Simulations showing the performance of such damaged insulation in the validation test are reported in Figure 42a. When the damage is assumed to occur at the beginning of the experimental test, a significant overestimation of the internal pressure is evident. Conversely, when the damage of the insulation is assumed to occur 30 minutes after the fire ignition, as happened during the experimental test, the model shows a good agreement with experimental data: predicted pressure values are comprised in a range between -5% and +5% deviation from measured test data.

As mentioned in Section 7.1.1, unstable temperature measurements were obtained during the test campaign. However, as indicated in the test report (Kamperveen et al., 2016), the thermocouples provided stable and reliable values immediately before fire ignition and after fire was stopped. Therefore, to obtain at least an indicative representation of the transient heat-up process, a linear trend between the unbiased experimental thermocouple readings at the beginning and at the end of the fire test was considered.

The CFD model performance in reproducing time evolution of liquid and vapour temperatures was assessed following the method proposed by Hanna et al. (1991). This approach requires the calculation of the geometric mean bias ( $MG$ ) and the geometric mean variance ( $VG$ ) of both measured ( $T_{exp}$ ) and predicted ( $T_{CFD}$ ) values. Temperature data from the experimental test and CFD simulation were compared considering 5 minutes intervals. For each time step (identified by index  $i$ ),  $T_{exp,i}$  and  $T_{CFD,i}$  were used to calculate the quantities in Eq. 7.35 and Eq. 7.36.

$$MG = \exp[\overline{\ln(T_{exp})} - \overline{\ln(T_{CFD})}] \quad \text{Eq. 7.35}$$

$$VG = \exp[\overline{(\ln(T_{exp}) - \ln(T_{CFD}))^2}] \quad \text{Eq. 7.36}$$

Where the terms  $\overline{\ln(T_{exp})}$ ,  $\overline{\ln(T_{CFD})}$  and  $\overline{(\ln(T_{exp}) - \ln(T_{CFD}))^2}$  are calculated as follows:

$$\overline{\ln(T_{exp})} = \sum_i \ln(T_{exp,i}) / \sum_i 1 \quad \text{Eq. 7.37}$$

$$\overline{\ln(T_{CFD})} = \sum_i \ln(T_{CFD,i}) / \sum_i 1 \quad \text{Eq. 7.38}$$

$$\overline{(\ln(T_{exp}) - \ln(T_{CFD}))^2} = \sum_i (\ln(T_{exp,i}) - \ln(T_{CFD,i}))^2 / \sum_i 1 \quad \text{Eq. 7.39}$$

The bias in model predictions, i.e., its tendency to systematically over or under-predict temperature values, is expressed by  $MG$ , whereas the  $VG$  value is a measure of the scatter in the model predictions around a mean value. Points located to the left of  $MG = 1$  suggest a model over prediction, whereas points to the right of this value indicate under prediction. Confidence levels of  $MG = 0.5$  and  $MG = 2$  (representing a factor of two for over and under-prediction respectively) are also reported, defining a range for an “acceptable” model. Note that in Figure 43 a perfect model would be represented by a point at the vertex of the parabola.

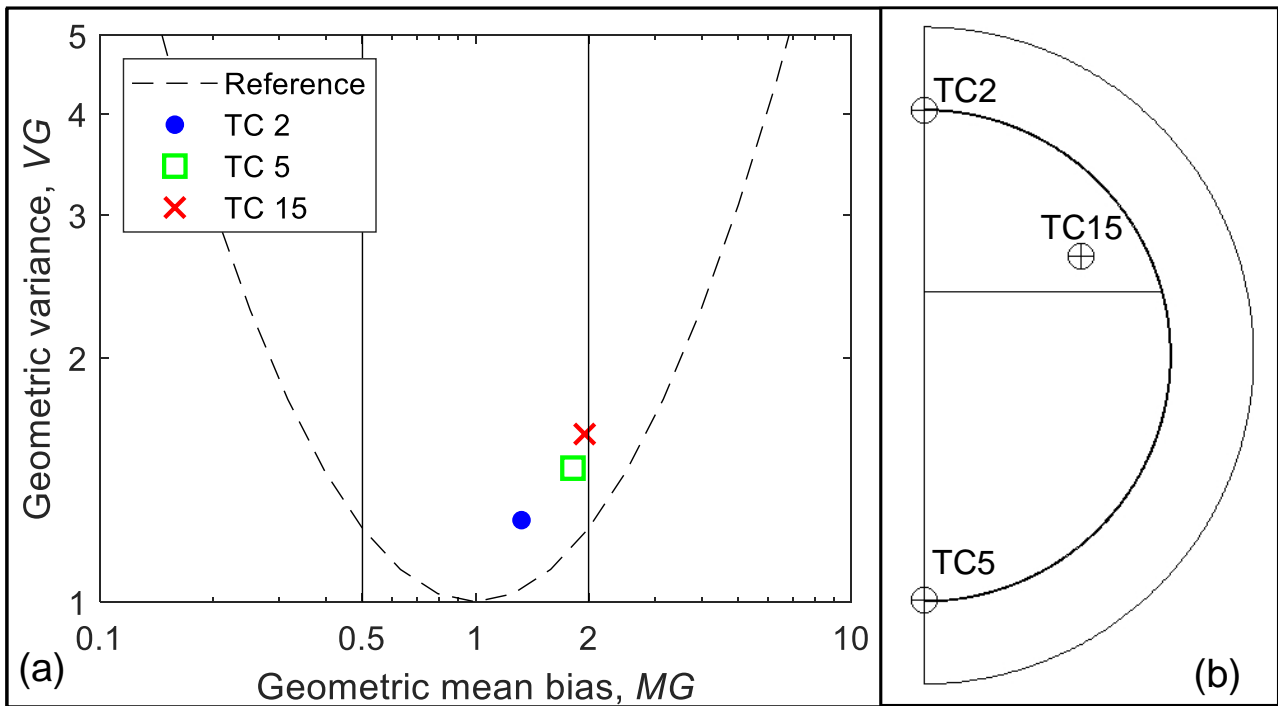


Figure 43: (a) Geometric mean bias ( $MG$ ) and variance ( $VG$ ) of model-predicted temperature values compared against experimental measures. (b) Position of thermocouples used for experimental temperature measurement and liquid-vapour interface for the validation case V66.

As illustrated in Figure 43, the vapour temperature (thermocouple TC2, located on the top part of vapour ullage) shows a good agreement with experimental data, whereas liquid temperature (TC5 on the tank bottom) and vapour temperature 8.5 cm above the liquid interface (TC15) experience more important deviations from test data, even if they remain below the  $MG = 2$  limit.

The results of all the four validation simulations were proven to be independent from computational grid, time step size and convergence criteria of governing equations. The model grid independence was studied using a finer mesh created by reducing the maximum element size and length, while the dimension of the first cell close to tank inner wall was held constant. This resulted in a mesh having around 2.3 times the number of elements reported in Table 25. Since the meshing parameters used for the proposed model, listed in Table 25, are similar to those adopted by Scarponi et al., (2018a, 2018b), who validated his 2D CFD model for several filling degrees, such analysis was not replicated in this work, hence the same meshing strategy was used for all the different tank filling degrees analysed. To investigate the effects of the selected time step size on modelling results, a transient simulation with a time step of 0.02 s (twice the size of the original value) was run. The last parameters analysed were the convergence criteria. To prove that modelling results are independent from the selected convergence criteria, an additional simulation was run with more stringent criteria. The sum of scaled residual for continuity, momentum and energy equations was required to be one order of magnitude lower than previous setting (from  $10^{-3}$  to  $10^{-4}$  for continuity and momentum;  $10^{-6}$  to  $10^{-7}$  for energy equation).

The results of model independence study are reported in Figure 44, in which the variation of pressure prediction from different model setups is plotted against the benchmark setup used for the validation case V66. It is possible to notice that the differences with the original setup are always comprised in the  $\pm 5\%$  range, indicating good robustness and stability of the adopted numerical setup.

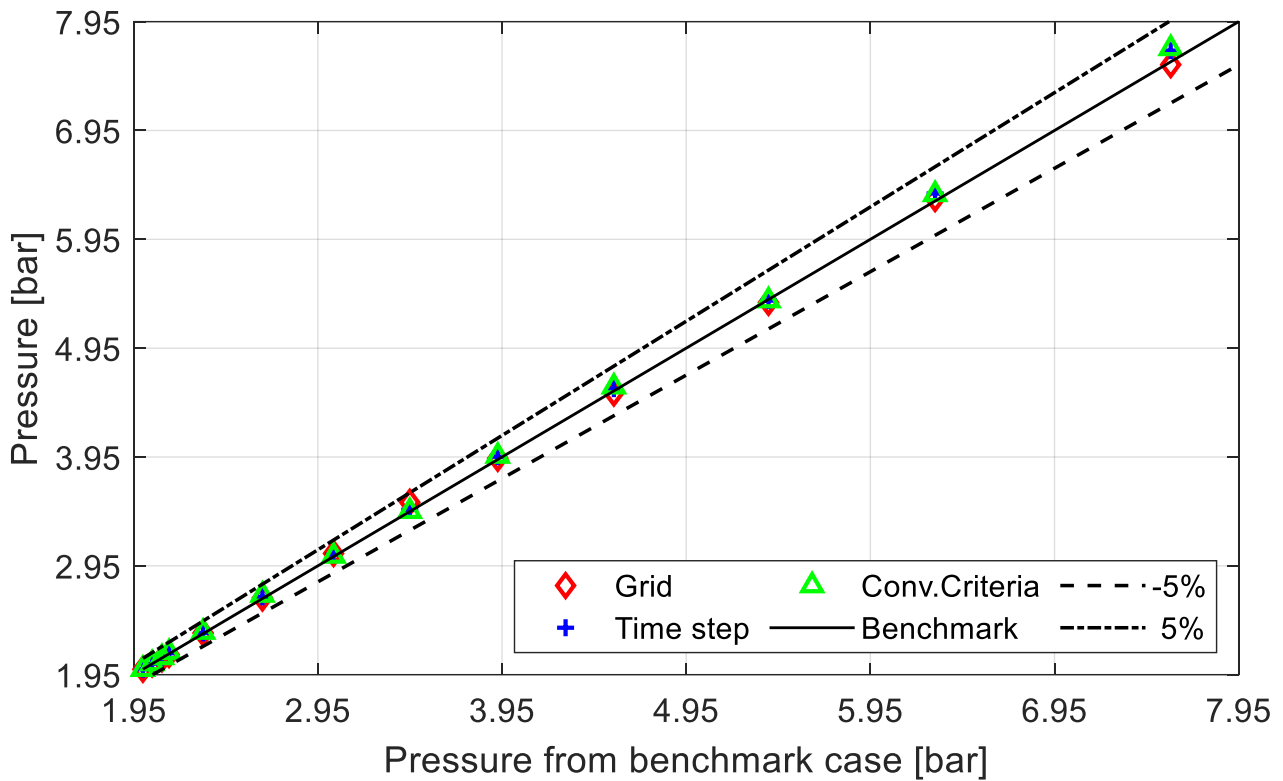


Figure 44: Parity plot for numerical model independence analysis.

### 7.3.2. Analysis of the results of the case studies

The pressurization profiles obtained for the case studies analysed are shown in Figure 45. Considering case-study A (the ship fuel tank), Figure 45a shows that even assuming a degraded thermal insulation layer since the beginning of the simulation, the PRV opening pressure (considered equal to the MAWP value reported in Table 24) can only be reached for low tank filling degrees (15%, see Table 24). The analysis of simulation results clearly indicates that higher tank filling degrees result in slower pressurization rates due to the slower heat-up of the tank lading.

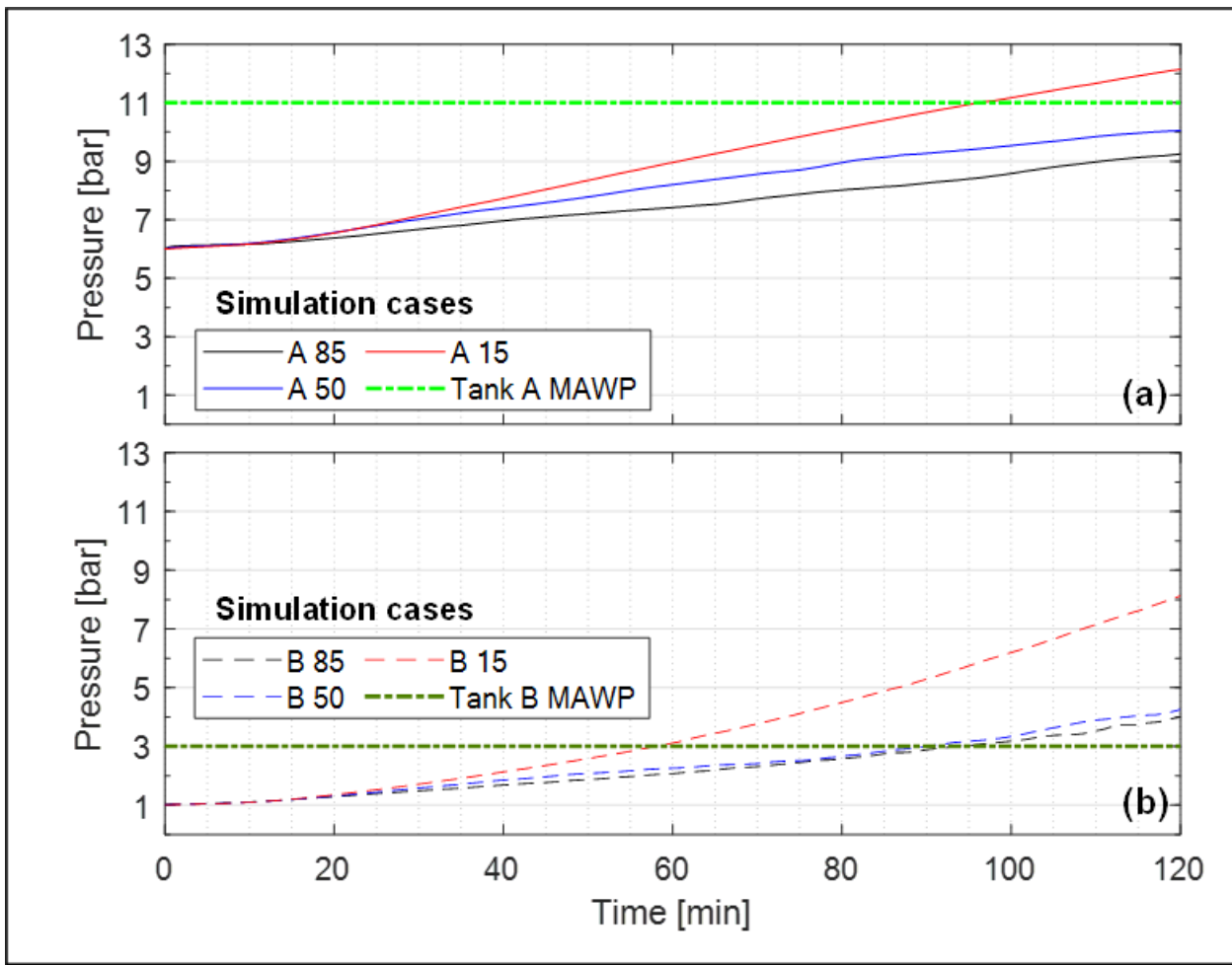


Figure 45: Pressurization profiles for 200 m<sup>3</sup> type C tank (a) and 58 m<sup>3</sup> road tanker (b) engulfed in fire. For the description of simulation cases refer to Table 24.

The relationship between tank filling degree and pressurization rate observed in the simulations is in accordance with the experimental results obtained by Van Drew et al. (1992) and the numerical results reported by Seo and Jeong (2010), obtained for liquid hydrogen and liquid nitrogen respectively, considering heat leaks in the order of 10 W/m<sup>2</sup>. After an initial period (approximately the first 10 minutes of simulation), in which the pressure build-up is limited, the pressurization rate starts to constantly increase, reaching overall average values of about 0.512, 0.337, and 0.271 bar/10 min for cases A15, A50, and A85, respectively. As illustrated in Figure 45a, the increase in the pressurization rate occurs approximately 20 minutes after the start of fire exposure.

Similar results were obtained for the case-study B, representative of a road tanker engulfed by flames. As for the previous case, a higher pressurization rate is observed when the filling degree is lower. However, in this case-study, the exposure to full engulfment conditions results critical for all the three filling degrees analysed. In simulation case B15, the tank MAWP is reached 30 minutes before case A15, whereas in cases B50 and B85 this value is reached about half an hour later than case B15. An average pressurization rate value of about 0.593 bar/10 min can be estimated for case B15, while cases B50 and B85 have pressurization rates of 0.270 and 0.249 bar/10 min, respectively. Furthermore, comparing Figure 45a and Figure 45b, it is possible to notice that cases B50 and B85 follow an almost identical pressurization trend, different to that observed for case A, where the tank size is larger.

Besides the pressurization effect related to the thermal expansion of the vapour, pressure rise inside the tank is directly related to the mass of the liquid evaporated during fire exposure as well. Regions of condensation and evaporation inside the tanks are represented in Figure 46.

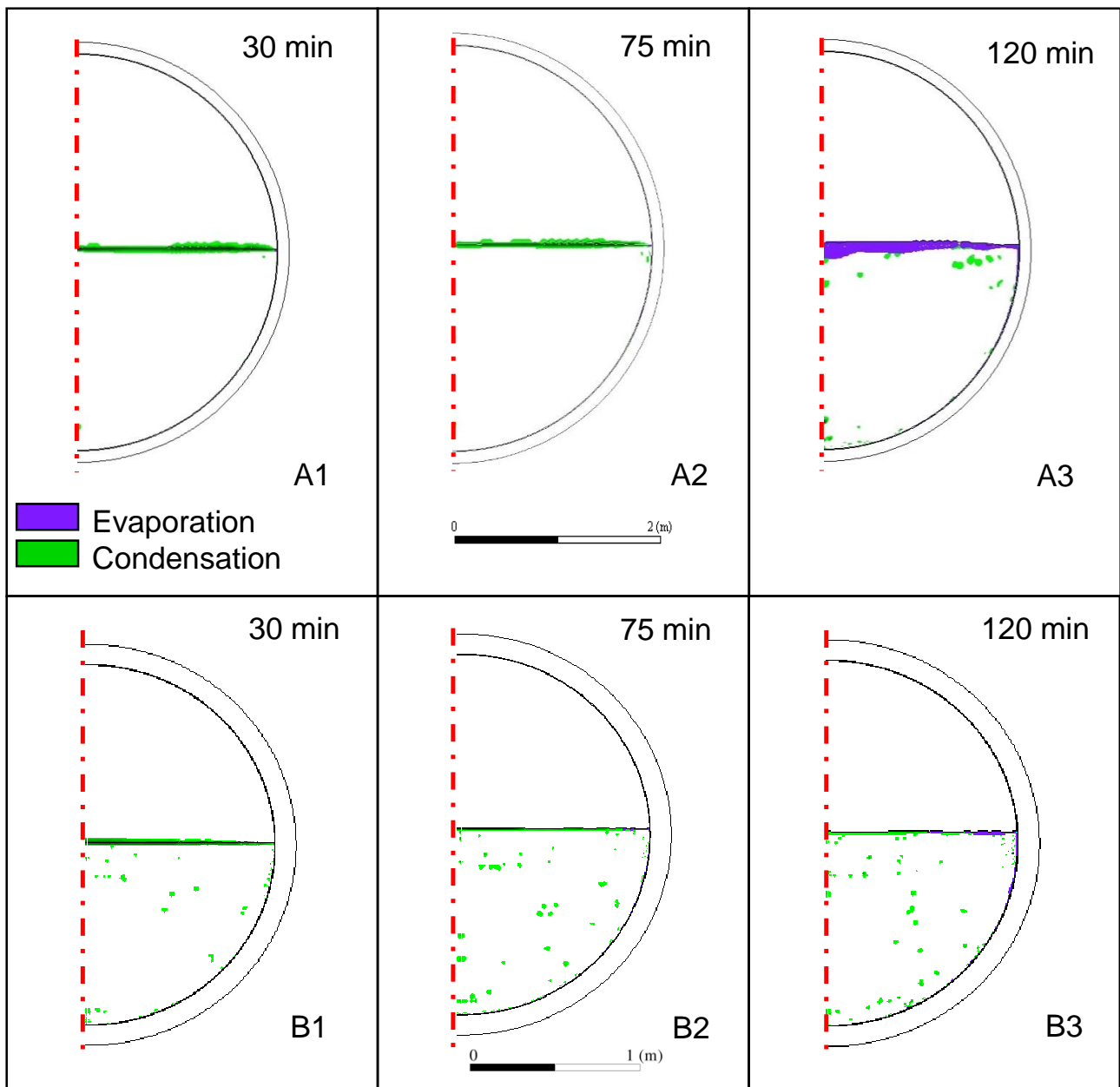


Figure 46: Time evolution of condensation and evaporation regions inside tank lading for simulation cases A50 (panels A1-A3) and B50 (panels B1-B3). Table 24 reports the details of the two simulation cases.

After more than one hour of fire exposure evaporation takes place only in a very thin region in contact with tank walls as can be seen in panels A2 and B2 of Figure 46. Condensation zones can be found close to the liquid-vapour interface regions, farther from the tank walls, where the vapour is being cooled down by the liquid, eventually condensing it. As the time passes, the size of the evaporation clusters in the proximity of the interface and in contact with the tank wall starts to grow. Small residual condensation regions are still present close to the tank bottom: these are zones where the small vapour pockets detaching from bottom walls reach the colder liquid bulk, promptly condensing. Comparing the results obtained for case-studies A and B, it can be noticed that the extension of the evaporating regions at the interface is more limited for case B. Such an effect might be caused by different initial conditions between the two cases or by the different tank sizes.

The liquid phase temperature distribution along the vertical profile perpendicular to the tank axis is reported in Figure 47 for different time steps. For the case-study A, a noticeable temperature difference between the liquid bulk and interface zones develops for higher filling degrees, whereas

for lower values of the filling degree the liquid temperature appears to be more homogeneous. This effect generally intensifies with time and becomes more significant closer to the liquid-vapour interface. A prolonged fire exposure of the vessel results in the gradual amplification of liquid thermal stratification: after 2 hours of heating, the liquid temperature spans from a minimum of 146 K measured close to the bottom of the tank, up to a maximum of around 147.5 K at the interface region (see case A85 at 120 min – Figure 47a), with a maximum difference of 1.5 K. The maximum temperature value of the liquid phase, which is obtained at the interface, ranges from about 147.5 K for case A85 to 153 K for case A15. These values equal the saturation temperature at the current pressure value of simulation case.

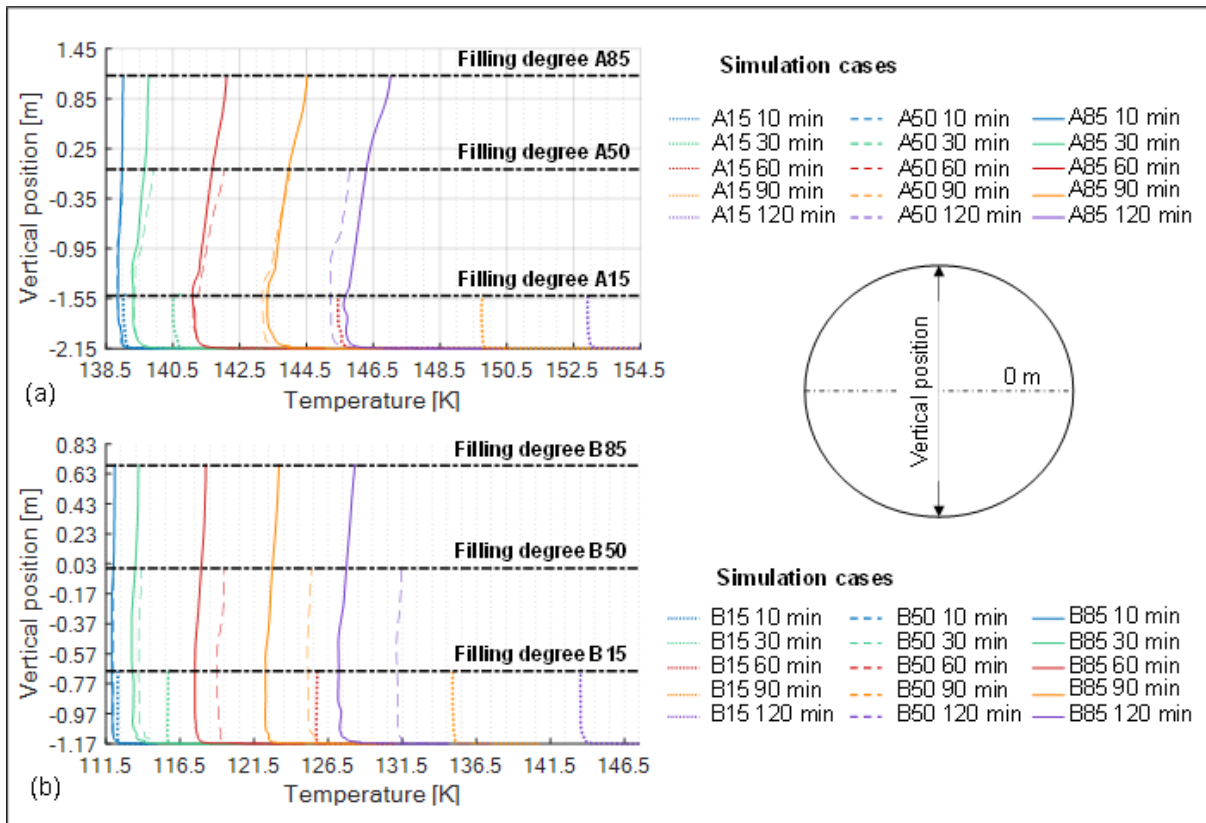


Figure 47: Liquid thermal stratification for 200 m<sup>3</sup> type C tank (a) and 58 m<sup>3</sup> road tanker (b) engulfed in fire. Temperature profile evolution on the vertical line perpendicular to tank axis is reported at different times after fire ignition. The liquid-vapour interface for the different simulation cases is represented by a dash-dotted line.

The liquid temperature stratification for case-study B follows a similar trend: the results reported in Figure 47b show that also for smaller tank diameters and lower pressure levels, the temperature gradient of the liquid is larger for higher filling degrees. For case B15, after 120 minutes since the fire start, the maximum temperature difference between bulk and interface region is about 1 K. At the end of the simulations, this case shows a liquid temperature about 13 K higher than simulation case B50, and 17 K higher than case B85. As observed for case-study A, the maximum liquid temperature value is equal to the saturation temperature for the pressure reached at the considered time step. Contour plots showing the extent of liquid temperature stratification are presented in Figure 48. Comparing the results for cases A and B, it can be noted that for the latter warmer liquid regions tend to be located closer to the interface than for case A and that these regions have a more limited extension through the tank liquid lading.

Focusing on case A results, it is possible to notice that the warmer liquid regions tend to be organized as layers, with a visible wall effect that slightly distorts the region shape.

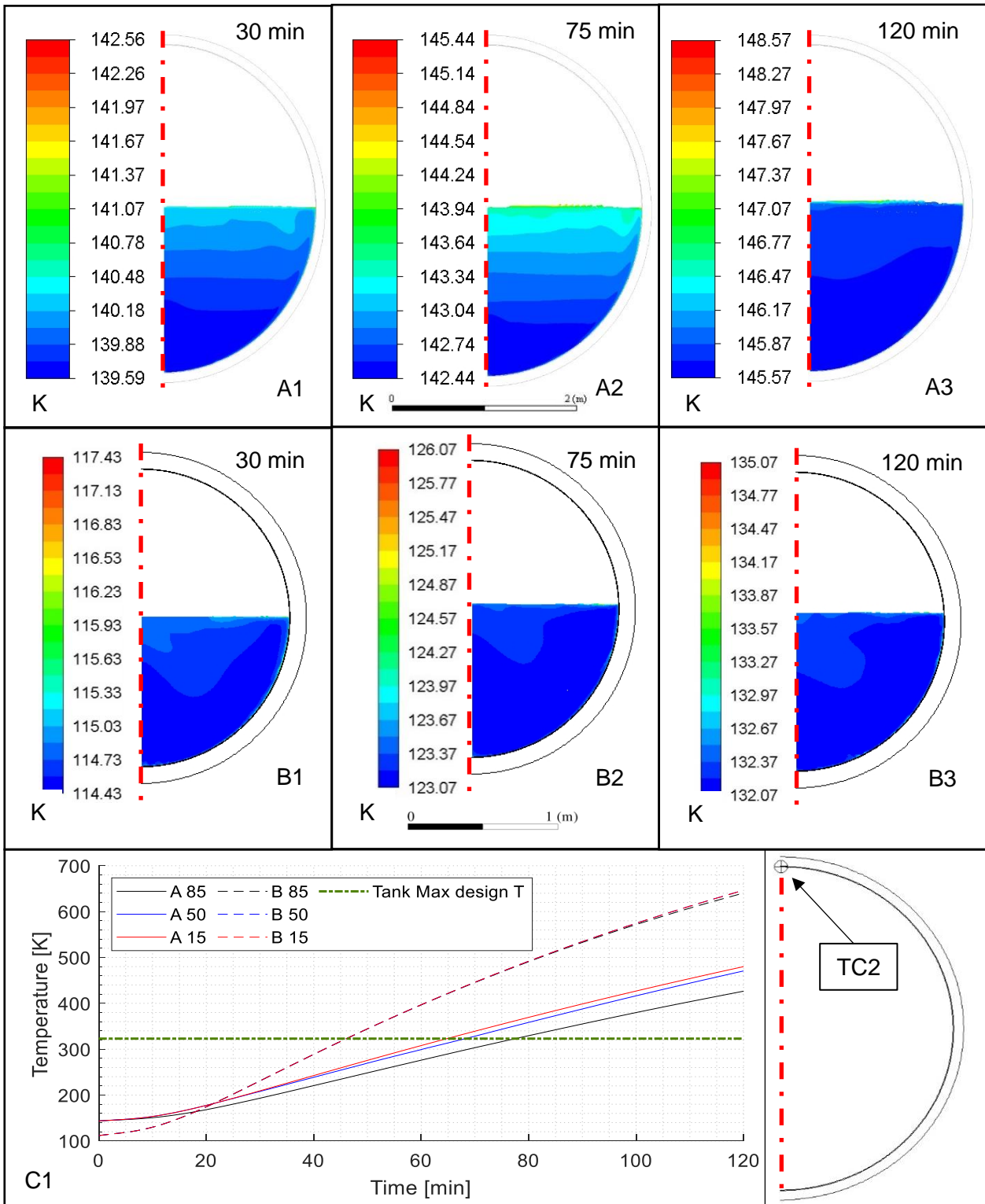


Figure 48: Liquid temperature contours for simulation cases A50 (A1-A3) and B50 (B1-B3) at different times. Panel C1 shows the dynamic evolution of tank inner wall temperature measured by thermocouple TC2.

The dynamic evolution of tank inner wall temperature is reported in panel C1 of Figure 48. This is the temperature value predicted by simulations for the point TC2 that corresponds to the top part of tank vapour ullage space. Here predicted wall temperature results are the highest due to the absence of the “cooling” effect promoted by the liquid.

As can be seen from the Figure, the temperature threshold equal to 323 K will be exceeded for all the cases, with tank B reaching the limit around 20 minutes earlier than case A.

As described in Section 7.2.1, flame engulfment is also responsible for the formation of natural convective cells inside the tank lading, as shown in Figure 49 that reports the calculated velocity fields. The pressurization rate increase described previously occurs simultaneously to the establishment of liquid motion inside the tank. Looking at panels A1 and B1 of Figure 49, it can be noticed that recirculation eddies are already developed after 30 minutes of fire engulfment. Regardless of tank size and filling degree, the warmer liquid layer that is present along tank walls starts to flow upward towards the vapour-liquid interface due to the development of a density gradient. This liquid motion results in the formation of the recirculation eddies, that enhance both mixing and progressive heating of the liquid layer at the interface, which controls the pressurization dynamics. The warmer fluid at the interface has a prevalent radial direction, towards the axis of the tank: here it mixes with the cold liquid and recirculates downwards to the bottom part of the tank, creating a macroscopic free convection cell inside the tank (clearly visible in panels A2-A3 and B2-B3 of Figure 49).

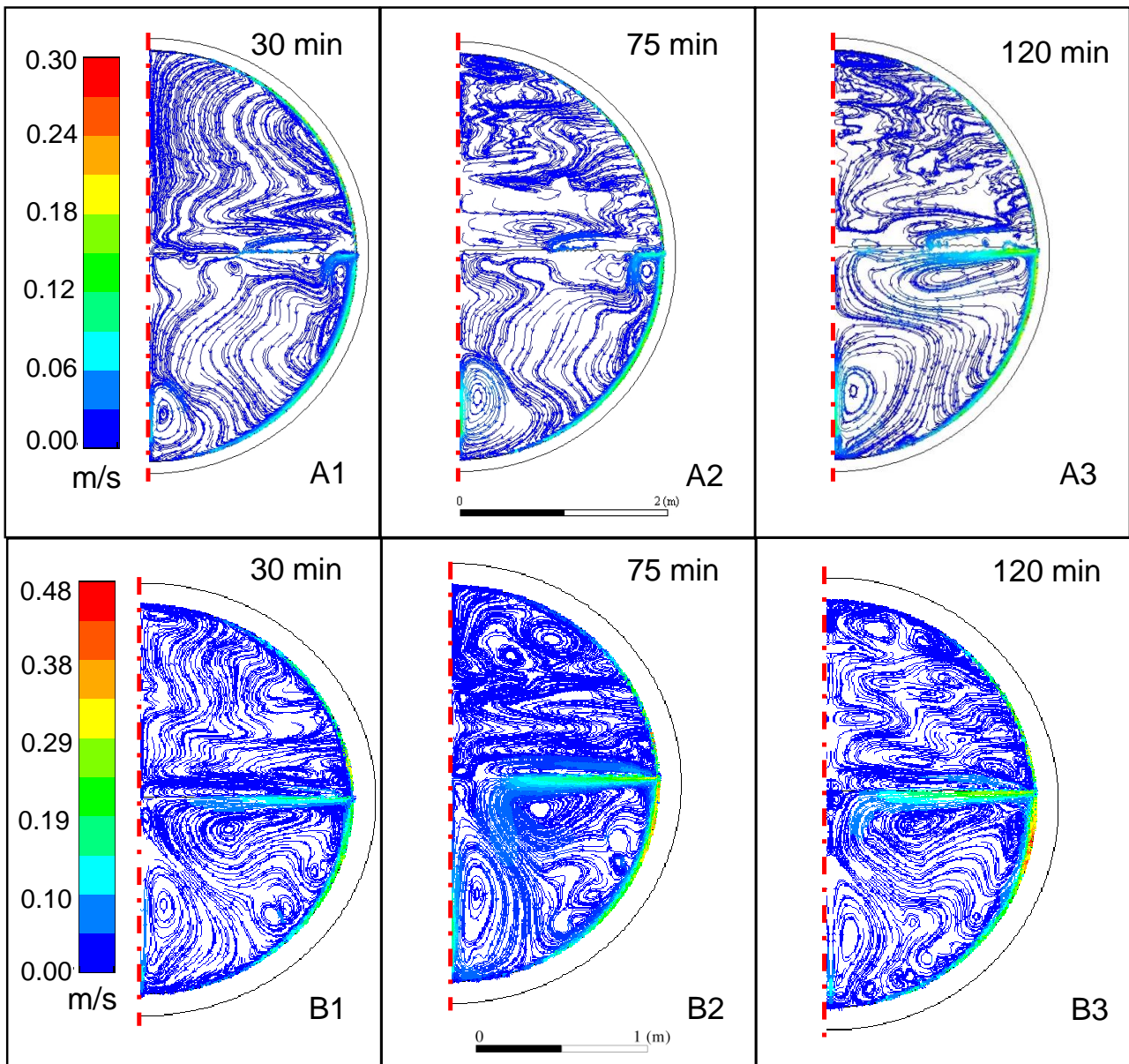


Figure 49: Velocity magnitude path-lines for simulation cases A50 (A1-A3) and B50 (B1-B3) at different time steps.

The velocity field features observed in Figure 49 are closely related to the shape and extent of warmer liquid regions of Figure 48. The numerous recirculation eddies characterizing case B might be a possible explanation for the more limited thermal stratification observed due to the enhanced mixing of the liquid lading.

The extents of the free convective layer and thermal boundary layer are reported in Table 27. Time evolution of temperature and vertical velocity profiles for cases A50 and B50 are illustrated in Figure 50 to support the discussion, while results for other cases are reported in Appendix D. For each case study, boundary data were extracted at the horizontal centreline (horizontal red line in Figure 50) at 30 and 120 min. The extent of the velocity boundary layer formed in proximity of the wall is of few centimetres for the tank considered in case-study A. In the case of tank B, the liquid velocity boundary layer is reduced by 30-60%, whilst vapour velocity boundary layer has an extension comparable to the other case. Comparing the results of case studies A and B, it can be noted that the thickness of fluid layer that is affected by natural convection in proximity of the wall increases with both the tank filling degree and diameter. However, when the thickness of velocity free convective layer is normalised with respect to the tank diameter, case-study B shows larger normalised convective layers. This is due also to the higher velocity magnitude values, which exhibits an increment of 20% and 80% respectively after 30 and 120 min since the start of the fire in case B50 when compared to case A50.

Table 27: Extent of velocity and thermal free convection layers evaluated at the horizontal centreline of the tank. Boundary layer thickness is normalised with respect to tank diameter.

Case ID	Velocity free convection layer		Thermal free convection layer		Maximum velocity magnitude [m/s]
	Thickness [mm]	Normalised thickness	Thickness [mm]	Normalised thickness	
<b>30 min</b>					
<i>Open-deck tank</i>					
A85	121.3	$2.820 \times 10^{-2}$	20.9	$4.866 \times 10^{-3}$	0.178
A50	118.2	$2.749 \times 10^{-2}$	29.3	$6.808 \times 10^{-3}$	0.086
A15	72.6	$1.689 \times 10^{-2}$	109.6	$2.549 \times 10^{-2}$	0.357
<i>Road tanker</i>					
B85	82.6	$3.593 \times 10^{-2}$	26.8	$1.165 \times 10^{-2}$	0.248
B50	68.1	$2.963 \times 10^{-2}$	24.9	$1.082 \times 10^{-2}$	0.155
B15	22.0	$9.575 \times 10^{-3}$	81.1	$3.527 \times 10^{-2}$	0.263
<b>120 min</b>					
<i>Open-deck tank</i>					
A85	99.0	$2.302 \times 10^{-2}$	18.4	$7.994 \times 10^{-3}$	0.183
A50	246.7	$5.738 \times 10^{-2}$	26.0	$1.130 \times 10^{-2}$	0.283
A15	18.4	$4.276 \times 10^{-3}$	30.2	$1.311 \times 10^{-2}$	0.187
<i>Road tanker</i>					
B85	67.0	$2.911 \times 10^{-2}$	13.4	$5.831 \times 10^{-3}$	0.162
B50	104.9	$4.560 \times 10^{-2}$	10.7	$4.645 \times 10^{-3}$	0.339
B15	7.3	$3.159 \times 10^{-3}$	22.0	$9.575 \times 10^{-2}$	0.184

The results obtained for the thermal boundary layer show that the previous behaviour is also present when dealing with the analysis of temperature profiles. The thermal boundary layer thickness, in fact, is higher for the larger diameter tank, with thickness values ranging between 10 and 120 mm. Compared to the thickness of velocity free convection layer, the thermal boundary is generally thinner, as expected (Bird et al., 2006). In fact, when Prandtl number ( $Pr$ ) is greater than unity the temperature boundary layer usually lies inside the velocity boundary layer, whereas for  $Pr < 1$  the relative thicknesses are reversed. Results for cases A15 and B15 reported in Table 27 refer to vapor phase, since the liquid interface is below the horizontal centreline of the tank. In these cases,  $Pr$  is about 0.5, which explains the larger thickness of the thermal free convective layer compared to the velocity layer. Moreover, the velocity free convection layer is much smaller when compared to that of the liquid phase (see cases A85, A50 and B85, B50). This difference is reversed when considering the thermal boundary layer extent.

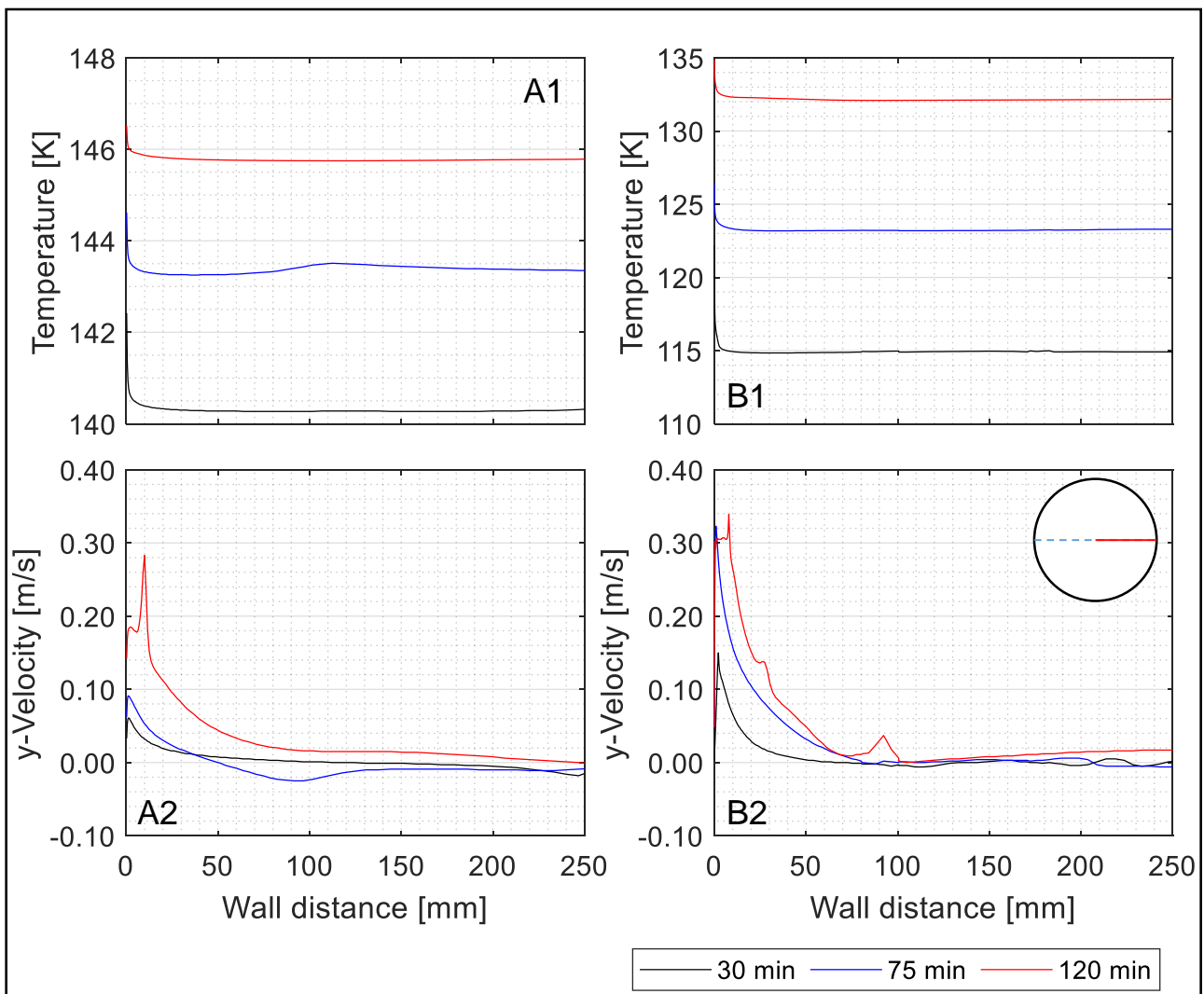


Figure 50: Comparison of thermal and vertical velocity profiles at different time steps for cases A50 (panels A1 and A2) and B50 (panels B1 and B2). Data refer to the tank horizontal centreline (horizontal segment in the sketch). The dashed segment indicates the tank filling degree.

### 7.3.3. Assessment of safety Key Performance Indicators

The results of 2D CFD simulations were used to evaluate the KPIs defined in Section 7.2.6, in order to explore the safety margins with respect to critical conditions of the LNG tanks exposed to fire. The definition of safety KPIs based on CFD simulation results allowed obtaining preliminary indications about the possible damage state of pressurized cryogenic vessels subject to hydrocarbon fire heat loads. Figure 51 reports the values of the KPIs obtained for the different simulation cases after 60, 90 and 120 minutes since the fire start.

Based on the threshold values defined for each KPI, three different volumes were determined in the space defined by the three safety KPIs:

1. a safe region, where all the KPI values considered are within the safety margin (green zones in Figure 51);
2. an intermediate region, in which at least one indicator expresses a potentially dangerous situation (yellow zone in Figure 51);
3. an unsafe region, in which all the KPI values fall over the relevant safety limits (red zone in Figure 51).

Figure 51a reports the values obtained for *IPI* and *TI* in the different simulation cases. Given the relatively high wall temperatures obtained in the simulations, none of the *TI* values fall in the safe region except for the case A85 at 60 min of fire exposure. This is due to the combined effect of high thermal inertia of the liquid lading (i.e., due to the high filling degree) and the limited time of fire exposure. The results obtained provide a simplified indication of the tank mechanical integrity reduction induced by the thermal weakening. Figure 51a also shows that most of the results are in the yellow intermediate region, due to the low *IPI* values obtained associated with the limited pressurization (see Figure 45). Only after very long fire exposures do simulation results fall in the unsafe region. This confirms that the risk of tank structural failure is enhanced by a thermal weakening of the steel. The thermal weakening is particularly relevant for tanks having lower filling degrees, due to the higher extension of the vapour space, in which higher temperature values are obtained. In the simulation case B15, after 60 minutes of fire exposure all KPIs fall inside the red area.

The values of *EI* and *IPI* are shown in Figure 51b. The results show that after 60 minutes of fire exposure, *EI* values are always in the unsafe region. This indicates that after 60 minutes of fire exposure, the energy released by a catastrophic failure of the tank would always be sufficient to cause a domino effect, escalating the accident.

Figure 51c shows the six cases identified as having the most critical conditions, as all the three KPIs fall in the unsafe region. Five of the cases are related to case-study B, whilst for the larger tank (case-study A) just case A15 falls in the unsafe region, only after two hours of fire exposure. This indicates that the more critical cases feature lower values of LNG inventories. This is due to combined effect of thermal weakening, which affects a higher portion of tank surface in contact with the vapour, and sufficient energy accumulation, able to lead to relevant escalation effects in case of tank failure, due limited thermal inertia of the tank lading.

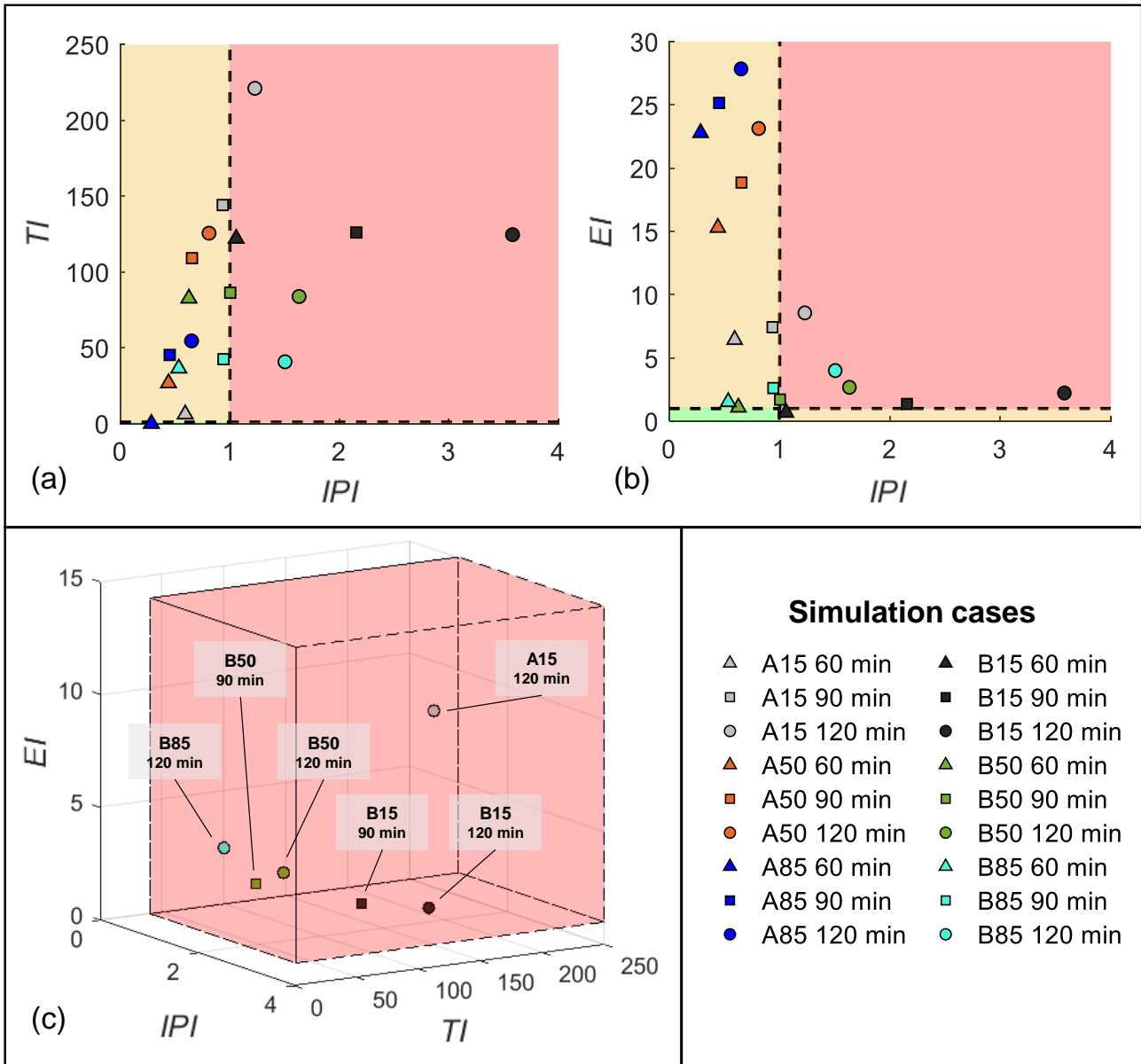


Figure 51: Comparison of safety KPIs for fire-engulfed cryogenic pressure tanks: a) TI (Temperature index) versus IPI (Internal Pressure index); b) EI (Energy index) versus IPI (Internal Pressure index); c) 3D representation of the unsafe volume where all the three KPIs are above the safe threshold.

## 7.4. LNG tanks exposed to distant pool fires

A further application of the CFD model described above is the prediction of pressurization rate of double-walled pressurized cryogenic tanks receiving heat loads from distant pool fires. Such a scenario, representative of a possible accident outcome in an LNG storage facility, introduces an element of non-uniformity in the boundary condition to which LNG tanks are subject, the effects of which are worth being assessed. A set of 2D CFD simulations was carried out considering the same tank geometries and initial conditions as case studies A and B listed in Table 24.

### 7.4.1. Definition of boundary condition

The same model setup detailed in Section 7.2.5 was used for the current simulations, with the exception of the boundary condition that needs to account for the geometrical effects due to relative positions of pool fire and storage tank. The distant fire heat load is principally transferred to the tank by radiation, while a smaller fraction is attributed to natural convection, generally less than 10% (Landucci and Birk, 2013).

Neglecting the amount of radiation absorbed by the atmosphere and assuming the fire as an emitting surface with a constant equivalent black body temperature ( $T_{f,BB}$ , that was set to a value of 860 °C), the incident radiation ( $I_P$ ) at point P on the tank surface can be expressed as:

$$I_P = \sigma \times (f_{P \rightarrow f} \times T_{f,BB}^4 + (1 - f_{P \rightarrow f}) \times T_{amb}^4) \quad \text{Eq. 7.40}$$

where  $\sigma$  is the Stefan-Boltzmann constant and  $T_{amb}$  is the ambient temperature (set to 16 °C for the analysis). The term  $f_{P \rightarrow f}$  is the view factor between point P and the fire. Prior to the characterization of boundary condition, it is fundamental to define a reference pool fire scenario, delineating its geometrical features. For the present analysis it was assumed to simulate the thermal effects produced by a pool fire resulting from a 3" (76.2 mm) diameter LNG transfer hose spillage. Using well-established source models (Van Den Bosh and Weterings, 2005) the spilled LNG mass was calculated and used as input for the pool fire model. The resulting pool fire, located 15 m from the tank centre, has a diameter of 3.2 m, and a flame height of 11.9 m. To account for the effect of the wind on the flame shape, the fire was modelled as a tilted cylinder following the solid flame approach. Assuming a wind velocity of 5 m/s, the flame resulted tilted by an angle of 57° in the direction of the tank (to reproduce a worst-case scenario). The numerical evaluation of view factors required the discretization of both fire and tank outer wall surfaces. These were discretized using grid elements with a maximum edge size of 0.1 and 0.2 m, for the tank and the fire surfaces, respectively. Referring to Figure 52a, the analytical expression of the view factor between a tank element  $T_i$  with area  $dA_1$  and an element  $F_j$  on the surface of the pool fire, with area  $dA_2$  is:

$$F_{T_i F_j} = \frac{1}{A_1} \int_{A_2} \int_{A_1} \frac{\cos \alpha_1 \cos \alpha_2}{\pi S^2} dA_1 dA_2 \quad \text{Eq. 7.41}$$

where  $\alpha_1$  and  $\alpha_2$  indicate the angle between the segment  $S$  (connecting  $T_i$  and  $F_j$ ) and surface normal vectors  $n_1$  and  $n_2$  respectively.

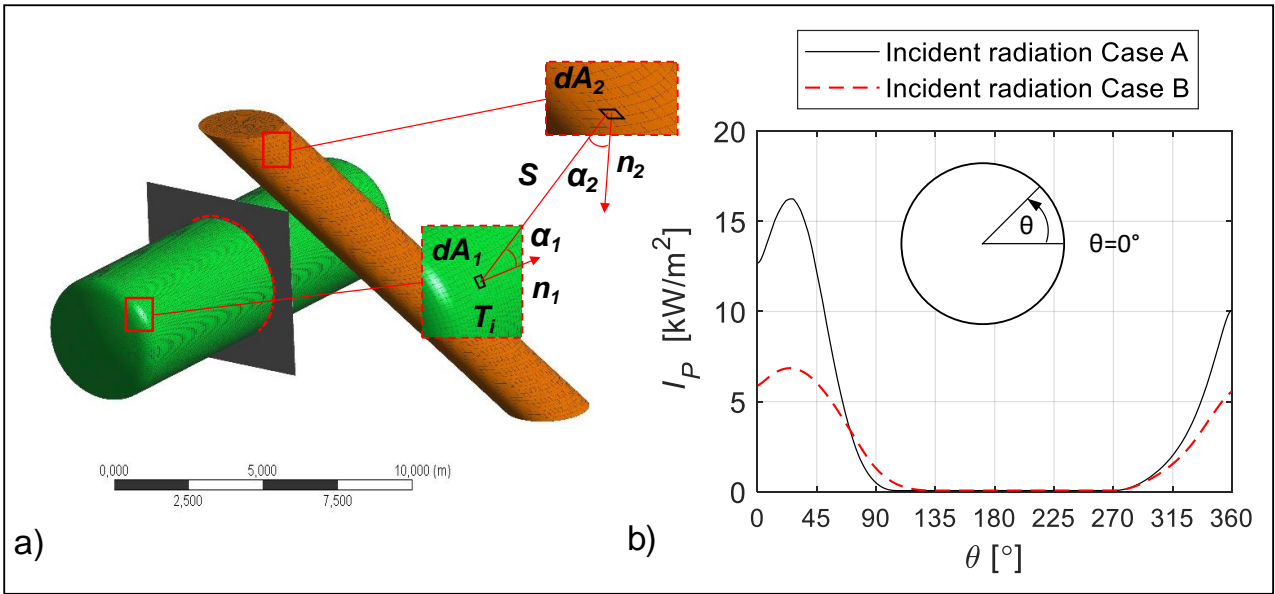


Figure 52: Meshed 3D geometries of pool fire and tank used for view factor calculation (a). Panel (b) shows the variation of the incident radiation as a function of the angular coordinate  $\theta$  on the central circular section.

The numerical solution of Eq. 7.41 was achieved approximating the integral with a summation over all mesh elements of the fire using a MATLAB<sup>®</sup> script. In this way, view factors were calculated for each mesh element on the tank surface. Thus, using Eq. 7.40, it was possible to obtain the values of the incident radiation over the red dashed circumference reported in Figure 52a, representing the external boundary of the 2D computational domain considered for the CFD simulations. The estimated incident radiation values for the two tanks under analysis are reported in Figure 52b.

At this point, it was possible to calculate an equivalent black body temperature,  $T_{BB,eq}$ , representative of the incident radiation hitting the tank wall, as expressed by the following equation:

$$T_{BB,eq}^4 = \frac{I_P}{\sigma} \quad \text{Eq. 7.42}$$

A profile file was then created and passed to the CFD solver to define the boundary condition. Knowing the value of  $T_{BB,eq}$  for all the points lying on the tank circumference, the solver calculates the entering heat flux ( $\dot{q}_P''$ ) for each point  $P$  on the tank circumference according to Eq. 7.43.

$$\dot{q}_P'' = \sigma \times \varepsilon_{wall} \times (T_{BB,eq}^4 - T_{wall}^4) \quad \text{Eq. 7.43}$$

Where,  $\varepsilon_{wall}$  is the tank outer wall emissivity (assumed equal to unity to account for worst case conditions, as done in Section 7.2.5), and  $T_{wall}$  is the tank outer wall temperature. To avoid introducing uncertainties due to the lack of specific measurements, the influence of natural convection on heat transfer from distant sources was neglected during the analysis. This approach was also followed by Scarponi et al. (2018c) in a similar work, avoiding the necessity of an empirical estimation of natural convection heat transfer coefficient.

### 7.4.2. Main results

Figure 53 reports the dynamic evolution of tank pressure for both case studies A and B for the different filling degrees considered. As predicted in case of full engulfing pool fires, the pressurization rate is higher for tanks with lower liquid levels. However, the pressure increase is limited to 1 bar above the initial pressure value for both the analysed cases: after two hours of pool fire exposure, both tanks reach a pressure level significantly lower than the MAWP reported in Table 24. Comparing Figure 53a and Figure 53b, it can be noticed how different operating conditions and tank size affect the pressure build-up: while case A shows a significant time lag of about 45 minutes before the pressure starts to rise, pressurization for case B appears not to be delayed.

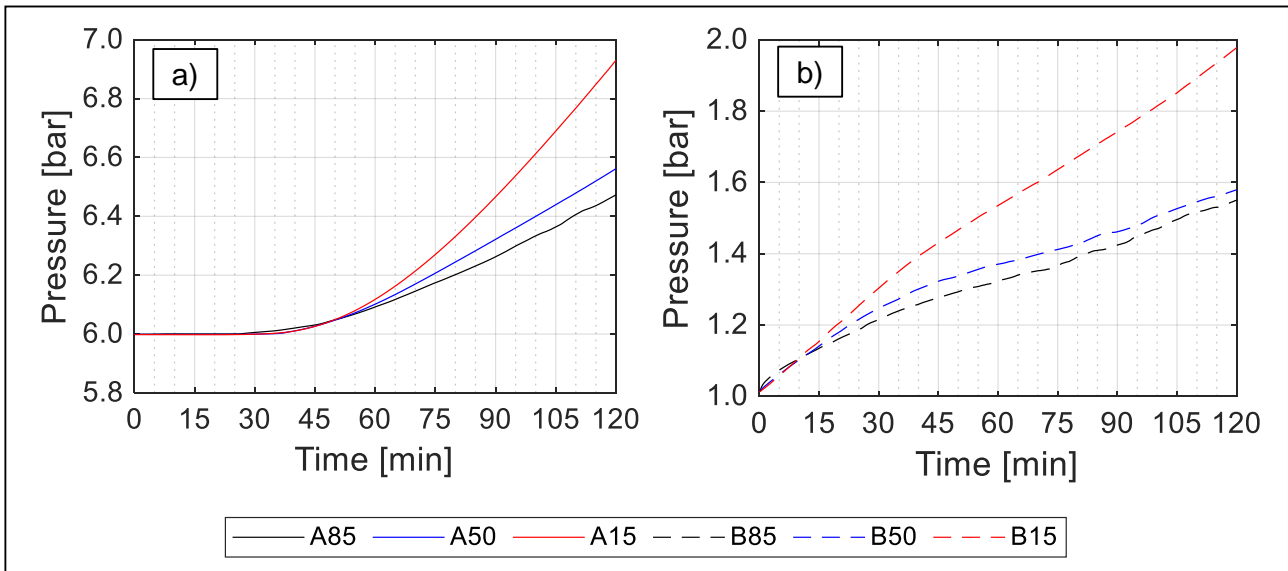


Figure 53: Pressurization curves obtained for the open-deck ship-fuel tank (a) and road tanker (b) exposed to distant pool fire.

As explained in Section 7.2.6, another important parameter for the assessment of integrity is the wall temperature. Figure 54 compares the variation of tank inner wall temperatures with the angular position for the case studies at two different time steps. It is clear how the higher heat transfer coefficients for the liquid phase contribute to keep the wetted part of tank wall at lower temperatures than the wall portion in contact with the vapour, possibly inducing thermal stresses. Moreover, the temperature predicted for the road tanker (case B) is far greater than the correspondent case A. This effect could be linked to the thinner insulation layer of Case B, that increases the heat flux reaching the inner wall, and to a higher surface-to-volume ratio characteristic of smaller diameter tanks. However, the maximum temperature reached by the wall section in contact with the vapour region is always lower than 323 K, regardless of the tank filling degree. As explained in Section 7.2.6, this value is taken as the maximum design temperature for static vacuum insulated austenitic steel vessels. A similar trend is predicted for the external wall temperatures that are about 120-250 °C higher than those of inner walls, reaching a maximum value of about 330 °C after two hours of fire exposure and at an angular coordinate close to 45°.

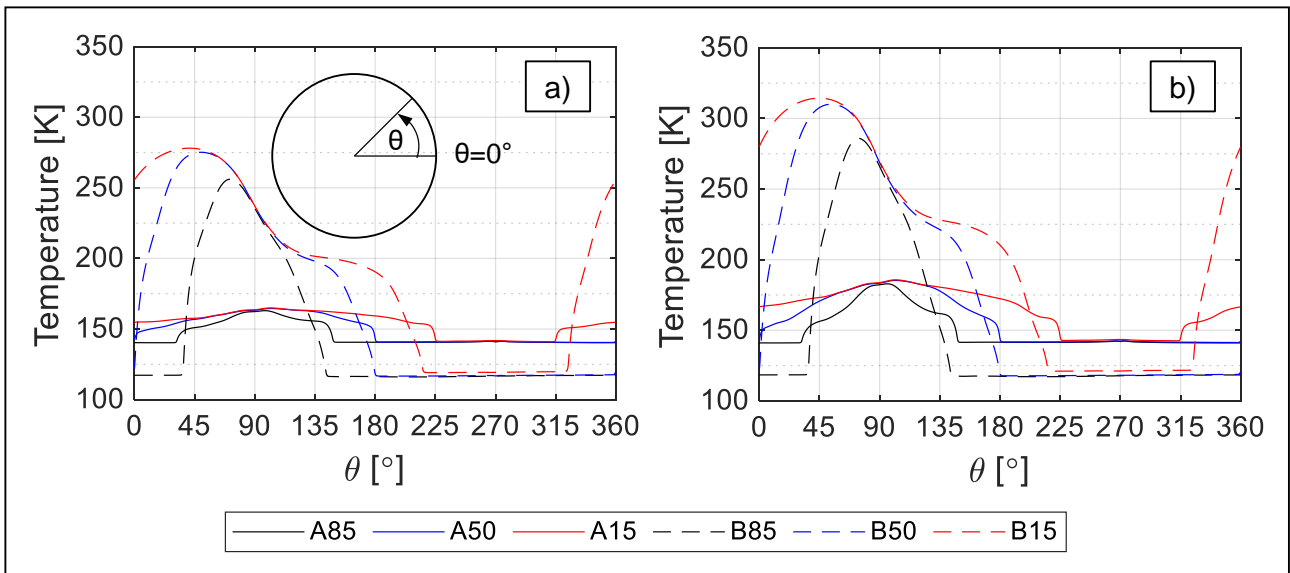


Figure 54: Inner wall temperature profiles at 90 min (a) and 120 min (b) as a function of the angular coordinate  $\theta$ .

Liquid temperature values for different simulation time steps of case study B are reported in Figure 55. The convective flows that develop following the exposure to distant pool fire promote the mixing of warmer liquid at the wall with the colder liquid bulk. Predicted liquid temperatures are measured on the central axis of the tank (shown in red in the figure). It is possible to notice that liquid stratification occurs for 50% and 85% filling degrees, for which the temperature differences between the bulk of the liquid and the vapor-liquid interface are in the order of 1 K, while for lower liquid level, the liquid tends eventually to de-stratify and approaches a uniform temperature value. A similar behaviour is predicted for case A with a maximum liquid temperature difference of about 0.5 K along the centreline axis.

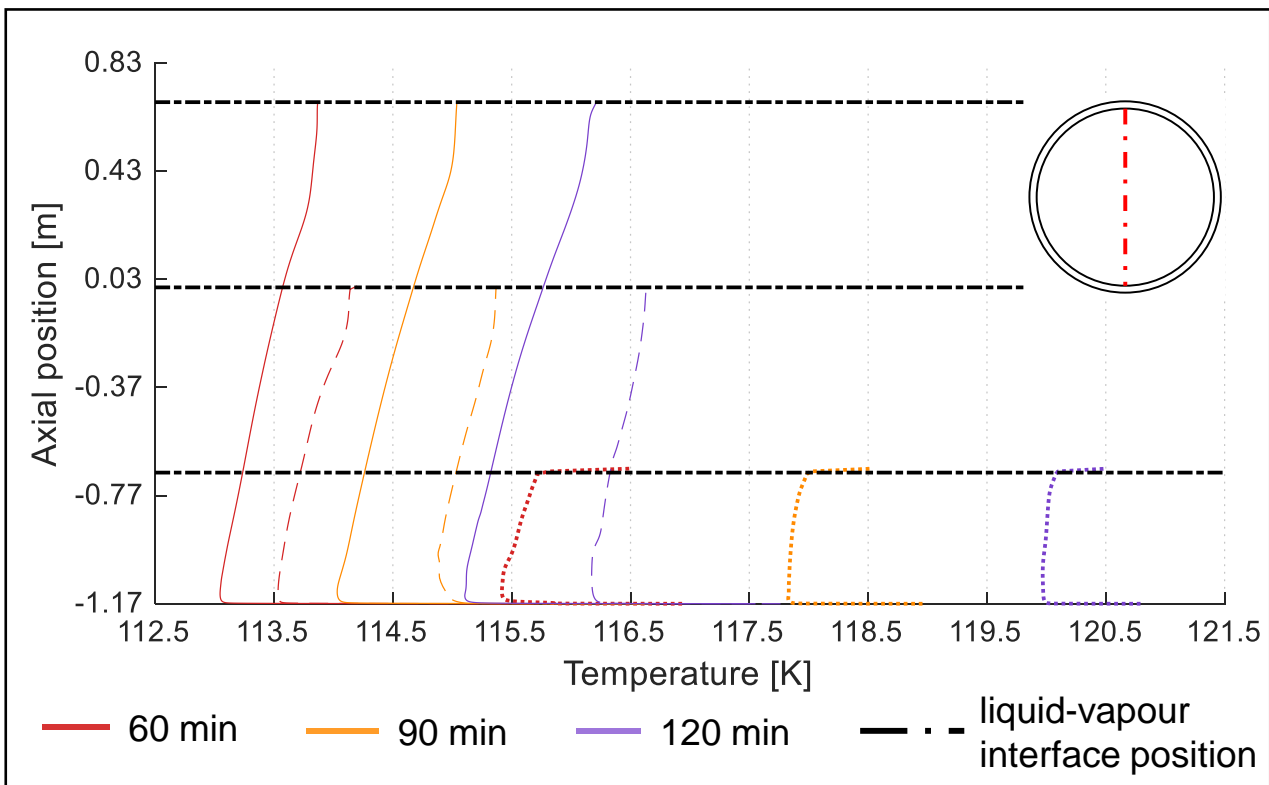


Figure 55: Liquid temperature variation with axial position at three different time steps. Solid lines: Case B85; dashed lines: Case B50; dotted lines: Case B15.

The further analysis of the CFD modelling results involved the calculation of the safety KPI defined in Section 7.2.6. When exposed to distant fire sources, under the conditions described in Section 7.4.1, the calculated value of the *IPI* safety KPI results always below the safety threshold as the tank internal pressure will not exceed the MAWP value under any circumstance. Similarly, the *TI* KPI will be always comprised within the safety margins since the tank internal wall temperature will not exceed 314 K in the worst situation (Case B15, after 2h of distant fire exposure). According to its definition, *TI* KPI for the condition considered in this analysis will be always equal to zero. A different situation is observed for the Energy Indicator, *EI* as shown in Figure 56. Calculated values for Case study A (see Figure 56a) give results higher than the safety threshold, thus all the points corresponding to different filling degrees fall in the intermediate safety region, as the resulting internal pressure level does not compromise tank structural integrity. Conversely, all the results of Case study B lie in the safe region (see Figure 56b) thanks to the combination of low *EI* and *IPI* indicators. Comparing these results with those addressing a full engulfment scenario, reported in Figure 51b, it is possible to notice that the same trend for *EI* values is maintained, with Case B showing lower values than correspondent Case A. Unlike what observed for the full engulfment condition, for which *EI* value results were higher than the safety threshold for the most part of considered time step and filling degree combinations, when assuming a distant radiation scenario all *EI* values for Case B fall below the safety threshold. This could be linked to the effect of relative position between the fire source and receiving tank, which considerably lowers the amount of energy received by Case B tank, as confirmed by the modest values of the pressure KPI. Furthermore, the lower amount of LNG stored in the smaller Case B tank contributes to maintain *EI* in the safe region.

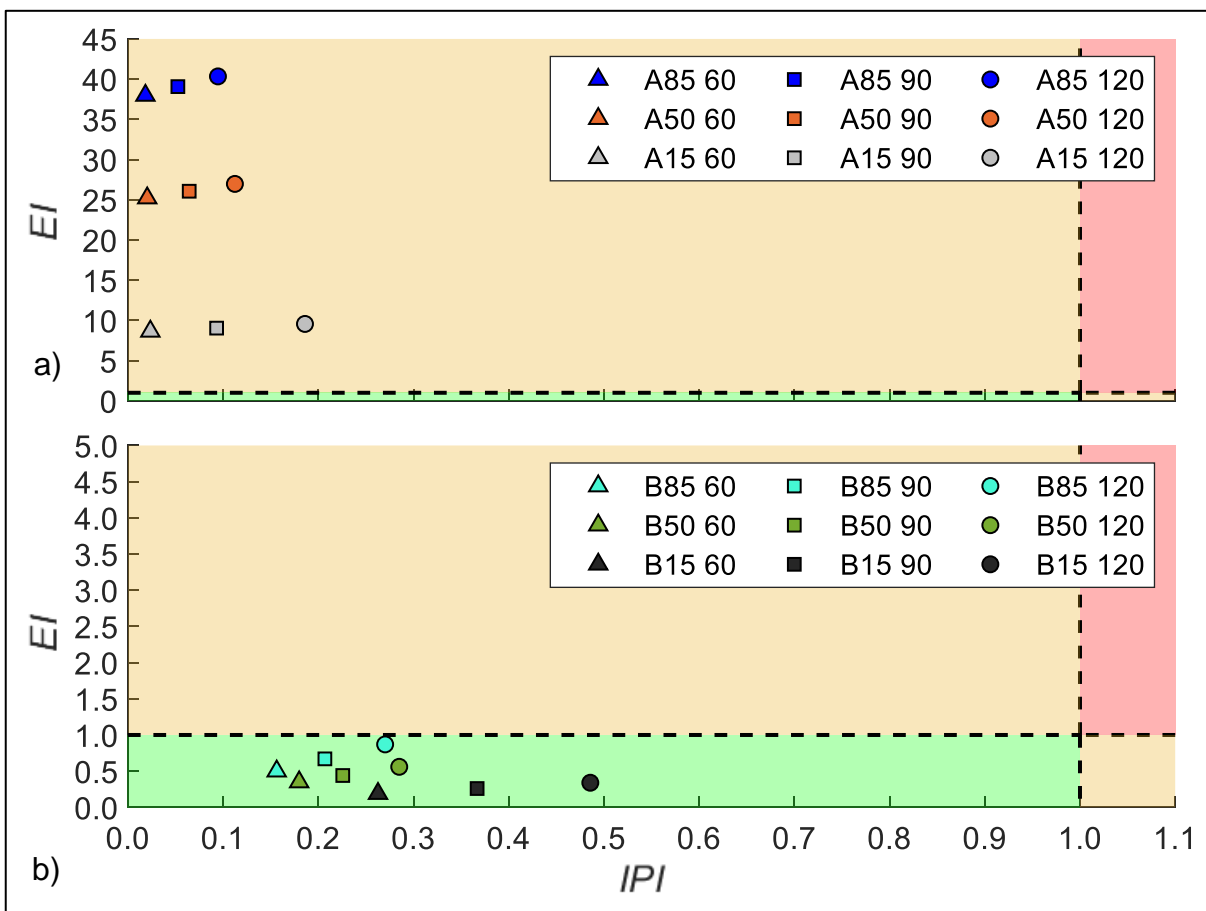


Figure 56: *EI* (Energy index) versus *IPI* (Internal Pressure index) safety KPIs for cryogenic pressure tanks exposed to a distant pool fire: a) Case A (Open-deck ship-fuel tank); b) Case B (Road Tanker).

## 7.5. Conclusions

The two-dimensional CFD model described in this Chapter laid the basis for a more accurate investigation of the thermal response of LNG tanks engulfed in fires. The developed model was exploited to simulate the response of double-walled cryogenic storage tanks of industrial interest under different fire attack conditions. The proposed case studies were aimed at investigating the behaviour of vacuum insulated horizontal bullet tanks with granular perlite filling in the annular gap. The predicted pressurization rate showed very good agreement with pressure data collected during experimental bonfire test and allowed validation of the developed CFD model, supported also by satisfactory temperature predictions of liquid and vapour phases.

Some uncertainty is related to the dearth of reliable experimental temperature measurements and to the lack of a detailed characterization of vacuumed perlite insulation operating in such extreme conditions. To cope with this latter aspect, a dedicated analysis was carried out to quantify the effect of relevant parameters on the thermal conductivity of the insulation. This allowed determination of the predominant heat transfer mechanisms inside granular perlite under vacuum conditions, supporting the detailed definition of boundary conditions for the 2D CFD simulations. Further experimental testing campaigns will be fundamental for the further development and validation of the CFD model, providing additional valuable data needed for an accurate description of boundary conditions experienced during a full engulfing fire and a sound validation of temperature predictions.

The results obtained in the present study provided insights into the pressurization rate, temperature, and velocity fields development, along with the spatial distribution of evaporation regions, advancing the simulation capabilities offered by lumped parameter models. In accordance with thermodynamics and with earlier experimental data, the predicted tank pressurization rate was found to be higher for tanks with lower filling degrees. However, a prolonged fire exposure is required to reach critical values of pressure-build up in the vessels. From the comparison of simulation results of the different case studies, the influence of thermodynamic and geometrical features over the spatial distribution of evaporating zones and velocity fields inside cryogenic tanks results is clear.

CFD predictions represent a fundamental input for the definition of a set of safety KPIs. The indicators were specifically designed to provide a tool for a holistic assessment of tank safety in case of fire exposure, encompassing different aspects such as loss of integrity and potential for domino effects resulting in accident escalation. The estimated KPI values highlighted the relationship between hazards originating from pressure-build up and thermal weakening of the tank structure. Moreover, despite the greater escalation potential of storage tanks with higher filling degrees, critical safety conditions are reached more rapidly for tanks with a lower liquid level. Tank safety KPIs may provide a useful support for future safety studies allowing for the identification of critical trends and unsafe conditions during fire exposure of LNG tanks.

Finally, some limitations of the proposed modelling approach must be remarked upon, apart from the uncertainties linked to insulation performance during fire incidents. A main restriction of the model lies in its bi-dimensional setup, which precludes the simulations of fire scenarios having variable characteristics along the longitudinal direction of the tank. As a consequence, the axial component of the flow field cannot be modelled, and the effect of tank ends over the development of flow and temperature fields inside the vessel must be neglected. Lastly, the 2D approach does not allow to simulate the fluid behaviour following the opening of the PRV, since this event is governed by three-dimensional effects. For these reasons, further research work is needed for the development of CFD modelling of cryogenic tanks exposed to fire scenarios, encompassing experimental test campaigns as well as progressing on numerical simulations. A future development of the described CFD approach would be to progress towards the setup of a more complete three-dimensional model as done by Scarponi et al., (2019) for LPG tanks.

## Chapter 8. Safety of fuel preparation room on-board LNG fuelled ships

Regardless of the gas engine technology used on board a ship, lay-out and space limitations may force to locate the fuel gas supply system process equipment inside a specific enclosed space: the fuel preparation room (FPR), usually sited below deck. Such an arrangement represents an inherently unsafe design solution that needs to be compensated by adequate safety measures and systems, especially on passenger ships, for which safety aspects are of utmost importance. A consequence assessment study for the credible accident scenarios of interest is presented in this Chapter. A case-study was considered, to provide a geometrical reference to the problem. Two different LNG pool fire scenarios, originating from onboard process equipment are analysed. The dynamic characteristics of the considered LNG pool fires are reproduced using a CFD software, exploiting the capabilities of such tools for the accurate estimation of dangerous scenario consequences. NIST's Fire Dynamics Simulator (FDS) was selected as the CFD solver for the present analysis since it has been extensively validated for large hydrocarbons pool fires and cryogenic fuel combustion applications (McGrattan et al., 2015a). The modelling results obtained, such as the radiation heat flux and the rate of heat generated, are presented. This data provides valuable information to assess the possibility of accident propagation inside an onboard enclosed space and may also support the evaluation of FPR structural resistance in case of fire.

Enclosure fires represent a scenario of interest for the nuclear industry and civil engineering field. Theoretical basis necessary for the understanding of enclosure fires phenomena can be found in the works by Quintiere, (2006, 1989) and in the Handbook of Fire Protection Engineering (Hurley et al., 2016). A consistent number of experimental studies were carried out to understand the peculiar characteristics of such events and the expected consequences. A summary of the principal enclosure fire tests is found in the report issued by the US Nuclear Regulatory Commission (Stroup et al., 2016), that presents key results of the experimental studies as well. A general summary of experimental fire tests in confined and ventilated multi-compartments is presented by Audouin et al., (2013). Several numerical and experimental studies are focused on the consequence modelling of large LNG spills occurring in an open environment, either on land or water, while others estimated the consequence of smaller LNG pool fires (Pio et al., 2019). A review of recent applications of CFD for enclosure fire modelling is presented by Shen et al., (2020). However, the reviewed literature lacks a study aimed at evaluating the consequences of small-scale LNG pool fires occurring inside confined spaces. The present study is thus a first attempt to fill this gap, providing a preliminary consequence assessment of enclosure LNG pool fires occurring in a ventilated compartment.

## 8.1. Description of the case study

To determine the safety level of an LNG FPR, a typical roll on/roll off (RORO) ferry ship was selected as a case study. As highlighted in Section 2.2, this ship type is currently the most common LNG-fuelled vessel and in case of accidents affecting the FGSS it can also potentially expose a higher number of people to harmful situations than cargo or other ship classes. General specifications of the ship are summarised in Table 28.

Table 28: General specifications of the case ship

Item	Value	Unit
Deadweight tonnage	1,273	t
Breadth	25	m
Length	102	m
Passenger number	1,000	-
Car capacity	135	-
Power	6 (2×3,000 kW)	MW
LNG capacity	140	m <sup>3</sup>
Approximate total gas fuel consumption	2,900	kg/h

The ship features a type C LNG storage tank that feeds the fuel system installed on board. Such types of RORO ferry can be fuelled by either LPDF or HPDF systems, therefore a comparison between these types of FGS systems is presented in this analysis. Two dual fuel main engines provide the necessary power. The FPR of the reference case ship is 23 m long, 5.1 m high and 5.5 m wide. Side walls of the FPR were assumed to be protected from fire by class A-60 material, following the requirements set by the IGF code.

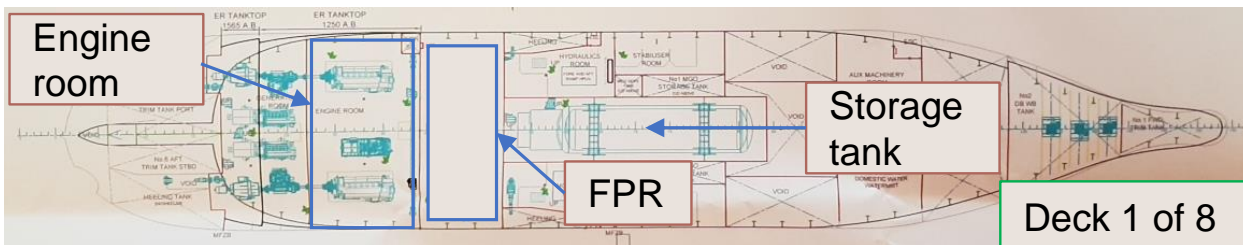


Figure 57: Example of general arrangement of LNG fuel system

Such spaces can alternatively be designed either as “gas safe”, for which any failure within the fuel system cannot lead to release of fuel gas, or as “ESD-protected”. In this latter case a single failure may result in a gas release into the space and subsequent activation of the ESD system. As required by the IMO IGF code, the fuel is supplied from the FPR to the engine room through double wall pipes. For such reasons, the present analysis was focused only on accidents occurring inside an ESD-protected FPR, for which double-walled pipes are not mandatory and, as a consequence, release events cannot be excluded. Among the minimum safety systems required by the IGF code for ESD-protected spaces, all confined spaces must be fitted with mechanical ventilation systems providing at least 30 air changes per hour. As stated in Section 13.6 of the IGF code, FPR ventilation systems shall be operative when pumps or compressors are working and can be therefore assumed as constantly in operation as long as ship’s engines are running.

The capacity of the FGSS was estimated based on the fuel gas consumption reported in Table 28. Process units featured by the high-pressure (HP) and low-pressure (LP) systems are illustrated in Figure 5a and Figure 5b, respectively. The FPR also accommodates the BOG heaters and BOG compressors that provide gas feed to the combustion systems at the necessary temperature and pressure values. The principal characteristics of the gas fuel systems considered in this study are summarised in Table 29.

Table 29: Main specifications and operating conditions of the FGSS.

Process unit	Parameter			
	Vol. Flowrate [m <sup>3</sup> /s]	Pressure [bar]	Temperature [K]	Phase
<b>HP FGSS</b>				
HP Fuel gas pump	7.19	300	146	Liquid
HP LNG Vaporizer	15.06	300	318	Vapour
Gas Heater	579.65	7	273	Vapour
BOG Compressor	590.88	7	278	Vapour
<b>LP FGSS</b>				
LNG Vaporizer	7.49	7	133	Liquid
HP Fuel gas heater	624.41	7	293	Vapour
Gas Heater	1,365.81	3	273	Vapour
BOG Compressor	590.88	7	278	Vapour

## 8.2. Detailed modelling of on-board LNG pool fires

The first steps of the approach followed to evaluate the safety level of FPR were identical to those illustrated in Chapter 6 for the quantitative risk assessment of bunkering operations. Firstly, the main process data was collected, providing the basis for the loss of containment (LOC) categorization, which was carried out considering the possible release events reported in Table 6.

Since the objective of the analysis is limited to the consequence evaluation of LNG pool fires, the LOC categorization was focused on liquid releases only. Therefore, this kind of release event was only applicable to the HP Fuel gas pump of the HPDF system and to the inlet section of the LNG Vaporizer featured in the LP FGSS. More specifically, LOC types R4 and R5 were considered for the mentioned process units. Release events were assumed to remain undetected for at least 90 s, as this was considered as the required timeframe for ESD system intervention, in accordance with assumptions reported in Section 6.2.3. The estimated release rates and total spilt mass for the considered LOC events, modelled as continuous releases using Eq. 6.22 are reported in Table 30.

Table 30: Release rate and total released mass for assessed LOC events

Process unit	LOC Type	Release rate [kg/s]	Released mass [kg]
<b>HP FGSS</b>			
HP Fuel gas pump	R4	1.215*	109.35
	R5	1.215*	109.35
<b>LP FGSS</b>			
LNG Vaporizer	R4	1.018	91.62
	R5	1.215*	109.35

\* Assumed as 150% of ordinary mass flowrate.

In the absence of more detailed specifications, release rates from the HP pump and full-bore rupture of the vaporizer inlet were limited to up 150% of the ordinary mass flow rate to approximately account for the loss of pressure head in the line and the consequent shift of the pump operating point as suggested by Uijt de Haag and Ale (2005).

### 8.2.1. Pool characteristics

When considering liquid releases, it is fundamental to estimate the pool evaporation rate which will be needed as a source term for the pool fire modelling. The dimension of the LNG pool and thus those of the fire depend both on the liquid spread and on the simultaneous vaporisation due to different heat sources, e.g., such as the heat received from the surface on which the pool is formed, and heat exchange due convection with air. Liquid pool thickness and radius can be calculated combining heat and mass balances. For continuous liquid releases, the pool will eventually reach a specific depth, for which surface evaporation balances the discharge flowrate. The pool will spread until the liquid release stops. Several pool evaporation models are available in the literature, accounting for different situations. A brief description of the model developed by Briscoe and Shaw (1980), which was used for the present analysis, is given in the following.

Following the spillage of LNG onto soil or water surfaces, a liquid pool will be formed and subsequently will spread until a balance among the release rate and vaporisation rate is reached. In general, vaporization from a pool is a mass and heat transfer limited process. Several heat transfer modes are involved in pool vaporisation, such as heat transfer by convection between the liquid surface and the atmosphere, and by radiation. However, for cryogenic spills, it is the heat conduction between the liquid and the ground that controls the rate of vaporisation (Mannan, 2012c). The dimension of the pool is determined by the spreading of the liquid and the concurrent vaporization due to the above-mentioned heat sources, as shown in Figure 58.

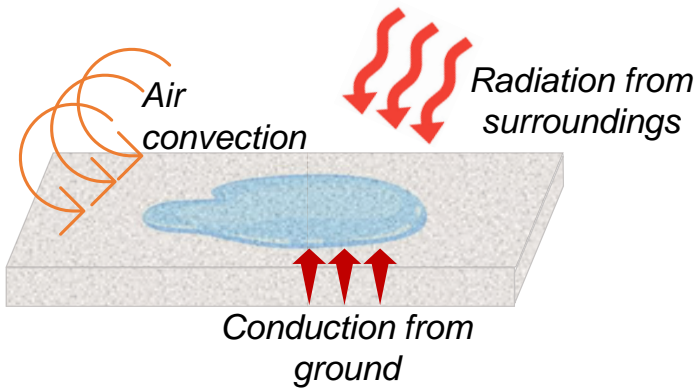


Figure 58: Illustration of heat contributions to pool evaporation.

Important aspects for the estimation of pool vaporisation are the liquid temperature of the pool, the heat received from the surroundings, and the heat removed from the liquid itself to provide the heat of vaporisation. Considering cryogenic pools, following a short period of very rapid vaporization, a relatively steady lower rate of vaporization is observed, as reported by Mannan, (2012b). For an unconfined release of LNG spilt over ground, the vaporisation rate ( $\dot{m}_{ev}$ ) can be estimated on the basis of the heat transferred to the pool. The following relationship, proposed by Briscoe and Shaw, (1980) was used:

$$\dot{m}_{ev} = 2\pi\theta \int_0^{r_2} \frac{r_1}{(t_2 - t_1)^{1/2}} dr \quad \text{Eq. 8.1}$$

where  $r_1$  is the pool radius at time  $t_1$ ,  $r_2$  is the radius at time  $t_2 > t_1$  and  $\theta$  is a parameter expressed as follows:

$$\theta = \frac{\chi_g k_g (T_g - T_{pool})}{\Delta H_{vap} \sqrt{\pi \alpha_g}} \quad \text{Eq. 8.2}$$

The term  $\chi_g$  accounts for the surface roughness, while  $\alpha_g$  is the ground thermal diffusivity.  $T_g$  and  $T_{pool}$  represent the ground and pool temperatures respectively, whereas  $k_g$  is the thermal conductivity value of the ground and  $\Delta H_{vap}$  is the latent heat of vaporization.

As reported by Pio et al., (2019), the heat release rate (*HRR*) generated by LNG pool fires can be approximated using the Hottel's correlation (Babrauskas, 1983), expressed by Eq. 8.3, which requires the knowledge of some characteristics pool quantities.

$$m'' = \frac{HRR}{\Delta H_c \cdot S_p} = m''_{\infty} \cdot (1 - e^{-k\beta D}) \quad \text{Eq. 8.3}$$

Here the term  $m''_{\infty}$  indicates the mass burning rate ( $m''$ ) obtained for a pool having an “infinite” diameter. Term  $D$  is the pool diameter,  $S_p$  represents the pool surface and  $\Delta H_c$  the heat of combustion, while terms  $k$  and  $\beta$  are the absorption-extinction and the beam length correction coefficients, respectively. As reported by Zhang et al., (2018), these two parameters are frequently aggregated for small and medium scale LNG pool fires. The majority of the reported values for  $k\beta$  range between 0.14 and 0.46  $\text{m}^{-1}$ . Concerning the values of  $m''$ , there is a certain variability among the experimental values since the mass burning rate depends on geometrical features of the pool and on the weather conditions (Zhang et al., 2018).

The amount of LNG evaporating from the pool, i.e., the evaporation rate  $\dot{m}_{ev}$ , is another crucial parameter to assess the effects of pool fires. For this study, the evaporation rate estimated with Eq. 8.1 was assumed equal to the burning rate, as suggested by Wahlqvist and van Hees, (2016). This allowed for the preliminary estimation of the quantities,  $\dot{Q}$ , the peak heat release rate of the fire, and the non-dimensional ratio  $D^*/\delta_x$  that provides guidance for the determination of mesh resolution. The quantity  $D^*$  is a characteristic fire diameter calculated according to the following criterion defined by Ma and Quintiere, (2003):

$$D^* = \left( \frac{\dot{Q}}{\rho_{\infty} \cdot C_p \cdot T_{\infty} \cdot \sqrt{g}} \right)^{\frac{2}{5}} \quad \text{Eq. 8.4}$$

Where  $\delta_x$  is the nominal size of a mesh cell;  $g$  is the gravity constant and  $\rho_{\infty}$ ,  $C_p$  and  $T_{\infty}$  indicates air density, specific heat, and temperature at infinite distance from the fire.

When a fire occurs inside an enclosure, the expansion of gases within the confined volume due to heat addition pressurizes the enclosure. Only a part of the heat released by the fire contributes to pressurization: in fact, a fraction is lost by heat transfer to the boundaries or to other surfaces within the enclosure. As a fire in a closed compartment diminishes due to oxygen depletion, the rate of heat losses to enclosure boundaries will become greater than the rate of heat addition due to the fire. This will cool down the smoke, causing the depressurization of the enclosure.

An energy balance for the enclosure control volume illustrated in Figure 59 can be written as:

$$\frac{dU}{dt} = \dot{Q}_{net} + \dot{m}_i \hat{H}_i + \dot{m}_o \hat{H}_o - p \frac{dV}{dt} \quad \text{Eq. 8.5}$$

where  $U$  is the total internal energy in the control volume and  $\dot{Q}_{net}$  is the net rate of heat addition into the space, equal to the difference between the actual *HRR* of the fire and the rate of heat losses.

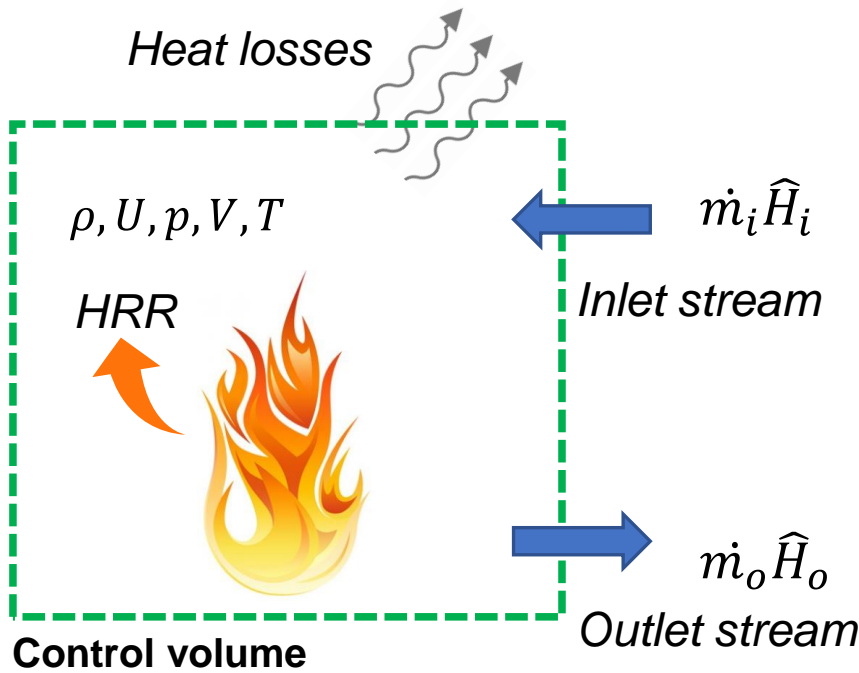


Figure 59: Control volume and streams considered for enclosure fire energy balance

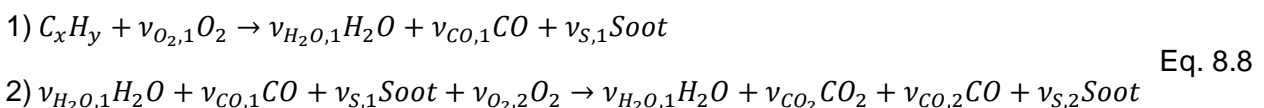
For a perfectly sealed compartment, the inlet and outlet mass flowrates ( $\dot{m}_i$  and  $\dot{m}_o$ ) will be equal to zero and the volume will remain constant. Assuming ideal gas behaviour, Eq. 8.5 can be rewritten as:

$$\frac{C_v}{R} V \frac{dp}{dt} = \dot{Q}_{net} + \dot{m}_i \hat{H}_i + \dot{m}_e \hat{H}_e \quad \text{Eq. 8.6}$$

Integrating between initial conditions (marked by subscript 0) and time  $t$ , a simplified expression for the estimation of enclosure pressurization can be obtained:

$$\frac{\Delta p}{p_0} = \frac{\int_0^t \dot{Q}_{net} dt}{\rho_0 C_v V T_0} \quad \text{Eq. 8.7}$$

Methane combustion reaction was modelled using a two-step Simple Chemistry kinetic model as suggested by Lock et al. (2008), who conducted experimental studies of under-ventilated compartment fires. The two-step scheme basically converts all of the carbon in the fuel molecule to  $CO$  and Soot in the first step, and then oxidizes most of the  $CO$  and Soot to form  $CO_2$  in the second step. The fuel hydrogen atoms can either form  $H_2$  or  $H_2O$  in the first step as well.



The post-flame yields of  $CO$ ,  $H_2$  and Soot were all set equal to the default value of zero for the present analysis, in the absence of more detailed data. However, it should be remarked that the two-step model acknowledges the fact that  $CO$  and Soot are present at much higher concentrations within the flame envelope than their post-flame yields would suggest (McGrattan et al., 2019).

In order to consider the fire suppression due to oxygen depletion inside the FPR, the FDS Flame Extinction model was used. Between the two options available, the simpler “Extinction 1” model was chosen. It determines whether combustion occurs at computational cell level on the basis of a Critical Flame Temperature (*CFT*), which is a parameter taking into account the calculation cell oxygen concentration as expressed by the following equation:

$$CFT = T_0 + y_{o_2,lim} \frac{\widetilde{\Delta H}_{c,o_2}}{n\overline{C}_p} \quad \text{Eq. 8.9}$$

where  $T_0$  is the initial temperature of the fuel/air mixture,  $y_{o_2,lim}$  is the limiting oxygen volume fraction which values can be found in the FDS user’s guide (McGrattan et al., 2019),  $\widetilde{\Delta H}_{c,o_2}$  indicates the heat of combustion per mole of oxygen consumed,  $n$  is the number of moles of combustion products per mole of fuel/air mixture, and  $\overline{C}_p$  is the average heat capacity of combustion products in the temperature range  $T_0$  to  $CFT$ .

The extinction model prevents the solver to model combustion inside cells with an oxygen concentration below a lower limiting value. Further details of the model and definition of *CFT* can be found in the FDS Technical Reference Guide (McGrattan et al., 2015b) and in the chapter by Beyler, (2016) of the SFPE Handbook of Fire Protection Engineering.

### 8.2.2. Definition of simulation cases and numerical setup

Following the release categorization, two different pool fire scenarios were modelled using FDS: a larger pool resulting from LOC events with higher release rate affecting the HP pump, and a slightly smaller pool formed ensuing the R4 LOC event affecting the vaporiser inlet. Furthermore, the influence on pool fire development of fresh air inlet brought by the ventilation system inside the FPR was modelled, leading to the definition of four different simulation cases as summarised in Table 31. The effect of inlet air was assessed comparing the results of a case with shut air inlets and the sole exhaust vents operative (cases HP-1 and LP-1) against the results obtained assuming a normal-operating ventilation system (i.e., with both inlet and outlet streams).

Table 31: Main characteristics of the cases analysed and location of pool and vents inside the FPR

Case ID	Pool diameter [m]	Ventilation	Cell number
HP - 1	2.36	No (exhaust only)	322,575
HP - 2		Yes (in/out)	
LP - 1	2.12	No (exhaust only)	
LP - 2		Yes (in/out)	

Turbulence characteristics were reproduced using the large eddy simulation (LES) model, which is a popular technique in CFD studies for fire related flows since it allows to resolve the large-scale flow unsteadiness and buoyancy effects that play an important role in fire modelling (Merci, 2016). The LES model is more accurate than the RANS approach since the large eddies contain most of the turbulent energy and are responsible for most of the momentum transfer and turbulent mixing, and LES captures these eddies in full detail directly whereas they are modelled in the RANS approach (Zhiyin, 2015).

Since FDS is a LES-based model, uniform meshing is preferred (McGrattan et al., 2015b), thus the computational domain was subdivided into uniform cells having a size  $\delta_x$ , chosen accordingly to the value of the  $D^*/\delta_x$  ratio. As suggested by the U.S. Nuclear Regulatory Commission (2016) in their report on the verification and validation of selected fire models, the cell size was defined in order to have a  $D^*/\delta_x$  ratio comprised in a range from 16 to 40. All simulations were run using a variable time step, initially set at 0.01 s which size was limited by a stability constraint on the Courant-Friedrichs-Lewy number (see McGrattan et al. (2015b) for additional details). Initial temperature and pressure inside the FPR were set at 15°C and 1 atm respectively, considering normal operating onboard conditions. The maximum duration considered for simulation cases HP-1 and LP-1 was set to 90 s to avoid numerical stability problems related to significant pressure decrease due to the lack of air ingress in the enclosure. On the other hand, additional 10 minutes of simulation (equal to 5 air changes) prior to fire ignition were considered for cases HP-2 and LP-2 to ensure reasonable steady state conditions for the air velocity field. To reproduce generic conditions inside the FPR, five exhaust vents with a surface of 1 m<sup>2</sup> each were assumed to be located on the longitudinal midsection of the FPR ceiling, equally distanced. Similarly, two 1 m<sup>2</sup> ventilation supply vents were placed at the transversal midsection of the FPR, at 1 m height. Supply and exhaust vent boundary conditions were defined specifying volumetric flowrates that reproduce the required 30 air changes per hour (i.e., 3,760 m<sup>3</sup>/h and 9,400 m<sup>3</sup>/h for each exhaust and supply vents, respectively). The exact location of FPR features and pool fire are reported in Table 32, whereas a schematic overview of the computational domain is shown in Figure 60.

*Table 32: Coordinates of pool fire centre and mechanical ventilation items for the modelled FPR. Refer to Figure 60 for additional reference.*

Item	Domain coordinates [m]		
	<i>x-axis</i>	<i>y-axis</i>	<i>z-axis</i>
Pool Centre	2.725	3.000	0.000
Exhaust vent #1	2.725	2.875	5.100
Exhaust vent #2	2.725	7.188	5.100
Exhaust vent #3	2.725	11.500	5.100
Exhaust vent #4	2.725	15.813	5.100
Exhaust vent #5	2.725	20.125	5.100
Supply vent #1	0.000	11.500	1.000
Supply vent #2	5.500	11.500	1.000

In accordance with the assessment carried out in the previous Chapters, LNG was modelled as pure methane. A more detailed analysis of the effects of different LNG compositions over thermal characteristics of small-scale pool fires can be found elsewhere (Pio et al., 2019).

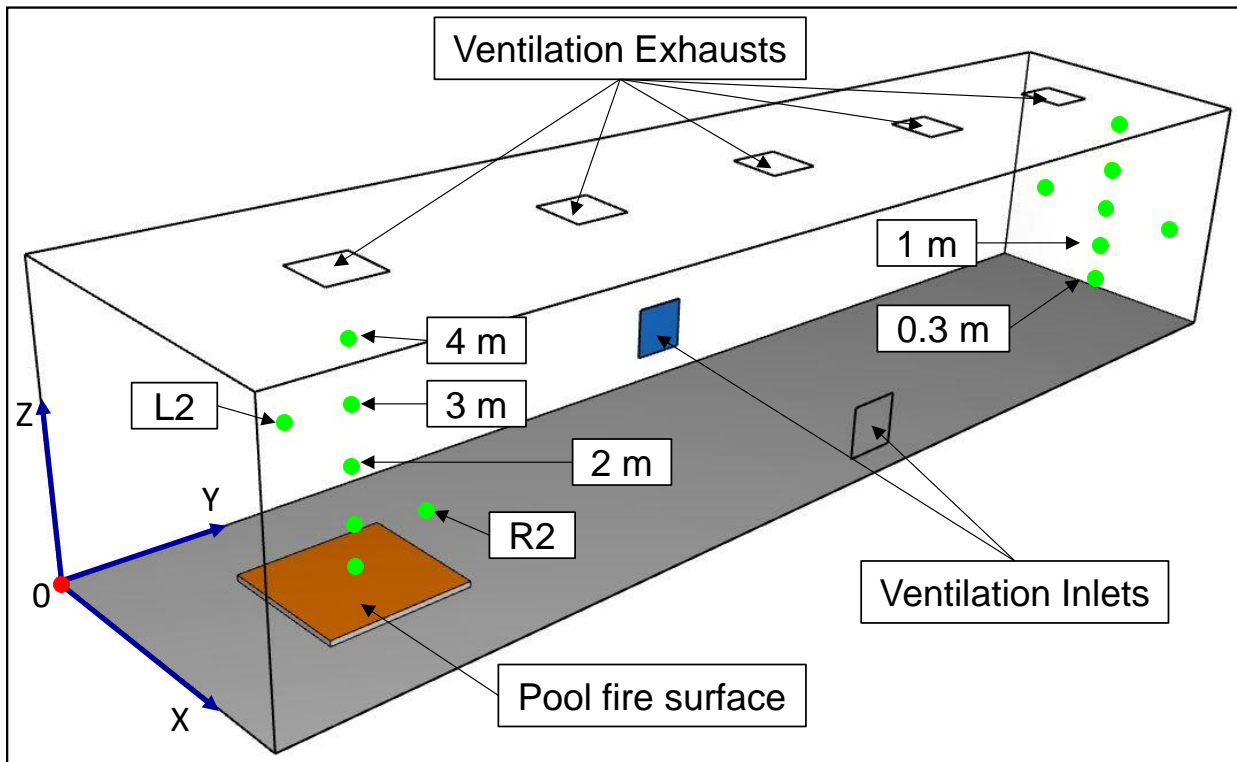


Figure 60: Schematic view of the FPR modelled in FDS. Green dots represent the location of heat flux measuring points. Only two arrays of measuring points are illustrated for ease of comprehension. The pool fire surface, even if displayed as a square, was modelled using a circular vent.

Since the determination of a pool spread rate could be influenced by numerous factors for the specific cases under analysis, such as the ship movements, a simplified approach was followed to reproduce the spreading of the LNG pools in the simulations. The pool fires were defined using a circular vent surface having the same area as the maximum pool area estimated by the previously described pool evaporation model. To replicate the time variation of the pool evaporation rates, a prescribed time ramp of  $\dot{m}_{ev}$  values was used, based on the rates estimated with Eq. 8.10. The values used in the simulations, expressed per unit surface of the pool, are reported in Figure 61.

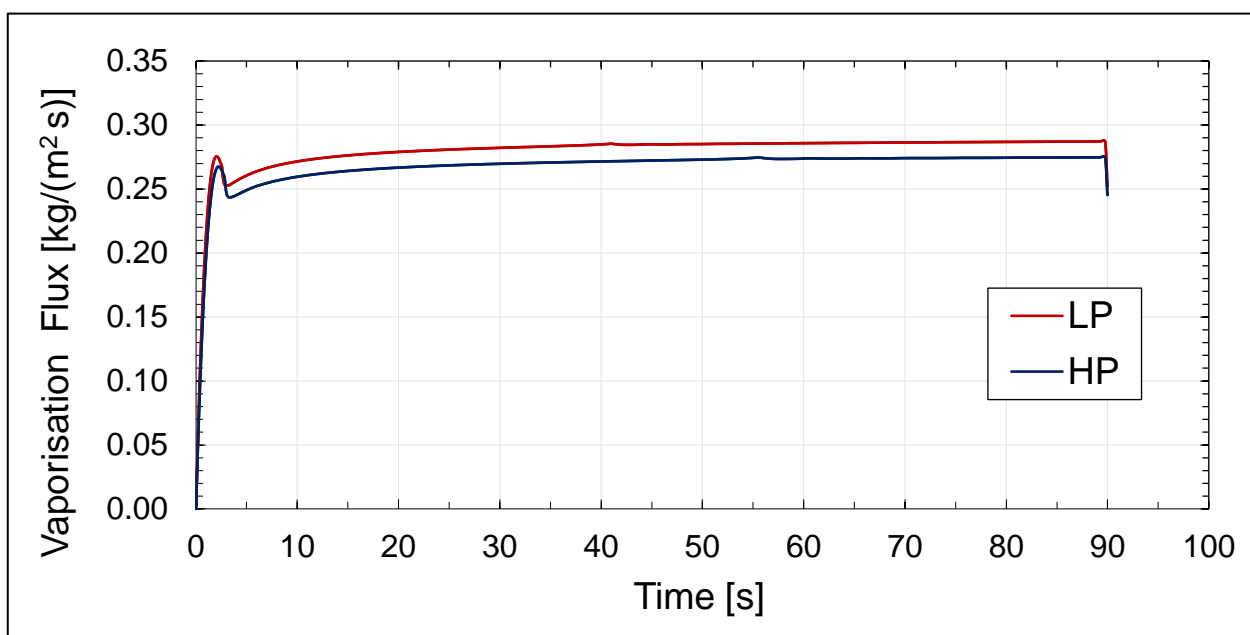


Figure 61: Time ramp considered for the pool vaporisation flux in the FDS model.

### 8.3. Modelling results

A preliminary evaluation of FDS results was performed reproducing a 1.0 m and a 2.12 m diameter LNG pool fire scenarios, comparing the results with a 3.0 m LNG pool fire investigated in the work by Pio et al. (2019). In particular, the spatial distribution of the radiative heat flux generated by pool fires having different diameters was compared, as illustrated in Figure 62. The L/D ratio represents a dimensionless distance from the pool centre: here D indicates the pool diameter and L is a distance value. The original study investigated pool fires occurring in an open field, therefore the 1.0 m diameter and the 2.12 m diameter fires were simulated as located on open ground for sake of comparison. As can be seen from Figure 62, larger pool diameters tend to shift the radiative heat flux curve towards the bottom left corner of the chart, in line with the results by Pio et al. (2019). Moreover, the open pool fire curve follows the same trend as the original curve from the cited work (green, dot-dashed in Figure 62). The same diameter pool fire was also modelled considering it as occurring inside the above described FPR (referred to as Compartment pool fire in Figure 62). In this case the radiative heat flux curve does not present any maximum and appears to be shifted towards lower heat flux values, possibly because of wall and ceiling confinement. However, a decreasing trend can still be observed in this case, and the obtained results can be deemed comparable to those obtained in open field simulations. It must be remarked that the discussed simulations were only intended to qualitatively compare modelling results with similar small-scale pool fire scenarios. As mentioned, several compartment fire experiments are reported in the literature. However, tested conditions were generally far different from those modelled in the present study.

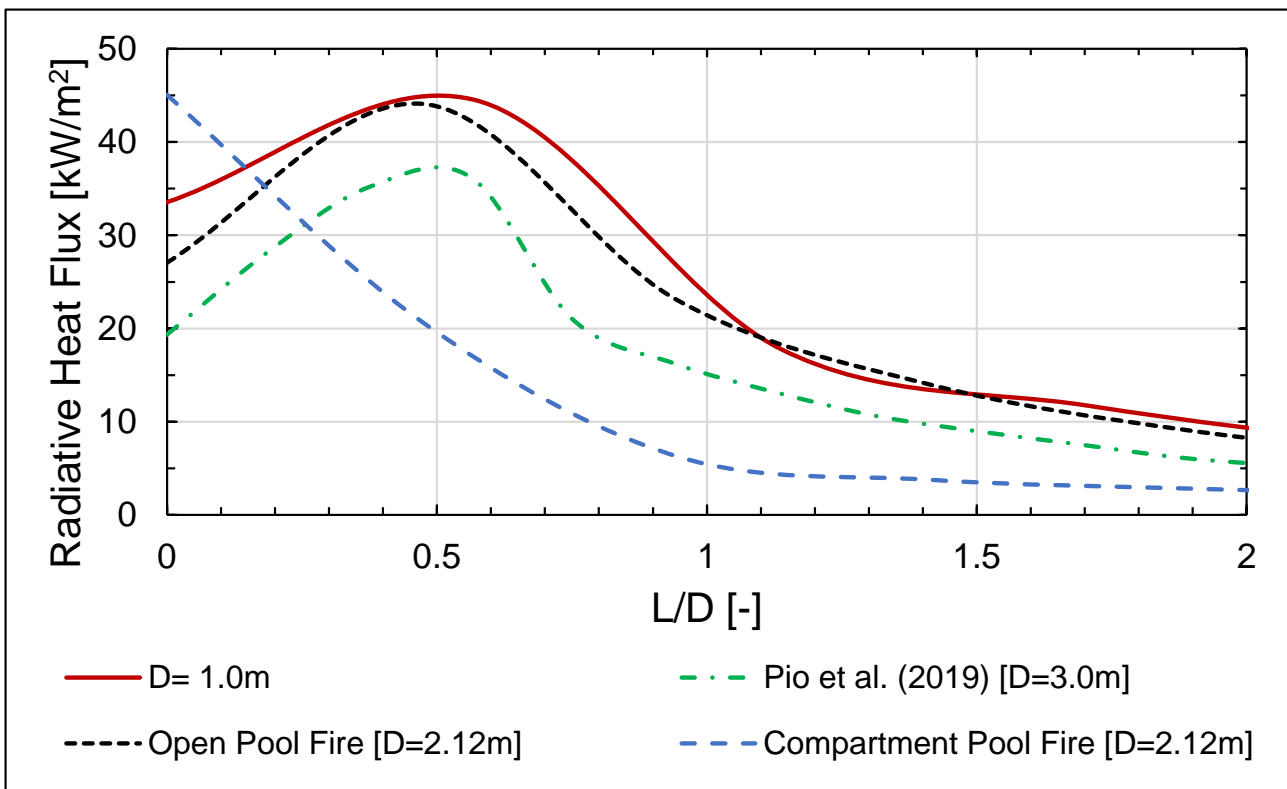


Figure 62: Variation of radiative heat flux with dimensionless distance from the pool center for different cases.

### 8.3.1. Grid independence

The independence of simulation results from the chosen calculation grid was evaluated comparing the modelled  $HRR$  for finer and coarser grids obtained from the base case calculation domain. As described in Section 8.2.2, the domain cell size was calculated on the basis of the  $D^*/\delta_x$  ratio. To determine this value, the maximum  $HRR$  was preliminary estimated using the  $\dot{m}_{ev}$  resulting from pool evaporation modelling, which maximum value was  $0.287 \text{ kg/m}^2\text{s}$ . Considering the methane specific heat of combustion which is approximately  $50,000 \text{ kJ/kg}$  as reported by Woodward and Pitblado (2010) a burning  $2.12 \text{ m}$  diameter pool of LNG has an ideal  $HRR$  of more than  $56,000 \text{ kW}$ . This resulted in a  $D^*$  value of  $4.8 \text{ m}$  that allowed to use cells having  $\delta_x = 0.15 \text{ m}$  for the base case (corresponding to  $\frac{D^*}{\delta_x} \sim 32$ ). Finer and coarser grids dimension is 33% smaller or larger than the base case, respectively.

Figure 63 shows the results obtained that evidence the grid independence of the FDS setup. As shown in the figure, the predicted  $HRR$  for the three cases follows an identical trend, except for some minor spikes, with average differences ranging between 1% and 4%. The agreement between results obtained using different calculation grids can be deemed satisfactory, therefore a uniform grid with  $\delta_x = 0.15 \text{ m}$  was used to model the cases listed in Table 31.

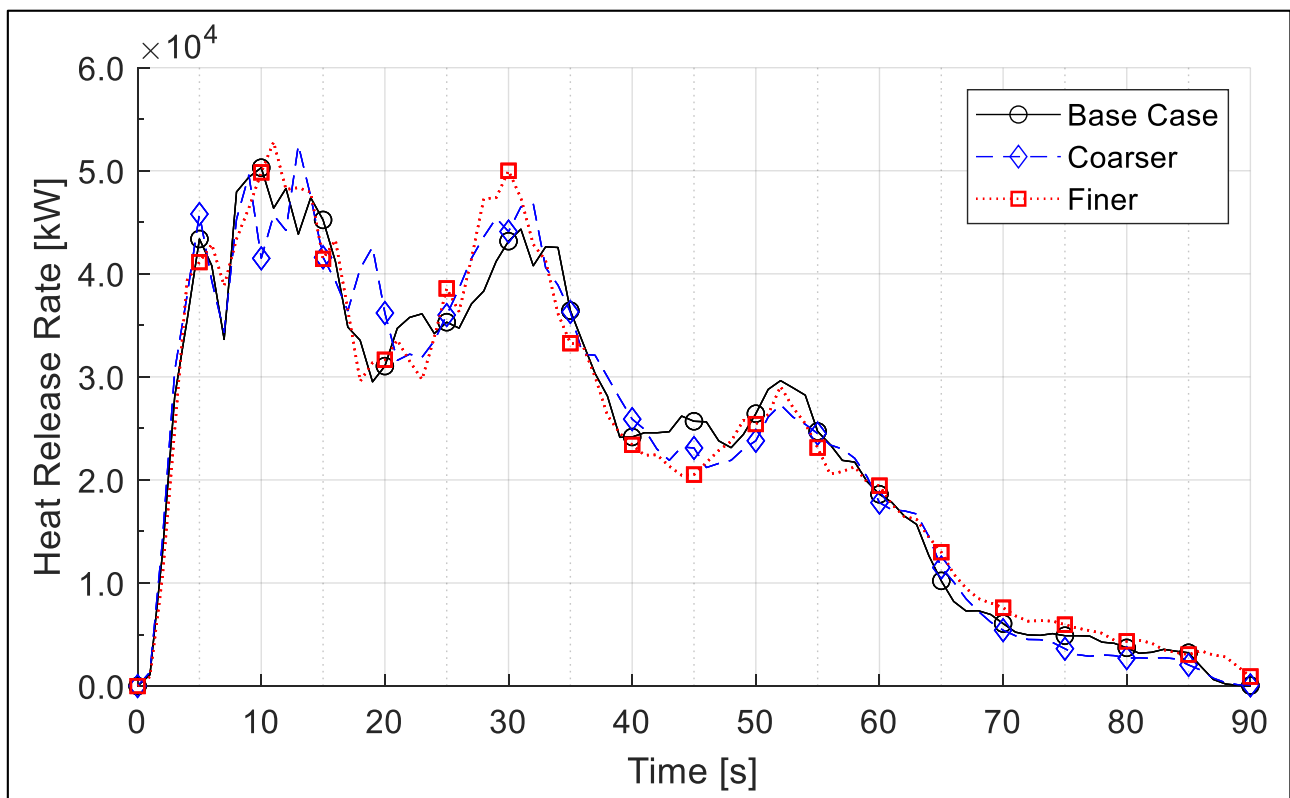


Figure 63: Comparison of the  $HRR$  estimated for different mesh cell sizes of case LP-1.

### 8.3.2. Pool fire consequences and gas species concentration inside FPR

Modelling results are reported here for cases LP-1 and LP-2 focusing on the influence of the ventilation system on fire effects. Results relative to cases HP-1 and HP-2 are reported in Appendix D.3.

Some clear differences can be noted observing the time evolution of gas concentration profiles of relevant species involved in the combustion reaction reported in Figure 64. Focusing on the oxygen concentration, it can be observed that in general this value decreases with time, as oxygen is consumed by the combustion reaction. This decreasing trend is similarly observed for both cases LP-1 (Exhaust only) and LP-2 (Ventilation On) for the first 30 seconds of combustion, then the oxygen rate of consumption decreases and stabilises for case LP-2, reaching an apparent steady state, while without fresh air inlet the concentration continues to drop until reaching values approaching zero after around 70 seconds from the fire ignition. This is an evident consequence of the combined effect of fire consumption and air extraction from the compartment and a key factor governing the evolution of the pool fire inside the FPR. As reflected by the methane concentration value, operational air inlets provide the necessary amount of oxygen for the combustion reaction thus keeping the methane concentration inside the room practically around zero. On the other hand, the limiting oxygen concentration eventually halts the combustion leading to the build-up of methane concentration, which enters in the flammability range around 70 second after fire start, creating a potentially explosive atmosphere, provided that oxygen re-enters the FPR before methane is completely vented out by the ventilation system.

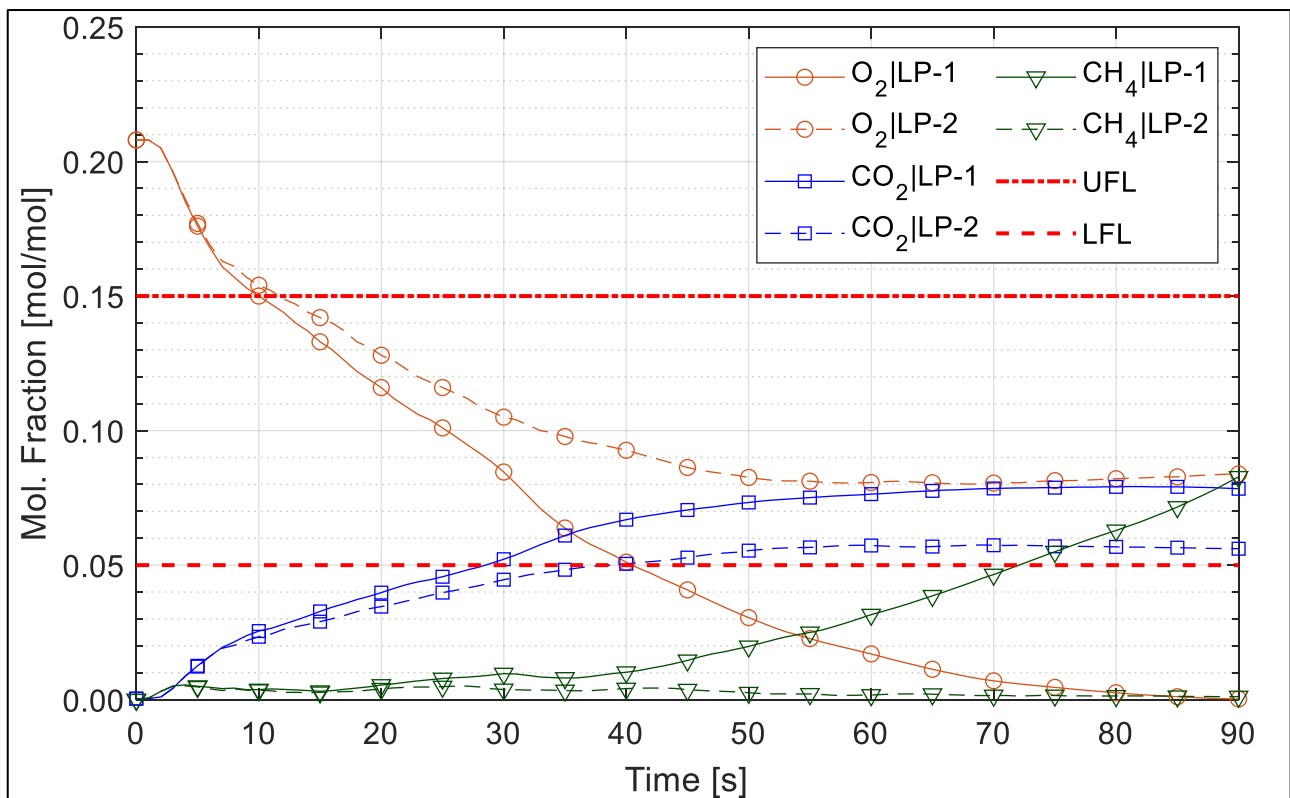


Figure 64: Comparison of the concentration profiles of different gas species involved in the combustion process for cases LP-1 and LP-2.

Lastly, the carbon dioxide concentration appears to be less affected by the working conditions of the ventilation system: the increasing trend reaches a stationary state in around 50 seconds for both cases. Carbon dioxide concentration results on average 20% lower when air is introduced in the FPR, compared to the LP-1 estimated concentration.

The decreasing trend showed by the *HRR* curve of case LP-1 reported in Figure 65 confirms that the oxygen concentration plays a determinant role in the evolution of an enclosure fire. For the case analysed, the pool fire starts to grow weaker when O<sub>2</sub> concentration drops below 6% vol. (around 35 seconds from fire ignition). As evident from the comparison with case LP-2, the oxygen depletion is the cause of fire self-extinction, which does not occur in presence of air inlets, even if a sensible reduction of the *HRR*, about 40% lower than the modelled peak value of 50,000 kW, can be observed during the simulation for this latter case.

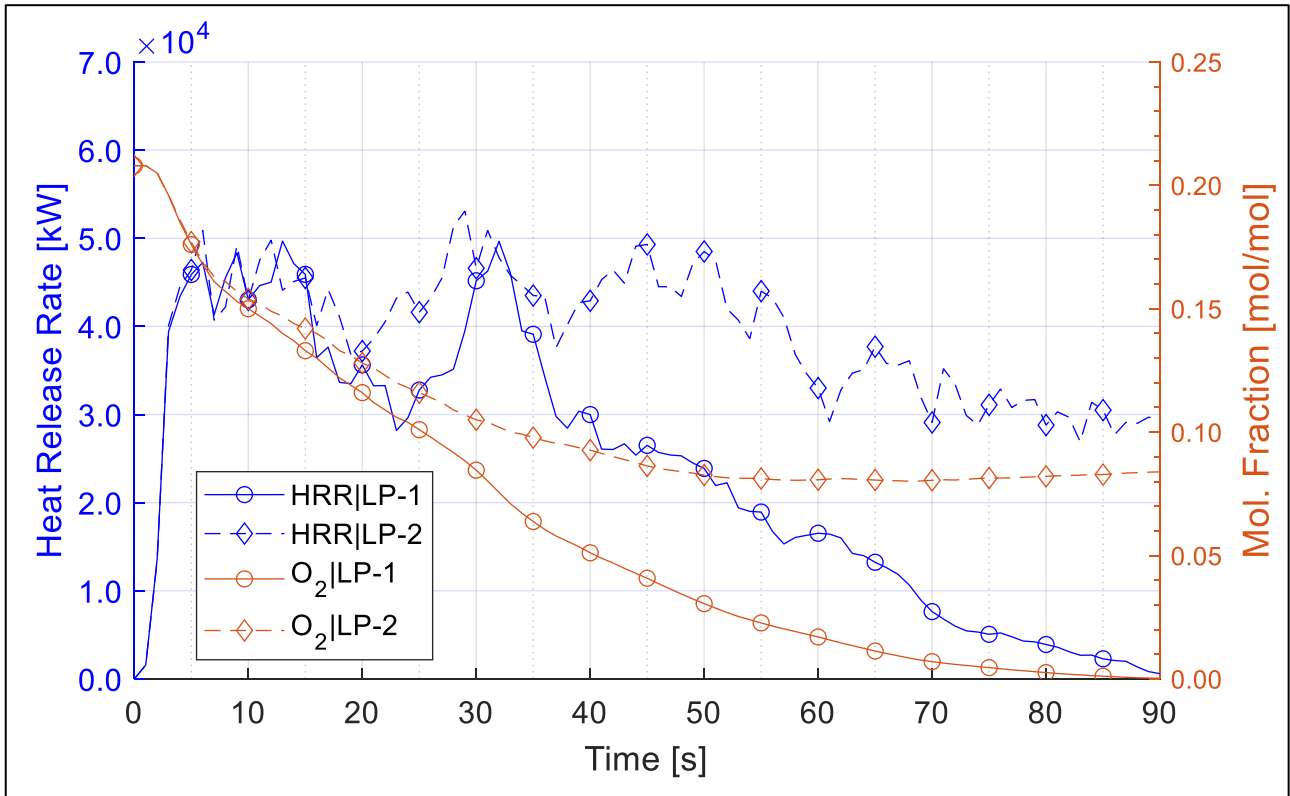


Figure 65: Comparison of the *HRR* for cases LP-1 and LP-2. The secondary y-axis shows the oxygen concentration.

Lastly, the time-averaged incident heat flux measured on some significant planes of the FPR is reported in Figure 66. More specifically, the figure compares the contour plots relative to the ceiling (panels a and b) and to the room end wall, opposite to the pool fire (see Figure 60) in panels c and d. As it can be observed, incident radiation fluxes received by FPR boundaries are significantly higher for the case LP-2, when air inlets are working, and the pool fire lasts for the whole duration of the simulation. Values as high as 500 kW/m<sup>2</sup> can be reached on the FPR ceiling, right above the location of the pool fire, while fluxes in a range between 150 and 100 kW/m<sup>2</sup> are reached as far as 23 metres from the fire (see Figure 66b). Lower heat fluxes were predicted for case LP-1, as depicted in Figure 66a, ranging between 240 and 80 kW/m<sup>2</sup>.

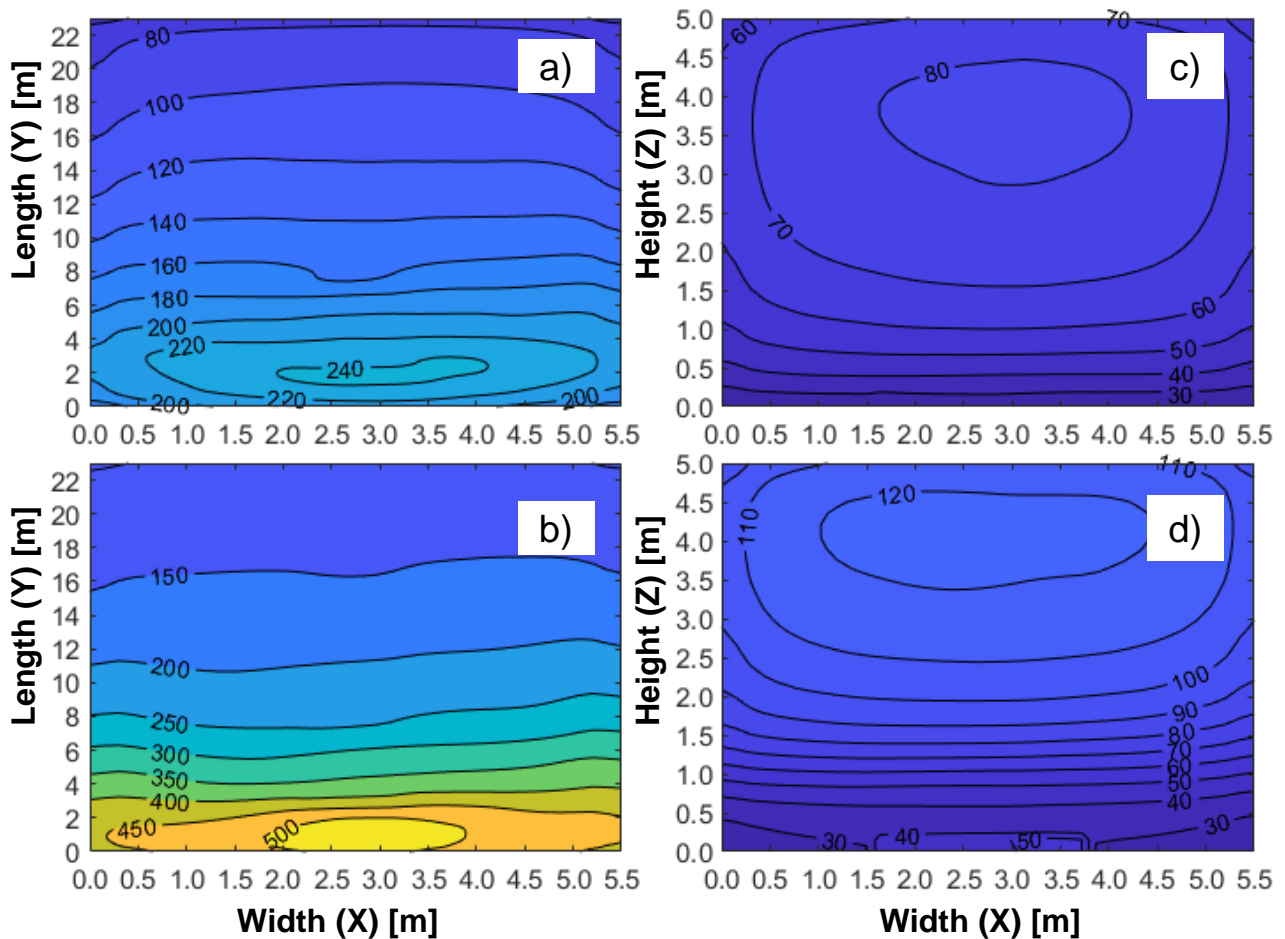


Figure 66: Comparison of time-averaged contours of incident radiation heat flux (in  $\text{kW/m}^2$ ) for FPR ceiling (panels a and b for cases LP-1 and LP-2 respectively) and for the XZ plane at  $Y=23$  m (opposite wall from pool fire location) (panels c and d for cases LP-1 and LP-2 respectively).

Similarly, the incident heat flux received by the end wall of the FPR resulted higher for the case LP-2 than for case LP-1, as reported in panels c and d of Figure 66. It can be noted that for both cases the wall regions subjected to the highest flux are located in the upper half of the wall, closer to the ceiling of the FPR. Lower heat flux values are predicted close to the floor, with values below  $50 \text{ kW/m}^2$  for heights of less than 1 metre. Comparing panels c and d, it can be noted that for the latter situation, referring to case LP-2, a zone with a slightly higher radiation flux can be observed at the ground level, approximately at the mid-section of the FPR. The presence of this region, not predicted for case LP-1, might be explained on the basis of pool fire duration, that for case LP-2 lasts for the entire simulation, thus contributing to increase the time-averaged heat fluxes around ground level.

An overview of the incident radiation heat flux evaluated at the boundaries of the enclosure is reported in Figure 67. Here, data obtained at different time steps for cases LP-1 and LP-2 are compared, together with flame visualization, to better understand the fire dynamics. It must be noted that smoke was not represented in the figure for the sake of clarity. As expected, the FPR ceiling, impinged in flames, receive the highest amounts of radiation. Furthermore, the effect of hot gases layering can be inferred by looking at radiation contours on the Z-Y plane: higher radiation values are predicted closer to the ceiling, where hot combustion gases accumulate. Additional results for cases HP-1 and HP-2 are reported in Appendix D.3.

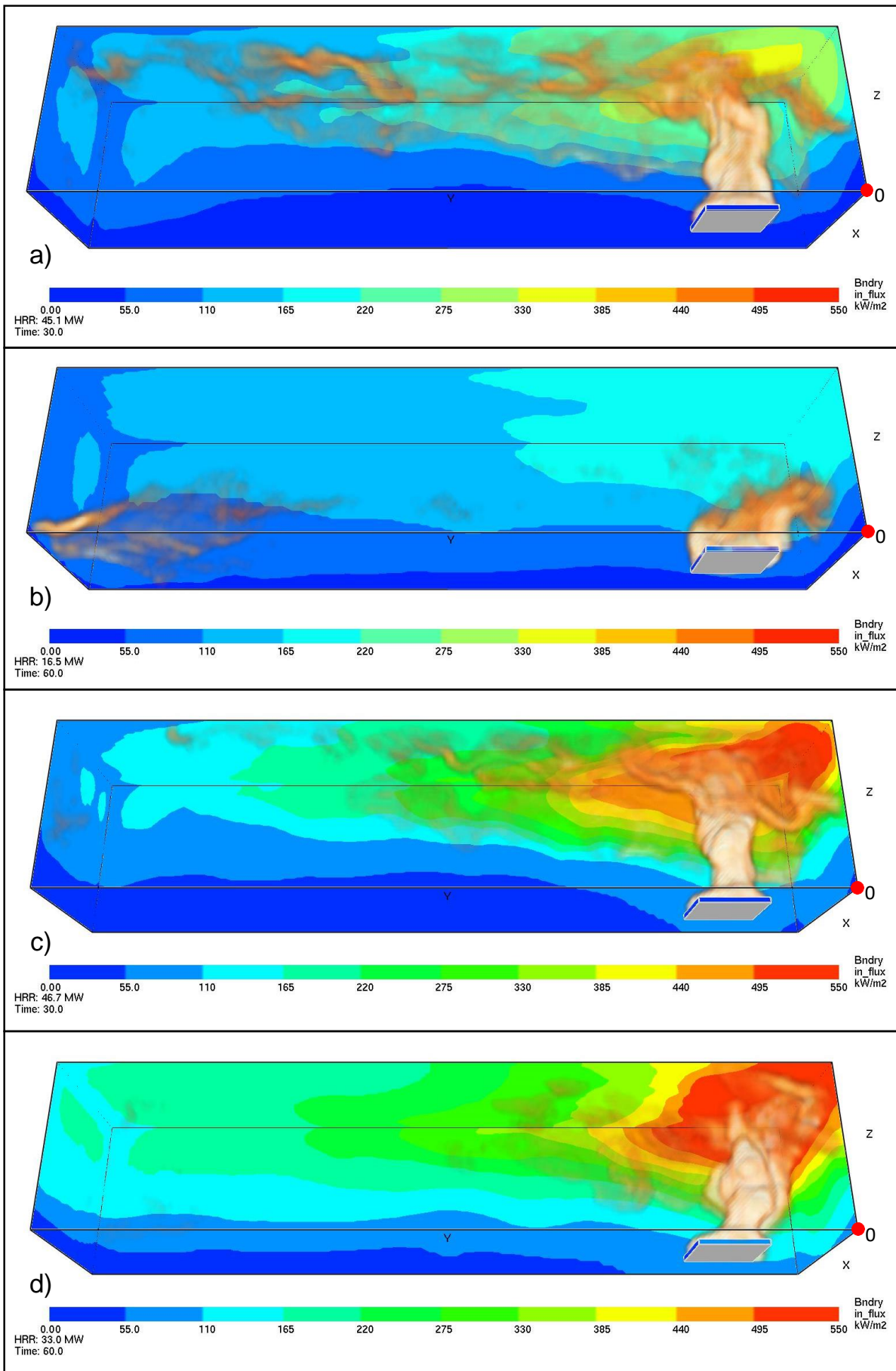


Figure 67: Overview of the incident radiation heat flux evaluated at FPR boundaries at various time steps for cases LP-1 (panels a & b) and LP-2 (panels c & d). Flame soot density is not displayed to facilitate reading of heat flux contours.

Variation of the incident radiation heat flux with height is shown in Figure 68, comparing results obtained for pool fires originating from LPDF and HPDF systems. Little difference can be observed for the heat flux predictions relative to HPDF and LPDF: for the latter case, heat flux values are always lower than correspondent values modelled for HP systems, possibly due to the slightly smaller pool fire dimension. It can be noted that in general the incident heat flux tends to increase with height, with the exception of the first two measurement locations: in particular, the heat flux measured at a height of 0.3 m gives results higher than the flux predicted at 1.0 m.

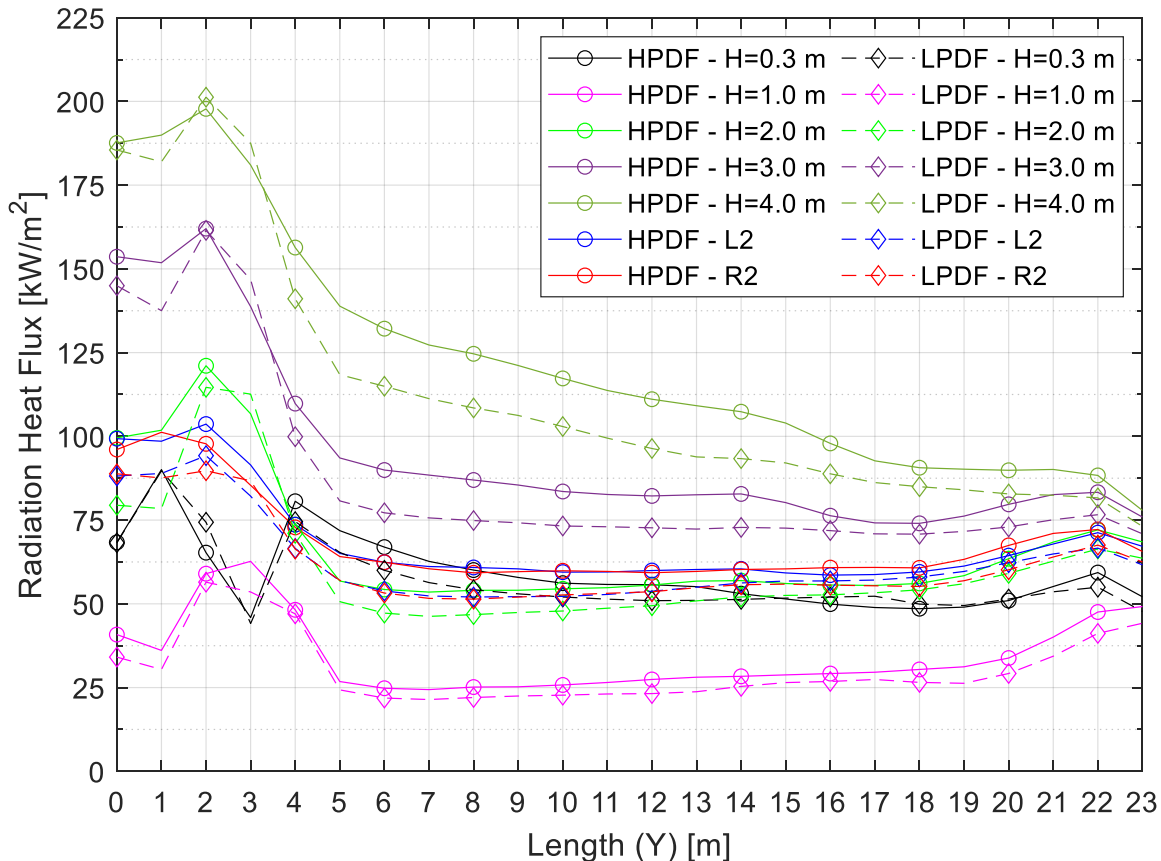


Figure 68: Comparison of time-averaged radiation heat flux measured at different locations for cases HP-1 and LP-1. See Figure 60 for the distribution scheme of measuring devices used in the simulations.

At this height, the average heat flux reaches a maximum value of around 63 kW/m<sup>2</sup> corresponding to the pool fire centre (located at Y=3 m). It then decreases to values around 25 kW/m<sup>2</sup> for most of the FPR length, to finally increase again close to the end wall of the room. For the other curves, the maximum in the radiation heat flux is reached generally at Y=2 m. However, the same trend observed at 1 m height is maintained, with a small increase of the heat flux predicted near the end of the FPR. The sole exception to this behaviour is represented by the curve referring to values measured at 4 m height, for which the radiation heat flux is constantly decreasing from the maximum value of about 200 kW/m<sup>2</sup> predicted at Y=2 m. Results obtained for simulation cases HP-2 and LP-2, reported in Appendix D.3, show analogous characteristics, with average heat fluxes in the “constant region” spanning from approximately 6 to 18 metres that are around 50 kW/m<sup>2</sup> higher than those reported in Figure 68, whereas the maxima values predicted near the pool fire centre can be up to 100 kW/m<sup>2</sup> higher than those relative to cases HP-1 and LP-1. Features similar to those described in Figure 64 and Figure 65 can be also observed for the HPDF system, for which the larger pool dimension give rise to slightly higher *HRR*. At the same time, methane concentration predicted afterwards the fire self-extinguishment for case HP-1 results about 33% higher than that relative to case LP-1, and the LFL is reached roughly 10 seconds earlier.

## 8.4. Conclusions

The effects of accidental LNG releases occurring inside an ESD-protected FPR were investigated defining a case study that considered both high- and low-pressure dual fuel systems. Pool fires with two different diameters were considered, resulting from releases affecting the HP fuel pumps and the LNG vaporiser featured in the LPDF system. Findings of the CFD modelling showed little differences between consequences stemming from HPDF and LPDF systems, since LNG pools having similar sizes will be formed. Conversely, substantial differences in the dynamic evolution of the enclosure pool fire were observed when comparing the results obtained assuming different operating modes of the FPR mechanical ventilation system. A strong reduction of the pool fire *HRR* was observed around 35 seconds after fire ignition, with a simultaneous depletion of the oxygen concentration inside the FPR that eventually led to the self-extinction of the pool fire when no fresh air inlet was considered, as opposed to the case considering normally operating conditions of the mechanical ventilation system. In this latter case the oxygen concentration reaches an equilibrium value sufficient to maintain the combustion process for the entire duration of the simulation. Regardless of the operating profile of the ventilation system, the modelled pool fires can generate incident heat fluxes high enough to undermine the structural integrity of exposed surfaces of the FPR and of the process equipment installed therein, possibly leading to accident escalation.

It can thus be concluded that release events occurring inside the FPR, even if deemed infrequent, might generate hazardous situations, affecting the safety of both passengers and ship structures due to the severity of accident consequences. The results of this assessment may provide a starting point from which parametric risk assessment studies aimed at evaluating the influence of structural design choices and operational profiles on the safety level of LNG-fuelled ships' FPRs can be developed. Lastly, safety recommendations can be drawn from the outcomes of this analysis, further improving the existing regulatory provisions.

# Conclusions

The shift towards the use of alternative marine fuels, among which LNG represents the most technologically ready and widespread solution, has fostered new investments in this field. Several gas-fuelled ships have been built, are under construction or are due to be built in the coming years, and many existing vessels have already been retrofitted. In order to support this expansion of the marine LNG market, an extensive small-scale LNG distribution chain is being developed.

At the same time, natural gas is a hazardous substance: although it has been safely traded for almost 60 years, its use as alternative fuel introduces safety challenges that should not be overlooked. To this end, a comprehensive study aimed at the assessment of different safety aspects of the supply chain of marine LNG fuel was carried out in this thesis, together with the evaluation of the sustainability fingerprint of existing LNG-based fuel systems for ship propulsion.

The sustainability assessment methodology described in Chapter 5 allowed definition of a framework for the comparison of alternative ship fuel systems during the early design phases. A tiered system of KPIs was defined to quantify the environmental, economic, and societal aspects of sustainability, integrating the inherent safety indicators that will be further developed in the inherent safety assessment of the LNG supply chain. A selection of the most relevant environmental impact indicators was made to capture the aspects related to pollutant emissions, and a profitability index was also defined to evaluate the economic attractiveness of the assessed alternatives. By performing a weighted aggregation of the multi-target impact indicators, an overall sustainability index was defined, providing a synthetic measure of the sustainability fingerprint. The proposed methodology was applied to a case study considering alternative fuel systems for cruise ships, allowing comparison of the sustainability performance of different LNG-based technologies against conventional diesel propulsion systems. The robustness of the obtained alternatives ranking was ultimately proven by a Monte Carlo sensitivity analysis.

The inherent safety assessment methodology developed for the analysis of alternative ship bunkering technologies allowed investigation of the hazard level of novel concepts proposed for LNG operations, making a comparison with the bunkering process of conventional marine fuels. The approach developed relies on a scoring system based on the quantification of KPIs calculated considering the expected consequences of accident scenarios, estimated using integral models, and credit factors that allowed the identification of the most credible LOC events associated with each process unit. Multiple targets were considered in the analysis, as specific KPIs were calculated addressing the human and escalation hazards independently, providing a comprehensive measure of the safety performance of bunkering processes. The methodology developed was applied to a case study, allowing the definition of a ranking of alternatives based on overall hazard indexes. This helped to identify the safety criticalities of the assessed bunkering technologies, highlighting the importance of inherent safety principles. In particular, the higher process complexity, and more severe operating conditions of the LNG transfer operations, together with the higher flammability of natural gas compared to IFO or MGO, resulted in a penalization of the expected safety performance of the LNG-based concepts. The proposed approach represents a starting point that may be used in different assessment methodologies, as it can be integrated into a wider analysis providing a metric of safety aspects or it can be used as a standalone tool for comparative inherent safety studies of bunkering activities.

The safety of LNG bunkering systems was also examined quantifying the risks associated with port-to-ship operations. Location-specific individual risk and societal risk levels of LNG bunkering operations were estimated following the QRA framework as recommended by relevant ISO standards. A novel approach to risk evaluation of LNG operations was developed in the present thesis to include managerial aspects in the risk analysis since they are rarely considered in this type of studies. The standard QRA procedure was combined with a methodology for the modification of process release frequency, which introduces organizational and operational factors in the assessment. Special attention was devoted to the definition of management quality levels and to the influence of simultaneous operations over the risk profile of bunkering activities. A case study reproducing the characteristics of a small-scale port serving an LNG-fuelled passenger ferry was used to demonstrate the application of the approach. The baseline risk level of PTS bunkering was evaluated assuming different population densities inside the port area. Individual and societal risks were thus calculated considering the influence of relevant operational and organizational factors. The weighted scoring system adopted for the estimation of frequency modification factors due to managerial aspects was the object of a dedicated sensitivity analysis aimed at evaluating the robustness of the calculated MMF with respect to the variation of the set of weights used in the assessment. The results demonstrated that managerial aspects significantly impact on risk profiles of bunkering operations. It was also concluded that the risk modification induced by simultaneous port operations, such as passenger boarding, will not raise the societal risk to intolerable levels provided that a safety-oriented management of bunkering operations is pursued. The approach developed can represent a useful tool to include a time-effective simplified evaluation of managerial aspects in a preliminary safety assessment of onshore LNG bunkering facilities, also supporting the decisional process required to authorise simultaneous port operations during LNG bunkering.

A relevant part of the present thesis was dedicated to analysis of LNG double-walled storage tanks involved in fire scenarios. The introduction to Chapter 7 reports a summary of the experimental investigations carried out for this topic that are still limited to a couple of fire tests, evidencing the need for additional experimental work overcoming the difficulties experienced with the mentioned tests. However, the data collected provided valuable information for the development of a CFD modelling setup used to simulate the response of cryogenic storage tanks completely engulfed in hydrocarbon fires. To clear out uncertainties related to the tank insulation performance, a dedicated parametric analysis of the thermal conductivity was carried out preliminarily to define the of the CFD model boundary conditions. This proved that loss of vacuum insulation and consequent discharge of granular insulating material is likely to determine a significant reduction of insulating properties during flame engulfment of double-walled storage tanks. The developed model showed good agreement with experimental pressure and temperature data and was thus used to study the effects induced by engulfing fires over two cases of interest for the bunker LNG supply chain. By using CFD tools, it was possible to overcome the main limitations of previous modelling approaches based on lumped parameters and to predict the liquid thermal stratification that controls the evaporation rate. The results obtained highlighted the influence of thermodynamic and geometrical features over the spatial distribution of evaporating zones and temperature fields inside fire-engulfed cryogenic tanks. Furthermore, the outputs of the CFD simulations provided fundamental values for the definition of a set of tank safety indicators, specifically designed to provide a rapid screening of tank safety in case of fire exposure. The defined KPIs addressed multiple aspects such as the loss of physical integrity and potential for accident escalation. The analysis of tank KPI values highlighted the relationship between hazards originating from pressure-build up and thermal weakening of the tank structure and showed that critical safety conditions are approached more rapidly for tanks with lower filling degrees. At the same time, KPIs addressing tank safety represent a valid support to emergency responders dealing with fire-engulfed pressurized cryogenic tanks.

The same modelling approach was exploited to simulate the exposure of double-walled cryogenic tanks to distant fires. A pool fire scenario, representative of a possible accident outcome in an LNG storage facility, was reproduced to define asymmetrical boundary conditions upon calculation of view factors between the fire and the tank. Wall temperatures, tank pressurization rates and liquid temperature stratification were estimated, assessing the influence of different tank dimensions and filling degrees. The analysis of tank safety KPIs demonstrated that critical safety conditions were not met for the modelled scenario, especially in case of a long-lasting exposure to the fire source.

Lastly, CFD simulations of small-scale LNG pool fires occurring on board gas-fuelled ships were performed to enhance the generic understanding of risks related to gas fuelling, providing a more detailed estimate of fire consequences. The case of a FPR located below deck was taken as reference to simulate different enclosure fire conditions, also considering the effect of the mechanical ventilation system. Following the estimation of pool diameter and evaporation rate with a well-established consequence model, initial and boundary conditions for the CFD setup were determined. The results of this simplified modelling approach described the dynamic evolution of LNG pool fires occurring inside confined spaces, also providing valuable information about the incident radiation received by the ship structure and process equipment inside the FPR.

Summarising, it can be concluded that the methodologies and approaches developed within the present work represent helpful tools for a comprehensive safety assessment of the LNG supply chain during the earliest phases of design. KPI-based methods offer a simple solution to evaluate the safety profile of LNG bunkering concepts and the overall sustainability of alternative ship fuel systems, supporting and orienting the selection of the most suitable solution throughout the decisional process. Additionally, CFD tools were proven to be a fundamental improvement for the detailed assessment of accident scenario consequences. The developed CFD model for the assessment of fire exposed cryogenic tanks represents an advancement in the field of safety for the small-scale LNG sector. The application of such tool represents a valuable help to deepen the understanding of LNG fire dynamics occurring onboard ships. More generally, the proposed works pave the way for the development of improved models, providing at the same time essential data for safety assessment studies.

## Limitations and suggestions for future research

There are some limitations of the present work, and aspects that deserve further attention in future research on the topic.

In general, it should be noted that in this thesis LNG was always assumed to be pure methane, following a simplified approach for consequence assessment. This assumption does not impair the general validity of the obtained results. However, it would be worthwhile to investigate the sensitivity of results to the actual composition of the LNG mixture.

Efforts should be directed towards the improvement of KPI-based metrics, especially aimed at getting better estimates of damage distances. The use of more detailed models, such as CFD, can enhance the prediction of flammable clouds extension and consequently increase the precision of the damage distances evaluation, thus allowing for the calculation of more realistic KPI values. The approaches that require the selection of indicators subsets and aggregation procedures, such as that outlined in Section 6.2, would be improved introducing the assessment by a panel of experts formed by port authorities' representatives, academics, and industry experts. In perspective, this may help the elicitation of weights and may lead to the definition of an *ad hoc* set of operational and organisational factors relevant for port and bunkering activities.

The literature review clearly showed the need for additional experimental campaigns aimed at the evaluation of LNG tank behaviour during fire scenarios. Particular attention should be given to the characterisation of the insulation performance and temperature fields of the tank lading during full engulfing fires. Such aspects would provide fundamental information for the improvement of future CFD analyses, strongly supporting their validation. Furthermore, an integration of CFD results with Finite Element Modelling would be desirable to deepen the understanding of tank structural response to the strong thermal gradients that develop inside the inner tank wall in proximity of the liquid-vapour interface.

Finally, the consequence evaluation of LNG pool fires occurring inside FPR could be further improved by investigating the pressurization induced by enclosure fires, along with the possibility of flow inversion in the forced ventilation system. Further simulations should be carried out enabling the FDS liquid pyrolysis model instead of prescribing a ramped fuel inlet condition to account for the heat transferred to the LNG pool by the flame. A parametric investigation of the influence of forced ventilation system may also be carried out to assess how vents position, number and flow rates will affect the enclosure fire dynamics. Moreover, the evaluation of the selected radiation model and material properties influence on the simulation results may be beneficial for a broader consequence assessment analysis aimed at the performance-based design of LNG-fuelled ships' fuel preparation rooms. Last but not least, an experimental campaign of small-scale LNG pool fire tests occurring inside confined spaces would be advisable to support the validation of CFD simulations. This would expand the collection of enclosure fire tests which currently do not cover the conditions encountered during FPR LNG pool fires, both in terms of enclosure arrangement and simulated heat release rates.

# Acknowledgments

Year by year I became more aware that the journey to achieve the PhD is really a tough one. Friends warned me back at the beginning, I honestly thought about quitting few times, but here we are eventually. Maybe I get to this point because of my stubbornness, but surely that was not enough, and I would not have reached this goal without the fundamental support of many people to whom I am profoundly grateful.

My deepest gratitude goes to my supervisor Professor Valerio Cozzani, who encouraged me to start the PhD course and whose experienced guidance helped me during these years. I would like to thank him for having given me the opportunity to develop my research project.

A heartfelt thank you to Professor Gabriele Landucci, from University of Pisa, for his unconfined patience and his commitment to review most of my papers. Without his precious support it probably would not have been possible to conclude this research work.

A special thanks goes to Dr. Giordano Emrys Scarponi who introduced me to the secrets of CFD modelling and who constantly assisted me during the work.

I would also like to thank Dr. Byongug Jeong from University of Strathclyde for his support during my period in Scotland and for the many research suggestions and inspirations he gave me.

I am also sincerely grateful to all my colleagues in the department for the stimulating discussions and the funny moments we have had in these years together.

Finally, but not for importance, I am profoundly grateful for the unconditioned support, patience and love of my parents and my brother who always encouraged and helped me to achieve this important goal. I also would like to thank all those whom I surely did not remember to mention explicitly.

# References

- Abbasi, T., Abbasi, S., 2007. The boiling liquid expanding vapour explosion (BLEVE): Mechanism, consequence assessment, management. *J. Hazard. Mater.* 141, 489–519. <https://doi.org/10.1016/j.jhazmat.2006.09.056>
- ABS (American Bureau of Shipping), 2017. Guide for LNG Bunkering. Houston, TX, USA.
- Acciaro, M., 2014. Real option analysis for environmental compliance: LNG and emission control areas. *Transp. Res. Part D Transp. Environ.* 28, 41–50. <https://doi.org/10.1016/j.trd.2013.12.007>
- Alderman, J.A., 2005. Introduction to LNG safety. *Process Saf. Prog.* 24, 144–151. <https://doi.org/10.1002/prs.10085>
- American Petroleum Institute (API), 2016. Assessing the Risks of Operations while Using LNG as a Marine Fuel [WWW Document]. URL <https://www.api.org/news-policy-and-issues/lng-exports/assessing-the-risks-of-operations-while> (accessed 6.16.20).
- Anderson, M., Salo, K., Fridell, E., 2015. Particle- and Gaseous Emissions from an LNG Powered Ship. *Environ. Sci. Technol.* 49, 12568–12575. <https://doi.org/10.1021/acs.est.5b02678>
- Aneziris, O., Koromila, I., Nivolianitou, Z., 2020. A systematic literature review on LNG safety at ports. *Saf. Sci.* 124, 104595. <https://doi.org/10.1016/j.ssci.2019.104595>
- Aneziris, O.N., Papazoglou, I.A., Konstantinidou, M., Nivolianitou, Z., 2014. Integrated risk assessment for LNG terminals. *J. Loss Prev. Process Ind.* 28, 23–35. <https://doi.org/10.1016/j.jlp.2013.07.014>
- ANSYS Inc., 2018a. ANSYS Fluent User Guide, Release 18.2.
- ANSYS Inc., 2018b. ANSYS Fluent Theory Guide, Release 18.2.
- Audouin, L., Rigollet, L., Prétrel, H., Le Saux, W., Röwekamp, M., 2013. OECD PRISME project: Fires in confined and ventilated nuclear-type multi-compartments - Overview and main experimental results. *Fire Saf. J.* <https://doi.org/10.1016/j.firesaf.2013.07.008>
- Babicz, J., 2015. Wartsila Encyclopedia of Ship Technology, Wartsila Corporation. <https://doi.org/10.1007/978-1-4614-9610-6>
- Babrauskas, V., 1983. Estimating large pool fire burning rates. *Fire Technol.* 19, 251–261. <https://doi.org/10.1007/BF02380810>
- Banawan, A.A., El Gohary, M.M., Sadek, I.S., 2009. Environmental and economical benefits of changing from marine diesel oil to natural-gas fuel for short-voyage high-power passenger ships. *Proc. Inst. Mech. Eng. Part M J. Eng. Marit. Environ.* 224, 103–113. <https://doi.org/10.1243/14750902JEME181>
- Bankes-Hughes, L., 2020. Delivery of world's largest LNG bunkering vessel [WWW Document]. Bunkerspot. URL <https://www.bunkerspot.com/global/50430-global-delivery-of-world-s-largest-lng-bunkering-vessel> (accessed 7.31.20).
- Bare, J., Gloria, T., Norris, G., 2006. Development of the Method and U.S. Normalization Database for Life Cycle Impact Assessment and Sustainability Metrics. *Environ. Sci. Technol.* 40, 5108–5115. <https://doi.org/10.1021/es052494b>
- Baresic, D., Smith, T., Raucci, C., Rehmatulla, N., Narula, K., Rojon, I., 2018. LNG as a marine fuel in the EU: Market, bunkering infrastructure investments and risks in the context of GHG reductions. London.

- Barron, R.F., Nellis, G.F., 2016. *Cryogenic Heat Transfer*, Second. ed. Boca Raton. <https://doi.org/https://doi.org/10.1201/b20225>
- Barsi, S., Kassemi, M., 2008. Numerical and experimental comparisons of the self-pressurization behavior of an LH2 tank in normal gravity. *Cryogenics (Guildf)*. 48, 122–129. <https://doi.org/10.1016/j.cryogenics.2008.01.003>
- Beikircher, T., Demharter, M., 2013. Heat Transport in Evacuated Perlite Powders for Super-Insulated Long-Term Storages up to 300 °C. *J. Heat Transfer* 135, 051301. <https://doi.org/10.1115/1.4023351>
- ben Brahim, T., Wiese, F., Münster, M., 2019. Pathways to climate-neutral shipping: A Danish case study. *Energy* 188, 116009. <https://doi.org/10.1016/j.energy.2019.116009>
- Beyler, C., 2016. Flammability Limits of Premixed and Diffusion Flames, in: Hurley, M.J., Gottuk, D., Hall, J.R., Harada, K., Kuligowski, E., Puchovsky, M., Torero, J., Watts, J.M., Wieczorek, C. (Eds.), *SFPE Handbook of Fire Protection Engineering*. Springer New York, New York, NY, pp. 529–553. [https://doi.org/10.1007/978-1-4939-2565-0\\_17](https://doi.org/10.1007/978-1-4939-2565-0_17)
- Bird, R.B., Stewart, W.E., Lightfoot, E.N., 2006. *Transport Phenomena*, Wiley International edition. Wiley.
- Birk, A.M., 1988. Modelling the response of tankers exposed to external fire impingement. *J. Hazard. Mater.* 20, 197–225. [https://doi.org/https://doi.org/10.1016/0304-3894\(88\)87013-4](https://doi.org/https://doi.org/10.1016/0304-3894(88)87013-4)
- Birk, A.M., Cunningham, M.H., 1996. Liquid temperature stratification and its effect on BLEVEs and their hazards. *J. Hazard. Mater.* 48, 219–237. [https://doi.org/https://doi.org/10.1016/0304-3894\(95\)00157-3](https://doi.org/https://doi.org/10.1016/0304-3894(95)00157-3)
- Birk, A.M., Cunningham, M.H., 1994. The boiling liquid expanding vapour explosion. *J. Loss Prev. Process Ind.* 7, 474–480. [https://doi.org/https://doi.org/10.1016/0950-4230\(94\)80005-7](https://doi.org/https://doi.org/10.1016/0950-4230(94)80005-7)
- Birk, A.M., Otremba, F., Gonzalez, F., Prabhakaran, A., Borch, J., Bradley, I., Bisby, L., 2016. Fire Testing of Total Containment Pressure Vessels. *Chem. Eng. Trans.* 48. <https://doi.org/10.3303/CET1648047>
- BP, 2007. *LNG Fire Protection and Emergency Response*, Second. ed, BP Process Safety Series. Institution of Chemical Engineers (IChemE), Rugby, UK.
- Briscoe, F., Shaw, P., 1980. Spread and evaporation of liquid. *Prog. Energy Combust. Sci.* 6, 127–140. [https://doi.org/https://doi.org/10.1016/0360-1285\(80\)90002-7](https://doi.org/https://doi.org/10.1016/0360-1285(80)90002-7)
- Brynolf, S., Fridell, E., Andersson, K., 2014a. Environmental assessment of marine fuels: Liquefied natural gas, liquefied biogas, methanol and bio-methanol. *J. Clean. Prod.* 74, 86–95. <https://doi.org/10.1016/j.jclepro.2014.03.052>
- Brynolf, S., Magnusson, M., Fridell, E., Andersson, K., 2014b. Compliance possibilities for the future ECA regulations through the use of abatement technologies or change of fuels. *Transp. Res. Part D Transp. Environ.* 28, 6–18. <https://doi.org/10.1016/j.trd.2013.12.001>
- Bunker Index, 2018. Europe regional bunker prices [WWW Document]. URL <https://bunkerindex.com/prices/europe.php> (accessed 12.28.18).
- Burel, F., Tacani, R., Zuliani, N., 2013. Improving sustainability of maritime transport through utilization of Liquefied Natural Gas (LNG) for propulsion. *Energy* 57, 412–420. <https://doi.org/10.1016/j.energy.2013.05.002>
- Canadian Natural Gas Vehicle Alliance, 2015. *Study on natural gas research and development priority setting for transportation in Canada*.

- Carnival Corporation & PLC, 2019. The Debut Of Costa Smeralda, Costa Cruises' New Ship Powered By LNG [WWW Document]. News release. <https://doi.org/https://www.carnivalcorp.com/news-releases/news-release-details/debut-costa-smeralda-costa-cruises-new-ship-powered-lng/>
- Casal, J., Darbra, R.-M., 2013. Analysis of Past Accidents and Relevant Case-Histories. *Domino Eff. Process Ind.* 12–29. <https://doi.org/10.1016/B978-0-444-54323-3.00002-6>
- Caterpillar, 2013. Diesel Fuel & Diesel Fuel Systems Application and Installation Guide.
- Caterpillar Motoren GmbH & Co. KG, 2018. M 43 C Propulsion. Kiel, Germany.
- Caterpillar Motoren GmbH & Co. KG, 2012. M 46 DF Propulsion. Kiel, Germany.
- CEN (European committee for standardization), 2016a. EN 1473:2016: Installation and equipment for liquefied natural gas - Design of onshore installations. CEN, Brussels, Belgium.
- CEN (European committee for standardization), 2016b. EN 1765:2016 Rubber hose assemblies for oil suction and discharge services - Specification for the assemblies. Brussels, Belgium.
- CEN (European committee for standardization), 2008. EN 1474:2008: Installation and equipment for liquefied natural gas - Design and testing of marine transfer systems. Brussels, Belgium.
- CEN (European committee for standardization), 2006. EN 14620:2006 Design and manufacture of site built, vertical, cylindrical, flat-bottomed steel tanks for the storage of refrigerated, liquefied gases with operating temperatures between 0°C and -165°C. Brussels, Belgium.
- CEN (European committee for standardization), 2002a. EN 13645:2002: Installations and equipment for liquefied natural gas — Design of onshore installations with a storage capacity between 5 t and 200 t. Brussels, Belgium.
- CEN (European committee for standardization), 2002b. EN 13458:2002: Cryogenic vessels. Static vacuum insulated vessels. Design, fabrication, inspection and testing. Brussels, Belgium.
- Center for Chemical Process Safety, 2010. Identifying Independent Protection Layers, in: Crowl, D.A. (Ed.), *Layer of Protection Analysis*. John Wiley & Sons, Inc., New York, NY, USA, pp. 75–113. <https://doi.org/10.1002/9780470935590.ch6>
- Chen, H., Deal, L., 2016. Considerations for Proponents when Conducting QRA for LNG Bunkering SIMOPS. Katy, TX, USA.
- CHIV International, 2014. Safety History of International LNG Operations Rev. 13. Houston, TX, USA.
- Choi, S.W., Lee, W. II, Kim, H.S., 2017. Numerical analysis of convective flow and thermal stratification in a cryogenic storage tank. *Numer. Heat Transf. Part A Appl.* 71, 402–422. <https://doi.org/10.1080/10407782.2016.1264771>
- Chorowski, M., Duda, P., Polinski, J., Skrzypacz, J., 2015. LNG systems for natural gas propelled ships. *IOP Conf. Ser. Mater. Sci. Eng.* 101. <https://doi.org/10.1088/1757-899X/101/1/012089>
- Corkhill, M., 2018. Cruise ships add new dimension to LNG passenger fleet [WWW Document]. LNG World Shipp. URL [https://www.lngworldshipping.com/news/view,cruise-ships-add-new-dimension-to-lng-passenger-fleet\\_51765.htm](https://www.lngworldshipping.com/news/view,cruise-ships-add-new-dimension-to-lng-passenger-fleet_51765.htm)
- Cozzani, V., Tugnoli, A., Bonvicini, S., Salzano, E., 2013. Threshold-Based Approach, in: *Domino Effects in the Process Industries: Modelling, Prevention and Managing*. Elsevier B.V., pp. 189–207. <https://doi.org/10.1016/B978-0-444-54323-3.00009-9>
- Curt, B., 2004. Marine transportation of LNG, in: *Intertanko Safety, Technical and Environmental Committee (ISTEC) Meeting*.

- Dal Pozzo, A., Guglielmi, D., Antonioni, G., Tugnoli, A., 2017. Sustainability analysis of dry treatment technologies for acid gas removal in waste-to-energy plants. *J. Clean. Prod.* 162, 1061–1074. <https://doi.org/10.1016/j.jclepro.2017.05.203>
- Danish Maritime Authority, 2012. North European LNG Infrastructure Project - A feasibility study for an LNG filling station infrastructure and test of recommendations. Copenhagen, Denmark.
- Demharter, M., 2011. Heat Transport in Evacuated Perlite Powder Insulations and Its Application in Long-Term Hot Water Storages. Technische Universität München.
- Deshpande, K.B., Zimmerman, W.B., Tennant, M.T., Webster, M.B., Lukaszewski, M.W., 2011. Optimization methods for the real-time inverse problem posed by modelling of liquefied natural gas storage. *Chem. Eng. J.* 170, 44–52. <https://doi.org/10.1016/j.cej.2011.03.025>
- DNV-GL, 2020. Alternative Fuels Insight Platform (AFI) [WWW Document]. URL <https://store.veracity.com/da10a663-a409-4764-be66-e7a55401275a> (accessed 6.26.20).
- DNV-GL, 2015a. Development and operation of liquefied natural gas bunkering facilities.
- DNV-GL, 2015b. LNG as ship fuel: Latest developments and projects in the LNG industry. Hamburg, Germany.
- DNV-GL, 2014. Liquefied Natural Gas (LNG) Bunkering Study. Katy, TX 77449.
- DNV, 2013a. Failure frequency guidance, Process equipment leak frequency data for use in QRA. Høvik, Norway.
- DNV, 2013b. QRA for Skangass LNG plant - Ferry bunkering project, Report No. 2013-4091. Stavanger, Norway.
- DNV, 2012. Port toolkit risk profile LNG bunkering. Høvik, Norway.
- DNV GL, 2019. Comparison of Alternative Marine Fuels. Høvik, Norway.
- DNV GL – Maritime, 2020. Current price development oil and gas [WWW Document]. URL <https://www.dnvgl.com/maritime/lng/current-price-development-oil-and-gas.html> (accessed 9.2.20).
- DNV GL – Maritime, 2018. Assessment of selected alternative fuels and technologies. Hamburg, Germany.
- Eliopoulou, E., Papanikolaou, A., Voulgarellis, M., 2016. Statistical analysis of ship accidents and review of safety level. *Saf. Sci.* 85, 282–292. <https://doi.org/10.1016/j.ssci.2016.02.001>
- EMSA, 2017. Guidance on LNG Bunkering to Port Authorities and Administration. Lisbon, Portugal.
- European Commission, 2017. Reducing emissions from the shipping sector [WWW Document]. URL [https://ec.europa.eu/clima/policies/transport/shipping\\_en#tab-0-0](https://ec.europa.eu/clima/policies/transport/shipping_en#tab-0-0) (accessed 6.24.20).
- European Commission, 2011. Impact Assessment: White Paper - Roadmap to a Single European Transport Area – Towards a competitive and resource efficient transport system. Com. Staff Work. Pap. 170. [https://doi.org/http://ec.europa.eu/transport/strategies/doc/2011\\_white\\_paper/white\\_paper\\_2011\\_ia\\_full\\_en.pdf](https://doi.org/http://ec.europa.eu/transport/strategies/doc/2011_white_paper/white_paper_2011_ia_full_en.pdf)
- European committee for standardization, 2015. Guidelines for systems and installations for supply of LNG as fuel to ships. CEN, Brussels, Belgium.
- European committee for standardization, 2014. Stainless steels Part 1 : List of stainless steels. CEN, Brussels, Belgium.
- European committee for standardization, 2008. Cryogenic vessels — Large transportable vacuum insulated vessels — Part 2: Design, fabrication, inspection and testing. CEN, Brussels, Belgium.

- European Environment Agency, 2018. TERM 2017 Aviation and shipping. Impacts on Europe's environment. Copenhagen, Denmark.
- European Environmental Agency, 2015. Marine protected areas in Europe's seas - An overview and perspectives for the future. Copenhagen, Denmark. <https://doi.org/10.2800/99473>
- European Parliament, 2017. Regulation (EU) 2017/352 of the European Parliament and of the Council of 15 February 2017 establishing a framework for the provision of port services and common rules on the financial transparency of ports [WWW Document]. URL <https://eur-lex.europa.eu/legal-content/EN/TXT/?uri=CELEX:02017R0352-20200528> (accessed 7.20.20).
- European Parliament, 2016. Directive (EU) 2016/802 of the European parliament and of the council of 11 May 2016 relating to a reduction in the sulphur content of certain liquid fuels. Off. J. Eur. Union.
- European Parliament, 2014. Directive 2014/94/EU of the European Parliament and of the Council of 22 October 2014 on the deployment of alternative fuels infrastructure. Off. J. Eur. Union.
- European Parliament, 2012. Council Directive 2012/18/EU of 4 July 2012 on the control of major-accident hazards involving dangerous substances, amending and subsequently repealing Council Directive 96/82/EC, Official Journal of the European Union. Brussels, Belgium.
- Faber, J., Nelissen, D., Ahdour, S., Harmsen, J., Toma, S., Lebesque, L., 2017. Study on the Completion of an EU Framework on LNG-fuelled Ships and its Relevant Fuel Provision Infrastructure. Analysis of the LNG market development in the EU. Brussels.
- Federal Energy Regulatory Commission (FERC), 2006. Draft Guidance for LNG Terminal Operator's Emergency Response Plan. Washington, D.C., USA.
- FLAGSHIPS Partners, 2019. FLAGSHIPS [WWW Document]. URL <https://flagships.eu/> (accessed 6.26.20).
- Gallarati, L., 2020. France sees first ship-to-ship LNG bunkering operation [WWW Document]. Arg. Media. URL <https://www.argusmedia.com/en/news/2105764-france-sees-first-shiptoship-lng-bunkering-operation> (accessed 8.19.20).
- Gas Infrastructure Europe, 2020. GIE Small Scale LNG Map [WWW Document]. URL <https://www.gie.eu/index.php/gie-publications/databases/lng-database> (accessed 7.3.20).
- Gong, M., Ma, J., Wu, J., Zhang, Y., Sun, Z., Zhou, Y., 2009. Nucleate pool boiling of liquid methane and its natural gas mixtures. *Int. J. Heat Mass Transf.* 52, 2733–2739. <https://doi.org/10.1016/j.ijheatmasstransfer.2008.12.011>
- Guinée, J., 2001. Handbook on life cycle assessment --- operational guide to the ISO standards. *Int. J. Life Cycle Assess.* 6, 255. <https://doi.org/10.1007/BF02978784>
- Gursu, S., Sherif, S.A., Veziroglu, T.N., Sheffield, J.W., 1993. Analysis and Optimization of Thermal Stratification and Self-Pressurization Effects in Liquid Hydrogen Storage Systems — Part 1: Model Development. *J. Energy Resour. Technol.* 115, 221–227.
- Gutteling Composite Hoses, 2020. Multi-LNG White STS Composite Hoses [WWW Document]. URL [https://www.gutteling.com/uploads/Gutteling/Hoses/Datasheets/Gutteling\\_Datasheet\\_2016\\_Hoses\\_Multi-LNG\\_White\\_STS.pdf](https://www.gutteling.com/uploads/Gutteling/Hoses/Datasheets/Gutteling_Datasheet_2016_Hoses_Multi-LNG_White_STS.pdf) (accessed 8.19.20).
- H2SHIPS Partners, 2019. H2SHIPS - System-Based Solutions for H2-Fuelled Water Transport in North-West Europe [WWW Document]. URL <https://www.nweurope.eu/projects/project-search/h2ships-system-based-solutions-for-h2-fuelled-water-transport-in-north-west-europe/>
- Hammer, L.S., 2019. Making LPG fuel an option for the shipping industry [WWW Document]. URL <https://www.dnvgl.com/expert-story/maritime-impact/Making-LPG-fuel-an-option-for-the-shiping-industry.html> (accessed 6.26.20).

- Hanna, S.R., Strimaitis, D.G., Chang, J.C., 1991. Hazard response modeling uncertainty (a quantitative method).
- Hansson, J., Brynolf, S., Fridell, E., Lehtveer, M., 2020. The potential role of ammonia as marine fuel-based on energy systems modeling and multi-criteria decision analysis. *Sustainability* 12, 10–14. <https://doi.org/10.3390/SU12083265>
- Helfre, J.-F., Boot, P.A.C., 2013. Emission reduction in the shipping industry: regulations, exposure and solutions [WWW Document]. URL [https://www.sustainalytics.com/sites/default/files/shippingemissions\\_july2013.pdf](https://www.sustainalytics.com/sites/default/files/shippingemissions_july2013.pdf) (accessed 4.26.19).
- Hirt, C., Nichols, B., 1981. Volume of fluid (VOF) method for the dynamics of free boundaries. *J. Comput. Phys.* 39, 201–225. [https://doi.org/10.1016/0021-9991\(81\)90145-5](https://doi.org/10.1016/0021-9991(81)90145-5)
- Horvath, S., Fasihi, M., Breyer, C., 2018. Techno-economic analysis of a decarbonized shipping sector: Technology suggestions for a fleet in 2030 and 2040. *Energy Convers. Manag.* 164, 230–241. <https://doi.org/10.1016/j.enconman.2018.02.098>
- HSE health and safety executive, 2019. Failure Rate and Event Data for use within Risk Assessments (02/02/19). Fail. Rate Event Data use within Risk Assessments 1–102.
- Hubert, A., Dembele, S., Denissenko, P., Wen, J., 2019. Predicting Liquefied Natural Gas (LNG) rollovers using Computational Fluid Dynamics. *J. Loss Prev. Process Ind.* 62, 103922. <https://doi.org/10.1016/j.jlp.2019.103922>
- Huczek, J., Blais, M., Friedman, K., 2020. Fire Performance of a UN-T75 Portable Tank Phase 1: Loaded with Liquid Nitrogen. Washington, DC.
- Hulsbosch-dam, C., Atli-veltin, B., Kamperveen, J., Velthuis, H., Reinders, J., Spruijt, M., 2017. Thermodynamic aspects of an LNG tank in fire and experimental validation. *EPJ Web Conf.* 143, 0–5. <https://doi.org/10.1051/epjconf/201714302039>
- Hurley, M.J., Gottuk, D., Hall, J.R., Harada, K., Kuligowski, E., Puchovsky, M., Torero, J., Watts, J.M., Wieczorek, C., 2016. SFPE handbook of fire protection engineering, fifth edition, SFPE Handbook of Fire Protection Engineering, Fifth Edition. Springer New York. <https://doi.org/10.1007/978-1-4939-2565-0>
- Hwang, Jeong, Jung, Kim, Zhou, 2019. Life Cycle Assessment of LNG Fueled Vessel in Domestic Services. *J. Mar. Sci. Eng.* 7, 359. <https://doi.org/10.3390/jmse7100359>
- IACS (International Association of Classification Societies), 2016. LNG Bunkering Guidelines. London, UK.
- IGU, 2020. 2020 World LNG Report. Barcelona, Spain.
- IGU, 2015. World LNG Report - 2015 Edition.
- Ikealumba, W.C., Wu, H., 2017. Effect of atmospheric and sea stability on liquefied natural gas (LNG) dispersion: Implications to Australian LNG marine transport. *Fuel* 197, 8–19. <https://doi.org/10.1016/j.fuel.2017.01.107>
- IMO, 2016. Studies on the feasibility and use of lng as a fuel for shipping. *Air Pollut. energy Effic. Stud.*
- IMO, 2000. Decision parameters including risk acceptance criteria, MSC 72/16.
- International Maritime Organization, 2018. Initial IMO Strategy on reduction of GHG emissions from ships. London, UK.

- International Maritime Organization, n.d. Data collection system for fuel oil consumption of ships [WWW Document]. URL <http://www.imo.org/en/OurWork/Environment/PollutionPrevention/AirPollution/Pages/Data-Collection-System.aspx> (accessed 6.24.20).
- International Maritime Organization (IMO), 2020. Fourth IMO GHG study. London, UK.
- International Maritime Organization (IMO), 2016. International Code for the construction and equipment of ships carrying liquefied gases in bulk (IGC Code).
- International Maritime Organization (IMO), 2015a. Third IMO Greenhouse Gas Study. 4 Albert Embankment, London SE1 7SR.
- International Maritime Organization (IMO), 2015b. International code of safety for ships using gases or other low-flashpoint fuels (IGF CODE).
- International Maritime Organization (IMO), 2015c. Amendments To The International Convention On Standards Of Training, Certification And Watchkeeping For Seafarers (STCW), 1978 [WWW Document]. URL [http://www.imo.org/en/KnowledgeCentre/IndexofIMOResolutions/Maritime-Safety-Committee-\(MSC\)/Documents/MSC.396\(95\).pdf](http://www.imo.org/en/KnowledgeCentre/IndexofIMOResolutions/Maritime-Safety-Committee-(MSC)/Documents/MSC.396(95).pdf) (accessed 7.7.20).
- International Maritime Organization (IMO), 2008. Revised MARPOL annex VI.
- International Maritime Organization (IMO), 1974. International Convention for the Safety of Life at Sea [WWW Document]. URL <https://treaties.un.org/doc/Publication/UNTS/Volume1184/volume-1184-I-18961-English.pdf> (accessed 7.7.20).
- International monetary fund, 2018. No Title [WWW Document]. URL <https://www.imf.org/en/Data> (accessed 8.30.18).
- ISO (International Organization for Standardization), 2015. ISO/TS 16901:2015 Guidance on performing risk assessment in the design of onshore LNG installations including the ship/shore interface. Geneva.
- Jafarzadeh, S., Paltrinieri, N., Utne, I.B., Ellingsen, H., 2017. LNG-fuelled fishing vessels: A systems engineering approach. *Transp. Res. Part D Transp. Environ.* 50, 202–222. <https://doi.org/10.1016/j.trd.2016.10.032>
- Jalkanen, J.P., Johansson, L., Kukkonen, J., 2016. A comprehensive inventory of ship traffic exhaust emissions in the European sea areas in 2011. *Atmos. Chem. Phys.* 16, 71–84. <https://doi.org/10.5194/acp-16-71-2016>
- Jeong, B., Jang, H., Zhou, P., Lee, J., 2019. Investigation on marine LNG propulsion systems for LNG carriers through an enhanced hybrid decision making model. *J. Clean. Prod.* 230, 98–115. <https://doi.org/10.1016/J.JCLEPRO.2019.05.054>
- Jeong, B., Lee, B.S., Zhou, P., 2017a. Quantitative risk assessment of fuel preparation room having high-pressure fuel gas supply system for LNG fuelled ship. *Ocean Eng.* 137, 450–468. <https://doi.org/10.1016/j.oceaneng.2017.04.002>
- Jeong, B., Lee, B.S., Zhou, P., Ha, S., 2017b. Evaluation of safety exclusion zone for LNG bunkering station on LNG-fuelled ships. *J. Mar. Eng. Technol.* 16, 121–144. <https://doi.org/10.1080/20464177.2017.1295786>
- Jeong, B., Lee, B.S., Zhou, P., Ha, S., 2018. Determination of safety exclusion zone for LNG bunkering at fuel-supplying point. *Ocean Eng.* 152, 113–129. <https://doi.org/10.1016/j.oceaneng.2018.01.066>
- Kalosh, A., 2019. AIDAnova becomes first LNG cruise ship to dock at Barcelona [WWW Document]. *Seatrade Cruise News*. URL <https://www.seatrade-cruise.com/news-headlines/aidanova-becomes-first-lng-cruise-ship-dock-barcelona> (accessed 7.31.20).

- Kamperveen, J.P., Spruijt, M.P.N., Reinders, J.E.A., 2016. Heat load resistance of cryogenic storage tanks – Results of LNG Safety Program. Utrecht, The Netherlands.
- Kassemi, M., Kartuzova, O., Hylton, S., 2018. Validation of two-phase CFD models for propellant tank self-pressurization: Crossing fluid types, scales, and gravity levels. *Cryogenics (Guildf)*. 89, 1–15. <https://doi.org/10.1016/J.CRYOGENICS.2017.10.019>
- Kinney, G.F., Graham, K.J., 1985. *Explosive Shocks in Air*. Springer Berlin Heidelberg. <https://doi.org/10.1007/978-3-642-86682-1>
- Kletz, T.A., 1978. What you don't have, can't leak. *Chem. Ind.* 6, 287--292.
- Knudsen, M., 1934. *The Kinetic Theory of Gases: Some Modern Aspects*.
- Kristenen, H.O., 2015. Energy demand and exhaust gas emissions of marine engines.
- Lagarrigue, V., Hermary, J., 2018. Re-Shaping LNG Transfer. *Offshore Technol. Conf.* <https://doi.org/10.4043/28780-MS>
- Landucci, G., Argenti, F., Tugnoli, A., Cozzani, V., 2015. Quantitative assessment of safety barrier performance in the prevention of domino scenarios triggered by fire. *Reliab. Eng. Syst. Saf.* 143, 30–43. <https://doi.org/10.1016/j.ress.2015.03.023>
- Landucci, G., Birk, M., 2013. Heat Radiation Effects, in: *Domino Effects in the Process Industries*. pp. 70–115. <https://doi.org/10.1016/B978-0-444-54323-3.00005-1>
- Landucci, G., D'Aulisa, A., Tugnoli, A., Cozzani, V., Birk, A.M., 2016. Modeling heat transfer and pressure build-up in LPG vessels exposed to fires. *Int. J. Therm. Sci.* 104, 228–244. <https://doi.org/10.1016/J.IJTHERMALSCI.2016.01.002>
- Landucci, G., Paltrinieri, N., 2016. A methodology for frequency tailorization dedicated to the Oil & Gas sector. *Process Saf. Environ. Prot.* 104, 123–141. <https://doi.org/10.1016/j.psep.2016.08.012>
- Landucci, G., Tugnoli, A., Cozzani, V., 2008. Inherent safety key performance indicators for hydrogen storage systems. *J. Hazard. Mater.* 159, 554–566. <https://doi.org/10.1016/j.jhazmat.2008.02.080>
- Lauder, B.E., Spalding, D.B., 1972. *Lectures in Mathematical Models of Turbulence*. Academic Press, London, England.
- Lee, S., 2020. Quantitative risk assessment of fire & explosion for regasification process of an LNG-FSRU. *Ocean Eng.* 197, 106825. <https://doi.org/10.1016/j.oceaneng.2019.106825>
- Lee, S., Seo, S., Chang, D., 2015a. Fire risk comparison of fuel gas supply systems for LNG fuelled ships. *J. Nat. GAS Sci. Eng.* 27, 1788–1795. <https://doi.org/10.1016/j.jngse.2015.10.0>
- Lee, S., Seo, S., Chang, D., 2015b. Fire risk comparison of fuel gas supply systems for LNG fuelled ships. *J. Nat. Gas Sci. Eng.* 27, 1788–1795. <https://doi.org/10.1016/j.jngse.2015.11.003>
- Lee, W.H., 1979. A pressure iteration scheme for two-phase modeling. Los Alamos Sci. Lab. Los Alamos, New Mex. Tech. Rep. LA-UR 79–975.
- Lemmon, E.W., McLinden, M.O., Friend, D.G., n.d. Thermophysical Properties of Fluid Systems, in: Linstrom, P.J., Mallard, W.G. (Eds.), *NIST Chemistry WebBook*, NIST Standard Reference Database Number 69. National Institute of Standards and Technology, Gaithersburg MD, USA. <https://doi.org/https://doi.org/10.18434/T4D303>
- Lloyd's Register, 2014. LNG Bunkering Infrastructure Survey 2014 [WWW Document]. URL [http://lng.wpci.nl/lng/sites/default/files/2014\\_Lloyds\\_Register\\_LNG\\_Bunkering\\_Infrastructure\\_Survey.pdf](http://lng.wpci.nl/lng/sites/default/files/2014_Lloyds_Register_LNG_Bunkering_Infrastructure_Survey.pdf) (accessed 7.7.20).

- Lo Brutto, F.M., 2019. Opportunities and constraints for a small-scale LNG development in the Mediterranean sea: Exploit experiences to apply locally, in: Offshore Mediterranean Conference and Exhibition 2019, OMC 2019. Ravenna, Italy, pp. 1–13.
- Lock, A., Bundy, M., Johnsson, E.L., Hamins, A., Ko, G.H., Hwang, C., Fuss, P., Harris, R., 2008. Experimental study of the effects of fuel type , fuel distribution , and vent size on full-scale underventilated compartment fires in an ISO 9705 Room, NIST Technical Note 1603. Gaithersburg MD, USA.
- Ma, T.G., Quintiere, J.G., 2003. Numerical simulation of axi-symmetric fire plumes: Accuracy and limitations. *Fire Saf. J.* 38, 467–492. [https://doi.org/10.1016/S0379-7112\(02\)00082-6](https://doi.org/10.1016/S0379-7112(02)00082-6)
- Mannan, S., 2012a. Chapter 16 – Fire, in: Lees’ Loss Prevention in the Process Industries (Volume 1-3). pp. 1075–1366. <https://doi.org/10.1016/B978-0-12-397189-0.00016-1>
- Mannan, S., 2012b. Chapter 16 - Fire, in: Mannan, S. (Ed.), Lees’ Loss Prevention in the Process Industries. Butterworth-Heinemann, Oxford, pp. 1075–1366. <https://doi.org/https://doi.org/10.1016/B978-0-12-397189-0.00016-1>
- Mannan, S. (Ed.), 2012c. Emission and Dispersion, in: Lees’ Loss Prevention in the Process Industries. Butterworth-Heinemann, Oxford, pp. 752–1074. <https://doi.org/https://doi.org/10.1016/B978-0-12-397189-0.00015-X>
- Maragkogianni, A., Papaefthimiou, S., 2015. Evaluating the social cost of cruise ships air emissions in major ports of Greece. *Transp. Res. Part D Transp. Environ.* 36, 10–17. <https://doi.org/10.1016/j.trd.2015.02.014>
- Market Observatory for Energy of the European Commission, 2019. Quarterly Report on European Gas Markets. Brussels, Belgium.
- Martins, M.R., Pestana, M.A., Souza, G.F.M., Schleder, A.M., 2016. Quantitative risk analysis of loading and offloading liquefied natural gas (LNG) on a floating storage and regasification unit (FSRU). *J. Loss Prev. Process Ind.* 43, 629–653. <https://doi.org/10.1016/j.jlp.2016.08.001>
- McGrattan, K., Hostikka, S., McDermott, R., Floyd, J., Vanella, M., 2019. Fire Dynamics Simulator User’s Guide, NIST Special Publication 1019. Gaithersburg, MD, USA. <https://doi.org/10.6028>
- McGrattan, K., Hostikka, S., McDermott, R., Floyd, J., Weinschenk, C., Overholt, K., 2015a. Fire Dynamics Simulator Technical Reference Guide Volume 3: Validation, NIST Special Publication 1018. Gaithersburg, MD, USA. <https://doi.org/10.6028/NIST.SP.1018-1>
- McGrattan, K., Hostikka, S., McDermott, R., Floyd, J., Weinschenk, C., Overholt, K., 2015b. Fire Dynamics Simulator Technical Reference Guide Volume 1: Mathematical Model, NIST Special Publication 1018. Gaithersburg MD, USA. <https://doi.org/10.6028/NIST.SP.1018-1>
- Merci, B., 2016. Introduction to fluid mechanics, in: SFPE Handbook of Fire Protection Engineering, Fifth Edition. Springer New York, pp. 1–24. [https://doi.org/10.1007/978-1-4939-2565-0\\_1](https://doi.org/10.1007/978-1-4939-2565-0_1)
- Metropolis, N., Ulam, S., 1949. The Monte Carlo Method. *J. Am. Stat. Assoc.* 44, 335–341. <https://doi.org/10.1080/01621459.1949.10483310>
- Migliore, C., 2013. Natural Gas Conditioning and Processing, in: Riazi, M., Eser, S., Agrawal, S., Pe&ntilde;a, J. (Eds.), Petroleum Refining and Natural Gas Processing. ASTM International, West Conshohocken, PA, pp. 249–287. <https://doi.org/10.1520/MNL58-EB>
- Migliore, C., Tubilleja, C., Vesovic, V., 2015. Weathering prediction model for stored liquefied natural gas (LNG). *J. Nat. Gas Sci. Eng.* 26, 570–580. <https://doi.org/10.1016/j.jngse.2015.06.056>
- Mohd Noor, C.W., Noor, M.M., Mamat, R., 2018. Biodiesel as alternative fuel for marine diesel engine applications: A review. *Renew. Sustain. Energy Rev.* <https://doi.org/10.1016/j.rser.2018.05.031>

- National Association of State Fire Marshals, 2005. Liquefied Natural Gas: An Overview of the LNG Industry for Fire Marshals and Emergency Responders. Washington, DC.
- National Institute of Standards and Technology, 2012. NIST/SEMATECH e-Handbook of Statistical Methods [WWW Document]. URL <https://www.itl.nist.gov/div898/handbook/eda/section3/eda366h.htm> (accessed 2.12.19).
- NFPA (National Fire Protection Association), 2018. NFPA 59A: Standard for the Production, Storage, and Handling of Liquefied Natural Gas (LNG). Quincy, MA, USA.
- NIST, n.d. Material Properties: 304 Stainless (UNS S30400) [WWW Document]. URL [https://trc.nist.gov/cryogenics/materials/304Stainless/304Stainless\\_rev.htm](https://trc.nist.gov/cryogenics/materials/304Stainless/304Stainless_rev.htm) (accessed 6.3.19).
- OCIMF (Oil Companies International Marine Forum), 2018. Mooring Equipment Guidelines. Witherby Seamanship International Ltd, London, UK.
- Oers, L. Van, 2016. CML-IA database, characterisation and normalisation factors for midpoint impact category indicators. Version 4.8, august 2016 [WWW Document]. URL <http://www.cml.leiden.edu/software/data-cmlia.html>
- OGP, 2010. Risk Assessment Data Directory - Ignition probabilities, Report No. 434 – 6.1.
- Øien, K., Tinmannsvik, R.K., Massaiu, S., Størseth, F., 2010. Development of new models and methods for the identification of early warning indicators (Building Safety project report). SINTEF Technology and Society, Trondheim, Norway.
- Oil Companies International Marine Forum (OCIMF), 2010. International Safety Guide for Inland Navigation Tank-barges and Terminals, First. ed. Central Commission for the Navigation of the Rhine, Strasbourg Cedex, France.
- Ovidi, F., Pagni, E., Landucci, G., Galletti, C., 2019. Numerical study of pressure build-up in vertical tanks for cryogenic flammables storage. *Appl. Therm. Eng.* 161, 114079. <https://doi.org/10.1016/j.applthermaleng.2019.114079>
- Parry, I., Heine, D., Kizzier, K., Smith, T., 2018. Carbon Taxation for International Maritime Fuels: Assessing the Options, IMF Working Papers. <https://doi.org/10.5089/9781484374559.001>
- Peng, D.-Y., Robinson, D.B., 1976. A New Two-Constant Equation of State. *Ind. Eng. Chem. Fundam.* 15, 59–64. <https://doi.org/10.1021/i160057a011>
- Pio, G., Carboni, M., Iannaccone, T., Cozzani, V., Salzano, E., 2019. Numerical simulation of small-scale pool fires of LNG. *J. Loss Prev. Process Ind.* 61, 82–88. <https://doi.org/10.1016/j.jlp.2019.06.002>
- Pio, G., Salzano, E., 2019. The effect of ultra-low temperature on the flammability limits of a methane/air/diluent mixtures. *J. Hazard. Mater.* 362, 224–229. <https://doi.org/https://doi.org/10.1016/j.jhazmat.2018.09.018>
- Planas-Cuchi, E., Gasulla, N., Ventosa, A., Casal, J., 2004. Explosion of a road tanker containing liquified natural gas. *J. Loss Prev. Process Ind.* 17, 315–321. <https://doi.org/10.1016/j.jlp.2004.05.005>
- Planas, E., Pastor, E., Casal, J., Bonilla, J.M., 2015. Analysis of the boiling liquid expanding vapor explosion (BLEVE) of a liquefied natural gas road tanker: The Zarzalico accident. *J. Loss Prev. Process Ind.* 34, 127–138. <https://doi.org/10.1016/j.jlp.2015.01.026>
- Quintiere, J.G., 2006. *Fundamentals of Fire Phenomena, Fundamentals of Fire Phenomena*. John Wiley & Sons, Ltd, Chichester, UK. <https://doi.org/10.1002/0470091150>
- Quintiere, J.G., 1989. Fundamentals Of Enclosure Fire “Zone” Models. *J. fire Prot. Eng.* 1, 99–119. <https://doi.org/10.1177/104239158900100302>

- Ren, J., Liang, H., 2017. Measuring the sustainability of marine fuels: A fuzzy group multi-criteria decision making approach. *Transp. Res. Part D Transp. Environ.* 54, 12–29. <https://doi.org/10.1016/j.trd.2017.05.004>
- Riviera Maritime Media Ltd, 2019. Growing LNG cargoes place emphasis on safety and training [WWW Document]. *LNG World Shipp.* March/April 2019. URL [https://issuu.com/rivieramaritimemedia/docs/lng\\_mar19\\_issuu](https://issuu.com/rivieramaritimemedia/docs/lng_mar19_issuu) (accessed 7.1.20).
- Riviera Maritime Media Ltd, 2016. Small-scale LNG supplement: LNG-fuelled passenger vessels grow and spread [WWW Document]. *Riviera Newsletters.* URL <https://www.rivieramm.com/opinion/small-scale-lng-supplement-lng-fuelled-passenger-vessels-grow-and-spread-33579> (accessed 7.30.20).
- Roh, S., Son, G., 2012. Numerical study of natural convection in a liquefied natural gas tank. *J. Mech. Sci. Technol.* 26, 3133–3140. <https://doi.org/10.1007/s12206-012-0820-x>
- Roman, J., 2020. LNG By Rail [WWW Document]. *NFPA Journal*, March/April 2020. URL <https://www.nfpa.org/News-and-Research/Publications-and-media/NFPA-Journal/2020/March-April-2020/Features/LNG-Trains> (accessed 7.1.20).
- Rukke, S., Katchmar, P., 2016. Failure Investigation Report – Liquefied Natural Gas (LNG) Peak Shaving Plant, Plymouth, Washington. Washington, D.C.
- Saleem, A., Farooq, S., Karimi, I.A., Banerjee, R., 2018. A CFD simulation study of boiling mechanism and BOG generation in a full-scale LNG storage tank. *Comput. Chem. Eng.* 115, 112–120. <https://doi.org/10.1016/j.compchemeng.2018.04.003>
- Sam Mannan, M., 2012. Case Histories, in: Sam Mannan, M. (Ed.), *Lees' Loss Prevention in the Process Industries*. Butterworth-Heinemann, p. 2561.
- Santoyo-Castelazo, E., Azapagic, A., 2014. Sustainability assessment of energy systems: Integrating environmental, economic and social aspects. *J. Clean. Prod.* 80, 119–138. <https://doi.org/10.1016/j.jclepro.2014.05.061>
- Scarponi, Giordano Emrys, Guglielmi, D., Casson Moreno, V., Cozzani, V., 2016. Assessment of inherently safer alternatives in biogas production and upgrading. *AIChE J.* 62, 2713–2727. <https://doi.org/10.1002/aic.15224>
- Scarponi, G.E., Landucci, G., Birk, A.M., Cozzani, V., 2019. An innovative three-dimensional approach for the simulation of pressure vessels exposed to fire. *J. Loss Prev. Process Ind.* 61, 160–173. <https://doi.org/10.1016/j.jlp.2019.06.008>
- Scarponi, G.E., Landucci, G., Birk, A.M., Cozzani, V., 2018a. LPG vessels exposed to fire: Scale effects on pressure build-up. *J. Loss Prev. Process Ind.* 56, 342–358. <https://doi.org/10.1016/J.JLP.2018.09.015>
- Scarponi, G.E., Landucci, G., Heymes, F., Cozzani, V., 2018b. Experimental and numerical study of the behavior of LPG tanks exposed to wildland fires. *Process Saf. Environ. Prot.* 114, 251–270. <https://doi.org/10.1016/J.PSEP.2017.12.013>
- Scarponi, G.E., Landucci, G., Ovidi, F., Cozzani, V., 2016. Lumped model for the assessment of the thermal and mechanical response of LNG tanks exposed to fire. *Chem. Eng. Trans.* 53, 307–312. <https://doi.org/10.3303/CET1653052>
- Scarponi, G.E., Landucci, G., Tugnoli, A., Cozzani, V., Birk, A.M., 2017. Performance assessment of thermal protection coatings of hazardous material tankers in the presence of defects. *Process Saf. Environ. Prot.* 105, 393–409. <https://doi.org/10.1016/J.PSEP.2016.10.009>
- Sciance, C.T., Colver, C.P., Sliepcevich, C.M., 1967. Pool Boiling of Methane between Atmospheric Pressure and the Critical Pressure. *Adv. Cryog. Eng.* 395–408. [https://doi.org/10.1007/978-1-4757-0489-1\\_42](https://doi.org/10.1007/978-1-4757-0489-1_42)

- SeaLNG LTD, 2019. LNG as a marine fuel – our zero emissions future starts now. Oxford, UK.
- Seo, M., Jeong, S., 2010. Analysis of self-pressurization phenomenon of cryogenic fluid storage tank with thermal diffusion model. *Cryogenics (Guildf)*. 50, 549–555. <https://doi.org/10.1016/j.cryogenics.2010.02.021>
- SGMF (Society For Gas As A Marine Fuel), 2017. Bunkering of ships with Liquefied Natural Gas (LNG) competency and assessment guidelines, Second. ed. London, UK.
- Sharples, J., 2019. LNG Supply Chains and the Development of LNG as a Shipping Fuel in Northern Europe, Oxford Institute for Energy Studies. <https://doi.org/10.26889/9781784671266>
- Shen, R., Jiao, Z., Parker, T., Sun, Y., Wang, Q., 2020. Recent application of Computational Fluid Dynamics (CFD) in process safety and loss prevention: A review. *J. Loss Prev. Process Ind.* 67, 104252. <https://doi.org/10.1016/j.jlp.2020.104252>
- SIGTTO, 2004. Liquefied Gas Fire Hazard Management, First. ed. Witherby & Co Ltd., London, England.
- SIGTTO, 2001. A Guide to Contingency Planning for Marine Terminals Handling Liquefied Gases in Bulk, Second. ed. Witherby & Co Ltd., London, England.
- SIGTTO (Society of International Gas Tanker & Terminal Operators), 2013. Ship to Ship Transfer Guide for Petroleum, Chemicals and Liquefied Gases, First. ed. Witherby Seamanship International Ltd, London, UK.
- Smith, T., Chester, L., Faber, J., Wilson, C., Deyes, K., 2019. Reducing the Maritime Sector's Contribution to Climate Change and Air Pollution. London, UK.
- SNAM, 2020. Small Scale LNG [WWW Document]. URL [https://www.snam.it/en/energy\\_transition/sustainable\\_mobility/small\\_scale\\_lng/](https://www.snam.it/en/energy_transition/sustainable_mobility/small_scale_lng/) (accessed 8.7.20).
- Speirs, J., Balcombe, P., Blomerus, P., Stettler, M., Brandon, N., Hawkes, A., 2019. Can natural gas reduce emissions from transport? Heavy goods vehicles and shipping. London, UK.
- Stalmokaite, I., Yliskylä-Peuralahti, J., 2019. Sustainability transitions in Baltic Sea shipping: Exploring the responses of firms to regulatory changes. *Sustainability* 11. <https://doi.org/10.3390/su11071916>
- Stenersen, D., Thonstad, O., 2017. GHG and NOx emissions from gas fuelled engines, SINTEF Ocean Report OC2017 F-107. Trondheim, Norway.
- Stokes, J., Owen, D., Moon, G., Wingate, K., Waryas, E., 2013. Understanding the human element in LNG bunkering, in: Proceedings of the 3rd Workshop on Marine Technology and Standards, July 24-25, 2013. Arlington, VA, USA, pp. 105–111.
- Stroup, D., Lindeman, A., McGrattan, K., Peacock, R., Overholt, K., Joglar, F., LeStrange, S., Montanez, S., 2016. Verification and validation of selected fire models for nuclear power plant applications. Washington, D.C., USA.
- The Maritime Executive, 2016. First Dual-Fuel, Air Lubricated Cruise Ship Delivered [WWW Document]. URL <https://www.maritime-executive.com/article/first-dual-fuel-air-lubricated-cruise-ship-delivered> (accessed 5.3.19).
- The World Bank Group, 2018. World development indicators [WWW Document]. URL <https://datacatalog.worldbank.org/dataset/world-development-indicators> (accessed 8.30.18).
- Thomson, H., Corbett, J.J., Winebrake, J.J., 2015. Natural gas as a marine fuel. *Energy Policy* 87, 153–167. <https://doi.org/10.1016/j.enpol.2015.08.027>

- Trelleborg, 2020. Cryoline LNG [WWW Document]. Prod. Solut. URL <https://www.trelleborg.com/en/fluidhandling/products--and--solutions/oil--and--marine/gas/cryoline--lng> (accessed 8.19.20).
- Trivyza, N.L., Rentizelas, A., Theotokatos, G., 2018. A novel multi-objective decision support method for ship energy systems synthesis to enhance sustainability. *Energy Convers. Manag.* 168, 128–149. <https://doi.org/10.1016/j.enconman.2018.04.020>
- Trozzi, C., 2010. Emission estimate methodology for maritime navigation, in: 9th International Emissions Inventory Conference. San Antonio, TX, USA.
- Tugnoli, A., Cozzani, V., Landucci, G., 2007. A consequence based approach to the quantitative assessment of inherent safety. *AIChE J.* 53, 3171–3182. <https://doi.org/10.1002/aic.11315>
- Tugnoli, A., Landucci, G., Cozzani, V., 2009. Key Performance Indicators for Inherent Safety: Application to the Hydrogen Supply Chain. *Process Saf. Prog.* 28, 156–170. <https://doi.org/10.1002/prs.10303>
- Tugnoli, A., Landucci, G., Cozzani, V., 2008. Sustainability assessment of hydrogen production by steam reforming. *Int. J. Hydrogen Energy* 33, 4345–4357. <https://doi.org/10.1016/j.ijhydene.2008.06.011>
- Tugnoli, A., Landucci, G., Salzano, E., Cozzani, V., 2012. Supporting the selection of process and plant design options by Inherent Safety KPIs. *J. Loss Prev. Process Ind.* 25, 830–842. <https://doi.org/10.1016/j.jlp.2012.03.008>
- Tugnoli, A., Paltrinieri, N., Landucci, G., Cozzani, V., 2010. LNG regasification terminals: comparing the inherent safety performance of innovative technologies. *Chem. Eng. Trans.* 19, 391–396. <https://doi.org/10.330/CET1019064>
- Tzannatos, E., 2010. Ship emissions and their externalities for the port of Piraeus - Greece. *Atmos. Environ.* 400–407. <https://doi.org/10.1016/j.atmosenv.2009.10.024>
- U.S. DOT PHMSA, 2020. Pipeline Incident 20 Year Trends [WWW Document]. URL <https://www.phmsa.dot.gov/data-and-statistics/pipeline/pipeline-incident-20-year-trends> (accessed 7.1.20).
- Uijt de Haag, P.A.M., Ale, B.J.M., 2005. Guidelines for quantitative risk assessment (Purple Book), third. ed, Committee for the Prevention of Disasters. The Hague.
- United Nations Economic Commission for Europe (UNECE), 2019. European Agreement concerning the International Carriage of Dangerous Goods by Inland Waterways (ADN). United Nations, European Agreement concerning the International Carriage of Dangerous Goods by Inland Waterways (ADN).
- United Nations Economic Commission for Europe (UNECE), 2018. European Agreement concerning the international carriage of dangerous goods by road. New York and Geneva. <https://doi.org/10.18356/e952b007-en>
- US Energy Information Administration, 2019. International Energy Outlook 2019. Washington, DC. <https://doi.org/10.5860/choice.44-3624>
- Valera-Medina, A., Xiao, H., Owen-Jones, M., David, W.I.F., Bowen, P.J., 2018. Ammonia for power. *Prog. Energy Combust. Sci.* 69, 63–102. <https://doi.org/10.1016/j.pecs.2018.07.001>
- Van Den Bosh, C.J.H., Twilt, L., 1992. Methods for the determination of possible damage (Green Book).
- Van Den Bosh, C.J.H., Weterings, R.A.P., 2005. Methods for the Calculation of Physical Effects (Yellow Book).

- Van Drew, N.T., Lin, C.S., Hasan, M.M., 1992. Self-Pressurization of a Flightweight Liquid Hydrogen Tank: Effects of Fill Level at Low Wall Heat Flux.
- Vílchez, J.A., Espejo, V., Casal, J., 2011. Generic event trees and probabilities for the release of different types of hazardous materials. *J. Loss Prev. Process Ind.* 24, 281–287. <https://doi.org/https://doi.org/10.1016/j.jlp.2011.01.005>
- Wahlqvist, J., van Hees, P., 2016. Implementation and validation of an environmental feedback pool fire model based on oxygen depletion and radiative feedback in FDS. *Fire Saf. J.* 85, 35–49. <https://doi.org/10.1016/j.firesaf.2016.08.003>
- Wang, K., Qian, X., He, Y., Shi, T., Zhang, X., 2020. Failure analysis integrated with prediction model for LNG transport trailer and thermal hazards induced by an accidental VCE: A case study. *Eng. Fail. Anal.* 108, 104350. <https://doi.org/10.1016/j.engfailanal.2019.104350>
- Wartsila, 2018. Small- and medium-scale LNG terminals 16.
- Wegener Sleeswijk, A., Oers, L. van, Guinée, J., Struijs, J., Huijbregts, M., 2008. Normalisation in product Life Cycle assessment: An LCA of the Global and European Economic Systems in the year 2000.
- Whall, C., Scarbrough, T., Stavrakaki, A., Green, C., Squire, J., Noden, R., 2010. UK Ship Emissions Inventory. London, England.
- Whall, C., Stavrakaki, A., Ritchie, A., Green, C., Shialis, T., Minchin, W., Cohen, A., Stokes, R., 2007. Ship Emissions Inventory - Mediterranean Sea. London, UK.
- WillyWeather, n.d. UK Wind Forecast [WWW Document]. URL <https://wind.willyweather.co.uk/> (accessed 12.28.19).
- Woodward, J.L., Pitblado, R., 2010a. LNG Risk Based Safety Modeling and Consequence Analysis. John Wiley & Sons, Inc., Hoboken, NJ, USA.
- Woodward, J.L., Pitblado, R., 2010b. LNG Risk Based Safety: modeling and consequence analysis. John Wiley & Sons.
- Xie, G.F., Li, X.D., Wang, R.S., 2012. Experimental study on the storage performance of high-vacuum-multilayer- insulation tank after sudden, catastrophic loss of insulating vacuum. *Heat Mass Transf.* 48, 757–766. <https://doi.org/10.1007/s00231-011-0928-z>
- Xie, G.F., Li, X.D., Wang, R.S., 2010. Experimental study of heat transfer in a HVMLI cryogenic tank after SCLIV. *Heat Mass Transf. und Stoffuebertragung* 46, 457–462. <https://doi.org/10.1007/s00231-010-0589-3>
- Xu, J., Testa, D., Mukherjee, P.K., 2015. The Use of LNG as a Marine Fuel: The International Regulatory Framework. *Ocean Dev. Int. Law* 46, 225–240. <https://doi.org/10.1080/00908320.2015.1054744>
- Zhang, B., Laboureur, D.M., Liu, Y., Gopalaswami, N., Mannan, M.S., Kay O’connor, M., 2018. Experimental Study of a Liquefied Natural Gas Pool Fire on Land in the Field. <https://doi.org/10.1021/acs.iecr.8b02087>
- Zhiyin, Y., 2015. Large-eddy simulation: Past, present and the future. *Chinese J. Aeronaut.* <https://doi.org/10.1016/j.cja.2014.12.007>

# Nomenclature

$A_{d,c}$	Critical size of tank insulation defect	
$A_{hole}$	Hole area	
$B$	Investment benefits	
$BHD$	Block domino hazard index	
$BHI$	Block inherent hazard index	
$BPD$	Block domino potential hazard index	
$BPI$	Block potential hazard index	
$C$	Investment costs	
$C_{cond}$	Condensation coefficient in the Lee model	Eq. 7.10
$C_D$	Discharge coefficient	
$C_{evap}$	Evaporation coefficient in the Lee model	Eq. 7.11
$Cf$	Credit factor	
$Cp$	Specific heat	
$d$	Traffic density value	Eq. 6.24
$d_{gap}$	Particle gap dimension	
$d_{pore}$	Perlite pores diameter	
$E$	Energy	Eq. 7.6, Eq. 7.7, Eq. 7.8
$E$	Emission amount	Eq. 5.1
$e$	Escalation distance	
$e^*$	Total mass-specific extinction coefficient	
$E_0$	Blast wave energy threshold	Eq. 7.33
$E_{VB}$	Vessel burst released energy	
$ef$	emission factor	
$EI$	Tank energy Safety KPI	
$EnvI$	Environmental index	
$EU$	Eutrophication impact indicator	
$f$	Event frequency	
$f'$	Modified event frequency	
$f_{P \rightarrow f}$	View factor between point P and the fire	
$f_S$	Modified dangerous scenario frequencies	Eq. 6.25
$g$	Gravity acceleration	
$G_K$	Generation of turbulent kinetic energy	
$G_\omega$	Generation of specific turbulent dissipation rate	
$GW$	Global warming impact indicator	
$h$	Damage distance	
$H$	Specific enthalpy	
$HD$	Overall domino inherent hazard index	
$HI$	Overall inherent hazard index	
$HT$	Human toxicity impact indicator	

$I$	Identity tensor	Eq. 7.5, Eq. 7.15
$I$	Generic indicator	Eq. 5.2, Eq. 5.7, Eq. 5.8
$I_c$	Score of the environmental indicator for impact category c	Eq. 5.2
$I_p$	Incident radiation at point P on tank surface	
$IPI$	Tank internal pressure Safety KPI	
$K$	turbulent kinetic energy	
$k$	Thermal conductivity	
$k_{air}$	Air thermal conductivity	
$k_{coupling}$	Coupling component of total effective thermal conductivity	
$k_{gas}$	Gaseous conduction component of total effective thermal conductivity	
$k_{rad}$	Radiation component of total effective thermal conductivity	
$k_{solid}$	Solid conduction component of total effective thermal conductivity	
$k_{tot}$	Total effective thermal conductivity	
$L$	Limiting function	Eq. 7.23
$LF$	Engine load factor	
LSIR	Location-Specific Individual Risk	
$M$	Molecular weight	
$\dot{m}$	Leak release rate	
$\dot{m}_{L \rightarrow V}$	Mass transfer rate from liquid to vapour phase	
$\dot{m}_{V \rightarrow L}$	Mass transfer rate from vapour to liquid phase	Eq. 7.1
$MG$	Geometric mean bias	
$MMF$	Management modification factor	
$N$	Expected number of fatalities	
$N_c$	Assumed cell population	
$NF$	Normalisation factor	
$NPV$	Net Present Value	
$OP$	Operational subfactor	
$OR$	Organizational subfactor	
$OSI$	Overall sustainability index	
$OSI_N$	Normalised overall sustainability index	
$p$	Pressure	
$p_{1/2}^c$	Half-value pressure for coupling conductivity term	
$p_{1/2}^g$	Half-value pressure for gas conductivity term	
$P_{Hum Err.}$	Operator failure probability	
$P_{Isolation failure}$	Leak isolation failure probability	
$P_d$	Death probability	
$P_{DI}$	Average delayed ignition probability	

$P_{ESD}$	ESD system failure probability	
$P_i$	Dangerous scenario probability	
$P_j$	Engine power	Eq. 5.1
$P_w$	Weather class and direction probability	
$PD$	Overall domino potential hazard index	
$PF$	Potential factor	Eq. 5.2
$PI$	Overall potential hazard index	
$PLL$	Potential Loss of Lives	
$Pr$	Prandtl number	
$Pr_T$	Turbulent Prandtl number	Eq. 7.6
$PrI$	Profitability index	
$PUI$	Process unit inventory	Eq. 5.4
$\dot{q}''$	Heat flux	
$R$	Universal gas constant	
$r$	Discount rate	
$RA$	Rain Acidification impact indicator	
$S$	Distance	
$S_{max}$	Tank surface above maximum design temperature	
$SOP$	Operational indicator score	
$SOR$	Organizational indicator score	
$T$	Temperature	
$T$	Navigation activity duration	Eq. 5.1
$t$	Time	
$T_{BB,eq}$	Equivalent black body temperature	
$T_{f,BB}$	Fire black body temperature	
$T_1, T_2$	Insulation boundary temperatures	Eq. 7.26, Eq. 7.28, Eq. 7.29
$T_{CFD}$	Calculated temperature	Eq. 7.35, Eq. 7.36, Eq. 7.37, Eq. 7.38, Eq. 7.39
$T_{exp}$	Measured temperature	Eq. 7.35, Eq. 7.36, Eq. 7.37, Eq. 7.38, Eq. 7.39
$T_r$	Insulation mean temperature value	Eq. 7.25, Eq. 7.26
$T_{wall}$	Tank wall temperature	
$TI$	Temperature Safety KPI	
$\mathbf{u}$	Velocity vector	
$\hat{U}$	Specific internal energy	
$u'_x, u'_y, u'_z$	Velocity components fluctuations	
$u^+$	Non dimensional velocity	
$u_\tau$	friction velocity	
$UHD$	Unit domino hazard index	
$UHI$	Unit inherent hazard index	
$UPD$	Unit domino potential hazard index	
$UPI$	Unit potential hazard index	

$\dot{V}$	Volumetric flow rate	Eq. 5.4
$VG$	Geometric mean variance	
$wOp$	Operational indicator weight	
$wOr$	Organizational indicator weight	
$y^+$	Non-dimensional wall distance	
$Y_K$	Dissipation of turbulent kinetic energy	
$Y_\omega$	Dissipation of specific turbulent dissipation rate	
$\widehat{\Delta H}_{TNT}$	TNT specific explosion energy	
$\Delta IR_{L,w,i}$	Scenario contribution to the overall LSIR	

## Greek letters

$\alpha$	Phase volume fraction	Eq. 7.1
$\gamma$	Specific heats ratio	Eq. 6.23
$\Gamma$	Ignition effectiveness	Eq. 6.24
$\Gamma_K$	Diffusivity of turbulent kinetic energy	
$\Gamma_\omega$	Diffusivity of specific turbulent dissipation rate	
$\delta$	Characteristic dimension	
$\varepsilon_{wall}$	Tank wall surface emissivity	
$\eta$	Fraction of internal energy converted into blast wave	Eq. 7.34
$\theta$	Angular coordinate	
$\mu$	Viscosity	
$\mu$	Overall management score	Eq. 6.19
$\mu_T$	Turbulent viscosity	
$\rho$	Density	
$\rho_{bulk}$	Bulk density of powder insulation	
$\sigma$	Stefan-Boltzmann constant	Eq. 7.25
$\tau$	Stress tensor	
$\overline{\tau'}$	Reynolds stresses tensor	
$\tau_w$	Wall shear stress	
$\varphi$	Generic material property	Eq. 7.3
$\varphi$	Generic variable	Eq. 7.12
$\varphi'$	Fluctuation of the generic variable	Eq. 7.12
$\overline{\varphi}$	Mean component of the generic variable	Eq. 7.12
$\Phi$	Fitting parameter	Eq. 7.27
$\omega$	Turbulent specific dissipation rate	
$\psi$	Weight factor	Eq. 6.19

## Subscripts

0	Initial conditions
<i>amb</i>	Ambient conditions
<i>B</i>	Block index
<i>c</i>	Impact category index
<i>eng</i>	Engine type index
<i>LOC</i>	Loss of Containment type index
<i>P</i>	Point-specific index
<i>p</i>	Pollutant species index
<i>S</i>	Dangerous scenario index
<i>s</i>	Solid
<i>Sat</i>	Saturation conditions

## Acronyms

ALARP	As Low As Reasonably Possible
BOG	Boil-Off Gas
DOT	U.S. Department of Transportation
ECA	Emission Control Area
EGR	Exhaust Gas Recirculation
ESD	Emergency shutdown system
ETA	Event Tree Analysis
EU	European Union
FDS	Fire Dynamic Simulator
FGSS	Fuel Gas Supply System
FPR	Fuel Preparation Room
FRA	Federal Railroad Administration
GHG	Greenhouse Gas
HPDF	High-Pressure Dual Fuel
IMO	International Maritime Organization
LNG	Liquefied Natural Gas
LOC	Loss of Containment
LPDF	Low-Pressure Dual Fuel
LPG	Liquefied Petroleum Gas
MAWP	Maximum Allowable Working Pressure
MGO	Marine Gas Oil
MMBtu	Millions of British Thermal Units
MMF	Managerial Modification Factor
MTPA	Million Tonnes Per Annum
NIST	National Institute of Standards and Technology
PM	Particulate Matter
PRV	Pressure Relief Valve
PTS	Port-to-Ship
QRA	Quantitative Risk Assessment
SCR	Selective Catalytic Reduction
SFPE	Society of Fire Protection Engineers
SIMOP	Simultaneous Operation
SSLNG	Small-scale LNG
STS	Ship-to-Ship
TNO	Netherlands Organization for Applied Scientific Research
TTS	Truck-to-Ship
VCE	Vapor Cloud Explosion
VOC	Volatile Organic Compounds

# List of figures

Figure 1: Bunker fuel price in \$/MMBtu. Data retrieved from DNV GL – Maritime (2020). .....	9
Figure 2: Total number of LNG-fuelled ships sorted by type as of July 2020. Source: Alternative Fuels Insight platform (DNV-GL, 2020).....	10
Figure 3: Schematic supply chain of LNG as maritime fuel. Adapted from (SNAM, 2020).....	11
Figure 4: Classification of onshore LNG storage tanks.....	12
Figure 5: Simplified FGSS schemes for different gas engine concepts: a) High pressure Dual-Fuel; b) Low pressure Dual-Fuel; c) Lean-Burn Spark Ignited.....	14
Figure 6: Main LNG bunkering options.....	15
Figure 7: Regulatory framework for the use of LNG as marine fuel. ....	18
Figure 8: Overview of the approach followed for the sustainability assessment. ....	32
Figure 9: Reference schemes considered for alternative fuel system technologies: a) Scheme 1 - LPDF; b) Scheme 2 - HPDF; c) Scheme 3 - LBSI; d) Scheme 4 - MGO. ....	34
Figure 10: Environmental impact tree used for the assessment of the impact of the alternative solutions considered. Potential emission factors, PF, values were collected from the study by Guinée (2001).35	
Figure 11: Hierarchy of considered sustainability key performance indicators.....	41
Figure 12: Radar plot showing the values of Level 2 indicators defined in Table 9 for the alternative fuel systems considered. Notice the different scale factor of <i>HI</i> axis. ....	47
Figure 13: Values of the overall normalised sustainability indicator, <i>OSIN</i> , and ranking resulting for the four alternatives considered based on the weight factors reported in Table 14. Colours indicate the contribution of the different impact domains to <i>OSIN</i> .....	47
Figure 14: Influence of different sets of weight factors on the <i>OSI</i> values for a conventional MGO fuel system (a); <i>PrI</i> percent impact over <i>OSIN</i> for different discount rate values (b).....	48
Figure 15: Distribution of cumulative probability for <i>OSI</i> differences ( $\Delta OSI$ ) between reference schemes .....	49
Figure 16: Overview of the different concepts and relative process blocks considered for the alternative ship bunkering systems analysed. Blue blocks refer to STS bunkering configuration, while dark yellow indicates a PTS arrangement.....	52
Figure 17: Reference schemes considered for the storage and supply blocks of LNG fueled vessels in Concepts A and B of Figure 16: a) S-LNG shore-based storage facility; b) B-LNG bunker vessel, and c) V-LNG fuel system onboard ship. For B-LNG and V-LNG blocks cryogenic submerged pumps are installed inside storage tanks.....	54
Figure 18: Reference schemes considered for the storage and supply blocks based on the utilization of conventional fuels in Concepts C and D of Figure 16: a) S-IFO and S-MGO shore-based storage facility; b) B-IFO and B-MGO bunker vessel; c) V-IFO and V-MGO fuel system onboard ship. ....	56
Figure 19: Overview of the methodology implemented for the inherent safety assessment of alternative technologies for marine fuel bunkering. ....	57

Figure 20: Normalised values of unit potential hazard and inherent hazard indexes for the bulk storage unit ( $UPI_{Storage}$ and $UHI_{Storage}$ ); maximum unit potential hazard and inherent hazard indexes ( $UPI_{MAX}$ and $UHI_{MAX}$ ); domino unit potential hazard and domino inherent hazard indexes for the bulk storage unit ( $UPD_{Storage}$ and $UHD_{Storage}$ ); maximum domino unit potential hazard and domino inherent hazard indexes ( $UPD_{MAX}$ and $UHD_{MAX}$ ).	61
Figure 21: KPI values for the single blocks of the alternative bunkering systems: a) block potential hazard index BPI ( $m^2$ ), b) block inherent hazard index BHI ( $m^2/y$ ), c) block domino potential hazard index BPD ( $m^2$ ), d) block domino inherent hazard index BHD ( $m^2/y$ ).	62
Figure 22: Overall KPIs for the alternative bunkering systems considered: a) overall potential hazard index PI ( $m^2$ ) and overall domino potential hazard index PD ( $m^2$ ); b) overall inherent hazard index HI ( $m^2/y$ ) and overall domino inherent hazard index HD ( $m^2/y$ ); c) qualitative ranking among the four Concepts considered based on overall inherent safety KPIs.	63
Figure 23: Workflow of the enhanced risk assessment analysis.	65
Figure 24: Sub-section of TEC2O method considered in the analysis (a) and procedure for the calculation of the management score and the MMF (b).	68
Figure 25: Layout and wind rose considered for the case study. Red dots indicate the assumed release points.	69
Figure 26: Simplified process flow diagram of the considered bunkering installation.	70
Figure 27: Example of event tree considered for the analysis. Dangerous scenarios originating from limited releases are shaded in blue, while scenarios resulting from an unlimited release are highlighted in red. Scenarios highlighted in green do not generate dangerous effects.	72
Figure 28: Iso-risk curves showing spatial distribution of LSIR for the baseline management situation	79
Figure 29: Comparison of maximum calculated LSIR values for different management situations as function of the distance from bunkering point.	80
Figure 30: F-N curves obtained for high port population density (a) and low population density (b) compared to upper and lower acceptability limits proposed by the IMO, (2000).	81
Figure 31: Comparison of calculated PLL values. Results for low population density are detailed in panel b) for clarity.	82
Figure 32: Relative contribution of dangerous scenarios to LSIR experienced at the bunkering point (a) and to estimated number of fatalities (b)	83
Figure 33: Impression of the vacuum insulated double-walled test tank engulfed in flames from Kamperveen et al., (2016).	86
Figure 34: Pressure time evolution during TNO test (a); example of highly disturbed thermocouple experimental measurement (b).	87
Figure 35: Impression of ISO LNG tank test from Huczek et al., (2020).	88
Figure 36: Pressure data for DOT FRA test.	89
Figure 37: Section of a double-walled LNG bullet tank showing perlite insulation (Kamperveen et al., 2016)	90

Figure 38: a) Example of pool boiling curve. Adapted from Barron and Nellis, (2016); b) Pure methane pool boiling curve. Adapted from Sciance et al., (1967). $T_{wall}$ is the tank internal wall temperature; $T_{sat}$ indicates the methane saturation temperature. ....	91
Figure 39: Subdivisions of the near-wall region.....	95
Figure 40: Contribution of the different heat transfer mechanisms and variation of overall perlite thermal conductivity ( $k_{tot}$ ) with bulk density for 1,013 mbar (a) and 1 mbar (b) pressure; (c) Variation of $k_{tot}$ with absolute pressure for different boundary temperatures ( $T_1$ : inner boundary temperature; $T_2$ : outer boundary temperature) assuming a bulk density value of $140 \text{ kg/m}^3$ ; $k_{solid}$ : contribution of solid conduction, $k_{gas}$ : contribution of gaseous conduction; $k_{rad}$ : contribution of heat radiation; $k_{coupling}$ : coupling term among the heat transfer mechanisms. ....	99
Figure 41: Representation of the computational domain: a) tank section considered for the 2D CFD analysis; b) mesh overview; c) detailed view of the mesh in proximity of the internal wall of the tank, highlighting the different material layers (i.e., insulation, tank inner wall and tank lading).....	102
Figure 42: (a) Comparison between experimental and modelled pressurization profiles for the validation case assuming different conditions of the insulation; (b) detail of the pressure build up obtained for bare tank simulation.....	105
Figure 43: (a) Geometric mean bias (MG) and variance (VG) of model-predicted temperature values compared against experimental measures. (b) Position of thermocouples used for experimental temperature measurement and liquid-vapour interface for the validation case V66.....	107
Figure 44: Parity plot for numerical model independence analysis.....	108
Figure 45: Pressurization profiles for $200 \text{ m}^3$ type C tank (a) and $58 \text{ m}^3$ road tanker (b) engulfed in fire. For the description of simulation cases refer to Table 24. ....	109
Figure 46: Time evolution of condensation and evaporation regions inside tank lading for simulation cases A50 (panels A1-A3) and B50 (panels B1-B3). Table 24 reports the details of the two simulation cases. ....	110
Figure 47: Liquid thermal stratification for $200 \text{ m}^3$ type C tank (a) and $58 \text{ m}^3$ road tanker (b) engulfed in fire. Temperature profile evolution on the vertical line perpendicular to tank axis is reported at different times after fire ignition. The liquid-vapour interface for the different simulation cases is represented by a dash-dotted line. ....	111
Figure 48: Liquid temperature contours for simulation cases A50 (A1-A3) and B50 (B1-B3) at different times. Panel C1 shows the dynamic evolution of tank inner wall temperature measured by thermocouple TC2. ....	112
Figure 49: Velocity magnitude path-lines for simulation cases A50 (A1-A3) and B50 (B1-B3) at different time steps. ....	113
Figure 50: Comparison of thermal and vertical velocity profiles at different time steps for cases A50 (panels A1 and A2) and B50 (panels B1 and B2). Data refer to the tank horizontal centreline (horizontal segment in the sketch). The dashed segment indicates the tank filling degree. ....	115
Figure 51: Comparison of safety KPIs for fire-engulfed cryogenic pressure tanks: a) $TI$ (Temperature index) versus $IPI$ (Internal Pressure index); b) $EI$ (Energy index) versus $IPI$ (Internal Pressure index); c) 3D representation of the unsafe volume where all the three KPIs are above the safe threshold. ....	117
Figure 52: Meshed 3D geometries of pool fire and tank used for view factor calculation (a). Panel (b) shows the variation of the incident radiation as a function of the angular coordinate $\theta$ on the central circular section.....	119

Figure 53: Pressurization curves obtained for the open-deck ship-fuel tank (a) and road tanker (b) exposed to distant pool fire. ....	120
Figure 54: Inner wall temperature profiles at 90 min (a) and 120 min (b) as a function of the angular coordinate $\theta$ . ....	121
Figure 55: Liquid temperature variation with axial position at three different time steps. Solid lines: Case B85; dashed lines: Case B50; dotted lines: Case B15. ....	121
Figure 56: <i>EI</i> (Energy index) versus <i>IPI</i> (Internal Pressure index) safety KPIs for cryogenic pressure tanks exposed to a distant pool fire: a) Case A (Open-deck ship-fuel tank); b) Case B (Road Tanker). ....	122
Figure 57: Example of general arrangement of LNG fuel system. ....	125
Figure 58: Illustration of heat contributions to pool evaporation. ....	127
Figure 59: Control volume and streams considered for enclosure fire energy balance. ....	129
Figure 60: Schematic view of the FPR modelled in FDS. Green dots represent the location of heat flux measuring points. Only two arrays of measuring points are illustrated for ease of comprehension. The pool fire surface, even if displayed as a square, was modelled using a circular vent. ....	132
Figure 61: Time ramp considered for the pool vaporisation flux in the FDS model. ....	132
Figure 62: Variation of radiative heat flux with dimensionless distance from the pool center for different cases. ....	133
Figure 63: Comparison of the HRR estimated for different mesh cell sizes of case LP-1. ....	134
Figure 64: Comparison of the concentration profiles of different gas species involved in the combustion process for cases LP-1 and LP-2. ....	135
Figure 65: Comparison of the HRR for cases LP-1 and LP-2. The secondary y-axis shows the oxygen concentration. ....	136
Figure 66: Comparison of time-averaged contours of incident radiation heat flux (in kW/m <sup>2</sup> ) for FPR ceiling (panels a and b for cases LP-1 and LP-2 respectively) and for the XZ plane at Y=23 m (opposite wall from pool fire location) (panels c and d for cases LP-1 and LP-2 respectively). ....	137
Figure 67: Overview of the incident radiation heat flux evaluated at FPR boundaries at various time steps for cases LP-1 (panels a & b) and LP-2 (panels c & d). Flame soot density is not displayed to facilitate reading of heat flux contours. ....	138
Figure 68: Comparison of time-averaged radiation heat flux measured at different locations for cases HP-1 and LP-1. See Figure 60 for the distribution scheme of measuring devices used in the simulations. ....	139

# List of tables

Table 1: List of LNG-related accidents .....	5
Table 2: Summary of the most relevant regulatory instruments for the use of LNG as a fuel .....	23
Table 3: Non-exhaustive list of information to be included in emergency response plans. ....	26
Table 4: Main data for the reference cruise ship type considered for the analysis.....	33
Table 5: Capital and operating costs for LNG and MGO fuelled ships.....	37
Table 6: Definition of LOC events considered in the present analysis and of related credit factors (1/y). Adapted from Tugnoli et al., (2009). n.a.: not applicable; n.c.: not considered. ....	38
Table 7: Threshold values adopted for damage distances evaluation. LFL: lower flammability limit; n.a.: not applicable. ....	39
Table 8: Normalisation factors adopted in the present work.....	40
Table 9: Summary of KPIs adopted in the study for the sustainability assessment. ....	41
Table 10: Considered time scheduling and engine load factors for environmental impact assessment. ....	43
Table 11: Emission factors and total emission amount of main and auxiliary engines. Values in brackets refer to navigation, the others to in-port activities. ....	43
Table 12: Results of economic impact assessment and calculated value of <i>PrI</i> indicator (not normalised) for the alternative fuel systems. ....	44
Table 13: Summary of non-normalised values for level 1 impact indicators and KPIs. Reference schemes are reported in Figure 9. ....	45
Table 14: Normalised values of Level 1, Level 2, and Level 3 indicators. Weight factors used for the aggregation of indices are reported in the last column of the table.....	46
Table 15: Process units and operating conditions considered for the analyzed bunkering operation.	70
Table 16: Criteria for the estimation of immediate and delayed ignition probabilities.....	73
Table 17: Considered baseline LOC event frequencies (1/y). n.a.: not applicable.....	74
Table 18: Estimated ignition probabilities. Values in italic are those subject to modification due to SIMOPs, as explained in Section 6.2.2. ....	74
Table 19: Baseline dangerous scenario probability values for limited and unlimited releases. Colour gradient highlights higher probability values.....	74
Table 20: Comparison among selected TEC2O indicators used for the calculation of LOC frequency modification factor. The original factor ID from Landucci and Paltrinieri, (2016) is reported in brackets for ease of reference.....	77
Table 21: Values of population density and indoor fraction considered for societal risk estimation. Refer to Figure 25 for the identification of the different port areas. ....	80
Table 22: Main dimensions and features of the TNO test tank.....	85
Table 23: Short description of simulations supporting the CFD model validation.....	100

Table 24: Main features of the tanks and initial conditions assumed for the simulation cases considered. MAWP: maximum allowable working pressure. ....	100
Table 25: Details of numerical setup. Values of under-relaxation factor are reported together with discretization schemes used and main mesh features. ....	103
Table 26: KPIs defined for the assessment of safety performance of pressurized cryogenic vessels. Specific parameters used in KPI definition are also defined.....	104
Table 27: Extent of velocity and thermal free convection layers evaluated at the horizontal centreline of the tank. Boundary layer thickness is normalised with respect to tank diameter.....	114
Table 28: General specifications of the case ship .....	125
Table 29: Main specifications and operating conditions of the FGSS. ....	126
Table 30: Release rate and total released mass for assessed LOC events.....	126
Table 31: Main characteristics of the cases analysed and location of pool and vents inside the FPR .....	130
Table 32: Coordinates of pool fire centre and mechanical ventilation items for the modelled FPR. Refer to Figure 60 for additional reference. ....	131
Table A1: Process conditions for LNG-based fuelling technologies. Process units and line tags are shown in Figure 9. ....	174
Table A2: Process conditions for conventional MGO technology. Process units and line tags are shown in Figure 9.....	175
Table A3: Calculated damage distances (h), and unit HIs for each LOC and process unit for LNG-based fuelling technologies. Equipment tags and features refer to Figure 9 and Table A1, respectively. ....	176
Table A4: Calculated damage distances (h), and unit HIs for each LOC and process unit for conventional MGO technology. Equipment tags and features refer to Figure 9 and Table A2, respectively.....	177
Table B1: Process conditions for the reference schemes considered for the storage and supply blocks of LNG fuelled vessels (Concepts A and B of Figure 16). Process units and line tags are shown in Figure 17 .....	179
Table B2: Process conditions for the reference schemes considered for the storage and supply blocks of IFO fuelled vessels (Concept C of Figure 16). Process units and line tags are shown in Figure 18. ....	180
Table B3: Process conditions for the reference schemes considered for the storage and supply blocks of MGO fuelled vessels (Concept D of Figure 16). Process units and line tags are shown in Figure 18. ....	181
Table B4: Calculated damage distances (h), escalation distances (e) and unit KPIs for each LOC and process unit in each block of Concepts A and B, based on LNG technologies. Equipment tags and features are reported in Figure 17 and Table B1 respectively. ....	182

Table B5: Calculated damage distances (h), escalation distances (e) and unit KPIs for each LOC and process unit in each block of Concept C, based on the utilization of IFO. Equipment tags and features are reported in Figure 18 and Table B2 respectively. .... 183

Table B6: Calculated damage distances (h), escalation distances (e) and unit KPIs for each LOC and process unit in each block of Concept D, based on the utilization of MGO. Equipment tags and features are reported in Figure 18 and Table B3 respectively. .... 184

Table B7: Calculated dangerous scenario frequencies for limited releases. JF: Jet Fire; FF: Flash Fire. .... 187

Table B8: Calculated dangerous scenario frequencies for unlimited releases. JF: Jet Fire; FF: Flash Fire; PF: Pool Fire..... 188

# Appendix

# Appendix A - Details of sustainability assessment

The main process conditions needed for the quantification of inherent safety KPI of each alternative fuelling technology are reported in Table A1 and Table A2 for LNG-based and conventional MGO options, respectively. Schematic process flow diagrams of each fuelling technologies are represented in Figure 9.

Table A1: Process conditions for LNG-based fuelling technologies. Process units and line tags are shown in Figure 9.

<b>1) Low Pressure dual fuel</b>							
Parameter	Process unit						
	Storage tank D01-D03	LNG Vaporizer E01-E02	Fuel gas heater E03-E04	BOG pre-heater E05-E06	BOG compressor P01-P02	MGO tank T01-T02	MGO booster pump G01-G02
Nominal capacity (m <sup>3</sup> )	1,200	-	-	-	-	10	-
Inventory (t)	495	-	-	-	-	7.34	-
Flowrate (kg/s)	-	0.81	0.81	2.78 ×10 <sup>-4</sup>	-	-	1.80 ×10 <sup>-2</sup>
Pressure (MPa)	0.30	0.70	0.70	0.31	0.60	0.12	0.80
Temperature (K)	130	131	131	153	-	318	318
State	Liquid	Liquid	Liquid	Vapor	-	Liquid	Liquid

<b>2) High Pressure dual fuel</b>							
Parameter	Process unit						
	Storage tank D01-D03	High pressure pump G01-G02	High pressure Vaporizer E01-E02	BOG compressor P01-P02	BOG pre-heater E03-E04	MGO tank T01-T02	MGO booster pump G03-G04
Nominal capacity (m <sup>3</sup> )	1,200	-	-	-	-	10	-
Inventory (t)	495	-	-	-	-	7.34	-
Flowrate (kg/s)	-	0.81	0.81	2.78 ×10 <sup>-4</sup>	2.78 ×10 <sup>-4</sup>	-	1.80 ×10 <sup>-2</sup>
Pressure (MPa)	0.30	30	30	0.60	0.60	0.12	0.80
Temperature (K)	130	146	318	278	293	318	318
State	Liquid	Liquid	Vapor	Vapor	Vapor	Liquid	Liquid

<b>3) Lean Burn Spark Ignition</b>					
Parameter	Process unit				
	Storage tank D01-D03	Pressure Build-up Unit E01-E03	LNG Vaporizer E04-E05	Fuel gas heater E06-E07	BOG pre-heater E08-E09
Nominal capacity (m <sup>3</sup> )	1,200	-	-	-	-
Inventory (t)	495	-	-	-	-
Flowrate (kg/s)	-	0.20	0.81	0.81	3.48 ×10 <sup>-3</sup>
Pressure (MPa)	0.60	0.60	0.60	0.60	0.60
Temperature (K)	140	143	150	293	293
State	Liquid	Vapor	Vapor	Vapor	Vapor

Table A2: Process conditions for conventional MGO technology. Process units and line tags are shown in Figure 9.

Parameter	Process unit							
	Storage tank D01- D05	Transfer pump G01-G02	Settling tank D06-D07	Feed pump G03- G04	Heater E01- E02	Service tank D08-D09	Heater E03- E04	Booster pump G07-G08
Nominal capacity (m <sup>3</sup> )	400	-	25	-	-	25	-	-
Inventory (t)	293.4	-	20.0	-	-	20.0	-	-
Flowrate (kg/s)	-	0.89	-	0.89	0.89	-	0.89	0.89
Pressure (MPa)	0.12	0.35	0.35	0.50	0.50	0.50	0.50	0.80
Temperature (K)	318	318	318	318	333	333	373	373
State	Liquid	Liquid	Liquid	Liquid	Liquid	Liquid	Liquid	Liquid

The key consequence assessment results and calculated values of the unit inherent safety KPI are summarized in Table A3 and Table A4 for calculated for LNG-based and MGO fuelling technologies, respectively. For each process unit, the considered LOC events and related  $Cf$  are reported, together with resulting damage distance ( $h$ ). LOC event categories are described in Table 6.

Table A3: Calculated damage distances ( $h$ ), and unit HIs for each LOC and process unit for LNG-based fuelling technologies. Equipment tags and features refer to Figure 9 and Table A1, respectively.

<b>1) Low Pressure dual fuel</b>				
Process Unit	Parameter			
	LOC	$C_f(1/y)$	$h$ (m)	UHI ( $m^2/y$ )
Storage tank D01-D03	R1	$1.00 \times 10^{-5}$	80.83	3.10
	R2	$5.00 \times 10^{-7}$	1,622.92	
	R3	$5.00 \times 10^{-7}$	1,855.95	
LNG vaporizer E01-E02	R1	$1.00 \times 10^{-3}$	55.96	3.51
	R3	$5.00 \times 10^{-5}$	86.49	
Fuel gas heater E03-E04	R1	$1.00 \times 10^{-3}$	6.69	0.12
	R3	$5.00 \times 10^{-5}$	38.60	
BOG pre-heater E05-E06	R1	$1.00 \times 10^{-3}$	5.00	0.13
	R3	$5.00 \times 10^{-5}$	46.50	
BOG compressor P01-P02	R4	$5.00 \times 10^{-4}$	7.29	0.37
	R5	$1.00 \times 10^{-4}$	56.32	
MGO tank T01-T02	R1	$1.00 \times 10^{-4}$	25.28	0.09
	R2	$5.00 \times 10^{-6}$	47.11	
	R3	$5.00 \times 10^{-6}$	45.24	
MGO booster pump G03-G04	R4	$5.00 \times 10^{-4}$	7.32	0.09
	R5	$1.00 \times 10^{-4}$	25.64	
<b>2) High Pressure dual fuel</b>				
Process Unit	Parameter			
	LOC	$C_f(1/y)$	$h$ (m)	UHI ( $m^2/y$ )
Storage tank D01-D03	R1	$1.00 \times 10^{-5}$	80.83	3.10
	R2	$5.00 \times 10^{-7}$	1,622.92	
	R3	$5.00 \times 10^{-7}$	1,855.95	
High pressure pump G01-G02	R4	$5.00 \times 10^{-4}$	105.94	7.27
	R5	$1.00 \times 10^{-4}$	128.81	
High pressure vaporizer E01-E02	R1	$1.00 \times 10^{-3}$	32.35	1.13
	R3	$5.00 \times 10^{-5}$	40.85	
BOG pre-heater E03-E04	R1	$1.00 \times 10^{-3}$	5.00	0.03
	R3	$5.00 \times 10^{-5}$	5.00	
BOG compressor P01-P02	R4	$1.00 \times 10^{-3}$	7.29	0.37
	R5	$1.00 \times 10^{-4}$	56.32	
MGO tank T01-T02	R1	$1.00 \times 10^{-4}$	25.28	0.09
	R2	$5.00 \times 10^{-6}$	47.11	
	R3	$5.00 \times 10^{-6}$	45.24	
MGO booster pump G03-G04	R4	$5.00 \times 10^{-4}$	7.32	0.09
	R5	$1.00 \times 10^{-4}$	25.64	
<b>3) Lean Burn Spark Ignition</b>				
Process Unit	Parameter			
	LOC	$C_f(1/y)$	$h$ (m)	UHI ( $m^2/y$ )
Storage tank D01-D03	R1	$1.00 \times 10^{-5}$	80.83	3.10
	R2	$5.00 \times 10^{-7}$	1,622.92	
	R3	$5.00 \times 10^{-7}$	1,855.95	
Pressure Build-up unit E01-E03	R1	$1.00 \times 10^{-3}$	10.17	0.21
	R3	$5.00 \times 10^{-5}$	46.11	
LNG vaporizer E04-E05	R1	$1.00 \times 10^{-3}$	55.96	3.51
	R3	$5.00 \times 10^{-5}$	86.49	
Fuel gas heater E06-E07	R1	$1.00 \times 10^{-3}$	7.20	0.13
	R3	$5.00 \times 10^{-5}$	38.60	
BOG pre-heater E08-E09	R1	$1.00 \times 10^{-3}$	5.00	0.03
	R3	$5.00 \times 10^{-5}$	5.00	

Table A4: Calculated damage distances ( $h$ ), and unit HIs for each LOC and process unit for conventional MGO technology. Equipment tags and features refer to Figure 9 and Table A2, respectively.

Process Unit	Parameter			
	LOC	$Cf(1/y)$	$h(m)$	UHI ( $m^2/y$ )
Storage tank D01-D05	R1	$1.00 \times 10^{-4}$	44.00	0.53
	R2	$5.00 \times 10^{-6}$	188.90	
	R3	$5.00 \times 10^{-6}$	178.76	
Transfer pump G01-G02	R4	$5.00 \times 10^{-4}$	27.63	0.93
	R5	$1.00 \times 10^{-4}$	73.91	
Settling tank D06 – D07	R1	$1.00 \times 10^{-5}$	51.96	0.04
	R2	$5.00 \times 10^{-7}$	116.07	
	R3	$5.00 \times 10^{-7}$	106.15	
Feed pump G03-G04	R4	$5.00 \times 10^{-4}$	32.14	1.06
	R5	$1.00 \times 10^{-4}$	73.91	
Heater E01-E02	R1	$1.00 \times 10^{-3}$	32.07	1.38
	R3	$5.00 \times 10^{-5}$	83.25	
Daily tank D08 – D09	R1	$1.00 \times 10^{-5}$	58.67	0.04
	R2	$5.00 \times 10^{-7}$	68.70	
	R3	$5.00 \times 10^{-7}$	98.26	
Heater E03-E04	R1	$1.00 \times 10^{-3}$	36.36	1.61
	R3	$5.00 \times 10^{-5}$	76.50	
Booster pump G07-G08	R4	$5.00 \times 10^{-4}$	52.64	1.99
	R5	$1.00 \times 10^{-4}$	77.48	

# Appendix B – Detailed results of inherent safety assessment

## B.1 Main features of reference schemes

The calculation of inherent safety KPIs is based on the quantitative consequence assessment of accident scenarios originating from process units. The characterization of operating conditions is necessary for the correct evaluation of the spilled amount of hazardous substance and subsequent accident scenario modelling. Process conditions considered for Concepts A and B, based on LNG technologies, are reported in Table B1, while data for Concept C (IFO bunkering) and Concept D (MGO bunkering) are reported in Table B2 and Table B3, respectively.

Process conditions and equipment features of the S-LNG block in concept A are representative of a 10,000 m<sup>3</sup> small scale LNG terminal based on data retrieved from Gas Infrastructure Europe, (2020). A storage tank size of 1450 m<sup>3</sup> was selected as representative for double-walled bullet tanks, thus obtaining seven storage units (D01-D07). In this concept, part of the stored LNG may be devoted to feed other end-users, such as truck loading bays and/or regasification units, with direct delivery to the natural gas network. In Concept B, the storage portion devoted to other users, which is about 30% considering the average value for current LNG medium- or small-scale terminals in Europe (Gas Infrastructure Europe, 2020), is not considered. Thus, the stored volume is reduced by 30%, obtaining a storage facility with only five tanks of 1,450 m<sup>3</sup> capacity (D01-D05). Material balances for the B-LNG bunker vessel and V-LNG fuel system onboard ship are based on fuel gas consumption data retrieved from technical documentation of installed dual fuel engines (DNV-GL, 2015b).

Process data for shore-based installation processing conventional marine fuels (both S-IFO and S-MGO) is taken from available process flow diagram of typical fuel depots sites on the western Italian coastline. The operating conditions for the on board fuel oil supply system for V-IFO and V-MGO blocks are retrieved from technical documentation of installed engines, such as that made available by Caterpillar Motoren GmbH & Co. KG, (2018).

Table B1: Process conditions for the reference schemes considered for the storage and supply blocks of LNG fuelled vessels (Concepts A and B of Figure 16). Process units and line tags are shown in Figure 17

**a) S-LNG shore-based storage facility**

Process unit	Parameter						State
	Nominal capacity (m <sup>3</sup> )	Inventory (t)	Line diameter (mm)	Flowrate (kg/s)	Pressure (bar)	Temperature (K)	
Storage tank D01-D07 (Concept A)	1,450	649	-	-	3.5	130	Liq.
Storage tank D01-D05 (Concept B)	-	-	-	-	-	-	-
Loading pumps G01 A/B	-	-	-	31.5	4.0	131	Liq.
LNG transfer arm S02	-	-	254	31.5	4.0	131	Liq.
BOG transfer arm S01	-	-	203.2	0.5	4.0	153	Vap.

**b) B-LNG bunker vessel**

Process unit	Parameter						State
	Nominal capacity (m <sup>3</sup> )	Inventory (t)	Line diameter (mm)	Flowrate (kg/s)	Pressure (bar)	Temperature (K)	
Storage tank D01	3,400 <sup>a</sup>	1,155	-	-	5.5	137	Liq.
Storage tank D02	2,700 <sup>a</sup>	906	-	-	5.5	137	Liq.
Vaporizer E01	-	-	-	0.11	8.5	140	Liq.
Fuel gas heater E02	-	-	-	0.14	6.5	293	Vap.
BOG pre-heater E03	-	-	-	0.04	5.6	273	Vap.
BOG compressor P01	-	-	-	0.04	7	278	Vap.
LNG bunker line S04	-	-	203.2	52.7	6	128	Liq.
BOG bunker line S03	-	-	152.4	1.24	6	145	Vap.

**c) V-LNG fuel system onboard ship**

Process unit	Parameter					State
	Nominal capacity (m <sup>3</sup> )	Inventory (t)	Flowrate (kg/s)	Pressure (bar)	Temperature (K)	
Storage tank D01	500 <sup>a</sup>	190.2	-	2.0	121	Liq.
Vaporizer E01	0	-	1.83	8.5	133	Liq.
Fuel gas heater E02	-	-	1.83	6.5	293	Vap.
BOG pre-heater E03	-	-	0.0035	2.1	273	Vap.
BOG compressor P01	-	-	0.0035	7.0	278	Vap.

Table B2: Process conditions for the reference schemes considered for the storage and supply blocks of IFO fuelled vessels (Concept C of Figure 16). Process units and line tags are shown in Figure 18.

**a) S-IFO shore-based storage facility**

Process unit	Parameter						State
	Nominal capacity (m <sup>3</sup> )	Inventory (t)	Line diameter (mm)	Flowrate (kg/s)	Pressure (bar)	Temperature (K)	
Storage tank T01-T06	2,550	2,527	-	-	1.2	318	Liq.
Bunker pumps G01/02	-	-	-	35.4	2.0	318	Liq.
Bunker hose S01	-	-	254	70.8	2.0	318	Liq.

**b) B-IFO auxiliary bunker vessel**

Process unit	Parameter						State
	Nominal capacity (m <sup>3</sup> )	Inventory (t)	Line diameter (mm)	Flowrate (kg/s)	Pressure (bar)	Temperature (K)	
Storage tank T01-T06	100	96	-	-	1.2	318	Liq.
Bunker pumps G01/02	-	-	-	27.5	2.0	318	Liq.
Bunker hose S01	-	-	76.2	27.5	2.0	318	Liq.

**c) V-IFO fuel system onboard ship**

Process unit	Parameter						State
	Nominal capacity (m <sup>3</sup> )	Inventory (t)	Flowrate (kg/s)	Pressure (bar)	Temperature (K)		
Storage tank D01-D02	80	71	-	1.2	318	Liq.	
Transfer pump G01	-	-	1.91	3.5	318	Liq.	
Settling tank D03-D04	25	22.3	-	3.5	333	Liq.	
Feed pump G02	-	-	1.91	5.0	333	Liq.	
Heater E01	-	-	1.91	5.0	353	Liq.	
Daily tank D05-D06	25	22.3	-	5.0	353	Liq.	
Heater E02	-	-	1.91	5.0	373	Liq.	
Booster pump G03	-	-	1.91	8.0	373	Liq.	

Table B3: Process conditions for the reference schemes considered for the storage and supply blocks of MGO fuelled vessels (Concept D of Figure 16). Process units and line tags are shown in Figure 18.

**a) S-MGO shore-based storage facility**

Process unit	Parameter						State
	Nominal capacity (m <sup>3</sup> )	Inventory (t)	Line diameter (mm)	Flowrate (kg/s)	Pressure (bar)	Temperature (K)	
Storage tank T01-T06	2,550	2,282	-	-	1.2	318	Liq.
Bunker pumps G01/02	-	-	-	33.1	2.0	318	Liq.
Bunker hose S01	-	-	152.4	66.2	2.0	318	Liq.

**b) B-MGO auxiliary bunker vessel**

Process unit	Parameter						State
	Nominal capacity (m <sup>3</sup> )	Inventory (t)	Line diameter (mm)	Flowrate (kg/s)	Pressure (bar)	Temperature (K)	
Storage tank T01-T07	100	77.5	-	-	1.2	318	Liq.
Bunker pump G01	-	-	-	22.6	2.0	318	Liq.
Bunker hose S02	-	-	76.2	22.6	2.0	318	Liq.

**c) V-MGO fuel system onboard ship**

Process unit	Parameter					State
	Nominal capacity (m <sup>3</sup> )	Inventory (t)	Flowrate (kg/s)	Pressure (bar)	Temperature (K)	
Storage tank D01-D02	80	61.2	-	1.2	318	Liq.
Transfer pump G01	-	-	1.91	3.5	318	Liq.
Settling tank D03-D04	25	20	-	3.5	318	Liq.
Feed pump G02	-	-	1.91	5.0	318	Liq.
Heater E01	-	-	1.91	5.0	333	Liq.
Daily tank D05-D06	25	20	-	5.0	333	Liq.
Heater E02	-	-	1.91	5.0	373	Liq.
Booster pump G03	-	-	1.91	8.0	373	Liq.

## B.2 Consequence evaluation for inherent safety assessment

A summary of the main consequence assessment results and calculated KPI values for the units included in all the process schemes considered are presented in this section. Results for Concepts A and B systems are reported in Table B4, while results for Concept C and Concept D are reported in Table B5 and Table B6, respectively. Equipment tags are described in Sections 6.1.1 and 6.1.2. For each concept considered, table entries report the LOC types associated with each single process unit in each block, and related credit factors ( $C_f$ ), hazard and escalation distances ( $h$  and  $e$ , respectively) and the calculated values of unit indexes:  $UPI$ ,  $UHI$ ,  $UDI$ , and  $UHD$ .

Table B4: Calculated damage distances ( $h$ ), escalation distances ( $e$ ) and unit KPIs for each LOC and process unit in each block of Concepts A and B, based on LNG technologies. Equipment tags and features are reported in Figure 17 and Table B1 respectively.

<b>a) S-LNG shore-based storage facility</b>								
Process Unit	LOC	$Cf(1/y)$	Parameter					
			$h$ (m)	$e$ (m)	UPI (m <sup>2</sup> )	UHI (m <sup>2</sup> /y)	UPD (m <sup>2</sup> )	UHD (m <sup>2</sup> /y)
Storage tanks D01-D07 (Concept A), D01-D05 (Concept B)	R1	$1.00 \times 10^{-5}$	45	44	$4.80 \times 10^6$	3.01	$4.78 \times 10^6$	2.99
	R2	$5.00 \times 10^{-7}$	2190	2185				
	R3	$5.00 \times 10^{-7}$	1086	1077				
Loading pump G01 A/B	R4	$5.00 \times 10^{-4}$	196	190	$2.40 \times 10^5$	43.30	$2.23 \times 10^5$	40.36
	R5	$1.00 \times 10^{-4}$	490	473				
LNG Transfer arm S02	R4	$6.00 \times 10^{-4}$	153	147	$1.84 \times 10^5$	25.05	$1.71 \times 10^5$	23.28
	R5	$6.00 \times 10^{-5}$	429	414				
BOG Transfer arm S01	R4	$6.00 \times 10^{-4}$	14	5	$4.94 \times 10^4$	3.09	$4.70 \times 10^4$	2.83
	R5	$6.00 \times 10^{-5}$	222	217				
<b>b) B-LNG bunker vessel</b>								
Process Unit	LOC	$Cf(1/y)$	Parameter					
			$h$ (m)	$e$ (m)	UPI (m <sup>2</sup> )	UHI (m <sup>2</sup> /y)	UPD (m <sup>2</sup> )	UHD (m <sup>2</sup> /y)
Storage tank D01	R1	$1.00 \times 10^{-5}$	139	134	$8.04 \times 10^6$	6.53	$7.87 \times 10^6$	6.41
	R2	$5.00 \times 10^{-7}$	2836	2805				
	R3	$5.00 \times 10^{-7}$	2153	2143				
Storage tank D02	R1	$1.00 \times 10^{-5}$	45	44	$6.52 \times 10^6$	5.17	$6.44 \times 10^6$	5.06
	R2	$5.00 \times 10^{-7}$	2554	2538				
	R3	$5.00 \times 10^{-7}$	1941	1906				
LNG vaporizer E01	R1	$1.00 \times 10^{-3}$	15	12	$2.13 \times 10^2$	0.22	$1.33 \times 10^2$	0.14
	R3	$5.00 \times 10^{-5}$	15	12				
Fuel gas heater E02	R1	$1.00 \times 10^{-3}$	7	5	$4.06 \times 10^3$	0.25	$9.49 \times 10^2$	0.07
	R3	$5.00 \times 10^{-5}$	64	31				
BOG pre-heater E03	R1	$1.00 \times 10^{-3}$	7	5	$4.59 \times 10^3$	0.27	$4.33 \times 10^3$	0.24
	R3	$5.00 \times 10^{-5}$	68	66				
BOG compressor P01	R4	$1.00 \times 10^{-3}$	7	5	$3.17 \times 10^3$	0.37	$3.00 \times 10^3$	0.33
	R5	$1.00 \times 10^{-4}$	56	55				
LNG bunker line S04	R4	$6.00 \times 10^{-4}$	131	126	$3.05 \times 10^5$	28.59	$2.86 \times 10^5$	26.62
	R5	$6.00 \times 10^{-5}$	553	535				
BOG bunker line S03	R4	$6.00 \times 10^{-4}$	14	5	$4.41 \times 10^3$	0.38	$3.88 \times 10^3$	0.25
	R5	$6.00 \times 10^{-5}$	66	62				
<b>c) V-LNG fuel system onboard ship</b>								
Process Unit	LOC	$Cf(1/y)$	Parameter					
			$h$ (m)	$e$ (m)	UPI (m <sup>2</sup> )	UHI (m <sup>2</sup> /y)	UPD (m <sup>2</sup> )	UHD (m <sup>2</sup> /y)
Storage tank D01	R1	$1.00 \times 10^{-5}$	81	78	$4.00 \times 10^6$	3.53	$3.92 \times 10^6$	3.45
	R2	$5.00 \times 10^{-7}$	1714	1690				
	R3	$5.00 \times 10^{-7}$	2000	1980				
LNG vaporizer E01	R1	$1.00 \times 10^{-3}$	58	55	$1.03 \times 10^4$	3.88	$9.76 \times 10^3$	3.49
	R3	$5.00 \times 10^{-5}$	102	99				
Fuel gas heater E02	R1	$1.00 \times 10^{-3}$	7	5	$4.06 \times 10^3$	0.25	$1.27 \times 10^3$	0.09
	R3	$5.00 \times 10^{-5}$	64	36				
BOG pre-heater E03	R1	$1.00 \times 10^{-3}$	5	5	$2.16 \times 10^3$	0.13	$1.97 \times 10^3$	0.12
	R3	$5.00 \times 10^{-5}$	47	44				
BOG compressor P01	R4	$1.00 \times 10^{-3}$	7	5	$3.17 \times 10^3$	0.37	$3.00 \times 10^3$	0.33
	R5	$1.00 \times 10^{-4}$	56	55				

Table B5: Calculated damage distances ( $h$ ), escalation distances ( $e$ ) and unit KPIs for each LOC and process unit in each block of Concept C, based on the utilization of IFO. Equipment tags and features are reported in Figure 18 and Table B2 respectively.

<b>a) S-IFO shore-based storage facility</b>								
Process Unit	Parameter							
	LOC	$C_f(1/y)$	$h$ (m)	$e$ (m)	UPI (m <sup>2</sup> )	UHI (m <sup>2</sup> /y)	UPD (m <sup>2</sup> )	UHD (m <sup>2</sup> /y)
Storage tank T01 – T06	R1	$1.00 \times 10^{-4}$	35	16				
	R2	$5.00 \times 10^{-6}$	634	301	$4.02 \times 10^5$	4.11	$9.08 \times 10^4$	0.92
	R3	$5.00 \times 10^{-6}$	629	297				
Bunker pumps G01 – G02	R4	$5.00 \times 10^{-4}$	93	32	$2.95 \times 10^4$	7.27	$5.36 \times 10^3$	1.05
	R5	$1.00 \times 10^{-4}$	172	73				
Bunker hose S01	R4	$6.00 \times 10^{-4}$	94	35	$8.57 \times 10^4$	10.46	$1.74 \times 10^4$	1.79
	R5	$6.00 \times 10^{-5}$	293	132				
<b>b) B-IFO auxiliary bunker vessel</b>								
Process Unit	Parameter							
	LOC	$C_f(1/y)$	$h$ (m)	$e$ (m)	UPI (m <sup>2</sup> )	UHI (m <sup>2</sup> /y)	UPD (m <sup>2</sup> )	UHD (m <sup>2</sup> /y)
Storage tank T01 – T07	R1	$1.00 \times 10^{-4}$	35	16				
	R2	$5.00 \times 10^{-6}$	191	69	$3.63 \times 10^4$	0.48	$4.79 \times 10^3$	0.07
	R3	$5.00 \times 10^{-6}$	189	67				
Bunker pump G01	R4	$5.00 \times 10^{-4}$	31	5	$5.18 \times 10^4$	5.66	$7.73 \times 10^3$	0.79
	R5	$1.00 \times 10^{-4}$	228	88				
Bunker hose S02	R4	$6.00 \times 10^{-4}$	78	27	$7.69 \times 10^4$	8.23	$1.42 \times 10^4$	1.30
	R5	$6.00 \times 10^{-5}$	277	119				
<b>c) V-IFO fuel system onboard ship</b>								
Process Unit	Parameter							
	LOC	$C_f(1/y)$	$h$ (m)	$e$ (m)	UPI (m <sup>2</sup> )	UHI (m <sup>2</sup> /y)	UPD (m <sup>2</sup> )	UHD (m <sup>2</sup> /y)
Storage tank D01 – D02	R1	$1.00 \times 10^{-4}$	29	10				
	R2	$5.00 \times 10^{-6}$	237	107	$5.16 \times 10^4$	0.59	$1.06 \times 10^4$	0.11
	R3	$5.00 \times 10^{-6}$	235	105				
Transfer pump G01	R4	$5.00 \times 10^{-4}$	26	9	$5.79 \times 10^3$	0.93	$7.05 \times 10^2$	0.11
	R5	$1.00 \times 10^{-4}$	76	27				
Settling tank D03 – D04	R1	$1.00 \times 10^{-5}$	51	20				
	R2	$5.00 \times 10^{-7}$	114	44	$1.30 \times 10^4$	0.04	$1.97 \times 10^3$	0.01
	R3	$5.00 \times 10^{-7}$	89	28				
Feed pump G02	R4	$5.00 \times 10^{-4}$	33	5	$6.20 \times 10^3$	1.16	$7.38 \times 10^2$	0.09
	R5	$1.00 \times 10^{-4}$	79	27				
Heater E01	R1	$1.00 \times 10^{-3}$	33	13	$6.14 \times 10^3$	1.42	$7.27 \times 10^2$	0.2
	R3	$5.00 \times 10^{-5}$	78	27				
Daily tank D05 – D06	R1	$1.00 \times 10^{-5}$	59	25				
	R2	$5.00 \times 10^{-7}$	123	53	$1.51 \times 10^4$	0.05	$2.85 \times 10^3$	0.01
	R3	$5.00 \times 10^{-7}$	104	33				
Booster pump G03	R4	$5.00 \times 10^{-4}$	59	5	$6.26 \times 10^3$	2.37	$7.93 \times 10^2$	0.09
	R5	$1.00 \times 10^{-4}$	79	28				
Heater E02	R4	$1.00 \times 10^{-3}$	34	5	$6.09 \times 10^3$	1.48	$7.31 \times 10^2$	0.06
	R5	$5.00 \times 10^{-5}$	78	27				

Table B6: Calculated damage distances ( $h$ ), escalation distances ( $e$ ) and unit KPIs for each LOC and process unit in each block of Concept D, based on the utilization of MGO. Equipment tags and features are reported in Figure 18 and Table B3 respectively.

<b>a) S-MGO shore-based storage facility</b>								
Process Unit	Parameter							
	LOC	$C_f(1/y)$	$h$ (m)	$e$ (m)	UPI (m <sup>2</sup> )	UHI (m <sup>2</sup> /y)	UPD (m <sup>2</sup> )	UHD (m <sup>2</sup> /y)
Storage tank T01 – T06	R1	$1.00 \times 10^{-4}$	27	5				
	R2	$5.00 \times 10^{-6}$	707	319	$5.00 \times 10^5$	5.05	$1.02 \times 10^5$	1.01
	R3	$5.00 \times 10^{-7}$	703	315				
Bunker pumps G01/G02	R4	$5.00 \times 10^{-4}$	65	21	$7.60 \times 10^4$	9.74	$9.01 \times 10^3$	1.12
	R5	$1.00 \times 10^{-4}$	276	95				
Bunker hose S01	R4	$6.00 \times 10^{-4}$	139	49	$1.89 \times 10^5$	22.92	$3.32 \times 10^4$	3.41
	R5	$6.00 \times 10^{-5}$	435	182				
<b>b) B-MGO auxiliary bunker vessel</b>								
Process Unit	Parameter							
	LOC	$C_f(1/y)$	$h$ (m)	$e$ (m)	UPI (m <sup>2</sup> )	UHI (m <sup>2</sup> /y)	UPD (m <sup>2</sup> )	UHD (m <sup>2</sup> /y)
Storage tank T01 – T07	R1	$1.00 \times 10^{-4}$	27	5				
	R2	$5.00 \times 10^{-6}$	188	65	$3.54 \times 10^4$	0.42	$4.24 \times 10^3$	0.04
	R3	$5.00 \times 10^{-6}$	186	62				
Bunker pump G01	R4	$5.00 \times 10^{-4}$	32	5	$4.74 \times 10^4$	5.26	$6.12 \times 10^3$	0.62
	R5	$1.00 \times 10^{-4}$	218	78				
Bunker hose S02	R4	$6.00 \times 10^{-4}$	76	26	$3.01 \times 10^4$	5.31	$4.27 \times 10^3$	0.67
	R5	$6.00 \times 10^{-5}$	173	65				
<b>c) V-MGO fuel system onboard ship</b>								
Process Unit	Parameter							
	LOC	$C_f(1/y)$	$h$ (m)	$e$ (m)	UPI (m <sup>2</sup> )	UHI (m <sup>2</sup> /y)	UPD (m <sup>2</sup> )	UHD (m <sup>2</sup> /y)
Storage tank D01 – D02	R1	$1.00 \times 10^{-4}$	23	5				
	R2	$5.00 \times 10^{-6}$	167	56	$2.79 \times 10^4$	0.33	$3.14 \times 10^3$	0.03
	R3	$5.00 \times 10^{-6}$	166	54				
Transfer pump G01	R4	$5.00 \times 10^{-4}$	28	5	$6.65 \times 10^3$	1.05	$6.82 \times 10^2$	0.08
	R5	$1.00 \times 10^{-4}$	82	26				
Settling tank D03 – D04	R1	$1.00 \times 10^{-5}$	52	20				
	R2	$5.00 \times 10^{-7}$	116	43	$1.35 \times 10^4$	0.04	$1.89 \times 10^3$	0.01
	R3	$5.00 \times 10^{-7}$	106	32				
Feed pump G02	R4	$5.00 \times 10^{-4}$	32	5	$6.72 \times 10^3$	1.19	$7.12 \times 10^2$	0.08
	R5	$1.00 \times 10^{-4}$	82	27				
Heater E01	R1	$1.00 \times 10^{-3}$	32	5	$6.56 \times 10^3$	1.36	$6.95 \times 10^2$	0.06
	R3	$5.00 \times 10^{-5}$	81	26				
Daily tank D05 – D06	R1	$1.00 \times 10^{-5}$	59	25				
	R2	$5.00 \times 10^{-7}$	122	51	$1.48 \times 10^4$	0.05	$2.55 \times 10^3$	0.01
	R3	$5.00 \times 10^{-7}$	106	32				
Booster pump G03	R4	$5.00 \times 10^{-4}$	53	5	$6.00 \times 10^3$	1.99	$6.98 \times 10^2$	0.08
	R5	$1.00 \times 10^{-4}$	77	26				
Heater E02	R4	$1.00 \times 10^{-3}$	36	5	$5.85 \times 10^3$	1.61	$6.31 \times 10^2$	0.06
	R5	$5.00 \times 10^{-5}$	77	25				

### B.3 Sensitivity analysis for the management modification factor

Monte Carlo method (Metropolis and Ulam, 1949) was hereby applied to assess how the variation of weight factors needed for the combination of TEC2O scores (see Eq. 6.17 and Eq. 6.18) affected the calculated  $f'_L$  values and, eventually, the risk figures. The sensitivity analysis was carried out considering a beta distribution of random weight values for the operational and organizational indicators scores (terms  $wOp_n$  and  $wOr_p$  in Eq. 6.17 and Eq. 6.18), considering a  $\pm 50\%$  variation from the equalitarian weight initially assigned. A total of  $10^4$  combinations was considered (the analysis was also repeated considering  $10^5$  combinations to ensure results convergence). Following the variation of operational and organizational score weights,  $MMF$  values were re-calculated, obtaining new  $f'_L$  frequency values. The weight value of term  $\psi$  in Eq. 6.19 was kept constant, thus giving the same relevance to operational and organizational aspects.

Different combinations of  $wOp_n$  and  $wOr_p$  weights were explored for the sensitivity analysis, with values ranging between 0.125 and 0.375, to account for a different priority of the managerial aspects considered. The effects of such modifications are reported in the box plots of Figure B1 for TEC2O-Good and TEC2O-Bad management situations. Frequency modification factors were calculated for the process units considered in Table 15.

It can be noted that differences from the frequency modification factor obtained considering an equal set of weights are limited to a maximum 0.02 difference (see Figure B1a, for TEC2O-Good case), whereas this difference is larger for the modification factor relative to the transfer hoses when considering the TEC2O-Bad management situation (see Figure B1b), for which a maximum 0.634 positive difference can be achieved. The variability range of the frequency modification factor reported in Figure B1a results the same for all the four process units assessed since operational and organizational indicators scores were assumed identical for the TEC2O-Good management situation. Conversely, the different score of factor #1 (that considers the number of SIMOPs performed in a month) attributed to transfer hoses S01/S02 and bunker manifolds S3/S4 is responsible for the diverse range of values that the frequency modification factor can get considering the TEC2O-Bad situation, since it negatively affects the operational subfactor of the hoses.

Considering this latter management situation, the maximum positive deviations from original frequency modification factor values are about 27% for transfer hoses and manifolds and 22% for storage tank and transfer pumps, as illustrated in Figure B1b. Nevertheless, up to 75% of the estimated frequency modification factor values for storage tank and transfer pumps will be just 6% greater than the modification factor calculated with equal weights (i.e., 1.189 as reported in Table 20) while for the transfer hoses and manifolds 75% of the estimated values will have a positive difference from the original modification factor value up to 0.16. Considering the ideal management situation, the probability of having a positive difference is again around 50%, and up to 75% of the estimated frequency modification factor values will be lower than 0.175 as can be seen in Figure B1a. For this management situation, the maximum increase of the modification factor is slightly higher than 10% with respect to the original value calculated considering an equal value for  $wOp_n$  and  $wOr_p$  weights.

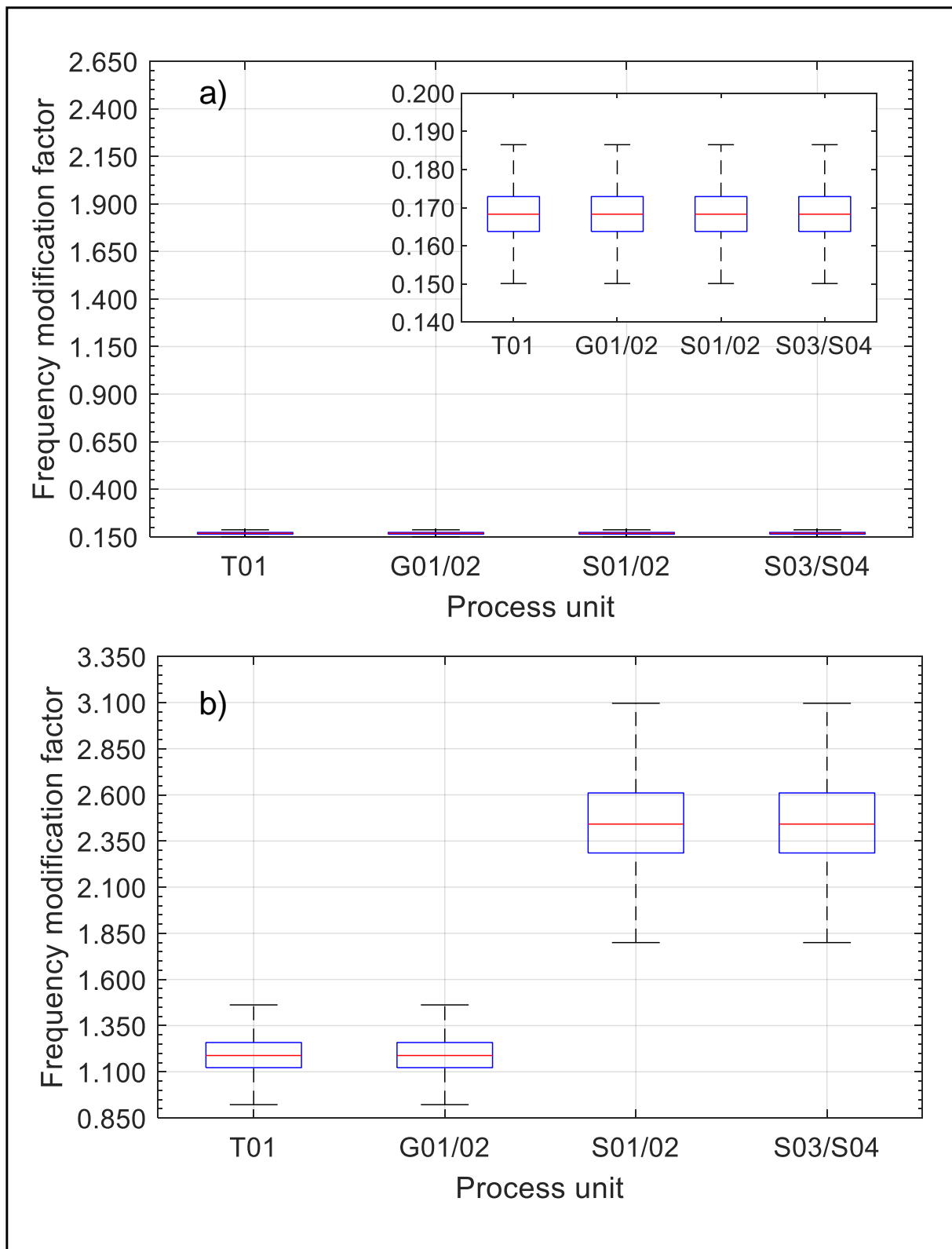


Figure B1: Results of Monte Carlo sensitivity analysis. Panel a) refers to TEC20 – Good management situation; panel b) refers to TEC20 – Bad management situation. Bottom and top edges of the blue box indicate the 25<sup>th</sup> and 75<sup>th</sup> percentiles respectively. The whiskers extend to the most extreme data points.

## B.4 Dangerous scenario frequencies

The complete list of dangerous scenario frequencies calculated with Eq. 6.25 is reported in Table B7 and Table B8 for limited and unlimited releases, respectively. The tables report scenario frequencies calculated for the baseline bunkering case and for TEC2O Good and TEC2O Bad management situations.

Table B7: Calculated dangerous scenario frequencies for limited releases. JF: Jet Fire; FF: Flash Fire.

Process unit	LOC Type	Scenario	TEC2O - Good	Baseline	TEC2O - Bad
			Frequency [ev./y]		
Tank T1	R1	JF	$1.453 \times 10^{-11}$	$8.640 \times 10^{-11}$	$1.027 \times 10^{-10}$
		FF	$2.179 \times 10^{-9}$	$1.296 \times 10^{-8}$	$1.541 \times 10^{-8}$
Transfer pump G01 A/B	R4	JF	$2.317 \times 10^{-8}$	$1.378 \times 10^{-7}$	$1.638 \times 10^{-7}$
		FF	$4.930 \times 10^{-7}$	$2.931 \times 10^{-6}$	$3.486 \times 10^{-6}$
	R5	JF	$8.864 \times 10^{-9}$	$5.270 \times 10^{-8}$	$6.268 \times 10^{-8}$
		FF	$2.187 \times 10^{-7}$	$1.300 \times 10^{-6}$	$1.547 \times 10^{-6}$
LNG hose S1	R4	JF	$4.185 \times 10^{-9}$	$2.488 \times 10^{-8}$	$6.086 \times 10^{-8}$
		FF	$3.738 \times 10^{-7}$	$5.295 \times 10^{-7}$	$9.296 \times 10^{-6}$
	R5	JF	$2.092 \times 10^{-9}$	$1.244 \times 10^{-8}$	$3.043 \times 10^{-8}$
		FF	$2.023 \times 10^{-7}$	$3.567 \times 10^{-7}$	$4.873 \times 10^{-6}$
BOG hose S2	R4	JF	$4.185 \times 10^{-10}$	$2.488 \times 10^{-9}$	$6.086 \times 10^{-9}$
		FF	$3.126 \times 10^{-7}$	$1.642 \times 10^{-7}$	$8.410 \times 10^{-6}$
	R5	JF	$2.092 \times 10^{-8}$	$1.244 \times 10^{-7}$	$3.043 \times 10^{-7}$
		FF	$2.005 \times 10^{-7}$	$3.535 \times 10^{-7}$	$2.916 \times 10^{-6}$
LNG manifold S3	R4	JF	$4.375 \times 10^{-10}$	$2.602 \times 10^{-9}$	$6.363 \times 10^{-9}$
		FF	$3.635 \times 10^{-7}$	$3.902 \times 10^{-7}$	$9.327 \times 10^{-6}$
	R5	JF	$9.901 \times 10^{-10}$	$5.887 \times 10^{-9}$	$1.440 \times 10^{-8}$
		FF	$9.575 \times 10^{-8}$	$1.688 \times 10^{-7}$	$2.306 \times 10^{-6}$
BOG manifold S4	R4	JF	$4.375 \times 10^{-10}$	$2.602 \times 10^{-9}$	$6.363 \times 10^{-9}$
		FF	$3.023 \times 10^{-7}$	$2.601 \times 10^{-8}$	$8.436 \times 10^{-6}$
	R5	JF	$9.901 \times 10^{-10}$	$5.887 \times 10^{-9}$	$1.440 \times 10^{-8}$
		FF	$8.843 \times 10^{-8}$	$1.253 \times 10^{-7}$	$2.199 \times 10^{-6}$

Table B8: Calculated dangerous scenario frequencies for unlimited releases. JF: Jet Fire; FF: Flash Fire; PF: Pool Fire.

Process unit	LOC Type	Scenario	TEC20 - Good	Baseline	TEC20 - Bad
			Frequency [ev./y]		
Tank T1	R1	PF	$2.287 \times 10^{-12}$	$1.360 \times 10^{-11}$	$1.617 \times 10^{-11}$
		FF	$3.431 \times 10^{-10}$	$2.040 \times 10^{-9}$	$2.426 \times 10^{-9}$
Transfer pump G01 A/B	R4	PF	$3.647 \times 10^{-9}$	$2.168 \times 10^{-8}$	$2.579 \times 10^{-8}$
		FF	$7.760 \times 10^{-8}$	$4.614 \times 10^{-7}$	$5.487 \times 10^{-7}$
	R5	PF	$1.395 \times 10^{-9}$	$8.296 \times 10^{-9}$	$9.866 \times 10^{-9}$
		FF	$3.443 \times 10^{-8}$	$2.047 \times 10^{-7}$	$2.434 \times 10^{-7}$
LNG hose S1	R4	PF	$6.587 \times 10^{-10}$	$3.917 \times 10^{-9}$	$9.579 \times 10^{-9}$
		FF	$5.883 \times 10^{-8}$	$8.334 \times 10^{-8}$	$1.463 \times 10^{-6}$
	R5	PF	$3.294 \times 10^{-10}$	$1.958 \times 10^{-9}$	$4.790 \times 10^{-9}$
		FF	$3.185 \times 10^{-8}$	$5.615 \times 10^{-8}$	$7.670 \times 10^{-7}$
BOG hose S2	R4	PF	$6.587 \times 10^{-11}$	$3.917 \times 10^{-10}$	$9.579 \times 10^{-10}$
		FF	$4.920 \times 10^{-8}$	$2.585 \times 10^{-8}$	$1.324 \times 10^{-6}$
	R5	PF	$3.294 \times 10^{-9}$	$1.958 \times 10^{-8}$	$4.790 \times 10^{-8}$
		FF	$3.362 \times 10^{-8}$	$6.786 \times 10^{-8}$	$7.900 \times 10^{-7}$
LNG manifold S3	R4	PF	$6.887 \times 10^{-11}$	$4.095 \times 10^{-10}$	$1.002 \times 10^{-9}$
		FF	$5.723 \times 10^{-8}$	$6.142 \times 10^{-8}$	$1.468 \times 10^{-6}$
	R5	PF	$1.559 \times 10^{-10}$	$9.267 \times 10^{-10}$	$2.266 \times 10^{-9}$
		FF	$1.507 \times 10^{-8}$	$2.657 \times 10^{-8}$	$3.630 \times 10^{-7}$
BOG manifold S4	R4	JF	$6.887 \times 10^{-11}$	$4.095 \times 10^{-10}$	$1.002 \times 10^{-9}$
		FF	$4.758 \times 10^{-8}$	$4.095 \times 10^{-9}$	$1.328 \times 10^{-6}$
	R5	JF	$1.559 \times 10^{-10}$	$9.267 \times 10^{-10}$	$2.266 \times 10^{-9}$
		FF	$1.392 \times 10^{-8}$	$1.972 \times 10^{-8}$	$3.462 \times 10^{-7}$

# Appendix C - One-dimensional transient heat conduction analysis

A one-dimensional transient model was used to calculate the temperature profile evolution inside the vacuumed perlite insulation of cryogenic bullet tanks studied in Chapter 7. The main objective of this analysis was to understand the dynamics of heat transfer across an undamaged layer of insulating material, estimating the time needed for the temperature effects generated by a full engulfing fire to cross all the tank insulating layer. The initial and boundary conditions are the same considered for the setup of case V66 (see Table 24) i.e., a linear temperature gradient between ambient condition (16 °C) and saturation temperature of nitrogen at 2 bar. The flame temperature is considered equal to 860°C.

As can be seen from Figure C1, a thermal steady state inside the insulation is not reached even after 1 hour of fire exposure. By applying the penetration theory for a semi-infinite slab (see Eq. C1), it is possible to express the time ( $t$ ) needed for temperature effects to cross all the insulation thickness ( $\delta$ ) as follows:

$$t = \frac{\delta^2}{16 \cdot \alpha} \tag{Eq. C1}$$

where  $\alpha$  is the thermal diffusivity of perlite, considered equal to  $1.314 \times 10^{-6} \text{ m}^2/\text{s}$ . Substituting the insulation thickness of the experimental tank, reported in Section 7.1.1, the required time is estimated in 2,900 s (around 48 minutes). This result supports the assumption made in Section 7.2.3 for which a degradation of insulation performance is one possible explanation for the increased pressurization rate exhibited by the tank during the experimental fire test.

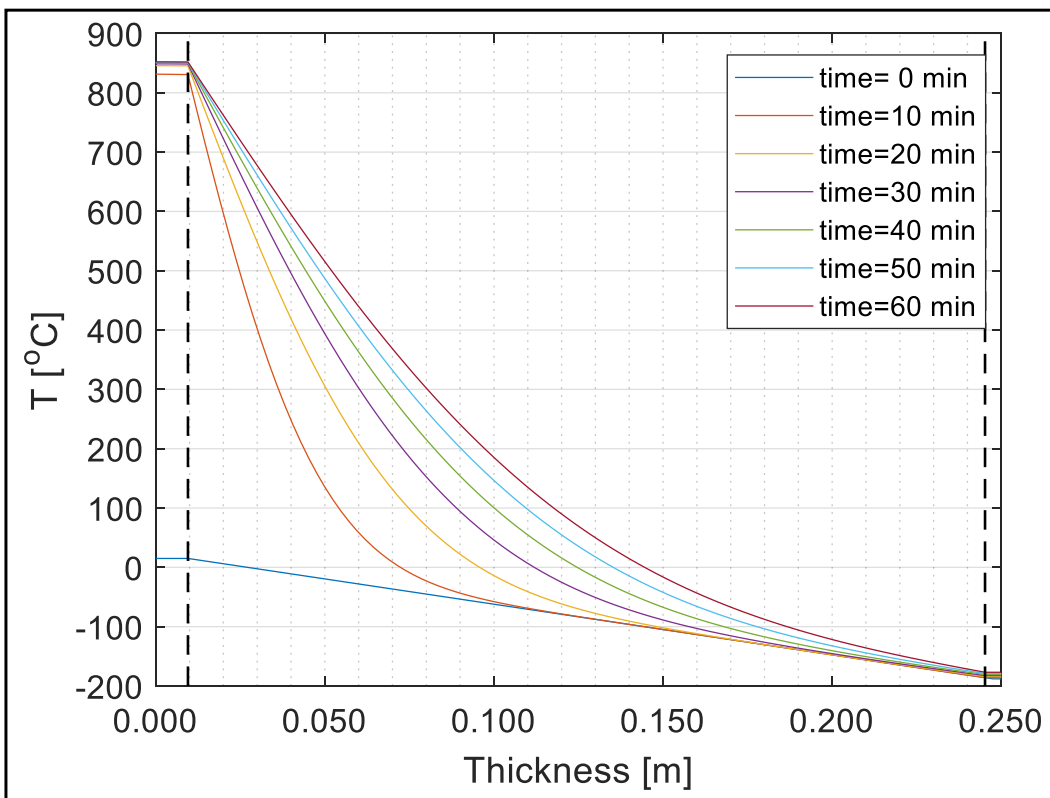


Figure C1: Transient thermal profile inside vacuumed perlite insulation (200 mbar) exposed to fire conditions. Vertical dashed lines delimit the extent of insulating material.

# Appendix D - Additional CFD results

## D.1 Cases A85 and B85

The results reported in this appendix are analogous to those presented in Section 7.3.2 for the cases A50 and B50. The extent of evaporation and condensation clusters inside the tank lading are shown in Figure D1 for three reference time steps (panels A1-A3 for case A85 and B1-B3 for case B85). The evaporation regions appear to be smaller than those highlighted in Figure 46 for both case A85 and B85. These results may be linked to the slower pressurization rate of storage tanks with a higher filling degree, as seen in Figure 45. A reduction of condensation zones in the bulk region of case B85 (panel B2) can be observed compared to analogous results of case B50.

The dynamic evolution of the velocity field inside the tank is illustrated in panels A1-A3 and B1-B3 of Figure D2. The macroscopic flow patterns identified in Figure 48 can still be found in cases A85 and B85. Compared to results from cases A50 and B50, the maximum predicted velocity magnitude is about 20% higher for case A85 and 30% lower for case B85.

Liquid temperature contour plots are reported in panels A1-A3 and B1-B3 of Figure D3 while temperature and velocity profiles are illustrated in Figure D4.

## D.2 Cases A15 and B15

The evaporation and condensation regions inside the tank lading are depicted in Figure D1 for three reference time steps (panels A4-A6 and B4-B6). Compared to the situation reported in Figure 46, the extent of evaporation zones for lower filling degrees is much higher and an evaporation cluster can be found in proximity of tank wall, close to the interface, already after 30 minutes of fire exposure. Process conditions of case B15 seems to be more favourable for the evaporation process than those encountered in case A15. The greater extension of evaporating regions for lower liquid levels can be correlated to the faster pressurization dynamic observed for these cases.

The dynamic evolution of the velocity field inside the tank is illustrated in Figure D2 (panels A4-A6 for case A15 and B4-B6 for case B15). The lower liquid level induces the formation of one or two macroscopic recirculation eddies. A radial flow from the tank walls toward the axis can still be observed at vapour-liquid interface as well as a bigger recirculation swirl located close to the tank bottom. Compared to results from cases A50 and B50, the maximum predicted velocity magnitude is about 20% higher for case A15 and 30% lower for case B15.

Figure D5 shows the time evolution of temperature and velocity profiles, whereas relevant contour plots showing the liquid temperature stratification are shown in panels A4-A6 and B4-B6 of Figure D3 for case A15 and B15, respectively. From the comparison of the different cases reported in Figure D3, it is evident how a lower tank filling degree results in a less thermal-stratified lading. Regardless of the amount of stratification, liquid temperature gradients measured along the tank axis do not exceed 1.3 K, while warmer liquid tends to accumulate at the vapour-liquid interface close to tank wall. In this spot, next to the tank wall, liquid temperatures can be up to 15 degrees higher than the colder bulk.

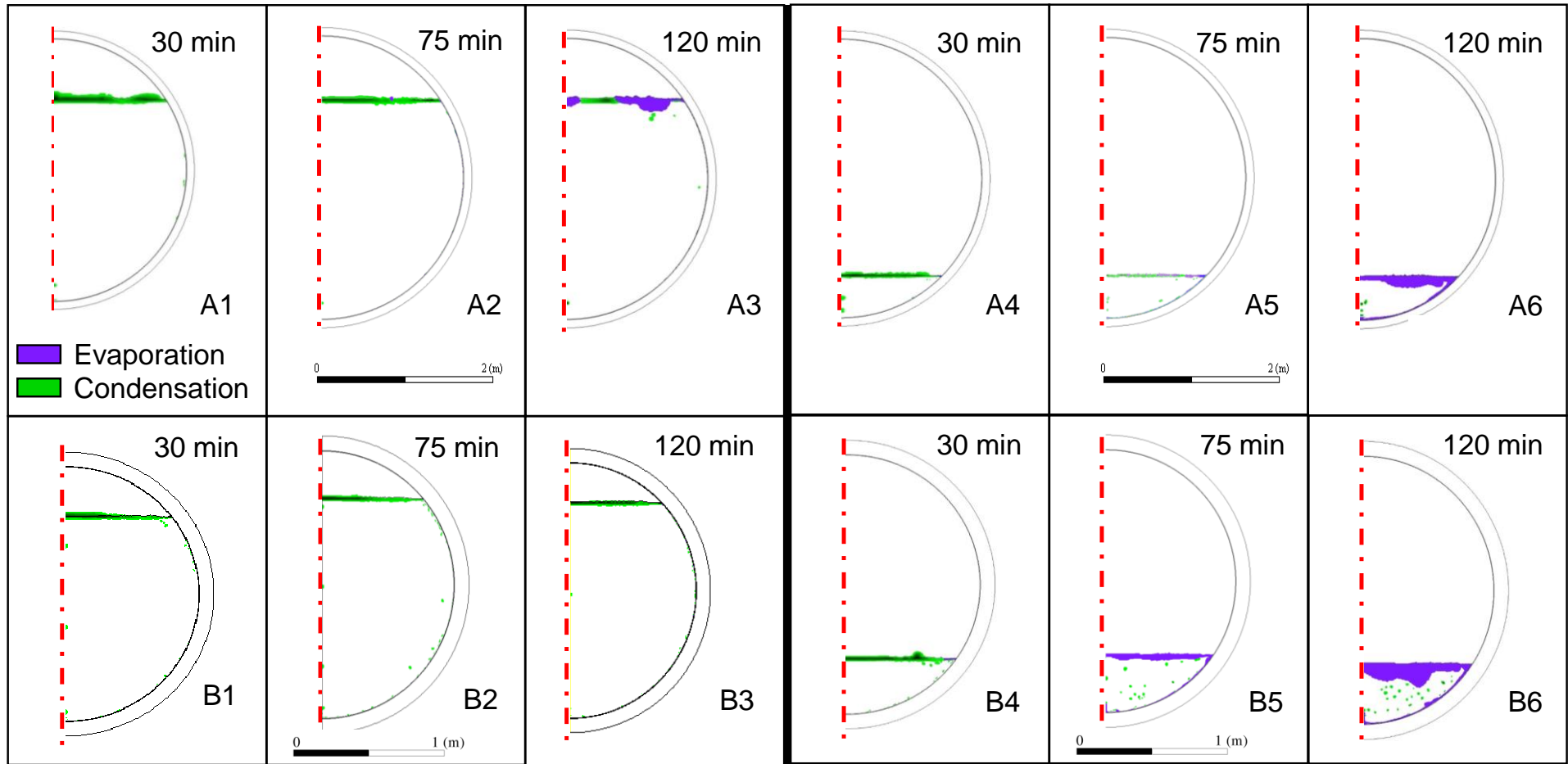


Figure D1: Time evolution of condensation and evaporation regions inside tank lading for cases A85 (A1-A3); B85 (B1-B3); A15 (A4-A6) and B15 (B4-B6).

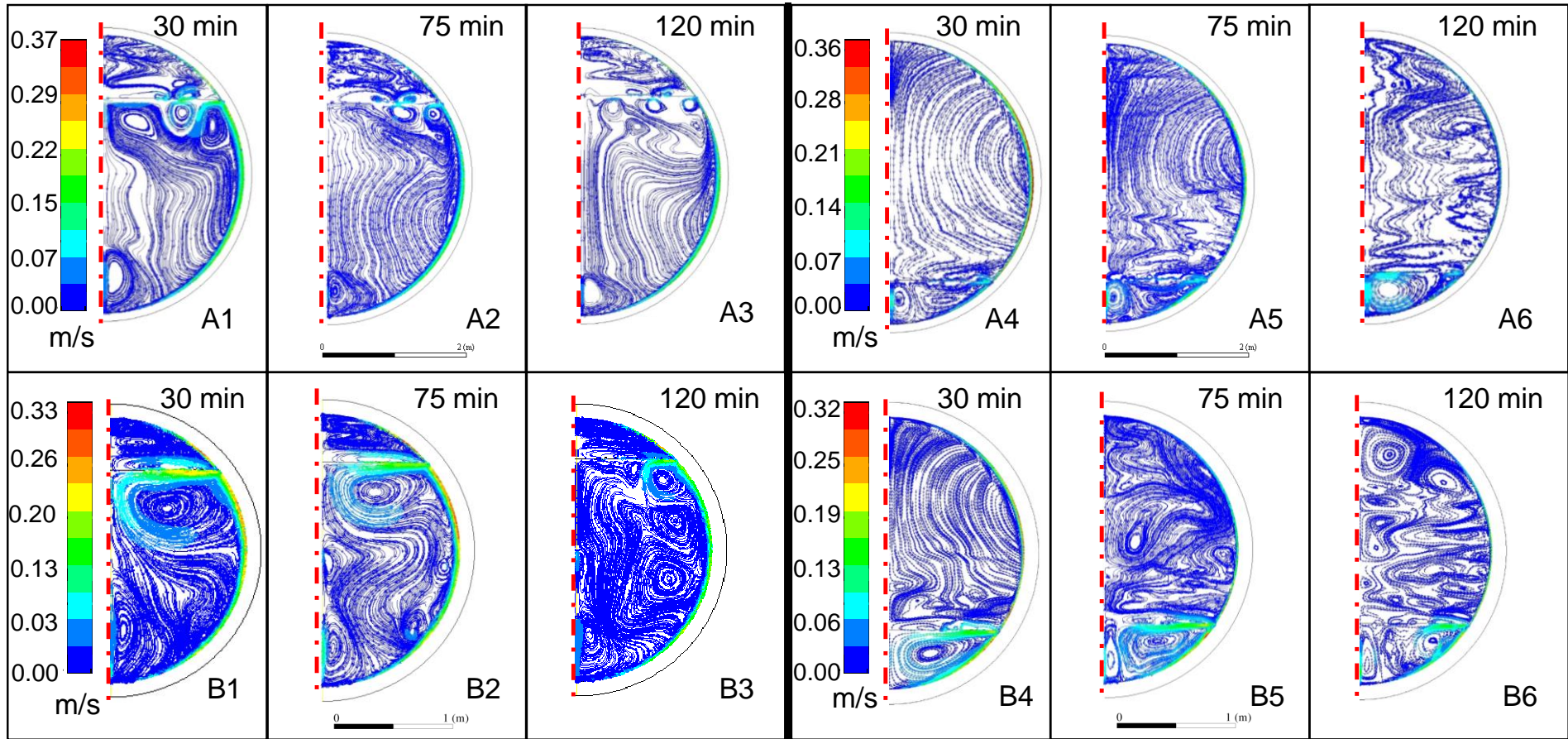


Figure D2: Velocity magnitude path-lines for cases A85 (A1-A3); B85 (B1-B3); A15 (A4-A6) and B15 (B4-B6) at different times.

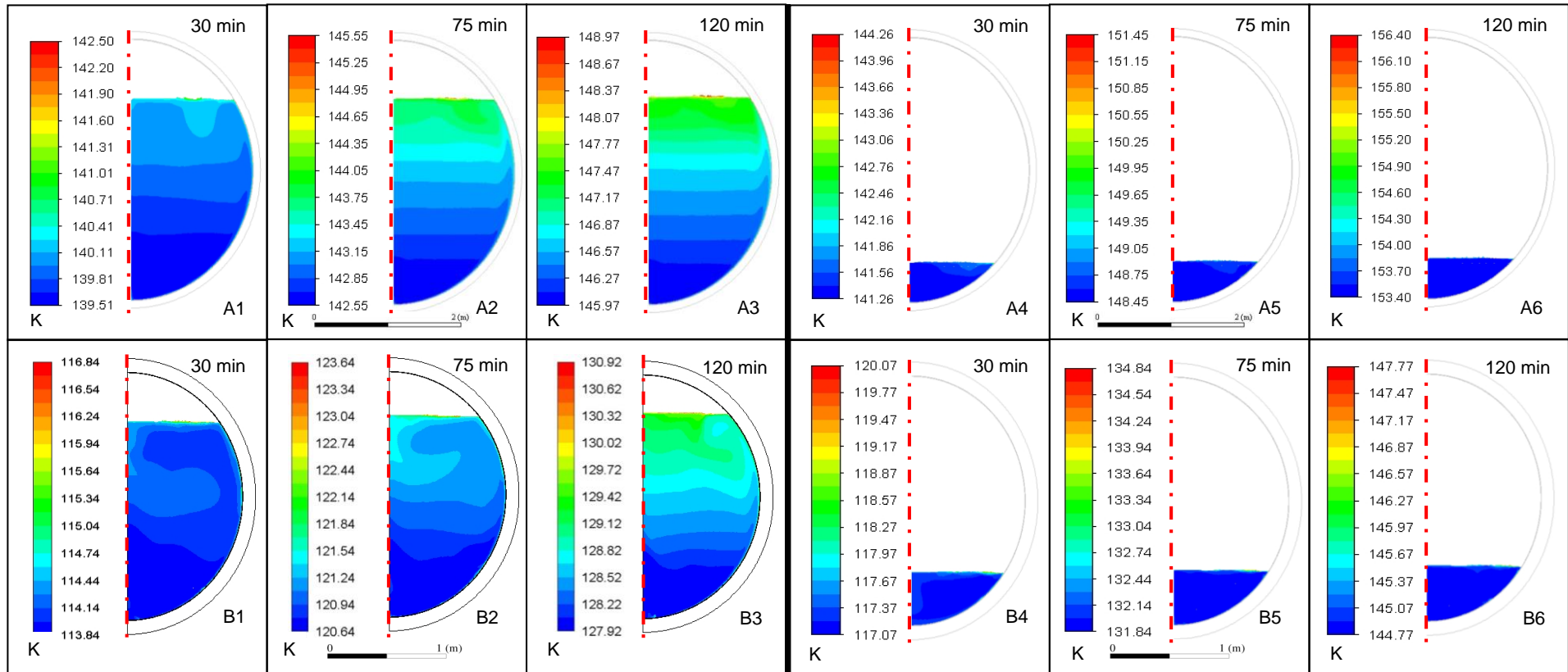


Figure D3: Liquid temperature contour plots for cases A85 (A1-A3); B85 (B1-B3); A15 (A4-A6) and B15 (B4-B6) at different times.

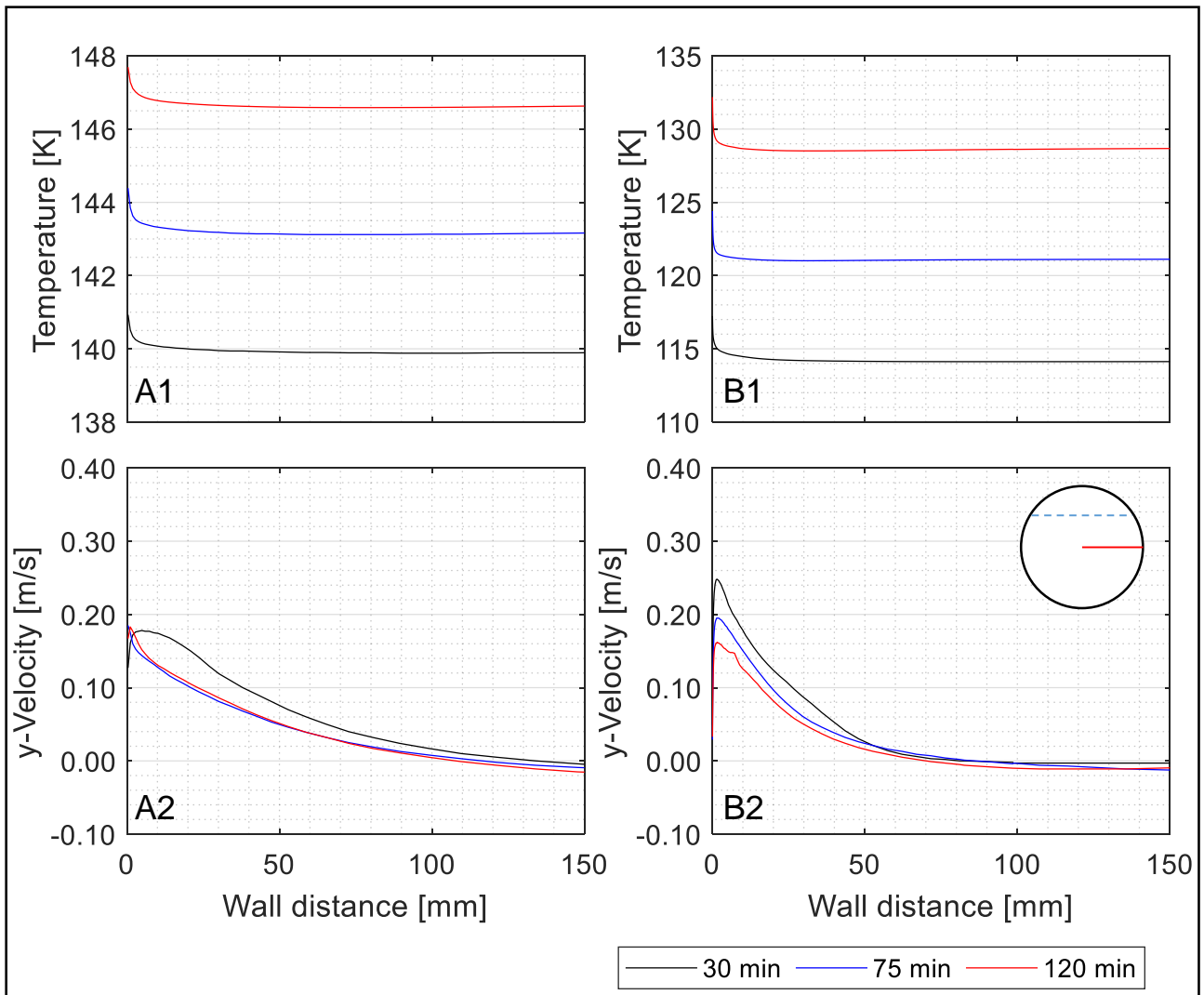


Figure D4: Comparison of thermal and vertical velocity profiles at different time steps for cases A85 (panels A1 and A2) and B85 (panels B1 and B2). Data refer to the tank horizontal centreline (horizontal segment in the sketch). The dashed segment indicates the tank filling degree.

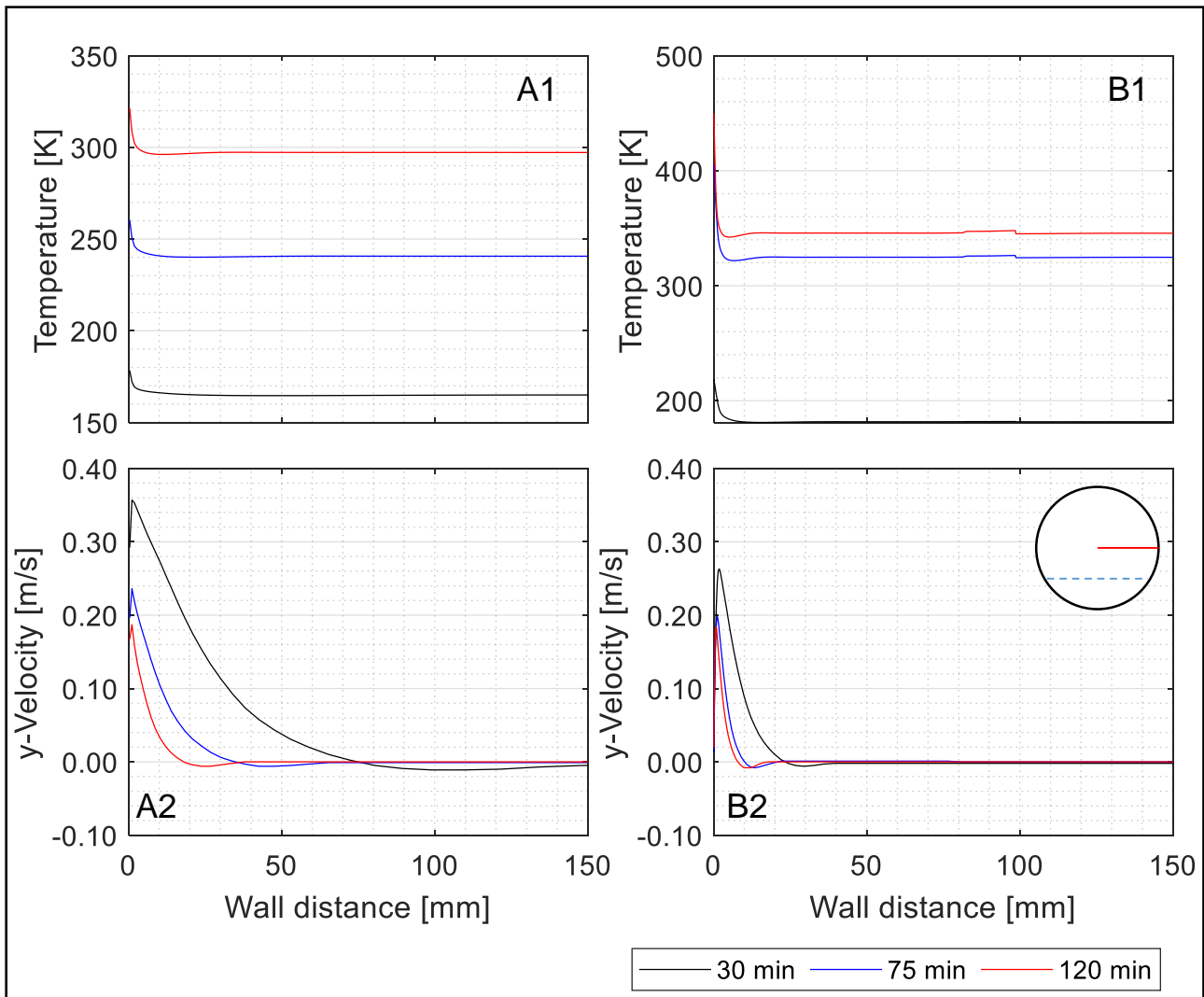


Figure D5: Comparison of thermal and vertical velocity profiles at different time steps for cases A15 (panels A1 and A2) and B15 (panels B1 and B2). Data refer to the tank horizontal centreline (horizontal segment in the sketch). The dashed segment indicates the tank filling degree.

### D.3 FDS modelling results for cases HP-1 and HP-2

Results showed in this Section refer to the CFD modelling of LNG pool fires occurring inside gas fuelled FPR as described in Chapter 8. More in detail, the results reported are relative to cases HP-1 and HP-2 (see Table 31) that describe the dynamics of pool fires originating following a release involving the HP fuel pumps featured in the HPDF fuel system.

The time variation of gas species concentration inside the FPR is illustrated in Figure D6. As can be seen, oxygen concentration steadily decreases with time for case HP-1, whereas an equilibrium value seems to be reached for case HP-2 (Ventilation On) after around 55 seconds from fire ignition. Looking at the methane concentration value, it can be noted that for case HP-1, the concentration grows constantly, entering in the flammability range around 60 second after fire start, about 10 seconds earlier than the analogous case LP-1 (see Figure 64). This result suggests that for case HP-1 the pool fire self-extinguishes due to oxygen deprivation, as no fresh air inlet from the ventilation system is considered in this case, nevertheless LNG continues to evaporate from the pool, thus raising the methane concentration inside the FPR. In line with results from cases LP-1 and LP-2, the CO<sub>2</sub> concentration appears to be less influenced by the operating mode of the ventilation system.

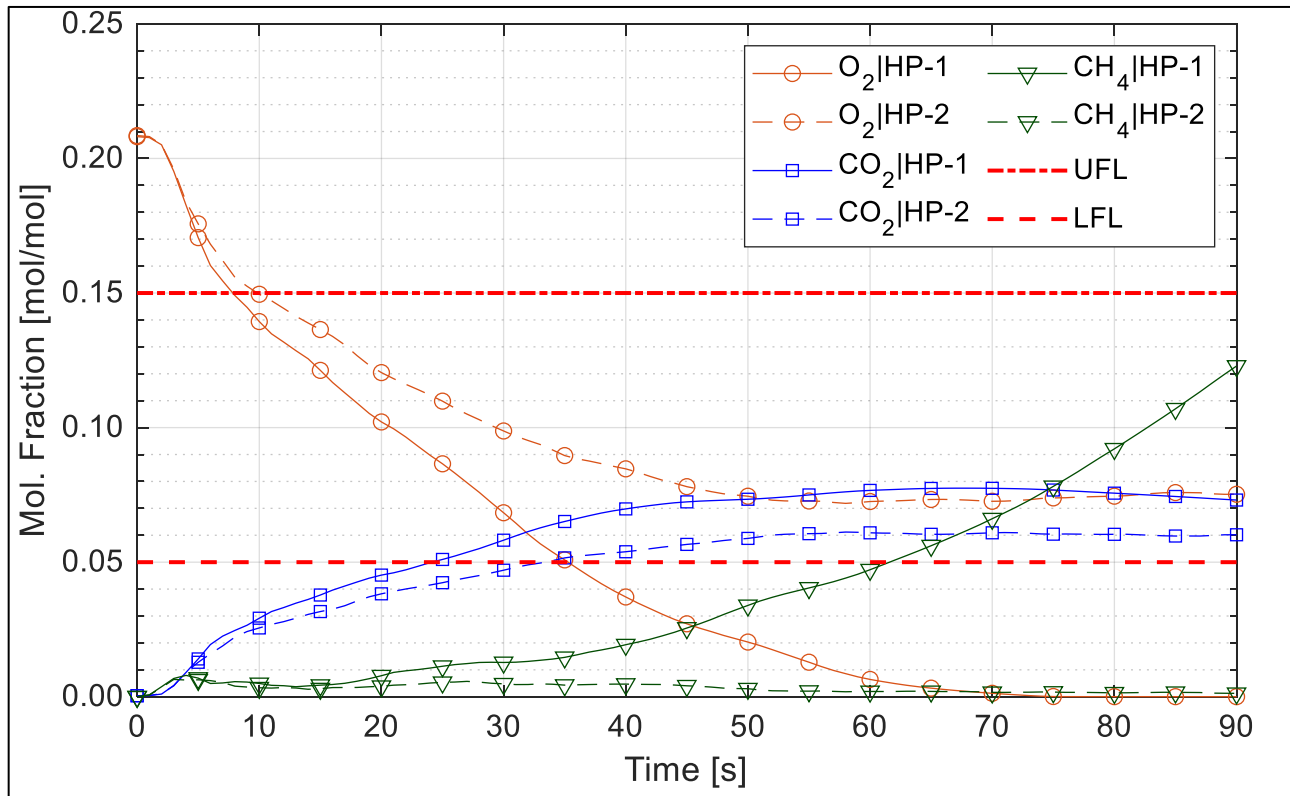


Figure D6: Comparison of the concentration profiles of different gas species involved in the combustion process for cases HP-1 and HP-2.

As expected, slightly higher *HRR* values were predicted for cases HP-1 and HP-2 because of bigger pool dimensions.

As showed in Figure D7, when the oxygen concentration plunges below 6% vol., the enclosure pool fire begins to grow weaker, eventually dying out before 90 seconds. Conversely, for case HP-2, for which air is introduced inside the FPR, the *HRR* decreases progressively, until reaching an equilibrium value around 35,000 kW that is about 54% of the modelled peak value of 65,000 kW reached during the initial phases of combustion.

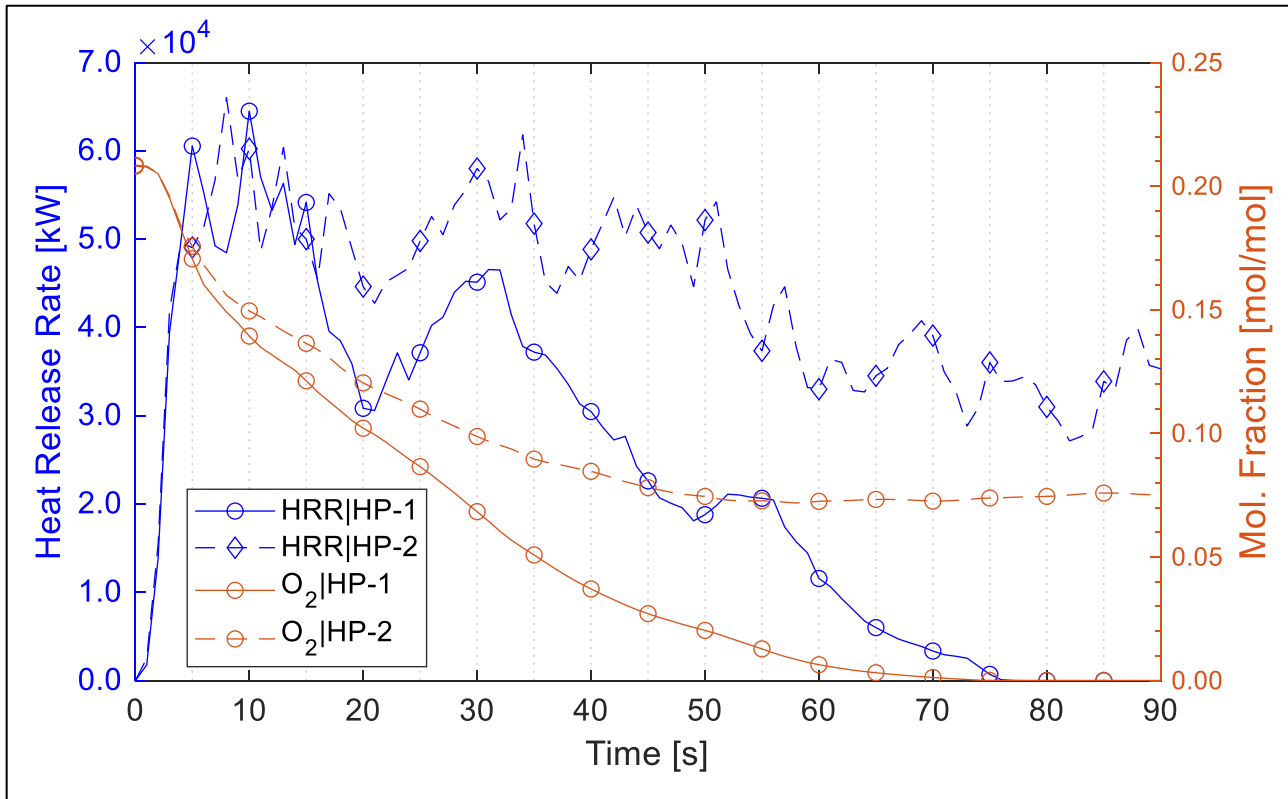


Figure D7: Comparison of the HRR for cases HP-1 and HP-2. The secondary y-axis shows the oxygen concentration.

Time-averaged values of the incident radiation heat flux predicted for a mechanically ventilated FPR are illustrated in Figure D8. Heat flux results evaluated at different heights obtained for LPDF and HPDF systems are compared. Generally, LPDF values are lower than correspondent measures for HPDF, possibly because of the smaller dimensions of LP-2 pool fire. Except for values predicted below 3 m height (excluded), the time-averaged radiation heat flux initially decreases with distance starting from  $Y=0$ , while at lower heights the heat flux value increases as it gets closer to the pool fire centre (located at  $Y=3$  m), then it stabilises in a range between 25 and 75  $\text{kW/m}^2$ , eventually to slightly rise again approaching the end of the FPR. As a general trend, the predicted heat flux increases with height as hot combustion gases form a layer in proximity of the FPR ceiling, contributing to increase thermal radiation at higher locations. The exception is represented by the array of measuring points located 0.3 metres above the ground, which predicted higher fluxes than points 1 metre high.

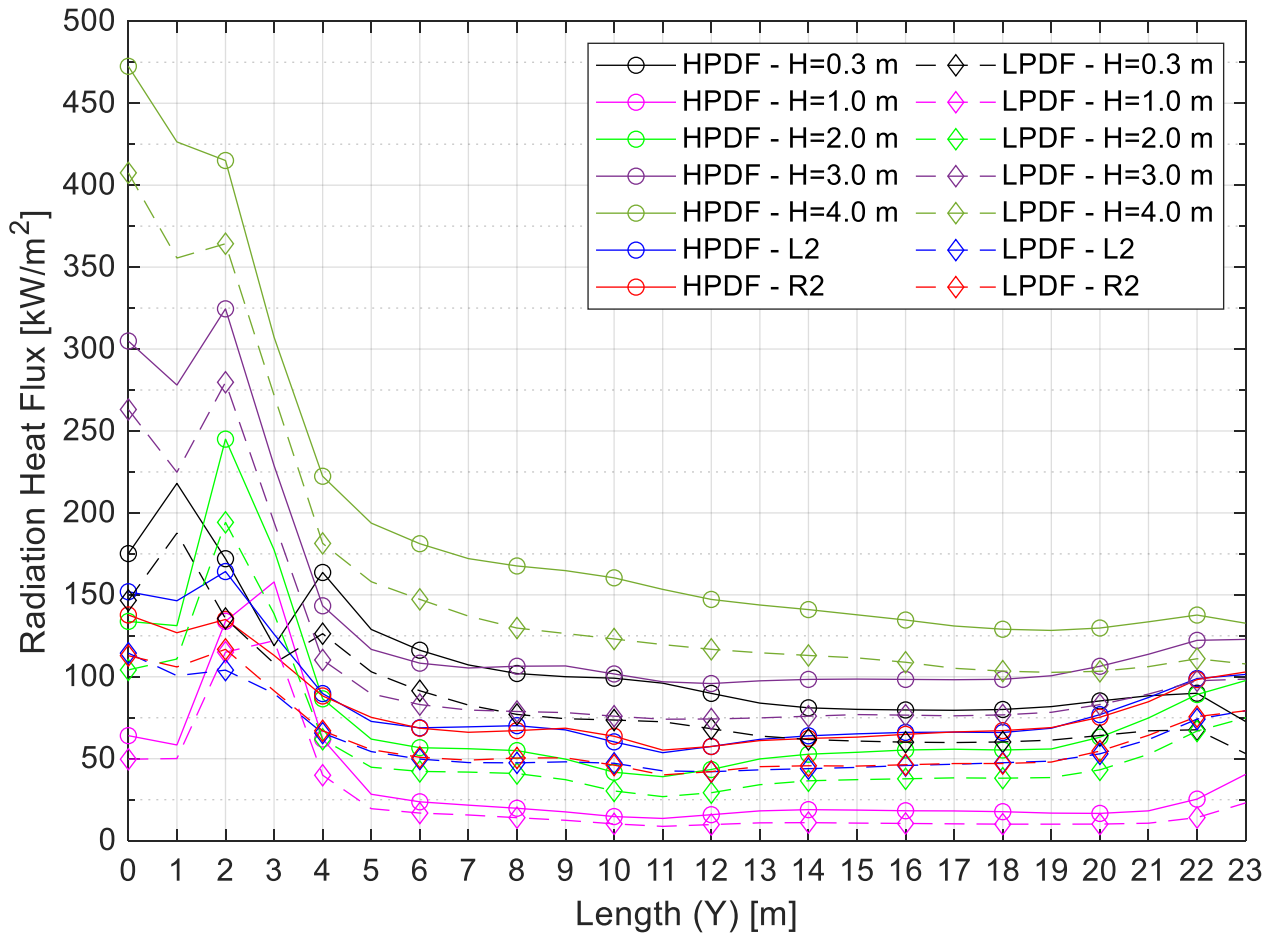


Figure D8: Comparison of time-averaged radiation heat flux measured at different locations for cases HP-2 and LP-2. See Figure 60 for the distribution scheme of measuring devices used in the simulations.

Additional incident radiation heat flux values evaluated at the boundaries of the enclosure are reported in Figure D9. Data for cases HP-1 and HP-2, obtained at different time steps, are reported, together with flame visualization, to better understand the fire dynamics. It must be noted that smoke was not represented in the figure for ease of illustration. As expected, the FPR ceiling, impinged in flames, receive the highest amounts of radiation. Furthermore, the effect of the ventilation systems is evident from the comparison of panels a and c: in this latter case, which considers fresh air inlet, the better combustion results in a higher *HRR* and higher heat fluxes received by the boundaries as a consequence. On the other hand, the effects of oxygen deprivation can be noted looking at panel b that clearly shows a smaller fire if compared to case HP-2 shown in panel d. Lastly, the effect of hot gases layering can be inferred by looking at radiation contours on the Z-Y plane: higher radiation values are predicted closer to the ceiling, where hot combustion gases tend to accumulate.

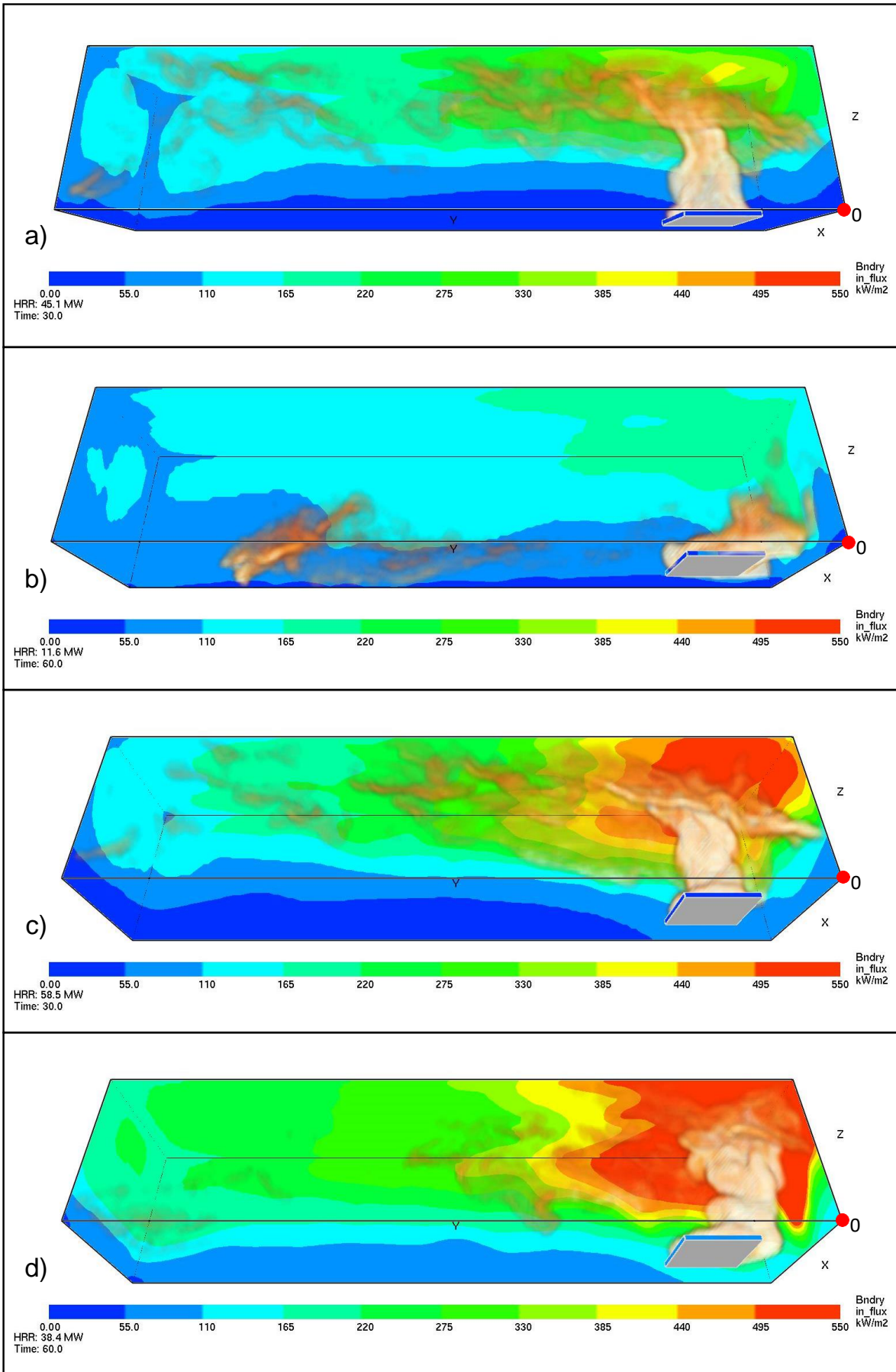


Figure D9: Overview of the incident radiation heat flux evaluated at FPR boundaries at various time steps for cases HP-1 (panels a & b) and HP-2 (panels c & d).